THE FIBER BUNDLE

EDITED BY: Ferenc Kun, Alex Hansen, Purusattam Ray and Srutarshi Pradhan
PUBLISHED IN: Frontiers in Physics

frontiers Research Topics

ISSN 1664-8714
ISBN 978-2-88974-011-6
DOI 10.3389/978-2-88974-011-6

About Frontiers

Frontiers is more than just an open-access publisher of scholarly articles: it is a pioneering approach to the world of academia, radically improving the way scholarly research is managed. The grand vision of Frontiers is a world where all people have an equal opportunity to seek, share and generate knowledge. Frontiers provides immediate and permanent online open access to all its publications, but this alone is not enough to realize our grand goals.

Frontiers Journal Series

The Frontiers Journal Series is a multi-tier and interdisciplinary set of open-access, online journals, promising a paradigm shift from the current review, selection and dissemination processes in academic publishing. All Frontiers journals are driven by researchers for researchers; therefore, they constitute a service to the scholarly community. At the same time, the Frontiers Journal Series operates on a revolutionary invention, the tiered publishing system, initially addressing specific communities of scholars, and gradually climbing up to broader public understanding, thus serving the interests of the lay society, too.

Dedication to Quality

Each Frontiers article is a landmark of the highest quality, thanks to genuinely collaborative interactions between authors and review editors, who include some of the world's best academicians. Research must be certified by peers before entering a stream of knowledge that may eventually reach the public - and shape society; therefore, Frontiers only applies the most rigorous and unbiased reviews.
Frontiers revolutionizes research publishing by freely delivering the most outstanding research, evaluated with no bias from both the academic and social point of view. By applying the most advanced information technologies, Frontiers is catapulting scholarly publishing into a new generation.

What are Frontiers Research Topics?

Frontiers Research Topics are very popular trademarks of the Frontiers Journals Series: they are collections of at least ten articles, all centered on a particular subject. With their unique mix of varied contributions from Original Research to Review Articles, Frontiers Research Topics unify the most influential researchers, the latest key findings and historical advances in a hot research area! Find out more on how to host your own Frontiers Research Topic or contribute to one as an author by contacting the Frontiers Editorial Office: frontiersin.org/about/contact

THE FIBER BUNDLE

Topic Editors:
Ferenc Kun, University of Debrecen, Hungary
Alex Hansen, Norwegian University of Science and Technology, Norway
Purusattam Ray, Institute of Mathematical Sciences, India
Srutarshi Pradhan, Norwegian University of Science and Technology, Norway

Citation: Kun, F., Hansen, A., Ray, P., Pradhan, S., eds. (2021). The Fiber Bundle. Lausanne: Frontiers Media SA. doi: 10.3389/978-2-88974-011-6

Table of Contents

frontiers in Physics

EDITORIAL
published: 18 November 2021
doi: 10.3389/fphy.2021.795803

Editorial: The Fiber Bundle

Alex Hansen[1]*, *Ferenc Kun*[2], *Srutarshi Pradhan*[1] and *Purusattam Ray*[3]

[1]PoreLab and Department of Physics, Norwegian University of Science and Technology, Trondheim, Norway, [2]Department of Theoretical Physics, Doctoral School of Physics, Faculty of Science and Technology, University of Debrecen, Debrecen, Hungary, [3]The Institute of Mathematical Sciences, Chennai, India

Keywords: fiber bundle model, damage, fracture, statistical physics, materials science

Editorial on the Research Topic

The Fiber Bundle

A long time has passed since Fredrick Thomas Peirce, an Australian physicist working for the British Cotton Industry Research Association, published the paper *Tensile tests for cotton yarns: "the weakest link" theorems on the strength of long and of composite specimens* in 1926 [1]. In it, he describes a simplified model for failure of yarn where the variations of the strength in the yarn competes with increased load it carries when there is a failure. Here it is in modern language: Imagine a set of fibers of equal length clamped between two parallel stiff plates. The fibers all have the same elastic constant, so that when the plates are moved apart, all the fibers carry the same load, which is the total load on the plates divided by the number of fibers. Assume each fiber has its own strength, that is the maximum load it can carry before it fails irreversibly. As the fibers fail one by one, the load on the remaining fibers increases as there are fewer and fewer left to share the total load.

Such a model seems overly simple. It cannot possibly contribute to our understanding of fracture phenomena! The mathematical statistician Henry Daniels did not think so. He did his PhD on the strength of fiber bundles and in 1945 he published a seminal paper on his work that moves the model beyond the strength of yarn [2], reshaping it into a general model for failure processes. Up to the point when he published his paper, we find six papers referring to the Peirce paper [1].[1] In the decade that follows 1945, there are 35 references to the Peirce paper, but the titles have now changed. We find e.g., "*The Fracture of Metals*" [3].[2]

It is in the seventies that the fiber bundle model really gains traction within the mechanics community [4]. Together with the statistics community, the subtleties of the model is gradually uncovered, while at the same time variants of it is being proposed, e.g., the *Local Load Sharing Model* [5].[3]

The statistical physics community, those with a background in critical phenomena, had in the mid eighties began to discover that fracture in fact is a very interesting problem with properties that sometimes created a *déjà vu* feeling among them [6]. This resulted in the creating of the *Fuse Network Model* [7]. This was network of fuses, e.g. a square lattice, where each link would be a fuse with a trip current drawn from some statistical distribution. What would happen when the current running through this network was increased? A lot of things would happen: there would be avalanches of fuses blowing simultaneously, there would be localization, i.e., the fuses that blew would be concentrated in some region, there would be instabilities where suddenly a crack of blown fuses would form zipping through the network. The problem with the fuse model, however, was that it was

OPEN ACCESS

Edited and reviewed by:
Daniel Bonamy, Commissariat à l'Energie Atomique et aux Energies Alternatives (CEA), France

***Correspondence:**
Alex Hansen
Alex.Hansen@ntnu.no

Specialty section:
This article was submitted to Interdisciplinary Physics, a section of the journal Frontiers in Physics

Received: *15 October 2021*
Accepted: *27 October 2021*
Published: *18 November 2021*

Citation:
Hansen A, Kun F, Pradhan S and Ray P (2021) Editorial: The Fiber Bundle. Front. Phys. 9:795803. doi: 10.3389/fphy.2021.795803

[1]There is one exception among the six: "*A Study of the Moisture in Soybeans*" [11]. The reference to Peirce is for a property of cellulose fibers he mentions unrelated to the model.

[2]Peirce is lauded in Reference [3] for his paper [1] being the first discussion strength as extreme value problem, and not for his model.

[3]The original Peirce model is by now called the *Global Load Sharing Model*.

almost impossible to approach it analytically—it was a model for the computer, and the computer only. The book by Herrmann and Roux from 1990 (and reprinted in 2014) covers the status of the field at that time [6].

In 1989 Sornette published a paper entitled *Elasticity and Failure of a Set of Elements Loaded in Parallel* [8]. This was the entrance of the fiber bundle model into the statistical physics community. It was the perfect model in some sense. It was almost as rich as the fuse network model, but it was at the same time simple enough to be analytically tractable to a considerable degree. In some sense, the fiber bundle model is gaining a status in the physics of fracture community similar to that of the Ising model in the critical phenomena community. Two reviews of the fiber bundle model have appeared in this community [9, 10]. There are hundreds of papers, if not more, that have appeared over the last years in this field.

The aim of this Research Topic has been to display some of the richness of ideas and uses that the fiber bundle model has produced. The eleven papers it contains does indeed do that. Hopefully, the research papers among them spawn new work and the reviews are useful for those that considers entering this field.

We describe the papers in the order in which they have been published.

The first paper (Kjellstadli) concerns the burst distribution in the global load sharing fiber bundle model. Earlier work had determined it for large bursts, but here Kjellstadli finds it for small bursts. This is important as large bursts are rare compared to small bursts so that the statistics is much better for the latter.

The second paper (Capelli et al.) uses the fiber bundle model to investigate failure of layers of snow, failures that can lead to avalanches.

Paper three (Domanski) implements the local load sharing fiber bundle model on a small-world network. The avalanches that are generated in such networks may be very relevant for other systems that has an underlying small-world structure, such as the financial markets.

Paper four (Hansen) is a review of the extreme value distributions, which are central for the fiber bundle model. Rather than approaching the subject in the traditional way, the entire review is built around the formula $\lim_{n\to\infty}(1 + x/n)^n = \exp(x)$.

Paper five (Chakrabarti et al.) is a review of how the dynamics in the fiber bundle model generates cooperativity. The failure dynamics has been demonstrated through recursion relations and their fixed-point solutions. In addition, the authors analyze the noise-induced failure dynamics through theory, simulation, and real data (Earthquake catalog) analysis discussing also the emergence of self-organizing mechanism in the model.

Paper six (Halász et al.) generalizes the fiber bundle model in order to describe the mechanical response of systems which undergo a sequence of stick-slip cycles like granular packings, biological materials, or tectonic plates. With analytic calculations and computer simulations the authors explore the capabilities of the approach.

Paper seven (Arango-Restrepo et al.) introduces heat exchange with the surroundings and thereby place the fiber bundle model in a thermodynamical context. This is important for the use of the fiber bundle model for e.g. polymeric systems.

Paper eight (Roy and Biswas) considers the energy avalanche statistics in the local load sharing fiber bundle model. A non-linear relation of the avalanche size and the released elastic energy is established and a scale free energy distribution is revealed with a high degree of robustness.

Paper nine (Engelbrecht-Wiggans and Phoenix) places the fibers in an elastically responding matrix in order to model creep rupture in fiber-reinforced composites.

Paper ten (Dębski et al.) tests out a prediction based on the fiber bundle model for when catastrophic failure of a loaded structure is imminent. The authors use a discrete element system to demonstrate that indeed the fiber bundle model prediction holds.

Paper eleven (Roy) constructs the phase diagram of the fiber bundle model in the three-dimensional parameter space of threshold disorder, range of load sharing, and system size. He explores the complex phase structure of the model and characterizes the emerging failure modes.

AUTHOR CONTRIBUTIONS

All authors have made a substantial, direct and intellectual contribution to the work, and approved it for publication.

FUNDING

This work was supported by the Research Council of Norway through its Centres of Excellence funding scheme, project number 262644 and it was supported by the National Research, Development and Innovation Fund of Hungary, financed under the 2020-4.1.1-TKP2020 funding scheme Project no. TKP2020-NKA-04 and K 119967.

REFERENCES

1. Peirce FT. 32-X.-Tensile Tests for Cotton Yarns v.-"The Weakest Link" Theorems on the Strength of Long and of Composite Specimens. *J Textile Inst Trans* (1926) 17:T355–T368. doi:10.1080/19447027.1926.10599953
2. Daniels HE. The Statistical Theory of the Strength of Bundles of Threads. I. *Proc R Soc Lond A* (1945) 183:405–35. doi:10.1098/rspa.1945.0011
3. Petch NJ. The Fracture of Metals. *Prog Metal Phys* (1954) 5:1–52. doi:10.1016/0502-8205(54)90003-9
4. Harlow DG, Phoenix SL. The Chain-Of-Bundles Probability Model for the Strength of Fibrous Materials I: Analysis and Conjectures. *J Compos Mater* (1978) 12:195–214. doi:10.1177/002199837801200207
5. Harlow DG, Phoenix SL. Approximations for the Strength Distribution and Size Effect in an Idealized Lattice Model of Material Breakdown. *J Mech Phys Sol* (1991) 39:173–200. doi:10.1016/0022-5096(91)90002-6
6. Herrmann HJ, Roux S. *Statistical Models for the Fracture of Disordered media*. ISBN 0444–88551x. Amsterdam: Elsevier (2014).
7. de Arcangelis L, Redner S, Herrmann HJ. A Random Fuse Model for Breaking Processes. *J Phyique Lett* (1985) 46:585–90. doi:10.1051/jphyslet:019850046013058500

8. Sornette D. Elasticity and Failure of a Set of Elements Loaded in Parallel. *J Phys A: Math Gen* (1989) 22:L243–L250. doi:10.1088/0305-4470/22/6/010
9. Pradhan S, Hansen A, Chakrabarti BK. Failure Processes in Elastic Fiber Bundles. *Rev Mod Phys* (2010) 82:499–555. doi:10.1103/RevModPhys.82.499
10. Hansen A, Hemmer PC, Pradhan S. *The Fiber Bundle Model: Modeling Failure in Materials*. ISBN: 978-3-527-41214-3. Weinheim: Wiley-VCH (2015).
11. Beckel AC, Earle FR. Study of Moisture in Soybeans. *Ind Eng Chem Anal Ed* (1941) 13:40–3. doi:10.1021/i560089a013

Conflict of Interest: The authors declare that the research was conducted in the absence of any commercial or financial relationships that could be construed as a potential conflict of interest.

Publisher's Note: All claims expressed in this article are solely those of the authors and do not necessarily represent those of their affiliated organizations, or those of the publisher, the editors and the reviewers. Any product that may be evaluated in this article, or claim that may be made by its manufacturer, is not guaranteed or endorsed by the publisher.

frontiers in Physics

ORIGINAL RESEARCH
published: 28 November 2019
doi: 10.3389/fphy.2019.00201

Burst Distribution by Asymptotic Expansion in the Equal Load Sharing Fiber Bundle Model

*Jonas T. Kjellstadli**

PoreLab, Department of Physics, Norwegian University of Science and Technology, Trondheim, Norway

We derive an asymptotic series expansion for the burst size distribution in the equal load sharing fiber bundle model, a predominant model for breakdown in disordered media. Earlier calculations give expressions with correct asymptotic behavior for large bursts, but low accuracy for small bursts, up to an order of magnitude off. The approximations from the expansion we present here give relative errors of at most several percent when compared with exact results or simulation results for large systems. We also solve the burst size distribution exactly for the Weibull threshold distributions.

Keywords: fiber bundle model, equal load sharing, asymptotic series expansion, fracture, burst size distribution

OPEN ACCESS

Edited by:
Ferenc Kun,
University of Debrecen, Hungary

Reviewed by:
Soumyajyoti Biswas,
Max-Planck-Institute for Dynamics and Self-Organisation, Max Planck Society (MPG), Germany
Federico Bosia,
University of Turin, Italy

***Correspondence:**
Jonas T. Kjellstadli
jonas.kjellstadli@outlook.com

Specialty section:
This article was submitted to Interdisciplinary Physics, a section of the journal Frontiers in Physics

Received: *09 September 2019*
Accepted: *11 November 2019*
Published: *28 November 2019*

Citation:
Kjellstadli JT (2019) Burst Distribution by Asymptotic Expansion in the Equal Load Sharing Fiber Bundle Model. Front. Phys. 7:201. doi: 10.3389/fphy.2019.00201

1. INTRODUCTION

The fiber bundle model [1–4] is a prime example of what Bouchaud calls a metaphorical model [5]; that is, a model which reveals mechanisms that lie hidden beneath layers of complexity in realistic models and are completely lost in phenomenological models. Even in its simplest form, the *equal load sharing* (ELS) model, the number of papers written on the fiber bundle model may now be counted in the thousands. This is evidence of great richness.

The distribution of bursts, or avalanches, is important in the study of fiber bundle models. Its behavior can signal how close the bundle is to catastrophic failure, even in single samples [6]. There are many variations of the fiber bundle model, but we will only study the ELS model here. We will also limit ourselves to continuous (i.e., infinitesimal) load increase; finite load increases gives a different distribution of bursts [7, 8].

For the ELS model with continuous load increase, Hemmer and Hansen [9] demonstrated that bursts follow a power law with an exponent 5/2 for a wide class of disorder distributions. Sornette [10] derived this power law behavior separately with a different approach. This work was followed up Pradhan et al. [6, 11], who showed that the power law exponent changes to 3/2 as the bundle is approaching catastrophic failure. Raischel et al. [12] showed that this kind of crossover is present also in the γ-model [13], which has a variable range of interaction with the equal and local load sharing model as its two limits.

By following the development of the crossover burst size—that is, the burst size that constitutes the watershed between bursts following the 5/2 law and the bursts following the 3/2 law—it is possible to quantitatively measure of how far the bundle is from collapse. However, this approach has the problem that it requires knowledge of large (and hence rare) bursts, which have poor statistics. It would be better to predict failure from the smallest bursts, which happen often and can be measured with higher accuracy. This makes it important to have access to accurate analytic estimates of these values to compare with. Hence, we provide in this article a method to analytically calculate the burst distribution accurately for small bursts.

2. THE EQUAL LOAD SHARING FIBER BUNDLE MODEL

Consider an equal load sharing fiber bundle model with N fibers [1, 2]. The externally applied force (or load) F is distributed identically on all intact fibers, and a fiber acts as Hookean spring until its elongation reaches a certain threshold, where it breaks. Due to the equal load sharing, fibers will always fail in order from smallest to largest threshold as the load increases.

The thresholds are drawn independently from a probability density $p(t)$, with a corresponding cumulative distribution $P(t) = \int_{-\infty}^{t} p(u)\mathrm{d}u$. Let $\{t_k\}$ be the ordered sequence of thresholds, such that $t_1 \leq t_2 \leq \cdots \leq t_N$. Then the force F_k required to break the kth fiber is

$$F_k = \big(N + 1 - k\big)\, t_k. \tag{1}$$

Equation (1) shows that F_k consists of two factors: the decreasing number of intact fibers $N + 1 - k$, and the increasing threshold t_k of the kth fiber. Due to the irregularities of $\{t_k\}$, F_k doesn't increase or decrease smoothly. Instead, it fluctuates up and down around a general increasing trend. Or decreasing, depending on where in the fracture process we are.

If the force F is the control parameter during the breaking process, this causes bursts (or avalanches) of several fibers that break under the same load. There is a burst of size Δ beginning with the failure of the kth fiber if $F_k > F_j$ for $j < k$, $F_{k+j} \leq F_k$ for $j < \Delta$, and $F_{k+\Delta} > F_k$. This simply means that when the force reaches F_k, Δ fibers break under that load with no further load increase required, and the burst stops at the $\Delta + 1$th fiber, which is strong enough to withstand the load.

The average of Equation (1) over samples is the load curve [4]

$$\sigma(x) = x\big[1 - P(x)\big], \tag{2}$$

which is also the limit of equation (1) as $N \to \infty$. Here $\sigma = F/N$ is the applied force per fiber in the bundle, both broken and intact, and x is the elongation of the fiber bundle. For most threshold distributions σ has a single parabolic maximum at elongation x_c, where $1 - P(x_c) = x_c p(x_c)$.

The burst distribution is usually defined as $D(\Delta)$: the expected number of bursts of size Δ during the breaking of a single fiber bundle [3, 4, 9]. This definition makes $D(\Delta) \propto N$ for large systems, and hence it diverges as $N \to \infty$. We will instead use the notation $\bar{D}(\Delta) = D(\Delta)/N$, with the physical interpretation that $\Delta\bar{D}(\Delta)$ is the fraction of fibers broken in bursts of size Δ — which converges to a finite number as $N \to \infty$.

Hemmer and Hansen [9] showed that for continuous load increase, the burst distribution to first order in N has the asymptotic behavior (as $\Delta \to \infty$)

$$\bar{D}(\Delta) \sim C\Delta^{-5/2}, \tag{3}$$

where $C = (2\pi)^{-1/2}\, x_c p(x_c)^2 \left[2p(x_c) + x_c p'(x_c)\right]^{-1}$. This result is universal for threshold distributions where the load curve has a single parabolic maximum.

Pradhan et al. [6, 11] generalized this asymptotic behavior to threshold distributions starting from a lower limit $t_0 \geq 0$, and found that there is a crossover

$$\begin{aligned}\bar{D}(\Delta) &\sim C\Delta^{-5/2}\left(1 - \mathrm{e}^{-\Delta/\Delta_c}\right) \\ &\propto \begin{cases}\Delta^{-3/2} & \text{for } \Delta \ll \Delta_c \\ \Delta^{-5/2} & \text{for } \Delta \gg \Delta_c,\end{cases}\end{aligned} \tag{4}$$

with $\Delta_c = 4\pi C^2 p(x_c)^{-2}\,(t_0 - x_c)^{-2}$ and C as in Equation (3). This crossover to a different exponent as t_0 increases has been proposed as a method to detect imminent failure [3, 6, 11].

Equation (4) is also an asymptotic behavior in the limit $\Delta \to \infty$, and hence it also requires information about large bursts (which are rare events) to predict failure. Our goal is to find a way to calculate the burst distribution accurately for small bursts, which the asymptotic expressions in Equations (3, 4) cannot do. To this end, we use a threshold distribution with a lower limit $t_0 \geq 0$. The burst distribution is then, to first order in N [4],

$$\begin{aligned}\bar{D}(\Delta) = \frac{\Delta^{\Delta-1}}{\Delta!}\int_{t_0}^{x_c}&\Big[a(t)\mathrm{e}^{-a(t)}\Big]^{\Delta} a(t)^{-1} \\ &\times\big[1 - a(t)\big]p(t)\mathrm{d}t\end{aligned} \tag{5}$$

for $t_0 < x_c$, where

$$a(t) = \frac{tp(t)}{1 - P(t)}. \tag{6}$$

At x_c, the critical elongation of Equation (2), this function satisfies $a(x_c) = 1$.

3. EXACT BURST DISTRIBUTION

Is it possible to solve the burst distribution exactly? The deciding factor is the function $a(t)$. Instead of first choosing a threshold distribution and then checking whether Equation (5) is solvable, we can instead do it in the opposite order: choose a function $a(t)$ for which the integral can be solved, and then use Equation (6) to find the corresponding threshold distribution.

3.1. Constant $a(t)$

The simplest expression would be a constant $a(t)$, which implies $a(t) = 1$ because $a(x_c) = 1$. This gives $\bar{D}(\Delta) = 0$ when inserted into Equation (5). To see why, set $a(t) = 1$ in Equation (6), which gives the differential equation

$$\frac{p'(t)}{p(t)} = -\frac{2}{t}, \tag{7}$$

with the normalized solution $P(t) = 1 - t_0/t$ for $t \in [t_0, \infty)$. This makes the load curve in Equation (2) constant: $\sigma(x) = t_0$, i.e., $x_c = t_0$. Thus, there is no burst distribution and $\bar{D}(\Delta) = 0$.

3.2. Power Law $a(t)$

Other than $a(t) = 1$, the most intuitive choice for a solvable integral is a power law $a(t) = C(k)t^k$ with $k > 0$. Inserting this into Equation (6) gives the first-order differential equation

$$p(t) + C(k)t^{k-1}P(t) = C(k)t^{k-1} \tag{8}$$

for $P(t)$. It can be solved with the integrating factor method: multiplying the equation with $\mu(t) = \exp\left(\int_{t_0}^{t} \mathrm{d}\tau\ C(k)\tau^{k-1}\right) = \exp\left[C(k)\left(t^k - t_0^k\right)/k\right]$ and integrating from t_0 to t gives the solution

$$P(t) = \frac{C(k)}{k}\left[1 - \mathrm{e}^{\frac{C(k)}{k}\left(t_0^k - t^k\right)}\right]. \tag{9}$$

Normalization on the interval $[t_0, \infty)$, i.e., $P(t = \infty) = 1$, yields $C(k)/k = 1$. Thus,

$$P(t) = 1 - \mathrm{e}^{t_0^k - t^k}, \tag{10}$$

which is a Weibull distribution with shape parameter k and a lower limit t_0. The lower limit corresponds to breaking all fibers with thresholds $t < t_0$ from a fiber bundle with $P(t) = 1 - \mathrm{e}^{-t^k}$. Hence the lower limit is equivalent to studying a bundle with $P(t) = 1 - \mathrm{e}^{-t^k}$ that has already sustained a damage $d = 1 - \mathrm{e}^{-t_0^k}$.

The Weibull distribution in Equation (10) has a critical extension $x_c = k^{-1/k}$, which gives $a(x_c) = 1$, as required for consistency. We can now solve the burst distribution exactly for the Weibull distribution. Inserting $a(t) = kt^k$ and $p(t) = kt^{k-1}\mathrm{e}^{t_0^k - t^k}$ into Equation (5) gives

$$\begin{aligned}\bar{D}(\Delta) = \frac{\Delta^{\Delta-1}}{\Delta!}\int_{t_0}^{k^{-1/k}} &\left(kt^k\mathrm{e}^{-kt^k}\right)^{\Delta}\left(kt^k\right)^{-1} \\ &\times\left(1 - kt^k\right)kt^{k-1}\mathrm{e}^{t_0^k - t^k}\mathrm{d}t.\end{aligned} \tag{11}$$

Use the substitution $z = t^k$ to get

$$\begin{aligned}\bar{D}(\Delta) = \frac{(k\Delta)^{\Delta-1}}{\Delta!}\mathrm{e}^{t_0^k}\Bigg[&\int_{t_0^k}^{1/k} z^{\Delta-1}\mathrm{e}^{-z(k\Delta+1)}\mathrm{d}z \\ &-k\int_{t_0^k}^{1/k} z^{\Delta}\mathrm{e}^{-z(k\Delta+1)}\mathrm{d}z\Bigg].\end{aligned} \tag{12}$$

Combining integration by parts and induction yields

$$\begin{aligned}\int_{t_0^k}^{1/k}\mathrm{d}z\, z^n\mathrm{e}^{-\alpha z} = \frac{n!}{\alpha^{n+1}}\Bigg[&\mathrm{e}^{-\alpha t_0^k}\sum_{i=0}^{n}\frac{\left(\alpha t_0^k\right)^i}{i!} \\ &-\mathrm{e}^{-\alpha/k}\sum_{i=0}^{n}\frac{(\alpha/k)^i}{i!}\Bigg],\end{aligned} \tag{13}$$

which gives the exact burst distribution

$$\begin{aligned}\bar{D}(\Delta) = &\frac{\Delta^{\Delta-1}\mathrm{e}^{t_0^k}}{\Delta!(k\Delta+1)}\left[\mathrm{e}^{-(\Delta+1/k)}\right. \\ &\left.-\left(kt_0^k\right)^{\Delta}\mathrm{e}^{-t_0^k(k\Delta+1)}\right] \\ &+\frac{(k\Delta)^{\Delta-1}\,\mathrm{e}^{-k\Delta t_0^k}}{\Delta(k\Delta+1)^{\Delta+1}}\sum_{i=0}^{\Delta-1}\frac{\left[(k\Delta+1)t_0^k\right]^i}{i!} \\ &-\frac{(k\Delta)^{\Delta-1}\,\mathrm{e}^{t_0^k-(\Delta+1/k)}}{\Delta(k\Delta+1)^{\Delta+1}}\sum_{i=0}^{\Delta-1}\frac{(k\Delta+1)^i}{i!k^i}.\end{aligned} \tag{14}$$

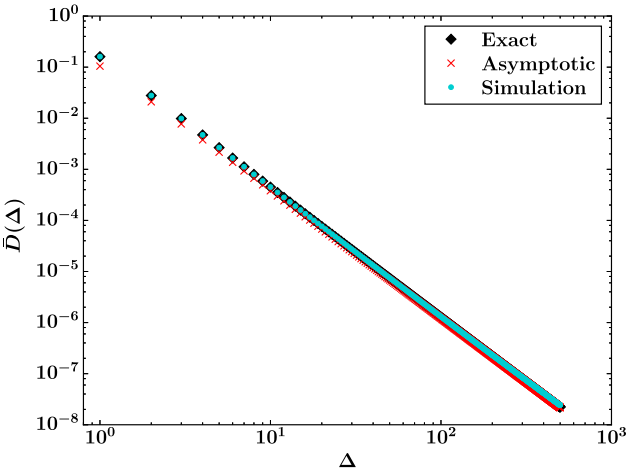

FIGURE 1 | Burst distribution $\bar{D}(\Delta)$ for a Weibull threshold distribution with $k = 2$ and $t_0 = 0$. The exact result (black) is Equation (14) and the asymptotic result (red) is Equation (4). The simulation results (turquoise) were found by averaging $\bar{D}(\Delta)$ over 10^6 sample systems with $N = 1024^2$.

This expression can easily be evaluated for small bursts, which is what we are interested in. Equation (14) for $k = 2$ and $t_0 = 0$ is shown in **Figure 1** together with the asymptotic result from Equation (4) and simulation results. The agreement between the exact and simulation results is excellent, particularly for small Δ where finite size effects from the simulations are negligible. The asymptotic result from Equation (4) is inaccurate for small Δ—it is 35% smaller than the exact result for $\Delta = 1$—but becomes more and more accurate as Δ increases, which is consistent with the fact that Equation (4) is asymptotically correct in the limit $\Delta \to \infty$.

For the special case $\Delta = 1$, Equation (14) becomes

$$\begin{aligned}\bar{D}(\Delta = 1) = &\frac{\mathrm{e}^{t_0^k}}{(k+1)^2}\left[k\mathrm{e}^{-(1+1/k)}\right. \\ &\left.+\left(1 - (k+1)kt_0^k\right)\mathrm{e}^{-(k+1)t_0^k}\right].\end{aligned} \tag{15}$$

For large bursts Equation (14) is impractical to use, but for $\Delta \gg \Delta_c$ the first term is dominant. The equation then simplifies to

$$\bar{D}(\Delta) \simeq \frac{\Delta^{\Delta-1}\mathrm{e}^{-\Delta}}{\Delta!(k\Delta+1)}\mathrm{e}^{t_0^k - 1/k} \simeq \frac{\mathrm{e}^{t_0^k - 1/k}}{\sqrt{2\pi k}}\Delta^{-5/2}, \tag{16}$$

via Stirling's approximation, $\Delta! \simeq \sqrt{2\pi\Delta}\Delta^{\Delta}\mathrm{e}^{-\Delta}$. This is the expected asymptotic power law from Equation (3) for the Weibull distribution from Equation (10).

4. ASYMPTOTIC SERIES EXPANSION

The simplicity of the Weibull threshold distribution is an exception, and for other threshold distributions we cannot expect to find an exact result for the burst distribution. We therefore

return to Equation (5) to make an asymptotic series expansion, and note that the equation has the form of a Laplace integral [14]

$$I(\Delta) = \int_{t_0}^{x_c} f(t) \mathrm{e}^{\Delta\phi(t)} \mathrm{d}t, \tag{17}$$

with

$$f(t) = p(t) \frac{1 - a(t)}{a(t)} \tag{18}$$

$$\phi(t) = -a(t) + \ln(a(t)). \tag{19}$$

For large Δ the integral is dominated by a small interval around the maximum of $\phi(t)$ in the interval $[t_0, x_c]$. In our case ϕ has its maximum at $a(t) = 1$, i.e., at the critical extension x_c, the upper limit of integration. Hence the asymptotic behavior of Equation (17) as $\Delta \to \infty$ is

$$I(\Delta) \sim \int_{x_c - \epsilon}^{x_c} f(t) \mathrm{e}^{\Delta\phi(t)} \mathrm{d}t \tag{20}$$

where ϵ is a small number. In the small interval $[x_c - \epsilon, x_c]$ we can Taylor expand $f(t)$ and $\phi(t)$ around x_c,

$$\begin{aligned} f(t) &= f_1(t - x_c) + f_2(t - x_c)^2 \\ &\quad + f_3(t - x_c)^3 + \cdots \\ \phi(t) &= \phi_0 + \phi_2(t - x_c)^2 + \phi_3(t - x_c)^3 \\ &\quad + \phi_4(t - x_c)^4 + \cdots \end{aligned} \tag{21}$$

Note that f_n and ϕ_n are not identical to the nth derivatives of $f(t)$ and $\phi(t)$ evaluated at x_c, only proportional to them. The exact expressions for these coefficients in terms of $a(t)$ are shown in Equations (34, 36). Also note that the vanishing terms $f_0 = f(x_c) = 0$ and $\phi_1 \propto \phi'(x_c) = 0$ (ϕ has its maximum at x_c) are not included here.

In the limit $\Delta \to \infty$, when the interval $[x_c - \epsilon, x_c]$ can be chosen arbitrarily small, the two first terms in the expansion of ϕ will dominate the others. We therefore separate these terms by factorizing the exponential in the integrand of Equation (20) as

$$\begin{aligned} \mathrm{e}^{\Delta\phi(t)} &= \exp\left(\Delta\phi_0 + \Delta\phi_2(t - x_c)^2\right) \\ &\quad \times \exp\left(\Delta\left[\phi_3(t - x_c)^3 + \phi_4(t - x_c)^4 + \cdots\right]\right), \end{aligned} \tag{22}$$

and then Taylor expand the second factor

$$\begin{aligned} \exp\left(\Delta\left[\phi_3(t - x_c)^3 + \phi_4(t - x_c)^4 + \cdots\right]\right) &= 1 \\ + \Delta\left[\xi_{1,3}(t - x_c)^3 + \xi_{1,4}(t - x_c)^4 + \cdots\right] \\ + \Delta^2\left[\xi_{2,6}(t - x_c)^6 + \xi_{2,7}(t - x_c)^7 + \cdots\right] \\ + \cdots, \end{aligned} \tag{23}$$

which defines $\xi_{n,m}$. Inserting these expansions into Equation (20) and extending the lower integration limit back down to t_0 gives

$$\begin{aligned} I(\Delta) \sim \mathrm{e}^{\Delta\phi_0} \int_{t_0}^{x_c} & \mathrm{e}^{\Delta\phi_2(t - x_c)^2} \\ & \times \left[f_1(t - x_c) + f_2(t - x_c)^2 + \cdots\right] \\ & \times \left\{1 + \Delta\left[\xi_{1,3}(t - x_c)^3 + \cdots\right]\right. \\ & \left. + \Delta^2\left[\xi_{2,6}(t - x_c)^6 + \cdots\right] + \cdots\right\} \mathrm{d}t. \end{aligned} \tag{24}$$

The standard approach is to extend the lower limit of integration to $-\infty$ because the integral over $[-\infty, x_c - \epsilon]$ is subdominant to the integral over $[x_c - \epsilon, x_c]$ in the limit $\Delta \to \infty$ [14]. But our goal is to use the asymptotic series to calculate an approximation for $\bar{D}(\Delta)$ for small Δ, and we know that the lower limit t_0 is important for small bursts [6].

To solve this integral, multiply the Taylor expansions and separate terms with even and odd powers of $t - x_c$ into $I_{\mathrm{even}}(\Delta)$ and $I_{\mathrm{odd}}(\Delta)$, respectively. The odd terms are

$$\begin{aligned} I_{\mathrm{odd}}(\Delta) = \mathrm{e}^{\Delta\phi_0} \int_{t_0}^{x_c} & \mathrm{e}^{\Delta\phi_2(t - x_c)^2} \\ & \times \left\{\left[f_1(t - x_c) + f_3(t - x_c)^3 + \cdots\right]\right. \\ & + \Delta\left[\omega_{1,5}(t - x_c)^5 + \omega_{1,7}(t - x_c)^7 + \cdots\right] \\ & + \Delta^2\left[\omega_{2,7}(t - x_c)^5 + \omega_{2,9}(t - x_c)^9 + \cdots\right] \\ & \left. + \cdots\right\} \mathrm{d}t, \end{aligned} \tag{25}$$

where $\omega_{n,m}$ is defined in Equation (38). Then choose $u = \Delta\phi_2(t - x_c)^2$, which yields

$$\begin{aligned} I_{\mathrm{odd}}(\Delta) = \frac{\mathrm{e}^{\Delta\phi_0}}{2\Delta\phi_2} \int_{\Delta\phi_2(t_0 - x_c)^2}^{0} & \mathrm{e}^{u} \\ & \times \left\{\left[f_1 + f_3 \frac{u}{\Delta\phi_2} + \cdots\right]\right. \\ & + \Delta\left[\omega_{1,5}\left(\frac{u}{\Delta\phi_2}\right)^2 + \omega_{1,7}\left(\frac{u}{\Delta\phi_2}\right)^3 + \cdots\right] \\ & + \Delta^2\left[\omega_{2,7}\left(\frac{u}{\Delta\phi_2}\right)^3 + \omega_{2,9}\left(\frac{u}{\Delta\phi_2}\right)^4 + \cdots\right] \\ & \left. + \cdots\right\} \mathrm{d}u, \end{aligned} \tag{26}$$

We can now group these terms by the integrands' dependence on Δ:

$$\begin{aligned} I_{\mathrm{odd}}(\Delta) = \frac{\mathrm{e}^{\Delta\phi_0}}{2\Delta\phi_2} & \left(\Omega_0(\Delta) + \Omega_1(\Delta)\Delta^{-1}\right. \\ & \left. + \Omega_2(\Delta)\Delta^{-2} + \cdots\right), \end{aligned} \tag{27}$$

where Ω_n—see Equation (40)—-depends on Δ due to the lower limit of integration.

The even terms in $t - x_c$ are

$$\begin{aligned} I_{\text{even}}(\Delta) = \mathrm{e}^{\Delta\phi_0} \int_{t_0}^{x_c} \mathrm{e}^{\Delta\phi_2(t-x_c)^2} \\ \times \left\{ \left[f_2(t-x_c)^2 + f_4(t-x_c)^4 + \cdots \right] \right. \\ + \Delta \left[\omega_{1,4}(t-x_c)^4 + \omega_{1,6}(t-x_c)^6 + \cdots \right] \\ + \Delta^2 \left[\omega_{2,8}(t-x_c)^8 + \omega_{2,10}(t-x_c)^{10} + \cdots \right] \\ \left. + \cdots \right\} \mathrm{d}t. \end{aligned} \tag{28}$$

Since $\phi_2 < 0$, choose $u = \sqrt{-\Delta\phi_2}(t - x_c)$. Then

$$\begin{aligned} I_{\text{even}}(\Delta) = \frac{\mathrm{e}^{\Delta\phi_0}}{\sqrt{-\Delta\phi_2}} \int_{\sqrt{-\Delta\phi_2}(t_0-x_c)}^{0} \mathrm{e}^{-u^2} \\ \times \left\{ \left[f_2 \left(\frac{u}{\sqrt{-\Delta\phi_2}} \right)^2 + f_4 \left(\frac{u}{\sqrt{-\Delta\phi_2}} \right)^4 + \cdots \right] \right. \\ + \Delta \left[\omega_{1,4} \left(\frac{u}{\sqrt{-\Delta\phi_2}} \right)^4 + \omega_{1,6} \left(\frac{u}{\sqrt{-\Delta\phi_2}} \right)^6 + \cdots \right] \\ + \Delta^2 \left[\omega_{2,8} \left(\frac{u}{\sqrt{-\Delta\phi_2}} \right)^8 + \omega_{2,10} \left(\frac{u}{\sqrt{-\Delta\phi_2}} \right)^{10} + \cdots \right] \\ \left. + \cdots \right\} \mathrm{d}u. \end{aligned} \tag{29}$$

Grouping these terms by the integrands' dependence on Δ yields

$$\begin{aligned} I_{\text{even}}(\Delta) = \frac{\mathrm{e}^{\Delta\phi_0}}{\sqrt{-\Delta\phi_2}} \left(\Theta_1(\Delta)\Delta^{-1} + \Theta_2(\Delta)\Delta^{-2} \right. \\ \left. + \Theta_3(\Delta)\Delta^{-3} + \cdots \right), \end{aligned} \tag{30}$$

with Θ_n as shown in Equation (39).

Combining Equations (27, 30) with $\phi_0 = -1$ (from Equation 36) and Equation (5) gives the full asymptotic series for the burst size distribution as

$$\begin{aligned} \bar{D}(\Delta) &\sim \frac{\Delta^{\Delta-1}\mathrm{e}^{-\Delta}}{\Delta!} \left[\frac{1}{2\Delta\phi_2} \left(\Omega_0(\Delta) + \Omega_1(\Delta)\Delta^{-1} + \cdots \right) \right. \\ &\quad \left. + \frac{1}{\sqrt{-\Delta\phi_2}} \left(\Theta_1(\Delta)\Delta^{-1} + \Theta_2(\Delta)\Delta^{-2} + \cdots \right) \right] \\ &= \frac{\Delta^{\Delta-2}\mathrm{e}^{-\Delta}}{\Delta!} \left(C_1(\Delta) + C_2(\Delta)\Delta^{-1/2} \right. \\ &\quad \left. + C_3(\Delta)\Delta^{-1} + C_4(\Delta)\Delta^{-3/2} + \cdots \right). \end{aligned} \tag{31}$$

Unfortunately, the "coefficients" C_n depend on Δ, and the terms in the asymptotic series must therefore be evaluated separately for each value of Δ. To do this evaluation, the relations between the various coefficients that have been introduced in the series expansions are needed.

4.1. Coefficient Expressions

To define the coefficients from the asymptotic series expansion, use

$$\begin{aligned} A_n(\Delta, t_0) &\equiv \int_{\Delta\phi_2(t_0-x_c)^2}^{0} \mathrm{d}u\, \mathrm{e}^u u^n \\ B_n(\Delta, t_0) &\equiv \int_{\sqrt{-\Delta\phi_2}(t_0-x_c)}^{0} \mathrm{d}u\, \mathrm{e}^{-u^2} u^{2n} \end{aligned} \tag{32}$$

for the integrals that will show up in the expressions.

4.1.1. Definition of *f*

To determine the coefficients f_n, expand Equation (18) around $a = 1$:

$$f(t) = p(t) \left[(1-a) + (1-a)^2 + (1-a)^3 + \cdots \right]. \tag{33}$$

Then Taylor expand $a(t)$ and $p(t)$ around x_c as $a(t) = 1 + a_1(t - x_c) + a_2(t-x_c)^2/2 + \cdots$ and $p(t) = p_0 + p_1(t-x_c) + p_2(t-x_c)^2/2 + \cdots$, where $a_n \equiv a^{(n)}(x_c)$ and $p_n \equiv p^{(n)}(x_c)$ are the nth derivatives of $a(t)$ and $p(t)$ evaluated at x_c. Comparison with Equation (21) gives the relation

$$\begin{aligned} f_n = \sum_{m=0}^{n-1} \frac{p_m}{m!} \sum_{l=1}^{n-m} (-1)^l l! \\ \times \sum_{\substack{\sum_{i=1}^{\infty} k_i = l \\ \sum_{i=1}^{\infty} i k_i = n-m}} \prod_{i=1}^{n-m-l+1} \frac{1}{k_i!} \left(\frac{a_i}{i!} \right)^{k_i}, \end{aligned} \tag{34}$$

where $n \geq 1$ since $f_0 = 0$, and $k_i \in \mathbb{N}$.

4.1.2. Definition of ϕ

To determine ϕ_n, expand Equation (19) around $a = 1$:

$$\phi(t) = -1 - \frac{(1-a)^2}{2} - \frac{(1-a)^3}{3} - \frac{(1-a)^5}{4} - \cdots. \tag{35}$$

Then expand $a(t) = 1 + a_1(t - x_c) + a_2(t - x_c)^2/2 + \cdots$ in the above equation. Comparison with Equation (21) gives

$$\begin{aligned} \phi_0 &= -1 \\ \phi_1 &= 0 \\ \phi_n &= -\sum_{m=2}^{n} \frac{(-1)^m}{m} \sum_{\substack{\sum_{i=1}^{\infty} k_i = m \\ \sum_{i=1}^{\infty} i k_i = n}} m! \\ &\quad \times \prod_{i=1}^{n-m+1} \frac{1}{k_i!} \left(\frac{a_{(i)}}{i!} \right)^{k_i}, \end{aligned} \tag{36}$$

where $n \geq 2$ and $k_i \in \mathbb{N}$.

4.1.3. Definition of ξ

From Equation (23) we get

$$\xi_{n,m} = \sum_{\substack{\sum_{i=3}^{\infty} k_i = n \\ \sum_{i=3}^{\infty} i k_i = m}} \prod_{i=3}^{m-3n+3} \frac{\phi_i^{k_i}}{k_i!}, \tag{37}$$

where $n \geq 1$, $m \geq 3n$, and $k_i \in \mathbb{N}$.

4.1.4. Definition of ω

Comparing Equation (24) with Equations (25, 28) yields

$$\omega_{n,m} = \sum_{i=3n}^{m-1} f_{m-i}\xi_{n,i}, \tag{38}$$

where $n \geq 1$ and $m \geq 3n+1$.

4.1.5. Definitions of Θ and Ω

By examining the expressions in Equations (29, 30) we see that the coefficients $\Theta_n(\Delta)$ are

$$\begin{aligned}\Theta_n(\Delta) = &\frac{f_{2n}B_n(\Delta,t_0)}{(-\phi_2)^n} \\ &+ \sum_{i=1}^{2n-1} \frac{B_{n+i}(\Delta,t_0)}{(-\phi_2)^{n+i}}\omega_{i,2(n+i)},\end{aligned} \tag{39}$$

with $n \geq 1$ and B_n from Equation (32). Similarly, from Equations (26, 27) we get

$$\begin{aligned}\Omega_n(\Delta) = &\frac{f_{2n+1}A_n(\Delta,t_0)}{\phi_2^n} \\ &+ \sum_{i=1}^{2n} \frac{A_{n+i}(\Delta,t_0)}{\phi_2^{n+i}}\omega_{i,2(n+i)+1},\end{aligned} \tag{40}$$

with $n \geq 0$ and A_n from Equation (32).

4.1.6. Definition of C

From Equation (31), we get

$$\begin{aligned}C_{2n-1}(\Delta) &= \frac{\Omega_{n-1}(\Delta)}{2\phi_2} \\ C_{2n}(\Delta) &= \frac{\Theta_n(\Delta)}{\sqrt{-\phi_2}},\end{aligned} \tag{41}$$

where $n \geq 1$.

4.2. Crossover

We know from Equation (4) that around Δ_c, the burst distribution contains a crossover from $\Delta^{-3/2}$ to $\Delta^{-5/2}$ behavior. Does Equation (31) reproduce this? The first term in the series is

$$\begin{aligned}C_1(\Delta)\frac{\Delta^{\Delta-2}\mathrm{e}^{-\Delta}}{\Delta!} &\approx \frac{\Omega_0(\Delta)}{2\sqrt{2\pi}\phi_2}\Delta^{-5/2} \\ &= \frac{f_1 A_0(\Delta,t_0)}{2\sqrt{2\pi}\phi_2}\Delta^{-5/2}.\end{aligned} \tag{42}$$

Using the Stirling approximation $\Delta! \approx \sqrt{2\pi}\Delta^{\Delta+1/2}\mathrm{e}^{-\Delta}$ and inserting for f_1, $A_0(\Delta,t_0)$, and ϕ_2 from Equations (32, 34, 36) gives

$$\begin{aligned}C_1(\Delta)\frac{\Delta^{\Delta-2}\mathrm{e}^{-\Delta}}{\Delta!} &\approx \frac{-p_0 a_1}{2\sqrt{2\pi}\phi_2}\Delta^{-5/2}\int_{\Delta\phi_2(t_0-x_c)^2}^{0}\mathrm{e}^u \mathrm{d}u \\ &= C\Delta^{-5/2}\left(1-\exp\left[-\Delta/\Delta_c\right]\right),\end{aligned} \tag{43}$$

where $C = (2\pi)^{-1/2}x_c p_0(2p_0+x_c p_1)^{-1}$ is the same as in Equation (3) and $\Delta_c = 2a_1^{-2}(x_c-t_0)^{-2} = 4\pi C^2 p_0^2(x_c-t_0)^{-2}$ is the same as in Equation (4).

The first term of the asymptotic series is exactly Equation (4), and the asymptotic series therefore reproduces the known crossover behavior in the limit $\Delta \to \infty$.

5. APPROXIMATION FOR SMALL BURSTS

The asymptotic expansion in Equation (31) is done in the limit of infinitely large bursts, and one should not expect the series to give a perfect approximation of $\bar{D}(\Delta)$ when Δ is finite. In general, the infinite series might not converge for finite Δ. However, one can still use the asymptotic series to find an approximation for $\bar{D}(\Delta)$ for small bursts.

5.1. Optimal Approximation for Finite Burst Size

For a finite Δ we use the general procedure outlined by Bender and Orzag [14]:

First choose a fixed value of Δ. Then locate the smallest term (in absolute value) of the asymptotic series in Equation (31): $C_m(\Delta)\Delta^{\Delta-2-(m-1)/2}\mathrm{e}^{-\Delta}/\Delta!$. When summing the series up to (but not including) a certain term, then that term gives a measure of the error from the exact result [14]. Hence, we sum the asymptotic series up to (but not including) the smallest term, so that we get the smallest possible error estimate. If term number m is the smallest one, the optimal approximation is

$$\bar{D}(\Delta) \approx \sum_{i=1}^{m-1} C_i(\Delta)\frac{\Delta^{\Delta-2-(i-1)/2}\mathrm{e}^{-\Delta}}{\Delta!}. \tag{44}$$

Note that this method is applicable even when the infinite asymptotic series does not converge. The caveat is that it has to be done separately for each value of Δ where we wish to approximate the burst distribution.

There is a practical limit to how many terms from Equation (31) one can calculate. The smallest term m must be chosen among the terms that are calculated. Hence we cannot guarantee that the smallest term we find is the smallest one in the entire infinite series. If it is not, then the accuracy of the approximation will be reduced.

Truncating the series at the smallest term does not necessarily give the best approximation. For certain values of Δ there will exist better choices of truncation. However, Equation (44) provides the method with the best *guaranteed* error without a priori knowledge of the burst distribution.

5.2. Comparison With Exact Result

To test the accuracy of Equation (44) we compare it with the exact result from Equation (14) for the Weibull distribution. This is easier than relying on simulations, as both expressions are derived in the limit $N \to \infty$ where there are no finite size effects.

We have calculated the first 13 terms of Equation (31) for small to intermediate burst sizes. With this limitation of 13 terms, we use Equation (44) to calculate the optimal approximation. For a

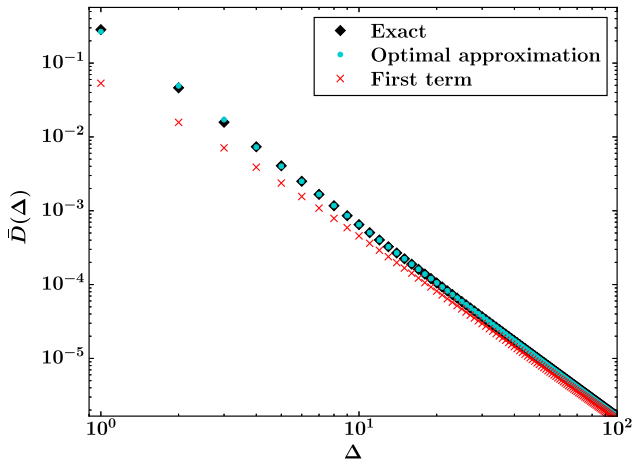

FIGURE 2 | Optimal approximation from Equation (44) with 13 available terms (turquoise) and exact result (black) for the burst distribution. The first term of the asymptotic series (red), which is Equation (4), is shown for comparison. The threshold distribution is a Weibull distribution with $k = 1$ and $t_0 = 0$.

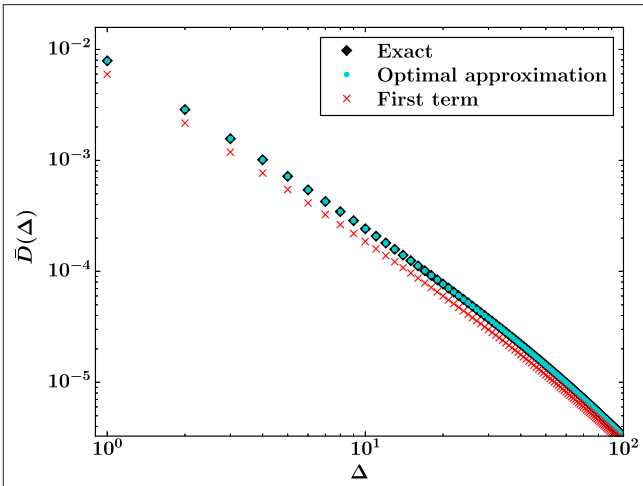

FIGURE 4 | Optimal approximation from Equation (44) with 13 available terms (turquoise) and exact result (black) for the burst distribution. The first term of the asymptotic series (red), which is Equation (4), is shown for comparison. The threshold distribution is a Weibull distribution with $k = 1$ and $t_0 = 0.8$.

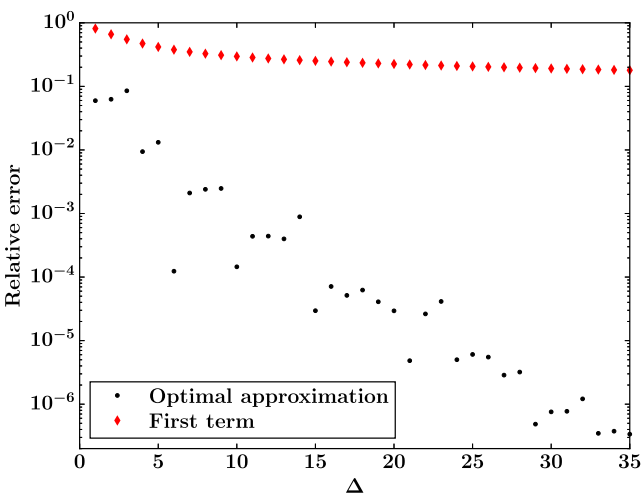

FIGURE 3 | Relative errors for the burst distribution with respect to the exact result from Equation (14): for the optimal approximation from Equation (44) with 13 available terms (black) and for the first term of the asymptotic series (red), which is Equation (4). The threshold distribution is a Weibull distribution with $k = 1$ and $t_0 = 0$.

Weibull distribution with $k = 1$ and $t_0 = 0$, **Figure 2** shows this approximation, the exact result from Equation (14), and Equation (4). The corresponding relative errors with respect to the exact solution, calculated as $\left|\bar{D}_{\text{exact}} - \bar{D}_{\text{approximation}}\right| / \bar{D}_{\text{exact}}$, are shown in **Figure 3**.

Both approximations converge to the exact solution as $\Delta \to \infty$, but the optimal approximation converges much faster and is consistently a better estimate of the exact result. From **Figure 3**, we see that the ratio between the two relative errors is at its smallest for small bursts, but the difference is still big, as evident from **Figure 2**. For the smallest bursts, the optimal approximation gives an estimate of the exact result with moderate accuracy (relative errors of order 10%), whereas Equation (4) is unusable as an estimate (relative errors of order 50% − 80%).

The errors in the optimal approximation seem to stem from the fact that 13 terms is insufficient to find the smallest term in the asymptotic series for small Δ. With 13 available terms, we can achieve higher accuracy with other parameters for the threshold distribution. For a Weibull distribution with $k = 1$ and $t_0 = 0.8$, we show the exact solution, optimal approximation, and Equation (4) in **Figure 4**, with the corresponding relative error of the optimal approximation in **Figure 5**.

In this case, with $t_0 = 0.8$ much closer to $x_c = 1$, 13 terms seem to be sufficient to locate the smallest term in the asymptotic series even for small Δ. Hence the errors of the optimal approximation (of order 10^{-9} for the smallest bursts) are negligible, as seen from **Figure 5**. In the figure we have not shown the errors of Equation (4), since they are on a completely different scale from the errors of the optimal approximation, roughly 24% for the smallest bursts.

5.3. Comparison With Simulations

To test the general applicability of the asymptotic expansion, we also use Equation (44) with the uniform threshold distribution on $[t_0, 1]$ (which has $x_c = 1/2$), a widely used probability distribution in the study of fiber bundles [3, 4]. Since the exact solution is valid only for Weibull distributions, we compare the asymptotic series results with simulation results for large systems ($N = 1024^2$) where finite size effects for small Δ are small. As with the Weibull distributions, we again calculate the first 13 terms of Equation (31), and then use them to calculate the optimal approximation via Equation (44).

Figure 6 shows a comparison of the optimal approximation, simulation results, and Equation (4) for the uniform threshold

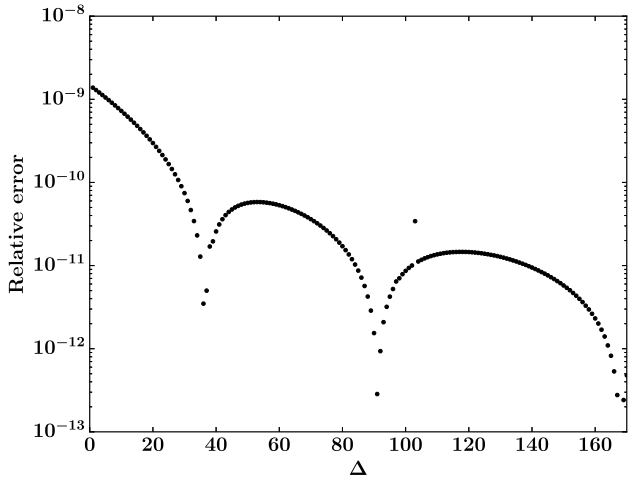

FIGURE 5 | Relative error for the burst distribution with respect to the exact result from Equation (14) for the optimal approximation from Equation (44) (with 13 available terms). The threshold distribution is a Weibull distribution with $k = 1$ and $t_0 = 0.8$.

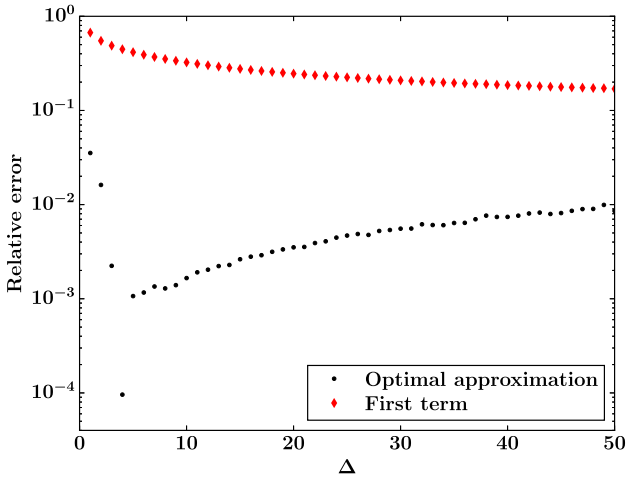

FIGURE 7 | Relative errors for the burst distribution with respect to simulation results that are averaged over 10^6 sample systems of size $N = 1024^2$: for the optimal approximation from Equation (44) with 13 available terms (black) and for the first term of the asymptotic series (red), which is Equation (4). The threshold distribution is uniform on [0, 1].

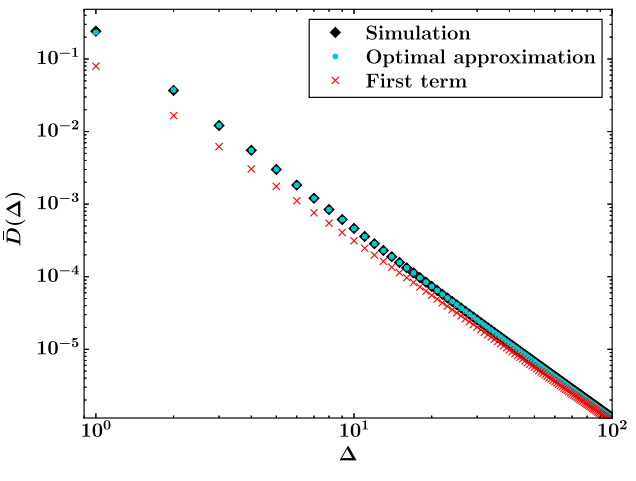

FIGURE 6 | Optimal approximation from Equation (44) with 13 available terms (turquoise) and simulation results (black, $N = 1024^2$, 10^6 samples) for the burst distribution. The first term of the asymptotic series (red), which is Equation (4), is shown for comparison. The threshold distribution is uniform on [0, 1].

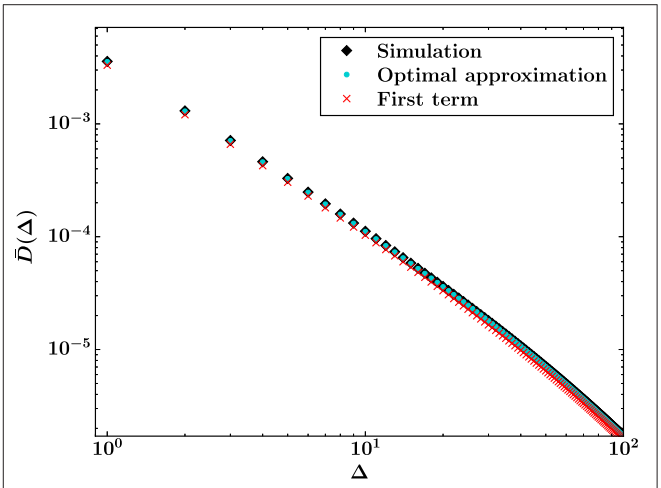

FIGURE 8 | Optimal approximation from Equation (44) with 13 available terms (turquoise) and simulation results (black, $N = 1024^2$, 10^6 samples) for the burst distribution. The first term of the asymptotic series (red), which is Equation (4), is shown for comparison. The threshold distribution is uniform on [0.45, 1].

distribution with $t_0 = 0$. The corresponding relative errors with respect to the simulation results, calculated as $\left|\bar{D}_{\text{simulation}} - \bar{D}_{\text{approximation}}\right| / \bar{D}_{\text{simulation}}$, is shown in **Figure 7**. The optimal approximation is accurate to within a few percent for small bursts, and the relative error decreases rapidly as Δ increases, as in **Figures 3**, **5**. However, the error quickly begins to increase again, presumably due to finite size effects from the simulations. Equation (31) is derived from Equation (5), which is only exact in the limit $N \to \infty$. Equation (4) becomes more accurate as Δ increases, but is consistently less accurate than the optimal approximation.

Figure 8 shows a comparison of the optimal approximation, simulation results, and Equation (4) for the uniform threshold distribution with $t_0 = 0.45$, with corresponding relative errors in **Figure 9**. In this case neither approximation becomes more accurate as the burst size increases, but Equation (4) is much more accurate than for $t_0 = 0$. However, the optimal approximation is still more accurate than Equation (4), with relative errors roughly an order of magnitude smaller.

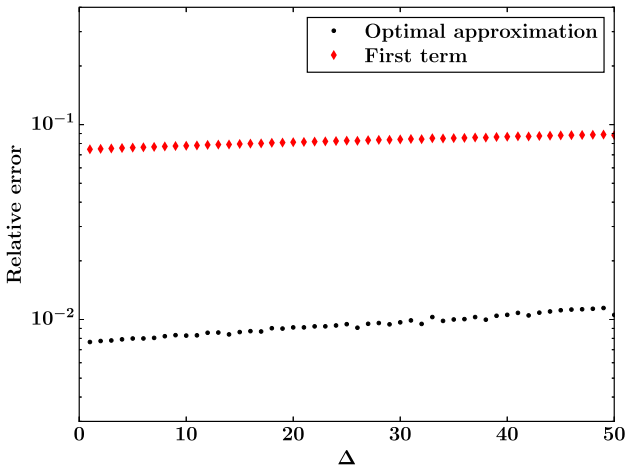

FIGURE 9 | Relative errors for the burst distribution with respect to simulation results that are averaged over 10^6 sample systems of size $N = 1024^2$: for the optimal approximation from Equation (44) with 13 available terms (black) and for the first term of the asymptotic series (red), which is Equation (4). The threshold distribution is uniform on [0.45, 1].

6. DISCUSSION AND CONCLUSION

In the equal load sharing fiber bundle model, we have found an analytic solution of the burst size distribution for Weibull threshold distributions: Equation (14). This is a significant improvement over previous results, which describe the asymptotic behavior as the burst size diverges.

The exact result is impractical to use for large burst sizes Δ, but can easily be evaluated for small Δ. In this sense it complements the existing asymptotic result; Equation (14) can be used for small Δ, and for sufficiently large Δ we can use Equation (4) instead. Together, these results provide a highly accurate way to calculate the burst size distribution for Weibull threshold distributions.

For other threshold distributions where the burst distribution cannot be solved exactly, another method is needed to calculate the burst distribution for small Δ. We have therefore derived the full asymptotic series expansion for the burst size distribution, Equation (31). Even if the full infinite series is valid only in the limit $\Delta \to \infty$, it can still be used to find approximations for small Δ through Equation (44).

Our results indicate that, with a fixed number of available terms, this optimal approximation is more accurate the smaller $x_c - t_0$ is. This seems to stem, at least partially, from the fact that more terms are needed in the asymptotic series expansion to find the smallest term.

The accuracy of the optimal asymptotic approximation depends on the threshold distribution and the number of calculated terms. With 13 terms, the relative error for the smallest bursts ranges from several percent to $\sim 10^{-9}$ for the Weibull and uniform threshold distributions we have investigated. This is consistently more accurate than Equation (4).

Neither Equation (44) nor Equation (4) take finite size effects into account, since they are derived in the limit of infinitely big systems. The optimal approximation provides decent estimates of simulation results from large systems, when finite size effects are small, but the accuracy should be expected to be much smaller when comparing with results from small system sizes. It might be possible to use a similar approach that also incorporates finite size effects, but then one would first need to derive an expression like Equation (5) that contains the finite size effects.

Estimating the burst distribution via Equation (44) is much more computationally efficient than relying on simulations of very large systems. However, simulations can in theory give more accurate estimates, provided that the simulation results converge to the thermodynamic limit quickly enough when the system size increases. Then one can use results for different system sizes to extrapolate to $N \to \infty$. Simulations should still be preferred when studying finite size effects, especially for small systems where simulations are not time-consuming. The optimal asymptotic approximation gives decent estimates for simulations results from large systems, as shown in **Figures 7**, **9**, but we expect the accuracy to be smaller for smaller system sizes.

DATA AVAILABILITY STATEMENT

The datasets generated for this study are available on request to the corresponding author.

AUTHOR CONTRIBUTIONS

JK performed the research and wrote the manuscript.

FUNDING

This work was partly supported by the Research Council of Norway through its Centres of Excellence funding scheme, project number 262644.

ACKNOWLEDGMENTS

I would like to thank Alex Hansen for suggesting to look for an exact solution, and for assisting with writing the abstract, introduction, and conclusion. I would also like to thank Martin Hendrick and Srutarshi Pradhan for helpful discussions and good suggestions.

REFERENCES

1. Peirce FT. 32—X.—Tensile tests for cotton yarns v.—"The Weakest Link" Theorems on the strength of long and of composite specimens. *J Text Inst*. (1926) **17**:T355–68. doi: 10.1080/19447027.1926.10599953
2. Daniels HE. The statistical theory of the strength of bundles of threads. I. *Proc R Soc A*. (1945) **183**:405–35. doi: 10.1098/rspa.1945.0011
3. Pradhan S, Hansen A, Chakrabarti BK. Failure processes in elastic fiber bundles. *Rev Mod Phys*. (2010) **82**:499–555. doi: 10.1103/RevModPhys.82.499

4. Hansen A, Hemmer PC, Pradhan S. *The Fiber Bundle Model*. Berlin: Wiley-VCH (2015).
5. Bouchaud JP. Econophysics: still fringe after 30 years? *Europhys News*. (2019) **50**:24–7. doi: 10.1051/epn/2019103
6. Pradhan S, Hansen A, Hemmer PC. Crossover behavior in burst avalanches: signature of imminent failure. *Phys Rev Lett*. (2005) **95**:125501. doi: 10.1103/PhysRevLett.95.125501
7. Pradhan S, Bhattacharyya P, Chakrabarti BK. Dynamic critical behavior of failure and plastic deformation in the random fiber bundle model. *Phys Rev E*. (2002) **66**:016116. doi: 10.1103/PhysRevE.66.016116
8. Hemmer PC, Pradhan S. Failure avalanches in fiber bundles for discrete load increase. *Phys Rev E*. (2007) **75**:046101. doi: 10.1103/PhysRevE.75.046101
9. Hemmer PC, Hansen A. The distribution of simultaneous fiber failures in fiber bundles. *J Appl Mech*. (1992) **59**:909–14. doi: 10.1115/1.2894060
10. Sornette D. Mean-field solution of a block-spring model of earthquakes. *J Phys I* . (1992) **2**:2089–96. doi: 10.1051/jp1:1992269
11. Pradhan S, Hansen A, Hemmer PC. Crossover behavior in failure avalanches. *Phys Rev E*. (2006) **74**:016122. doi: 10.1103/PhysRevE.74.016122
12. Raischel F, Kun F, Herrmann HJ. Local load sharing fiber bundles with a lower cutoff of strength disorder. *Phys Rev E*. (2006) **74**:035104. doi: 10.1103/PhysRevE.74.035104
13. Hidalgo RC, Moreno Y, Kun F, Herrmann HJ. Fracture model with variable range of interaction. *Phys Rev E*. (2002) **65**:046148. doi: 10.1103/PhysRevE.65.046148
14. Bender CM, Orszag SA. *Advanced Mathematical Methods for Scientists and Engineers: Asymptotic Methods and Perturbation Theory*. New York, NY: Springer (1999).

Conflict of Interest: The author declares that the research was conducted in the absence of any commercial or financial relationships that could be construed as a potential conflict of interest.

frontiers in Physics

REVIEW
published: 17 July 2020
doi: 10.3389/fphy.2020.00236

Studying Snow Failure With Fiber Bundle Models

Achille Capelli[1]*, *Ingrid Reiweger*[2] and *Jürg Schweizer*[1]

[1] WSL Institute for Snow and Avalanche Research SLF, Davos, Switzerland, [2] Department of Civil Engineering and Natural Hazards, Institute of Mountain Risk Engineering, BOKU University of Natural Resources and Life Sciences, Vienna, Austria

Snow is a highly porous material with properties that may strongly differ depending on the environmental conditions. On slopes, the layered snowpack may fail and avalanches occur. Hence, knowing how snow deforms and fails is essential for understanding and modeling snow avalanche release and flow. The response of snow to imposed load or deformation and the failure behavior depends on the rate of the applied load or of displacement and follows from the complex, foam like, microstructure of snow and the properties of ice. The mechanical response and failure of snow can well be captured with fiber bundle models (FBM). We review the use of FBMs for studying snow failure. In particular, we show how FBMs have been used for studying the micromechanical processes, such as ice sintering and viscous deformation, to reproduce the results of snow failure experiments. Moreover, FBMs can reproduce signatures of acoustic emissions (AE) preceding snow failure, ease the AE interpretation, and shed light on the underlying progressive failure process.

Keywords: fiber bundle model, snow, avalanche, sintering, healing, viscosity, acoustic emissions, failure

OPEN ACCESS

Edited by:
Ferenc Kun,
University of Debrecen, Hungary

Reviewed by:
Srutarshi Pradhan,
Norwegian University of Science and Technology, Norway
Purusattam Ray,
Institute of Mathematical Sciences, Chennai, India

***Correspondence:**
Achille Capelli
achille.capelli@slf.ch

Specialty section:
This article was submitted to Interdisciplinary Physics, a section of the journal Frontiers in Physics

Received: *10 April 2020*
Accepted: *29 May 2020*
Published: *17 July 2020*

Citation:
Capelli A, Reiweger I and Schweizer J (2020) Studying Snow Failure With Fiber Bundle Models. Front. Phys. 8:236. doi: 10.3389/fphy.2020.00236

INTRODUCTION

Studying snow failure and its dependency on the rate of the applied load or of displacement is of particular interest for snow avalanche formation. Among the various types of avalanches, dry-snow slab avalanches are the most hazardous and cause the largest number of fatalities—at least about 200 per year worldwide (e.g., [1]). Slab avalanches start by a failure nucleating under mixed-mode loading in a weak layer below a cohesive slab. Once this so-called initial crack reaches a critical size it propagates within the weak layer across the slope, leading to detachment and downhill sliding of the slab provided the slope-parallel gravitational force overcomes friction (e.g., [2]). The formation of this initial crack is still not fully understood for the case of spontaneously releasing avalanches and a crucial point for modeling avalanche release.

Snow is a highly porous material constituted by an ice matrix formed by ice grains welded together whereas the pore space is filled with air. The mechanical properties of snow are determined by its microstructure and the mechanical properties of ice. The loading or displacement rate dependency of the mechanical and failure properties of snow are believed to be due to two ice properties: ice sintering—i.e., ice bonds form on contact immediately with bond strength increasing with time—and the viscous deformation of ice (e.g., [3]).

Fiber bundle models have been widely used for studying snow failure (e.g., [4, 5]). Moreover, since FBMs replicate the macroscopic mechanical properties and failure behavior of materials through a large set of single elements with simple mechanical properties, they are an ideal choice for studying the micromechanical drivers of snow failure. We provide a review of the use of the fiber bundle model in snow science. We first describe the FBMs that have been

used for simulating snow failure. Then we describe the inclusion of fiber healing and viscous fibers in FBM and discuss the effects of these properties on the bundle mechanics and failure dynamics. In a third part, we demonstrate how FBMs can reproduce the results of snow failure experiments. Finally, we introduce the use of FBMs to study the effects of sound wave attenuation and of acoustic emissions (AE) for snow failure prediction and application of AE to provide early warnings for snow avalanche prediction.

Fiber Bundle Models

Originally developed for studying the strength of cotton yarns [6, 7] fiber bundle models (FBM) are a family of statistical models widely used for studying the failure of heterogeneous materials [8, 9]. In a FBM the material consists of a set of single elements (fibers) with heterogeneous strengths (**Figure 1**). An external load or displacement is applied to the fiber bundle and the single fibers fail when the load exceeds the strength. For load-controlled FBMs the load of the failing fibers is redistributed to intact fibers possibly causing a cascade of further fiber failures. The complex damage process of the bulk material arises from the interaction of multiple fibers (load redistribution) and the heterogeneous fiber strengths representing the material disorder. In the classical FBM the fibers are assumed to respond in a linearly elastic manner. The influence of local microscopic mechanisms on the global failure (i.e., failure of the whole system) can be investigated by changing the mechanical properties of the fibers [10]. There exist numerous applications as the study of local load distribution (e.g., Hansen and Hemmer [11] Hidalgo et al. [12]), creep failure [13, 14], or fatigue [15]. Moreover, FBMs are used to analyze the failure process in the context of critical phenomena and phase transitions [9, 16].

Snow

Snow is a highly porous material (porosity 0.5–0.95) consisting of an ice matrix with air filling the connected pore space[1]. The ice matrix is a continuous structure, as shown by micro-CT images (**Figure 2**; e.g., [17]), consisting of welded discrete ice elements (grains). The snow microstructure (e.g., size, form and connectivity of the ice matrix elements) strongly influences the snow mechanical properties (e.g., [18, 19]). Moreover, the high homologous temperature (i.e., temperature near to the melting point) of ice under natural conditions leads to peculiar material properties. The ice matrix undergoes a continuous recrystallization known as snow metamorphism. The type and speed of metamorphism depends on meteorological conditions. At isothermal conditions the crystal shape is first transformed from dendritic to small rounded particles and later from smaller to larger round particles, as the water vapor pressure is higher with higher curvature of the ice surface. This type of metamorphism generally increases the strength of snow [20–22]. Faceting (or temperature gradient) metamorphism is induced by the temperature gradients typically caused by snow surface cooling due to emission of longwave radiation. Temperature gradients cause vapor transport from warmer to the cooler ice surfaces leading to the growth of large faceted and depth hoar crystals if the vapor flow persists (e.g., [23]). Faceting metamorphism generally reduces snow strength and can lead to the formation of weak layers. Simultaneously, the gravitational load induced by the overlaying snow can contribute to compaction of the snowpack (settlement) and increase of snow strength.

The large range in porosity and microstructure of snow leads to corresponding large differences in physical properties. For example, the elastic modulus spans over several orders of magnitude depending on density and snow type (e.g., [18]). Therefore, a great challenge for finding a unified model for describing the snow microstructure is given by the broad range of density and snow types. Moreover, the ice particles bond immediately on contact (sintering) and the bond strength increases with time [24, 25] allowing to heal damage in the snow. The increase of bond strength with time is initially fast, then gradually slows down, but nevertheless continues with time leading to the increase of strength and stiffness over several days for new or sieved snow (e.g., [19, 22]).

Finally, the ice is subjected to viscous deformation or creep (e.g., [26, 27]) leading to snow creep and relaxation of localized stress. These phenomena result in the highly rate dependent failure behavior of snow. Whereas under high strain rates ($\dot{\epsilon} > 10^{-3}$ s^{-1}) snow fails in a brittle manner with very little deformation before fracture, at low strain rates ($\dot{\epsilon} < 10^{-3}$ s^{-1}) snow can sustain large strain and undergoes ductile failure—i.e., large irreversible deformation occurs before failure or the snow does not fail at all [28]. Sintering is considered one of the driving mechanism of the rate dependence of snow failure by some authors [4, 29, 30]. On the other hand, Kirchner et al. [31] used an open foam model including viscous deformation and a ductile-to-brittle transition in ice (at much lower strain rates $\dot{\epsilon} = 10^{-6}$ s^{-1}) to reproduce the ductile-to-brittle transition in snow. Moreover, the stress and time dependent creep deformation of ice may cause the relaxation of local load concentrations and influence the damage process. More recently Löwe et al. [3] developed a scalar model with rate-dependent, elastoplastic constitutive law and sintering that correctly reproduces mechanical experiments. Hence, a combination of the above-mentioned effects contributes to the ductile-to-brittle transition observed for snow.

Slab Avalanche Formation

Snow avalanches are a serious hazard for human life and infrastructures in snow-covered mountainous regions around the world; they cause on average about 100 fatalities annually in the European Alps [32]. The majority of avalanche accidents are due to dry-snow slab avalanches (see **Figure 3A**) [33]. For the release of a slab avalanche a so-called weak layer below cohesive slab layers is necessary. Weak layers typically consist of large poorly bonded crystals (**Figure 3B**, mainly faceted crystals and depth hoar, surface hoar, or new snow layers [34]). After an initial crack of sufficient size has formed in the weak layer, the crack propagates below the slab due to the stress concentrations at the crack tip, which is caused by lack of support of the weight of

[1]For wet snow at 0°C, we additionally have water within the pore space. Within this paper, we consider dry snow only.

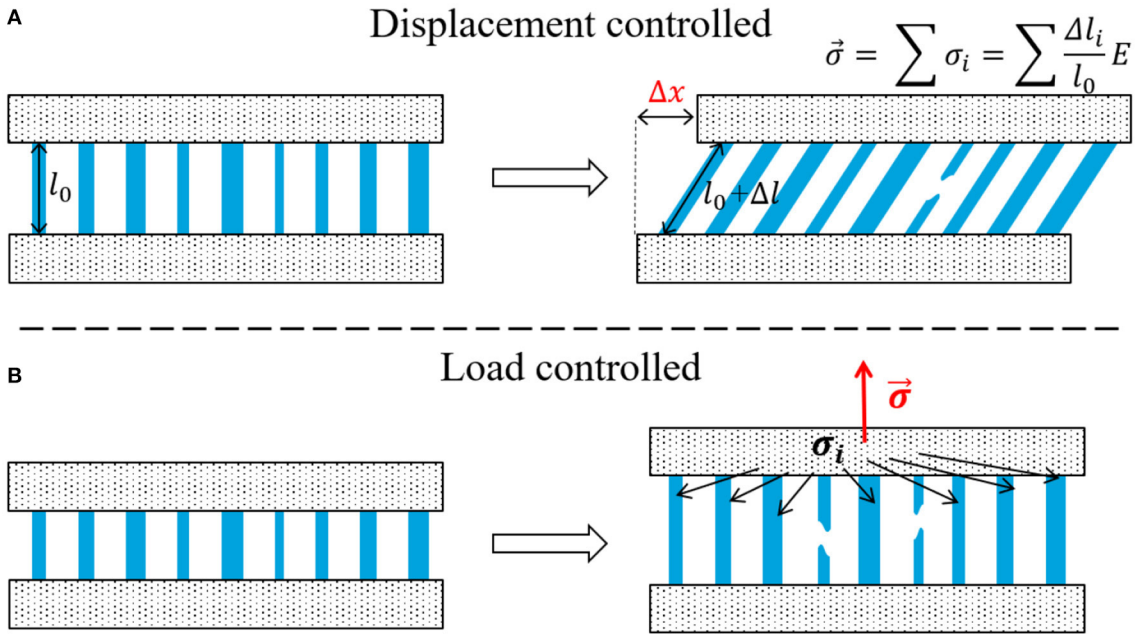

FIGURE 1 | Schematic representation of **(A)** displacement-controlled FBM in shear [4] and **(B)** load-controlled FBM in tension [5]. The fiber width illustrates the variability in fiber strength.

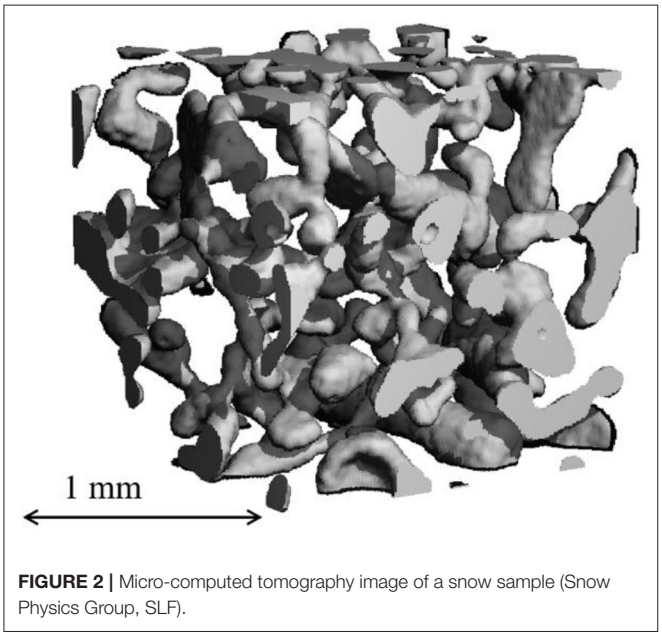

FIGURE 2 | Micro-computed tomography image of a snow sample (Snow Physics Group, SLF).

the overlaying slab over the cracked area. The critical crack size when rapid self-propagation starts, depends on both weak layer and slab properties, primarily the specific fracture energy of the weak layer and the thickness, density and stiffness of the slab layers [35, 36]. Crack propagation in the weak layer arrests by slope perpendicular fracture through the slab (**Figure 3B**). Once the slab is detached, it slides downslope if the gravitational force overcomes the friction, generally for slope angles $>30^\circ$ [37], and an avalanche is released (**Figure 3A**).

In case of artificially triggered avalanches the initial crack is caused by rapid near-surface loading due to e.g., a skier or an explosion. For natural (spontaneous) avalanches the load increase is much slower (additional weight due to precipitation or snow drift by wind), and the initial crack is believed to be the result of a progressive damage process at the microscale [34]. The exact processes involved in initial crack formation are, however, not well-understood. It is therefore fundamental to increase our understanding of snow avalanche formation by modeling snow failure.

Models in Snow Mechanics

Snow failure leading to avalanche release is a process involving different scales with different types of heterogeneity—going from the snow microstructure, through the vertical variation in snow properties (stratigraphy), to the spatial variability at the slope-scale. Modeling snow and avalanche formation requires dealing with these heterogeneities at the different respective scales. Generally different models are applied at the different scales. The microscopic snow structure and ice properties must be considered for modeling snow mechanical properties and failure initialization. Snow stratigraphy and mechanical properties of snow need to be considered for modeling crack propagation (e.g., [36, 38, 39]). At the slope-scale, spatial variations of snow stratigraphy and terrain are essential to model avalanche release (e.g., [40, 41]). More recently, Gaume et al. [2] introduced a model based on the material point method that can cope with both snow stratigraphy and terrain variability covering the multi-scale processes involved in avalanches: from failure initiation and crack propagation to avalanche flow [42, 43]. However, even these

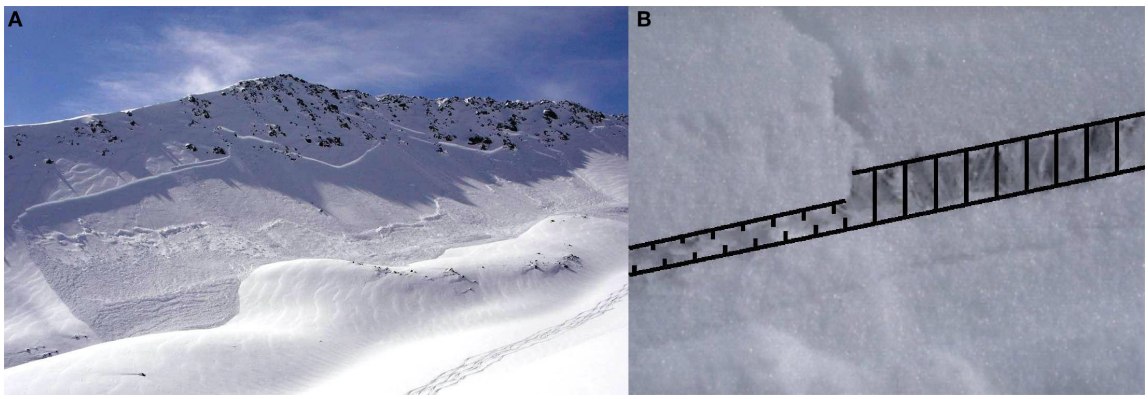

FIGURE 3 | (A) Dry-snow slab avalanche (R. Pajarola). **(B)** Snow weak layer (surface hoar) buried below a cohesive slab. On the right side the weak layer is intact. On the left side the weak layer failed leading to volumetric collapse of the porous structure. The black lines are a schematic representation of the FBM. Reprinted from the Journal of Glaciology with permission of the International Glaciological Society [4].

advanced models rely on appropriate parametrizations of snow including correct failure behavior and rate-dependent response.

Models aiming to reproduce the mechanical behavior of snow and the failure process have to take into account both the snow microstructure as well as the mechanical properties of ice. These models can be grouped into (i) Continuum models that include some parametrization of the microstructure – e.g. the snow viscosity model of Bartelt and von Moos [44], the open-cell foam model for snow [45, 46], or other models considering damage healing [3, 47, 48]. (ii) Models reproducing the microstructure in simplified form with discrete elements (beams, spheres) with some random variations such as the discrete element models [49–51]. (iii) Models that use the full 3-D representation of the microstructure obtained by micro-tomography as input for a finite-element model (e.g., [52–54]). Statistical models as the FBM belong to the second group of models.

FIBER BUNDLE MODELS APPLIED TO SNOW

The FBM was first applied to snow by Reiweger et al. [4]. Incorporating healing of broken fibers representing the fast sintering of broken bonds in snow, they were able to reproduce the characteristics of displacement-controlled snow failure experiments for different strain rates. Capelli et al. [5] introduced a load-controlled FBM including both healing of broken fibers and viscous deformation and described the effects of these two mechanisms on the failure behavior. With the same model it was possible to reproduce the mechanical characteristics and the concurrent acoustic emissions (AE) characteristics of load-controlled snow failure experiments with different loading rates spanning over the ductile-to-brittle transition [55]. Acoustic emissions are acoustic waves generated by the occurrence of damage in solid materials. An example of AE is the crackling noise produced by wood under load (e.g., [56]). AE are widely used for monitoring the damage process of heterogeneous materials (e.g., [57]). Attenuation of acoustic waves is a limitation for the application of AE for early warning, since it reduces the detection range and alters the AE signature. Attenuation in snow is particularly high due to the high porosity (e.g., [58]). The attenuation of AE is therefore particularly critical for applications aiming at using AE for early warning of snow avalanches. Faillettaz et al. [59] used a FBM for studying the effects of attenuation of AE on the failure prediction and proposed to use co-detection of AE for natural hazard early warning. Their FBM results were supported by AE data from snow failure experiments. In the following sections, we recap the working principle of the FBMs applied to snow.

Fiber Strength Distribution

The intrinsic disorder of heterogeneous materials (such as snow) is represented in the FBM by a large number of fibers with varying strengths (**Figure 1**). The Weibull distribution, which is commonly used for strength distributions in statistical models [8], was also employed in snow models for fiber strength [4, 5, 55]. The density function for the fiber strength σ_{th} is given by:

$$p\left(\sigma_{\text{th}}|\mu,k\right) = k\mu^{-k}{\sigma_{\text{th}}}^{k-1}e^{-\left(\frac{\sigma_{\text{th}}}{\mu}\right)^{k}}, \tag{1}$$

where μ is a scaling factor and k controls the amount of damage in the system (lower k correspond to larger amount of disorder). The disorder parameter k should depend on the snow microstructure. There is, however, no measurement method that allows determining k, so k must be assumed. Reiweger et al. [4] looked at the sensitivity to k in the range of 0.5 to 3 on the FBM and used $k = 0.7$ for fitting their mechanical experiments. Further studies used the value $k = 1.1$ [5, 55].

Displacement-Controlled FBM

In the displacement-controlled model presented by Reiweger et al. [4] a constant shear rate is imposed (**Figure 1A**). Assuming elastic fibers, the stress on the single fibers increases linearly with fiber strain. If the stress on a fiber reaches its strength, the fiber fails. Thus, the total stress on the fiber bundle decreases. When

half of the fibers failed, the entire bundle is considered as broken. Reiweger et al. [4] introduced a variation to the classical FBM. They assumed that the fibers are subjected to shear perpendicular to the initial direction. The fiber elongation Δl is then:

$$\Delta l = \sqrt{l_0^2 + \Delta x^2} - l_0, \tag{2}$$

where Δx is the shear deformation of the bundle and l_0 is the fiber length. The stress is then given by:

$$\sigma = E\epsilon = E\frac{\Delta l}{l_0}, \tag{3}$$

where E is the elastic modulus. Introducing shear deformation shifts the stress-strain curve toward higher deformations [4], since initially the fiber stress increase is slower than for the FBM with displacement parallel to the fibers (Equations 2, 3).

Load-Controlled FBM

In case of load-controlled FBMs [5, 55], the load on the fibers is increased step wise to the strength of the weakest fiber that consequently fails. As a fiber fails, its load is distributed to the other surviving fibers according to a redistribution rule (**Figure 1B**). For the FBM described by Capelli [5] a "democratic" or "equal" load-sharing rule was used. Meaning that the load was redistributed equally to the surviving fibers. This is equivalent to the assumption of stiff plates clamping the fibers and makes the spatial position of the fibers irrelevant (0 dimensional material). Other models use local load-sharing rules, where the load is distributed to the neighboring fibers only [59]. With local load-sharing rules the fiber position becomes relevant (one or more dimensional material). Distributing the load of failing fibers among the surviving fibers can cause a cascade of failures. The number of fibers failing in a cascade following a failure due to load increase is expressed as the burst size S. For linear elastic fibers the bundle strain ϵ_J is obtained from the sum of the strain increase at each load increase step up to the step J:

$$\epsilon_J(\sigma) = \sum_{j=0}^{J} \Delta\epsilon_{el,j} = \sum_{j=0}^{J} \underbrace{\frac{1}{U_j E}\Delta\sigma_j}_{\text{load increase}} + \underbrace{\frac{1}{U_j E}\sum_{k\epsilon s_j}\sigma_{k,j}}_{\text{redistribution}}, \tag{4}$$

where U_j is the fraction of intact fibers, $\sigma_{k,j}$ is the load of the fiber k, and S_j is the set of fibers that failed at the load step j.

FBM WITH HEALING FIBERS

When two ice particles are brought in contact, a bond is immediately created with increasing bond strength with increasing time [25, 60]. This process, known as sintering, allows damage in snow to heal with time. The FBM is well-suited to study the effects of healing on the mechanical properties of snow as implementing a healing mechanism is quite straight forward. Healing has been incorporated in FBMs in different ways in the past, e.g., in the stick-slip FBM the fibers regain strength immediately after failure [61, 62].

Reiweger et al. [4] were the first to apply a FBM to snow that included healing of broken fibers (**Figure 4A**). In their displacement-controlled FBM at each time step Δt a broken fiber regains strength with the probability p_s depending on the number of brocken fiber N_b available for forming a new bond with $p_s = p_{max}\frac{N_b}{N}$. The strength of a new bond is initially zero but increases with time:

$$\sigma_{th,i}(t) = \left(1 - e^{\frac{-t}{t_s - t}}\right)\sigma_{th,i,final} \tag{5}$$

for $t < t_s$ where t_s is the sintering time and $\sigma_{th,i,final}$ is drawn from the same initial distribution.

Similarly, fiber healing has been implemented in the load-controlled FBM with the probability of a broken fiber to regain strength during the time Δt being:

$$p_s(\Delta t) = \left(1 - e^{\frac{-\Delta t}{t_p}}\right)\frac{N_b}{N} \tag{6}$$

with the characteristic time t_p [5]. In this case, it was assumed that the fibers regain full strength immediately.

The fiber healing speed is higher with either lower characteristic time or lower loading rate. If the characteristic time in the model by Capelli et al. [5] is compared to that of Reiweger et al. [4], then the sintering probability in Reiweger et al. [4] is linear with $p_{max} = \frac{\Delta t}{t_{p,Reiw.}}$. The characteristic time used by Reiweger et al. [4] for fitting the model to mechanical experiments was $t_{p,Reiw.} = \frac{\Delta t}{p_{max}} = 0.66$ s. Capelli et al. [55] reported a larger characteristic time of healing $t_{p,Cap.} = 20$ s. The difference in time scale may be due to the different snow type and testing mode (displacement- vs. load-controlled). Additionally, in the model by Reiweger et al. [4] the strength of the new bonds increases with time. The speed of the strength increase is controlled by the sintering time $t_s = 1.09$ s (Equation 7). A DEM model for snow including bond sintering on contact with increasing bond strength using a similar sintering time $t_s = 1$ s was proposed by Mulak and Gaume [50].

Effect of Healing on Mechanical Behavior and Failure Dynamics

For both displacement- and load-controlled FBMs healing results in higher stress at equal strain and in higher stress and strain at failure [4, 5]. Healing counterweighs the damage process as broken fibers regain strength. The number of intact fibers in the bundle increases so that they can support a higher load or, equivalent, a higher load is needed for equal deformation. Therefore, the material becomes stiffer and has higher strength.

The effects on the failure behavior differ between displacement- and load-controlled FBMs. For the displacement-controlled FBM, Reiweger et al. [4] reproduced the ductile-to-brittle transition of snow with the introduction of healing. For large displacement rates the healing process is slower than the damage process and does not affect the bundle's failure. After reaching the bundle strength the stress rapidly decreases and all fibers fails (brittle failure). For low strain rates, as the damage in the bundle increases and steady-state is reached (i.e., the damage process is compensated by healing of fibers), the number of broken fibers remaine constant with increasing strain and ductile failure is observed (**Figure 5**). The type of the stress-strain curve in the steady-state regime is controlled by

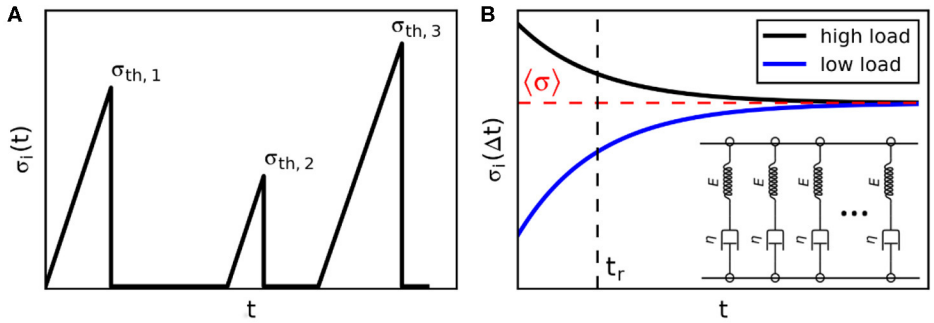

FIGURE 4 | (A) Load evolution for a single fiber when healing is included. The load increases until the strength $\sigma_{th,1}$ is reached and the fiber fails. After a certain random time, the fiber heals and is assigned a new strength $\sigma_{th,2}$ independent of the previous strength; subsequently it may fail and sinter again. **(B)** Relaxation of load on the single fibers toward the mean load $\langle\sigma\rangle$ for the FBM assuming viscoelastic fibers (schematic in inset). The speed of the load relaxation is controlled by the characteristic loading time t_r. Figures adapted from [5].

the fiber strength distribution. With higher disorder (Weibull parameter $k \leq 1$), strain strengthening and creep (increase of strain at constant stress) is observed. Whereas, with low disorder ($k \geq 1$) failure (stress peak) is followed by strain softening and final creep.

For the load-controlled FBM the steady state is not "visible" since when the imposed stress exceeds the bundle strength (stress peak in displacement-controlled strain-stress curve) all fibers fail. On the other hand, stress control allows observing the failure dynamics arising as the load sharing causes a catastrophic cascade of fiber ruptures resulting in the complete failure of the bundle. In the load-controlled FBM the damage process diverges approaching failure (e.g., [9, 16]). The fiber failure rate $\frac{dS}{d\sigma}$, which is commonly known as susceptibility, diverges approaching failure at σ_c with $\frac{dS}{d\sigma} \sim (\sigma_c - \sigma)^{-\alpha}$. The order parameter $O(\sigma) = U(\sigma_c) - U(\sigma)$ approaches zero following a power law with $O(\sigma) = (\sigma_c - \sigma)^{\kappa}$, where $U(\sigma)$ is the fraction of broken fibers. With healing the amount of damage (portion of broken fibers) immediately before failure is lower. Moreover, with healing the exponent α decreases, whereas the exponent κ increases (**Figure 6**) indicating that the period before failure, where the damage process accellerate, is shorter—a sign of increased brittleness. For the FBM the bursts size S is generally power-law distributed with $P(S) \sim S^{-b}$, similarly to the Gutenberg–Richter law for earthquakes (e.g., [9]). Generally, an apparent decrease of the exponent b toward failure is observed. This is explained by a truncated power-law distribution $P(S) \sim S^{-\tau} \exp(\frac{S}{S_0})$ with diverging cut-off burst size $S_0 \sim \Delta^{-\gamma}$ and $\Delta = \frac{\sigma_c - \sigma}{\sigma_c}$ (e.g., [63, 64]). The exponents are linked by $b = \tau + \frac{1}{\gamma}$. Capelli et al. [5] reported a decrease of b with increasing healing rate when all events were considered, whereas near to failure the exponent was unaffected by healing. This is equivalent to a constant exponent τ whereas the exponent γ increases with increasing healing rate (**Figure 6**). In the context of failure prediction, faster acceleration and lower apparent decrease of exponent b means that that time lag for prediction decreases and prediction becomes more difficult, yet not impossible.

FBM WITH VISCOUS FIBERS

As ice is a viscous material, Capelli et al. [5] introduced ice viscosity in their FBM assuming that the fibers are Maxwell elements (**Figure 4B**) with the corresponding constitutive equation:

$$\dot{\epsilon}_i = \frac{\sigma_i}{\eta} + \frac{\dot{\sigma}_i}{E} \tag{7}$$

where σ_i is the stress on a single fiber, E is the fiber's elastic modulus and η its viscosity. Incorporating viscosity results in the relaxation of load inhomogeneity in the bundle with time. The load is redistributed from the older fibers carrying more load to the younger ones carrying less load. The load of the single fiber i converges exponentially toward the mean load with:

$$\sigma_i(t + \Delta t) = \langle\sigma\rangle + (\sigma_i(t) - \langle\sigma\rangle)\, e^{-\frac{\Delta t}{t_r}}, \tag{8}$$

where $\langle\sigma\rangle$ is the intact fiber mean load, and the ratio between elastic modulus E and viscosity η is the characteristic relaxation time $t_r = \frac{E}{\eta}$ determinig the speed of relaxation (**Figure 4B**). In the model by Capelli et al. [5] the load inhomogeneity is due to the healing process, since new fibers initially do not carry load. If fiber viscosity is included, a viscous term is added to Equation (4) for the bundle strain ϵ_J:

$$\epsilon_J(\sigma) = \sum_{j=0}^{J} \left(\Delta\epsilon_{el,j} + \Delta\epsilon_{visc,j}\right) = \overbrace{\sum_{j=0}^{J} \underbrace{\frac{1}{U_j E}\Delta\sigma_j}_{\text{load increase}} + \underbrace{\frac{1}{U_i E}\sum_{k\epsilon s_j}\sigma_{k,j}}_{\text{redistribution}}}^{\text{elastic part}} + \overbrace{\sum_{j=0}^{J} \frac{1}{\eta}\frac{\langle\sigma\rangle_j}{U_i}\Delta t_j}^{\text{viscous part}}, \tag{9}$$

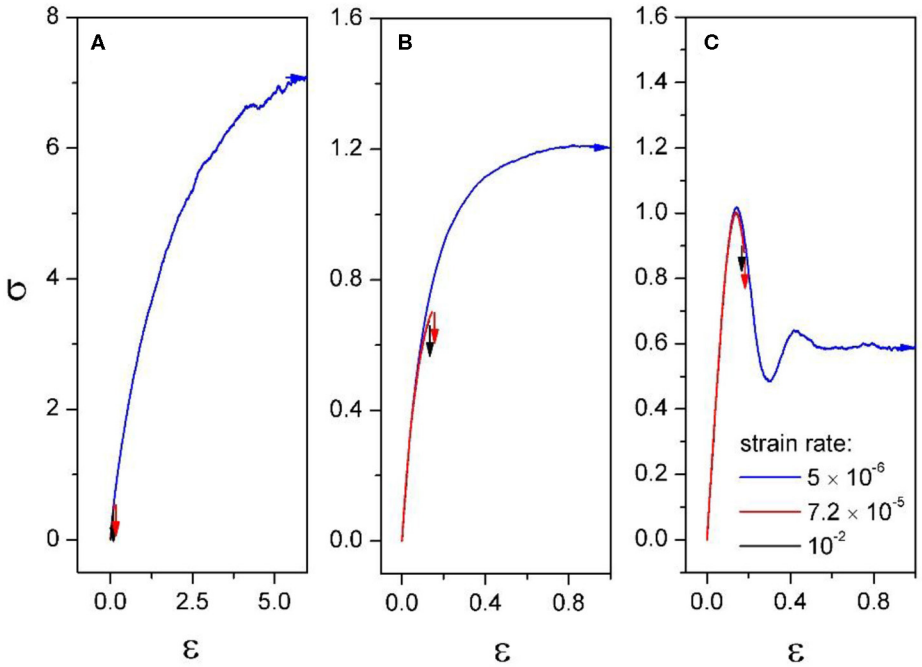

FIGURE 5 | FBM simulation results with varying shape factor k for the Weibull distributions of single fiber strength: **(A)** $k = 0.5$; **(B)** $k = 1$; and **(C)** $k = 3$. For each shape factor, stress–strain curves for three different strain rates (1×10^{-2}, 7.2×10^{-5}, and 5×10^{-6} s^{-1}) are given. The vertical arrows mark the point where the bundle fractures, while the horizontal arrows indicate that the bundle is still intact but the simulation was stopped. Reprinted from the Journal of Glaciology with permission of the International Glaciological Society [4].

The magnitude of the effects of viscosity can be expressed with the characteristic load $\sigma_r = \dot{\sigma}\ t_r = \dot{\sigma}\ \frac{\eta}{E}$. Load relaxation and viscous deformation are higher for low characteristic loads σ_r.

Effect of Viscous Fibers on Mechanical Behavior

If viscosity is added to the FBM, fiber deformation can be divided in an elastic and a viscous part. With the Maxwell model for viscoelasticity, the elastic deformation takes place immediately as the load is applied, whereas the viscous deformation increases linearly in time with the strain rate depending on the applied load (Equation 7). For high values of viscosity or high loading rate, the bundle deformation is mainly elastic. For lower values of loading rate or viscosity, the deformation is predominantly viscous and strain at equal stress is larger than with primarily elastic deformation (**Figure 7A** and [5]).

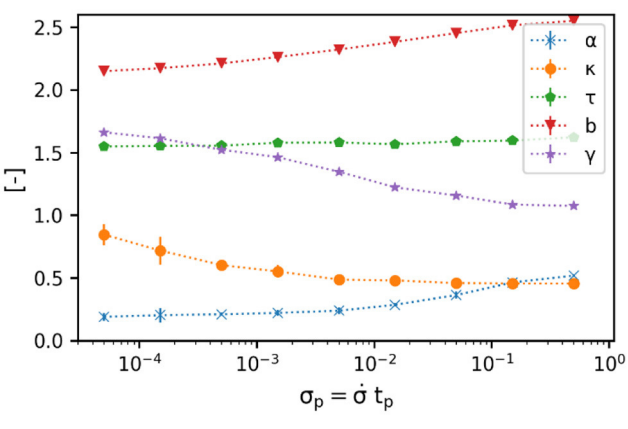

FIGURE 6 | Critical exponents for different increasing healing speeds. The healing speed increases with decreasing healing load $\sigma_p = \dot{\sigma}\ t_p$.

Effect of Viscous Fibers on Failure Dynamics

Fiber viscosity also has consequences for the internal distribution of fiber load. The viscous deformation rate is higher for fibers carrying higher load. Therefore, the fiber load relaxes toward the mean fiber load, transferring load from fibers carrying high loads to fibers carrying low loads. This is equivalent to a load transfer from older fibers to newly healed fibers, since with equal load-sharing fiber healing is the only source of load inhomogeneity. The load inhomogeneity in the bundle decreases for lower t_r leading to a more efficient distribution of load resulting in a bundle strength increase [5]. Load relaxation has a large effect on the failure dynamics. For high load relaxation speed the acceleration of damage prior to failure is suppressed (**Figure 7A**). No divergence of strain rate and fiber failure $\frac{dS}{d\sigma}$ is observed; the order parameter $O(\sigma)$ develops from a power law decrease approaching failure at σ_c with $O(\sigma) = (\sigma_c - \sigma)^{\kappa}$ to a linear decrease (**Figure 7B**). Fiber failure burst size distribution is

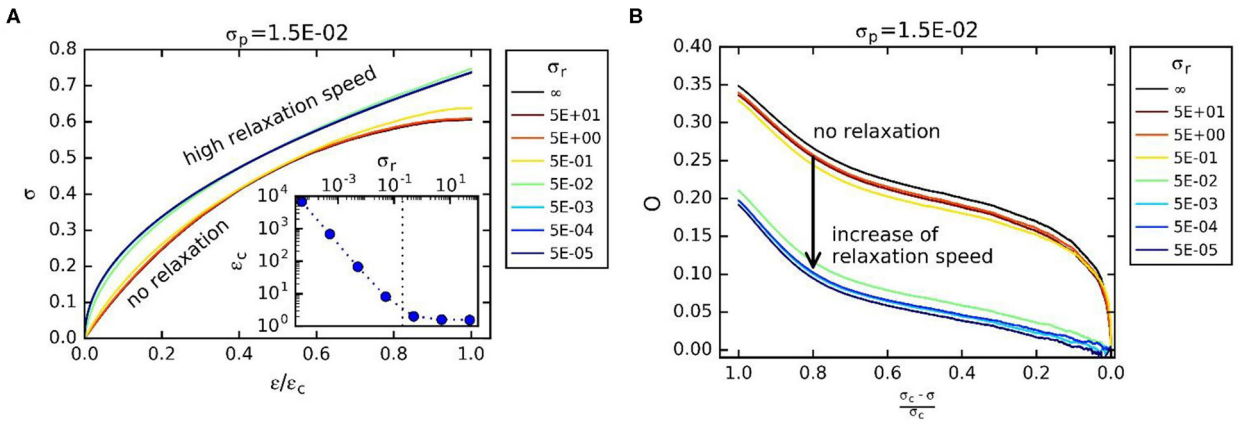

FIGURE 7 | (A) Stress-strain relations of FBM for different relaxation characteristic loads σ_r and a constant sintering characteristic load $\sigma_p = 1.5 \times 10^{-2}$. The strain was scaled with the strain at failure ϵ_c. The inset shows the strain at failure ϵ_c as a function of the relaxation characteristic load σ_r. **(B)** Evolution of the order parameter O toward failure for different σ_r and constant $\sigma_p = 1.5 \times 10^{-2}$. The characteristic times $t_{r/p}$ were scaled to characteristic loads with $\sigma_{r/p} = \dot{\sigma}\ t_{r/p}$. Reprinted from [5].

also affected by load relaxation. Both exponents b and τ of the burst size distribution $P(S)$ increase with increasing load relaxation speed indicating a shift to a larger share of small failure bursts.

The absence of damage acceleration suggests that load relaxation changes the type of transition at failure from continuous to abrupt indicating a change of the universality class. This interpretation is supported by the change of the power law exponent τ. Load relaxation causes a shift in the distribution of fiber strength with increasing main strength and decreasing disorder. Therefore, the fibers are likely to fail abruptly as a critical load is reached. A similar change in the type of transition at failure was reported by Biswas and Sen [65] for a FBM where the load of failing fibers was redistributed according to the fiber strength.

REPRODUCING SNOW FAILURE EXPERIMENTS

The FBMs presented above were used to reproduce snow failure experiments with the aim to investigate the micromechanical principles governing the macroscopic mechanical behavior of snow. In particular the FBM allowed to study the rate dependent mechanical response of snow with the well-known ductile-to-brittle transition [28].

Displacement-Controlled Experiments

With the FBM including healing Reiweger et al. [4] reproduced the displacement-controlled snow failure experiments at different strain rates presented by Schweizer [66]. Their FBM very well-captured the observed ductile-to-brittle transition (**Figure 8**) and reproduced the higher strength and strain at failure with decreasing strain rate. Both, snow samples and fiber bundle, showed brittle failure behavior for high strain rates ($> 3 \times 10^{-4}$ s^{-1}) and for low strain rates ductile failure followed by strain softening and creep. The stress-strain relations obtained with the FBM had a convex form at low strain. The convexity

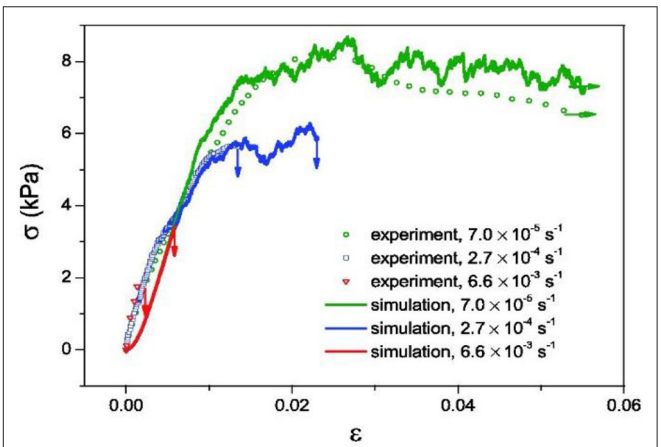

FIGURE 8 | Comparison of FBM and experimental results for displacement-controlled conditions. Reprinted from the Journal of Glaciology with permission of the International Glaciological Society [4].

is due to the arrangement of the fibers relative to the load. When the fibers are loaded in shear the fiber stress initially increases just slowly (Equation 2). The experimental curves did not show any convexity. The simple spatial arrangement of the fibers in the FBM can obviously not fully reproduce the complex structure of the ice matrix. A FBM with load parallel to the fibers (pure tension) would better fit the experimental results. Indeed, recent DEM studies suggest that under mixed-mode loading (compression and shear) the ice matrix mainly failed in tension [67]. The FBM results support this view.

Load-Controlled Experiments and Concurrent Acoustic Emissions

Capelli et al. [55] applied the FBM including healing of broken fibers and viscous fibers for modeling load-controlled snow failure experiments at different loading rates (32, 128, and

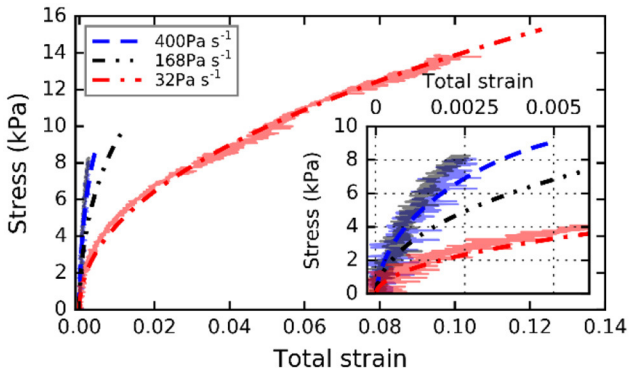

FIGURE 9 | FBM and experimental results for load-controlled conditions. The dotted line indicates the FBM results. Reprinted from [55].

400 Pa s^{-1}) and the concurrent acoustic emissions [68]. Using parameters in agreement with the snow values reported in the literature, they reproduced the main features of the experimental results. The stress-strain relations found in experiments and obtained with their FBM were similar with higher stress and strain at failure and higher strain at equal stress for lower loading rates (**Figure 9**). Capelli et al. [55] compared the energy of the AE with the elastic energy released at fiber failure—i.e., they assumed that the elastic energy stored in the fiber failing in a failure burst $U = \frac{\sum_j \sigma_j^2}{2E}$ is equivalent to the energy of measured AE. The FBM exhibited features similar to the loading rate dependent AE signatures observed for the snow failure experiments. For both, FBM and experiments, the AE energy rate increased toward failure and the energy distribution exponent τ was higher for the fast loading rates (**Figure 10**). Also, Pradhan et al. [69] claim that the elastic energy exhibits a peak prior to failure that can be used to predict the failure point of FBM. The elastic energy is, however, difficult to quantify for the snow experiments since the displacement measured includes elastic as well as viscous deformation. However, there were also differences between FBM and experimental results. For the FBM an apparent decrease of the exponent b, indicating a divergence of the cut-off energy of a truncated power law (see section FBM With Healing Fibers) was present for all loading rates. For the experiments, the apparent decrease of b was not observed for the low loading rates, although the exponent at failure τ was higher for low loading rates (**Figure 10A**). Moreover, the divergence in the damage process at failure for high loading rates, that is visible in the strain rate and the energy rate $\frac{dU}{d\sigma}$, was not observed in the experimental results.

The substantial differences in the failure dynamics of snow for different loading rates could only be reproduced with the FBM by including both healing of broken fibers and viscous deformation with resulting load relaxation. It follows that both, healing and load relaxation, are essential for understanding and modeling snow failure and should be taken into account in future models, which aim at reproducing snow behavior at low loading rates.

ATTENUATION OF AE AND CONSEQUENCES FOR FAILURE PREDICTION

The amplitude of acoustic waves propagating in natural media decreases with distance from the source due to geometrical spreading, absorption and scattering. Faillettaz et al. [59] introduced signal attenuation into the load-controlled FBM with equal and local load-sharing, which was developed by Faillettaz and Or [70]. The amplitude attenuation was computed for each fiber failure burst (i) assuming that the amplitude is proportional to the burst size S and (ii) accounting for geometrical spreading only (decrease of amplitude with $A(r) \sim \frac{1}{r}$ for the distance from the source r). The attenuated amplitude A_a of the burst S_j measured at the sensor at position x_{sensor} is then: $A_a = \sum_{i \in S_j} \frac{1}{\|x_i - x_{\text{sensor}}\|}$, with x_i being the position of the failing fiber i. Faillettaz et al. [59] showed that attenuation changes the frequency distribution of the recorded fiber failure bursts. The apparent decrease of the power law exponent ($b \rightarrow \tau$) is less pronounced when signal attenuation is taken into account. The decrease of the power law exponent is considered useful for assessing the stability of geological structures (e.g., [63]).

However, for real cases where attenuation is present the decrease is less prominent and occasionally hard to detect. Therefore, using the decrease of the exponent as precursor to failure for early warning purposes is limited. To overcome this problem Faillettaz et al. [59] proposed the number of co-detections (event detected by multiple sensor) as precursor to catastrophic failure, since small events are generally detected by nearby sensors only, whereas large events may be detected also by sensors at larger distances. Faillettaz et al. [59] tested the co-detection method with AE data from laboratory snow failure experiments [71]. An increase of the AE maximum amplitude was registered one second before failure, whereas a significant increase in the number of co-detections was recorded 10 s before failure increasing the early warning time lag by a factor 10.

CONCLUSIONS

The fiber bundle model (FBM) consists of a large number of fibers with variable strengths following simple mechanical laws (e.g., elastic or viscoelastic). Through the disorder and load sharing (fiber interaction) a complex behavior arises. FBMs are used to reproduce failure of heterogeneous materials and to study effects of micromechanical processes on global failure. For these reasons, the FBM is well-suited for studying the failure of snow. The displacement or loading rate dependence of snow failure observed experimentally, in particular the ductile-to-brittle transition, was reproduced. Whereas, displacement-controlled experiments were reproduced by including healing, for reproducing load-controlled experiment both healing and load relaxation (viscosity) were necessary. In particular, the loading rate dependent failure dynamics revealed by the AE signature preceding snow failure were reproduce only with both healing and load relaxation. Therefore, the results of the FBM studies on snow point out the importance of considering healing

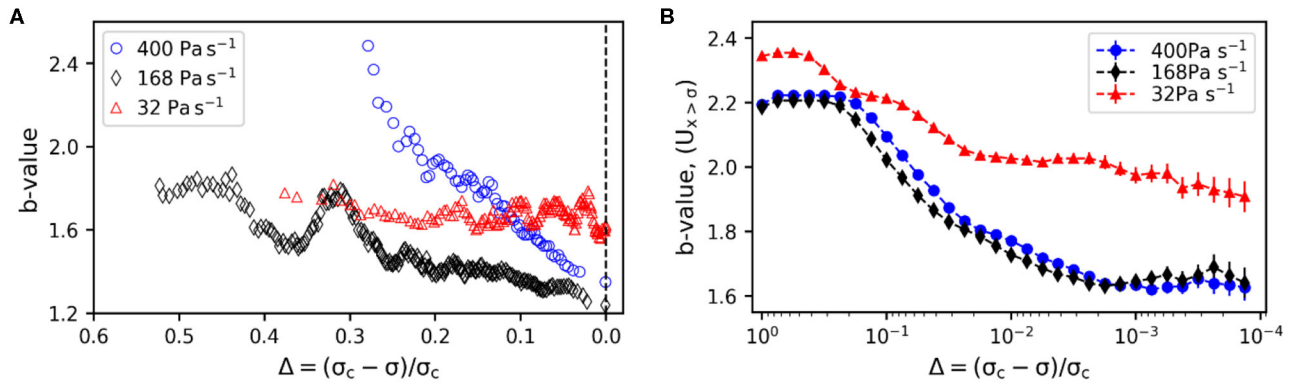

FIGURE 10 | Evolution of *b*-value with increasing load σ up to failure at σ_c for three different loading rates for: the AE energy E_{AE} **(A)** and the FBM burst elastic energy U **(B).** Adapted from [55].

and viscosity for modeling snow, especially at low displacement or loading rates. The FBM with healing and load relaxation shows that for low loading rates there is a lack of failure precursors suggesting that in some cases failure prediction is not possible.

The similarity between the fiber failure bursts in FBMs and the AE produced prior to failure is useful not just for interpreting the AE signatures, but can also be used for studying the effects of acoustic wave attenuation of the recorded AE. Using a FBM Faillettaz et al. [59] showed that the attenuation reduces the applicability of AE as precursor to failure. As alternative they suggested to use co-detection of AE for early warning and demonstrated the working principle with a FBM [59].

Simplicity is a strength of the FBM since it allows to study the effects of simple micromechanical drivers on failure. However, reproducing the complex 3D microstructure of snow is not possible. Nevertheless, it is important to include the findings obtained with FBM into models able to reproduce the 3D snow microstructure, such as the discrete element model (DEM). Rate dependent snow failure experiments at different temperatures in combination with FBM may be used for separating the effects of healing and viscosity since both ice sintering and viscosity are temperature dependent. The understanding of the damage process in snow gained with FBM should be applied to slope-scale models for studying natural avalanche release. The snow FBM may be even incorporated into a slope scale model as it has been done for modeling landslide release [72].

AUTHOR CONTRIBUTIONS

AC wrote the original draft of the manuscript. IR and JS provided feedback and edited the manuscript. All authors contributed to the article and approved the submitted version.

REFERENCES

1. Schweizer J, Bartelt P, van Herwijnen A. Chapter 12 - Snow Avalanches. In: Shroder JF, Haeberli W, Whiteman C, Editors. *Snow and Ice-Related Hazards, Risks and Disasters* Academic Press (2015). p. 395–436. doi: 10.1016/B978-0-12-394849-6.00012-3
2. Gaume J, Gast T, Teran J, van Herwijnen A, Jiang C. Dynamic anticrack propagation in snow. *Nat Commun.* (2018) **9**:3047. doi: 10.1038/s41467-018-05181-w
3. Löwe H, Zaiser M, Mösinger S, Schleef S. Snow mechanics near the ductile-brittle transition: compressive stick-slip and snow microquakes. *Geophys Res Lett.* (2020) **47**:e2019GL085491. doi: 10.1029/2019GL085491
4. Reiweger I, Schweizer J, Dual J, Herrmann HJ. Modelling snow failure with a fiber bundle model. *J Glaciol.* (2009) **55**:997–1002. doi: 10.3189/002214309790794869
5. Capelli A, Reiweger I, Lehmann P, Schweizer J. Fiber bundle model with time-dependent healing mechanisms to simulate progressive failure of snow. *Phys Rev E.* (2018) **98**:023002. doi: 10.1103/PhysRevE.98.023002
6. Peirce FT. Tensile tests for cotton yarns v. - "The weakest link" theorems on the strength of long and of composite specimens. *J Text Inst Trans.* (1926) **17**:T355–68. doi: 10.1080/19447027.1926.10599953
7. Daniels HE. The statistical theory of the strength of bundles of threads. *Proc R Soc A Math Phys Eng Sci.* (1945) **183**:405–35. doi: 10.1098/rspa.1945.0011
8. Herrmann HJ, Roux S. *Statistical Models for the Fracture of Disordered Media.* Amsterdam: Elsevier Science Publishers. (1990).
9. Alava MJ, Nukalaz PKVV, Zapperi S. Statistical models of fracture. *Adv Phys.* (2006) **55**:349–476. doi: 10.1080/00018730300741518
10. Kun F, Hidalgo RC, Raischel F, Herrmann HJ. Extension of fibre bundle models for creep rupture and interface failure. *Int J Fracture.* (2006) **140**:255–65. doi: 10.1007/s10704-005-2556-4
11. Hansen A, Hemmer PC. Burst avalanches in bundles of fibers: local versus global load-sharing. *Phys Lett A.* (1994) **184**:394–6. doi: 10.1016/0375-9601(94)90511-8
12. Hidalgo RC, Moreno Y, Kun F, Herrmann HJ. Fracture model with variable range of interaction. *Phys Rev E.* (2002) **65**:046148. doi: 10.1103/PhysRevE.65.046148
13. Hidalgo RC, Kun F, Herrmann HJ. Creep rupture of viscoelastic fiber bundles. *Phys Rev E.* (2002) **65**:032502. doi: 10.1103/PhysRevE.65.032502
14. Kun F, Moreno Y, Hidalgo RC, Herrmann HJ. Creep rupture has two universality classes. *Europhys Lett.* (2003) **63**:347–53. doi: 10.1209/epl/i2003-00469-9
15. Kun F, Costa MH, Costa RN, Andrade JS, Soares JB, Zapperi S, et al. Fatigue failure of disordered materials. *J Stat Mech Theor Exp.* (2007) **2007**:P02003. doi: 10.1088/1742-5468/2007/02/P02003
16. Pradhan S, Hansen A, Chakrabarti BK. Failure processes in elastic fiber bundles. *Rev Mod Phys.* (2010) **82**:499–555. doi: 10.1103/RevModPhys.82.499

17. Coléou C, Lesaffre B, Brzoska J-B, Ludwig W, Boller E. Three-dimensional snow images by X-ray microtomography. *Ann Glaciol.* (2001) **32**:75–81. doi: 10.3189/172756401781819418
18. Shapiro LH, Johnson JB, Sturm M, Blaisdell GL. Snow mechanics - review of the state of knowledge and applications. In: *CRREL Report 97-3*. Hanover, NH: US Army Cold Regions Research and Engineering Laboratory (1997). doi: 10.21236/ADA330695
19. Gerling B, Löwe H, van Herwijnen A. Measuring the elastic modulus of snow. *Geophys Res Lett.* (2017) **44**:11088–96. doi: 10.1002/2017GL075110
20. Perla R, Sommerfeld RA. On the metamorphism, morphology and microstructure of snow. In: *Proceedings ISSW 1986 International Snow Science Workshop, Lake Tahoe, California, U.S.A*. Homewood, AL: ISSW Workshop Committee (1987). p. 98–102.
21. Kaempfer TU, Schneebeli M. Observation of isothermal metamorphism of new snow and interpretation as a sintering process. *J Geophys Res Atmosph.* (2007) **112**:D24101. doi: 10.1029/2007JD009047
22. van Herwijnen A, Miller DA. Experimental and numerical investigation of the sintering rate of snow. *J Glaciol.* (2013) **59**:269–74. doi: 10.3189/2013JoG12J094
23. Pinzer BR, Schneebeli M, Kaempfer TU. Vapor flux and recrystallization during dry snow metamorphism under a steady temperature gradient as observed by time-lapse micro-tomography. *Cryosphere*. (2012) **6**:1141–55. doi: 10.5194/tc-6-1141-2012
24. Gubler H. Strength of bonds between ice grains after short contact times. *J Glaciol.* (1982) **28**:457–73. doi: 10.1017/S0022143000005050
25. Szabo D, Schneebeli M. Subsecond sintering of ice. *Appl Phys Lett.* (2007) **90**:151916. doi: 10.1063/1.2721391
26. Sinha NK. Short-term rheology of polycrystalline ice. *J Glaciol.* (1978) **21**:457–73. doi: 10.1017/S002214300003361X
27. Schulson EM, Duval P. *Creep and Fracture of Ice*. Cambridge: Cambridge University Press (2009). doi: 10.1017/CBO9780511581397
28. Narita H. Mechanical behaviour and structure of snow under uniaxial tensile stress. *J Glaciol.* (1980) **26**:275–82. doi: 10.1017/S0022143000010819
29. De Montmollin V. Shear tests on snow explained by fast metamorphism. *J Glaciol.* (1982) **28**:187–98. doi: 10.1017/S0022143000011898
30. Schweizer J. Review of dry snow slab avalanche release. *Cold Reg Sci Technol.* (1999) **30**:43–57. doi: 10.1016/S0165-232X(99)00025-7
31. Kirchner HOK, Michot G, Narita H, Suzuki T. Snow as a foam of ice: plasticity, fracture and the brittle-to-ductile transition. *Philos Mag A*. (2001) **81**:2161–81. doi: 10.1080/01418610108217141
32. Techel F, Jarry F, Kronthaler G, Mitterer S, Nairz P, Pavšek M, et al. Avalanche fatalities in the European Alps: long-term trends and statistics. *Geogr Helv*. (2016) **71**:147–59. doi: 10.5194/gh-71-147-2016
33. Jamieson JB, Johnston CD. Snowpack characteristics associated with avalanche accidents. *Can Geotech J.* (1992) **29**:862–6. doi: 10.1139/t92-093
34. Schweizer J, Jamieson JB, Schneebeli M. Snow avalanche formation. *Rev Geophys.* (2003) **41**:1016. doi: 10.1029/2002RG000123
35. Schweizer J, van Herwijnen A, Reuter B. Measurements of weak layer fracture energy. *Cold Reg Sci Technol.* (2011) **69**:139–44. doi: 10.1016/j.coldregions.2011.06.004
36. Gaume J, van Herwijnen A, Chambon G, Wever N, Schweizer J. Snow fracture in relation to slab avalanche release: critical state for the onset of crack propagation. *Cryosphere*. (2017) **11**:217–28. doi: 10.5194/tc-11-217-2017
37. van Herwijnen A, Heierli J. Measurement of crack-face friction in collapsed weak snow layers. *Geophys Res Lett.* (2009) **36**:L23502. doi: 10.1029/2009GL040389
38. Heierli J, Gumbsch P, Zaiser M. Anticrack nucleation as triggering mechanism for snow slab avalanches. *Science*. (2008) **321**:240–3. doi: 10.1126/science.1153948
39. Rosendahl PL, Weissgraeber P. Modeling snow slab avalanches caused by weak-layer failure - part 1: slabs on compliant and collapsible weak layers. *Cryosphere*. (2020) **14**:115–30. doi: 10.5194/tc-14-115-2020
40. Fyffe B, Zaiser M. The effects of snow variability on slab avalanche release. *Cold Reg Sci Technol.* (2004) **40**:229–42. doi: 10.1016/j.coldregions.2004.08.004
41. Gaume J, Chambon G, Eckert N, Naaim M, Schweizer J. Influence of weak layer heterogeneity and slab properties on slab tensile failure propensity and avalanche release area. *Cryosphere*. (2015) **9**:795–804. doi: 10.5194/tc-9-795-2015
42. Gaume J, Van Herwijnen A, Gast T, Teran J, Jiang C. Investigating the release and flow of snow avalanches at the slope-scale using a unified model based on the material point method. *Cold Reg. Sci. Technol.* (2019) **168**:102847. doi: 10.1016/j.coldregions.2019.102847
43. Li X, Sovilla B, Jiang C, Gaume J. The mechanical origin of snow avalanche dynamics and flow regime transitions. *Cryosphere Discuss.* (2020) **2020**:1–25. doi: 10.5194/tc-2020-83
44. Bartelt PA, Von Moos M. Triaxial tests to determine a microstructure-based snow viscosity law. *Ann Glaciol.* (2000) **31**:457–62. doi: 10.3189/172756400781819761
45. Gibson LJ, Ashby MF. *Cellular Solids: Structure and Properties*. Cambridge: Cambridge University Press (1997). doi: 10.1017/CBO9781139878326
46. Kirchner HOK. Brittle fracture of snow. In: Bouchaud E, Jeulin D, Prioul C and Roux S, editors. *Physical Aspects of Fracture (Proceedings of the NATO Advanced Study Institute on Physical Aspects of Fracture, Cargèse, France, 5-17 June 2000)* Dordrecht: Kluwer Academic Publishers (2001). p. 47–57.
47. Louchet F. Creep instability of the weak layer and natural slab avalanche triggerings. *Cold Reg Sci Technol.* (2001) **33**:141–6. doi: 10.1016/S0165-232X(01)00035-0
48. Barraclough T, Blackford JR, Liebenstein S, Sandfeld S, Stratford TJ, Weinlander G, et al. Propagating compaction bands in confined compression of snow. *Nat Phys*. (2017) **13**:272–5. doi: 10.1038/nphys3966
49. Gaume J, Van Herwijnen A, Chambon G, Birkeland KW, Schweizer J. Modeling of crack propagation in weak snowpack layers using the discrete element method. *Cryosphere*. (2015) **9**:1915–32. doi: 10.5194/tc-9-1915-2015
50. Mulak D, Gaume J. Numerical investigation of the mixed-mode failure of snow. *Comput Part Mech.* (2019) **6**:439–47. doi: 10.1007/s40571-019-00224-5
51. Bobillier G, Bergfeld B, Capelli A, Dual J, Gaume J, Van Herwijnen A, et al. Micromechanical modeling of snow failure. *Cryosphere*. (2020) **14**:39–49. doi: 10.5194/tc-14-39-2020
52. Schneebeli M. Numerical simulation of elastic stress in the microstructure of snow. *Ann Glaciol.* (2004) **38**:339–42. doi: 10.3189/172756404781815284
53. Hagenmuller P, Theile TC, Schneebeli M. Numerical simulation of microstructural damage and tensile strength of snow. *Geophys Res Lett.* (2014) **41**:86–9. doi: 10.1002/2013GL058078
54. Mede T, Chambon G, Hagenmuller P, Nicot F. Snow failure modes under mixed loading. *Geophys Res Lett.* (2018) **45**:13351–8. doi: 10.1029/2018GL080637
55. Capelli A, Reiweger I, Schweizer J. Modelling snow failure behavior and concurrent acoustic emissions signatures with a fiber bundle model. *Geophys Res Lett*. (2019) **46**:6653–62. doi: 10.1029/2019GL082382
56. Fuyuhiko K. An experiment on the progression of fracture (a preliminary report). *J Acoust Emission*. (1990) **9**:177–80.
57. Grosse CU, Ohtsu M. *Acoustic Emission Testing*. Berlin, Germany: Springer (2006).
58. Capelli A, Kapil JC, Reiweger I, Or D, Schweizer J. Speed and attenuation of acoustic waves in snow: laboratory experiments and modelling with Biot's theory. *Cold Reg Sci Technol.* (2016) **125**:1–11. doi: 10.1016/j.coldregions.2016.01.004
59. Faillettaz J, Or D, Reiweger I. Codetection of acoustic emissions during failure of heterogeneous media: new perspectives for natural hazard early warning. *Geophys Res Lett.* (2016) **43**:1075–83. doi: 10.1002/2015GL067435
60. Willibald C, Scheuber S, Löwe H, Dual J, Schneebeli M. Ice spheres as model snow: tumbling, sintering, and mechanical tests. *Front Earth Sci.* (2019) **7**:229. doi: 10.3389/feart.2019.00229
61. Halasz Z, Kun F. Fiber bundle model with stick-slip dynamics. *Phys Rev E.* (2009) **80**:027102. doi: 10.1103/PhysRevE.80.027102
62. Halasz Z, Kun F. Slip avalanches in a fiber bundle model. *Europhys Lett.* (2010) **89**:26008. doi: 10.1209/0295-5075/89/26008
63. Amitrano D. Variability in the power-law distributions of rupture events - how and why does b-value change. *Eur Phys J Spec Top.* (2012) **205**:199–215. doi: 10.1140/epjst/e2012-01571-9
64. Amitrano D, Girard L. Fiber bundle model under fluid pressure. *Phys Rev E.* (2016) **93**:033003. doi: 10.1103/PhysRevE.93.033003

65. Biswas S, Sen P. Maximizing the strength of fiber bundles under uniform loading. *Phys Rev Lett*. (2015) **115**:155501. doi: 10.1103/PhysRevLett.115.155501
66. Schweizer J. Laboratory experiments on shear failure of snow. *Ann Glaciol.* (1998) **26**:97–102. doi: 10.1017/S0260305500014634
67. Gaume J, Löwe H, Tan S, Tsang L. Scaling laws for the mechanics of loose and cohesive granular materials based on baxter's sticky hard spheres. *Phys Rev E*. (2017) **96**:032914. doi: 10.1103/PhysRevE.96.032914
68. Capelli A, Reiweger I, Schweizer J. Acoustic emissions signatures prior to snow failure. *J Glaciol.* (2018) **64**:543–54. doi: 10.1017/jog.2018.43
69. Pradhan S, Kjellstadli JT, Hansen A. Variation of Elastic Energy Shows Reliable Signal of Upcoming Catastrophic Failure. *Front Phy.* (2019) 7:106. doi: 10.3389/fphy.2019.00106
70. Faillettaz J, Or D. Failure criterion for materials with spatially correlated mechanical properties. *Phys Rev E*. (2015) **91**:032134. doi: 10.1103/PhysRevE.91.032134
71. Reiweger I, Mayer K, Steiner K, Dual J, Schweizer J. Measuring and localizing acoustic emission events in snow prior to fracture. *Cold Reg Sci Technol.* (2015) **110**:160–9. doi: 10.1016/j.coldregions.2014.12.002
72. Fan LF, Lehmann P, Or D. Effects of hydromechanical loading history and antecedent soil mechanical damage on shallow landslide triggering. *J Geophys Res Earth Surf.* (2015) **120**:1990–2015. doi: 10.1002/2015JF003615

Conflict of Interest: The authors declare that the research was conducted in the absence of any commercial or financial relationships that could be construed as a potential conflict of interest.

frontiers in Physics

ORIGINAL RESEARCH
published: 13 October 2020
doi: 10.3389/fphy.2020.552550

Spreading of Failures in Small-World Networks: A Connectivity-Dependent Load Sharing Fibre Bundle Model

Zbigniew Domanski *

Institute of Mathematics, Czestochowa University of Technology, Czestochowa, Poland

A rich variety of multicomponent systems operating under parallel loading may be mapped on and then examined by employing a family of the Fiber Bundle Models. As an example, we consider a system composed of N immobile units located in nodes of a network $\mathcal{G}$ and subjected to a growing external load F imposed uniformly on the units. Each unit, characterized by a load threshold δ, is classified as reliable or irreversibly failed, depending on whether δ is bigger, or respectively smaller, than the load felt by the unit. A pair of interdependent units is uniquely indicated by an edge of $\mathcal{G}$. Initially all the units are reliable. When a unit fails, its load is distributed locally among interdependent neighbors if they are reliable, or is otherwise shared globally by all the reliable units. Because of the growing F and the loads that are transferred according to such a see-saw switch between the local and global sharing rules (sLGS), a set of nodes, that holds the reliable units, evolves as $\mathcal{G} \to \varnothing$. During the evolution, a subset $\mathcal{G}_c \subset \mathcal{G}$ emerges that represents the limiting state of the system's functionality when the smallest group of n_c reliable units sustains the highest load F_c. We concentrate on how the Fiber Bundle Model and switching Local-Global-Sharing conspire to drive the system toward $\mathcal{G}_c$. Specifically, we assume that $\{\delta\}_{\mathcal{G}}$ are quenched-random quantities distributed uniformly over $(0, 1)$ or governed by the Weibull distribution and networks $\mathcal{G}$ are the Watts-Strogatz "small-world" graphs with the rewiring probability p that characterizes possible rearrangements of edges in $\mathcal{G}$. We have identified a range of values of p, where the mean highest load $f_c(N) = \langle F_c \rangle / N$, supported by reliable units, scales linearly with the average global-clustering coefficient of the host network. Similar scaling holds for $\langle n_c \rangle$ and $\langle F_c/n_c \rangle$. We have also found that in the large N limit $f_c(N) \to f_c^{\infty} > 0$, for all values of p and both considered distributions of $\{\delta\}_{\mathcal{G}}$. The symbol $\langle \ldots \rangle$ represents averaging over $\{\delta\}_{\mathcal{G}}$ and a suitable ensemble of networks $\{\mathcal{G}\}$.

Keywords: failure evolution, fiber bundle model, switchable load sharing, simulations, small-world network, statistics

OPEN ACCESS

Edited by:
Ferenc Kun,
University of Debrecen, Hungary

Reviewed by:
Soumyajyoti Biswas,
SRM University, India
Bikas K. Chakrabarti,
Saha Institute of Nuclear Physics (SINP), India
Zoltan Neda,
Babes-Bolyai University, Romania

***Correspondence:**
Zbigniew Domanski
zbigniew.domanski@im.pcz.pl

Specialty section:
This article was submitted to Interdisciplinary Physics, a section of the journal Frontiers in Physics

Received: *16 April 2020*
Accepted: *18 September 2020*
Published: *13 October 2020*

Citation:
Domanski Z (2020) Spreading of Failures in Small-World Networks: A Connectivity-Dependent Load Sharing Fibre Bundle Model. Front. Phys. 8:552550. doi: 10.3389/fphy.2020.552550

INTRODUCTION

Numerous systems, encountered in nature as well as in different areas of science and technology, are multicomponent, i.e., they are composed of a great number of functionally identical units. When loaded, the units process a given task in a fully parallel manner. It happens, however, that a unit becomes overloaded and fails. Its load has to be undertaken by other units, which in turn may trigger subsequent overloading followed by resulting failures. Such a chain of failures gradually degrades the

system performance and leads to an avalanche of failures. It may even happen that the avalanche becomes self-sustained giving rise to a catastrophe which overwhelms all the units. Different factors characterize a given system. This is important to identify those working together that push the system toward the catastrophic avalanche.

The Fiber Bundle Model (FBM) is a particular case of a wide class of cascading processes on networks [1]. It offers a flexible approach to study how multicomponent systems evolve under varying load [2–8]. The flexibility refers to such aspects as: a) range and symmetry of interactions among units [9], b) rate of load's variation, c) heterogeneity/uniformity of units [10, 11]), or d) varying quality of units [12, 13], to name a few. The aspects a) and b) especially refer to ingredients of the FBM that play a major role when a given system is mapped onto a bundle of interacting fibers [14]. Exemplary problems, from an ample set of systems expressed in the FBM framework, cover research fields that span from geophysics including earthquakes, snow or landslides, to technology with electrical and mechanical engineering systems.

In this context, we consider a toy model of failures spreading in a set of interconnected units. Our model consists of N units that reside at nodes of an undirected simple graph $\mathcal{G}$ whose edges represent pairs of interdependent units. The units are either reliable or irreversibly failed, and we assume that an externally applied load F is distributed identically on all reliable units. When F starts growing, some units begin to suffer from insufficient strength to bear the load and they fail. Their loads remain in the system and are shared either by the nearest neighboring units, if they are reliable, or by all other reliable units. If on a given node a failure emerges, this node is removed from the graph together with corresponding edges, i.e., $\mathcal{G}$ is reduced to $\mathcal{G}' \subset \mathcal{G}$. This means that under growing F, an initially connected $\mathcal{G}$ evolves toward the empty graph. In other words, unbounded growth of F pushes the set of reliable units to extinction. If the growth of F is sufficiently slow, then a distinct group of reliable units may be selected in the course of evolution:

$$\mathcal{G}_0 \supset \mathcal{G}(F>0) \supset \mathcal{G}(F'>F) \supset \ldots \supset \mathcal{G}(F_c> \ldots >F) \to \varnothing \qquad (1)$$

This group, identified by nodes of $\mathcal{G}_c = \mathcal{G}(F_c)$, is the smallest group of units that remain reliable under the highest load F_c, i.e., a load $F > F_c$ will trigger an ultimate, self-sustained avalanche of failures that overwhelms the entire system. The chain of inclusions 1 displays graphs that are stable under consecutive values of F whereas intermediate graphs, induced exclusively by loads sharing processes to be precise, are omitted for the sake of simplicity. We use the subscripts "c" to mark that the load F_c is critical to the systems and that $\mathcal{G}_c$ represents the smallest non-empty stable configuration that precedes extinction. We call this configuration the critical configuration.

Within this work we are interested in questions like: how small a group of units can be and/or to what extent we can apply the external load while still preventing the extinction of reliable units. Subsequently, we apply the FBM to study evolving failure on "small-world" networks that are omnipresent in life and technology. Specifically, we will focus on a family of random graphs generated by the Watts-Strogatz model [15]. The reason is that such graphs reveal short average path lengths and high clustering that are key features of social networks [16].

MODEL DESCRIPTION

Take a locally overloaded system which detects a failure of a unit. In the first instance the system attempts to solve the problem locally by distributing the load among nearest neighbors of the failed unit. If such a neighborhood does not exist, the entire set of reliable units is engaged into sharing the load from the unit being lost. Such a mode of load transfer yields a significant impact on the system's strength. Whenever an island of reliable units emerges during the evolution, its terminal load is shared globally by the system. This means that the net load transferred to reliable units that are located on the outer island's perimeter is lower than it would be if the local load sharing (LLS) rule has been in operation. In consequence, the switching Local-Global-Sharing (sLGS) mitigates the expansion of a dominantly large cluster (DLC) of failed units and thus, the strength of the system becomes higher than that one corresponding to the LLS rule [5].

In the following, we consider an ensemble of units assigned to nodes of a graph $\mathcal{G}$ and characterized by quenched load thresholds $\{\delta\}_{\mathcal{G}}$. Each unit, initially considered reliable, either stays reliable or switches irreversibly to failed if the load, acting on the unit becomes higher than corresponding δ. Units are not perfect and differ in their efficiency to sustain the load. Hence, the corresponding δs are different. For the sake of simplicity we assume that $\{\delta\}_{\mathcal{G}}$ are quench-random quantities. We employ two distributions, assuming that thresholds are: i) uniformly distributed over the segment $(0, 1)$ or ii) assigned according to the Weibull pdf. Specifically, the second distribution is employed to analyze networks with components of technological nature.

Watts-Strogatz Model and Small-World Networks

There exists an ample set of papers that discuss the Watts-Strogatz model in details [17]. Hence, for the purpose of our model, it is sufficient to present the simplest exemplary graph and sketch how its modifications enable a smooth passage from an ordered network to disordered ones through a multitude of "small-world" graphs. One such passage is shown in **Figure 1**. The presented graphs are generated in two steps:

- a ring over N nodes is created and each node is connected with its k nearest neighbors, k is even.
- for every node with uniform independent probability p, each edge is rewired to a node that is selected uniformly at random while avoiding loops and edge duplication.

These steps are illustrated in **Figure 1**, e.g., the first step corresponds to the graph with $p = 0$. In simulations we will employ graphs with $k = 4$.

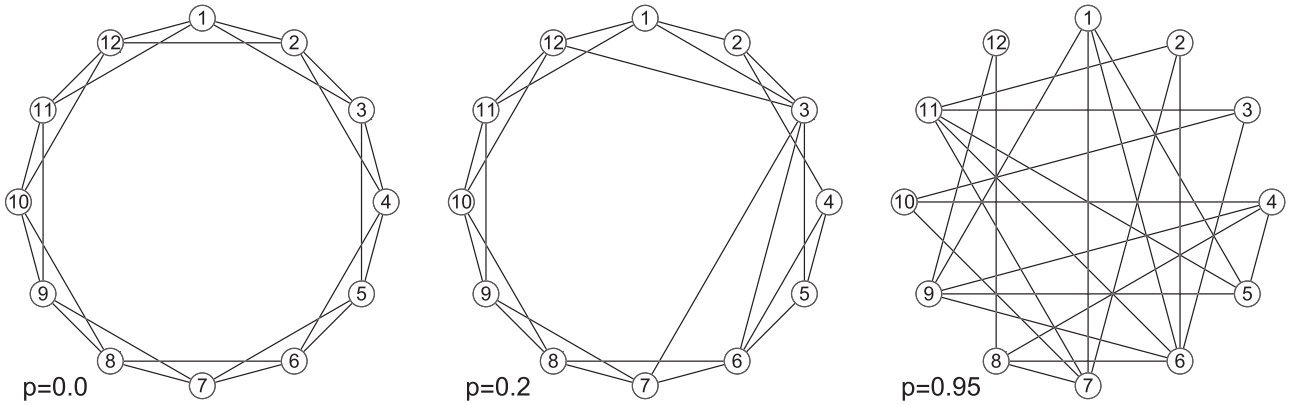

FIGURE 1 | Exemplary "small-world" networks generated by the Watts-Strogatz model with mean node degree $k = 4$ and growing probability p of rewiring.

Among the different characteristics of a network, one is particularly important in the view of our study, namely the global clustering coefficient C defined as:

$$C = \frac{3 \times \text{number of triangles}}{\text{number of connected triples}}, \tag{2}$$

where nodes of a triangle form a 3-clique, and a connected triple is a tree.

Applying External Load

We have assumed the external load F is distributed identically on all reliable units. Consider a load f_i that locally acts on i-th unit, out of M reliable ones that are present at a given stage of evolution. This f_i combines F/M with a load generated by shared loads agglomerated from previous failures that affected other units. An important feature of such a process is that the shared loads transferred from failed units and the externally applied load may together activate bursts of subsequent failures. The bursts may become self-sustained and they either eliminate all the reliable units or they cease and freeze the system in a stable configuration.

We consider a configuration $\mathcal{G}(F)$ being stable, if under a given F all reliable units keep their states unchanged. When no reliable unit exists the corresponding configuration is the empty graph $\varnothing$. Along with this notation, $\{f(F_t)\}_{\mathcal{G}(F_t)}$ is the pattern of load detected locally at nodes of $\mathcal{G}(F_t)$.

In order to identify F_c, along with the size of the smallest set of reliable units, we increase the load stepwise, according to the method known as quasi-static loading. In detail, when $F = 0$ all units are reliable and the initial configuration is stable. Consecutive load steps are adjusted according to the rule: if $F_t > 0$ and the system attains a stable configuration $\mathcal{G}(F_t)$, then $F_{t+1} = F_t + \min[\{f(F_t) - \delta\}_{\mathcal{G}(F_t)}]$ will either drive the system to another stable configuration $\mathcal{G}(F_{t+1})$ or initiate an avalanche of failures that destroys all still reliable units, i.e., the system reaches the configuration $\varnothing$.

From this, we derive the stopping rule:

$$\mathcal{G}(F_t) \neq \varnothing \wedge \mathcal{G}(F_{t+1}) = \varnothing \Rightarrow F_t = F_c \wedge n_c = |\mathcal{G}(F_c)| \tag{3}$$

where $n_c = |\mathcal{G}(F_c)|$ is the size of $\mathcal{G}(F_c)$, i.e., the size of the smallest group of reliable units. We use this rule in simulations.

Load Sharing Rule

The load transfer requires a rule that indicates how a load released by a failure is shared by other reliable units. We define our rule in a following way: the reliable network neighbors are obliged to equally share the load if they are accessible and all the reliable units acquire the load in the contrary case.

From this definition's point of view, our rule "dynamically" switches between two rules, which are known in the FBM framework as global load sharing (GLS) and LLS. These rules correspond to two extremal ranges of load transfer. In the GLS rule, a load originating from a failed unit is transferred equally to all the reliable units and thus, the range of transfer is maximal. The LLS rule, in turn, engages only the nearest neighbors of a node that fails, so the range of load transfer is minimal. As a consequence, the load distributed according to the GLS rule is the least harmful for the system, whereas the LLS represents the most damaging method of the load distribution.

In simulations, we call this rule the sLGS and assume that the load transfer is an almost instantaneous process that happens simultaneously. We can mathematically express the sLGS in a framework for cascading processes on networks [18]. For this purpose, let $\widehat{A}_{\mathcal{G}}$ be the adjacency matrix of $\mathcal{G}$, whose nonzero entries $A^{ij}_{\mathcal{G}} = 1$ appear only if the units i and j are interdependent and let $k_i = \sum_{j \neq i}^{|\mathcal{G}|} A^{ij}_{\mathcal{G}}$ denotes the degree of node i at the stage $t_{\mathcal{G}}$ of evolution characterized by $\mathcal{G}$. With this notation, a fraction of load f_i transferred from the failed unit i to a reliable unit j reads

$$\Delta f_{j \leftarrow i} = \left[A^{ij}_{\mathcal{G}} \cdot \frac{1}{k_i} + \left(1 - A^{ij}_{\mathcal{G}}\right) \frac{1}{|\mathcal{G}| - n_{\mathcal{G}}} \right] \cdot f_i, \tag{4}$$

where $n_{\mathcal{G}}$ represents the number of nodes that fail at the stage $t_{\mathcal{G}}$ and are not neighbors to site i.

Equation 4 has a structure that resembles schemes of load transfer known from the literature. Namely the mixed-mode load sharing (MMLS) [19] and the heterogeneous load sharing (HLS) [20] merge together the LLS and the GLS in order to study a

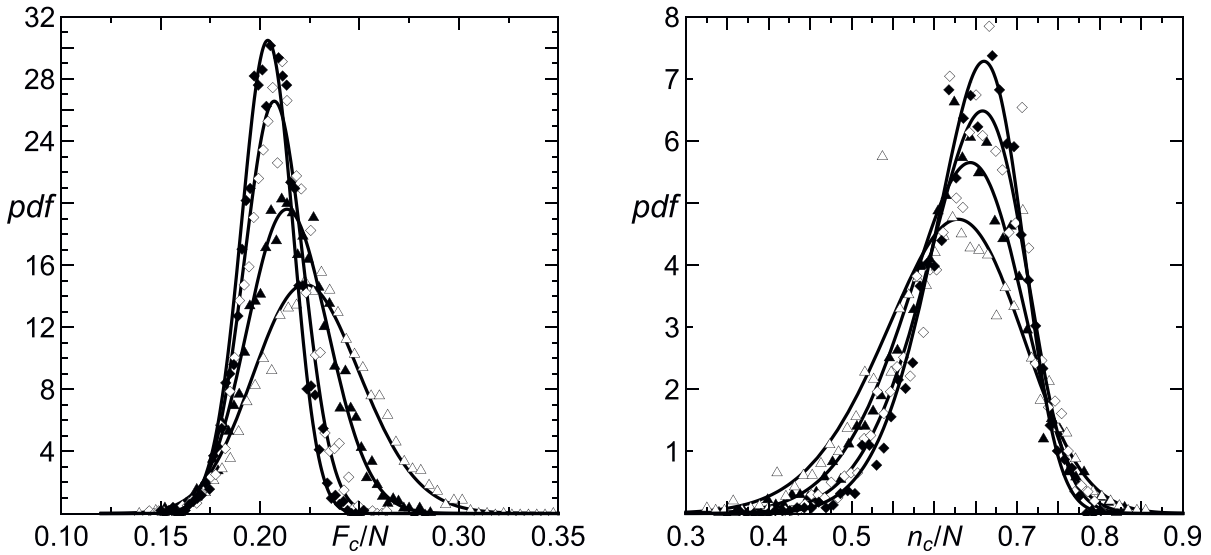

FIGURE 2 | Calculated distributions of F_c/N (left diagram) and n_c/N (right diagram) for an increasing number of units: $N = 100$ (white triangles), $N = 200$ (black triangles), $N = 400$ (white diamonds) and $N = 600$ (black diamonds). Each value of N corresponds to a population of 2,500 load thresholds $\{\delta_i\}_{i \in \{1,...N\}}$ distributed uniformly over $(0, 1)$ and an exemplary Watts-Strogatz graph with $p = 0.2$. The solid lines are drawn according to **Eq. 5** with parameters estimated from the simulations.

crossover behavior in FBM on regular lattices. The MMLS employs a constant quota q to split each transferred load into two streams: a portion q of the load goes to nearest neighbors under the LLS rule and the remaining portion is transferred according to the GLS rule. Thereby, the MMLS folds the LLS and the GLS in a manner that both rules are simultaneously activated in each failure. This is in contrast to the HLS, which in turn assigns units to two groups in order to discriminate between units located in "rigid nodes" and those residing in a "flexible" fraction of the support. If the "rigid" unit fails then the GLS transfers its load whereas the LLS governs the transfer from the "flexible" unit. The MMLS and the HLS are static, i.e., the corresponding values of q and sets of nodes at which q-weighted sharing rules operate are chosen and fixed prior to loadings. We also want to mention the modified LLS rule [21]. By employing the scheme $\Delta f_{j \leftarrow i} = A^{ij}_{\mathcal{G}} \cdot (f_i/k_i)$, this rule sheds loads released from isolated clusters of failed nodes rather than transferring these loads to remaining intact parts of the system.

It is worth noting that rules, similar to the sLGS have been applied recently in such contexts as a strategy for stopping failure cascades [22] or clogging in multichannel supply systems [23].

A Range of Possible Applications

The above-described load sharing rule operating among units interconnected through a small world network may serve as a toy model of cascading failures in economy or technology. A general scenario we have in mind concerns a default initiated by an unsupported on-site demand that spreads through the system in a form of a contagion from the defaulter, either to units which are closely associated or to other ones. Clearly, when a unit switches into default this affects other units. Depending on the context, units could be: a) institutions, as, e.g., banks belonging to an interbank network, b) workers with beneficial loans from a company, borrowers in micro financial markets or c) elements of power grids, especially of small scale smart grids. With this same spirit a load could be seen as a demand, e.g., for liquidity or electric power. Below we list some basic facts that are relevant to our model.

Interbank Market

Undirected graphs are suitable to modeling interbank networks, especially in the context of a financial contagion [24, 25]. Among representations which are convenient and applied in studies, a possible one connects a pair of banks by an undirected edge whenever there exists an interbank liability or claim [25]. When an ensemble of interdependent banks is mapped onto a graph, one can analyze its static and dynamic properties. A class of small world graphs certainly is relevant in this context. It was shown, e.g., that the interbank market of ~ 900 Austrian banks is a small-world network [25].

Microeconomy

Many companies offer beneficial loans to its employees. Specifically, to those suffering financial troubles. These employees-debtors, being colleagues and friends, are frequently mutual guarantors and can thus be considered as members of a resulting social network.

Power Grids

The small world topology is frequently reported as present in power grid networks [26–28]. This is equally true for large scale installations involving nationwide power systems in the US or Europe as well as for medium or small power grids [29, 30]. Particularly, in smart grids of renewable energy sources, such as small-scale photovoltaic systems or small-wind turbines [31, 32], the small world topology is beneficial. For example, networks

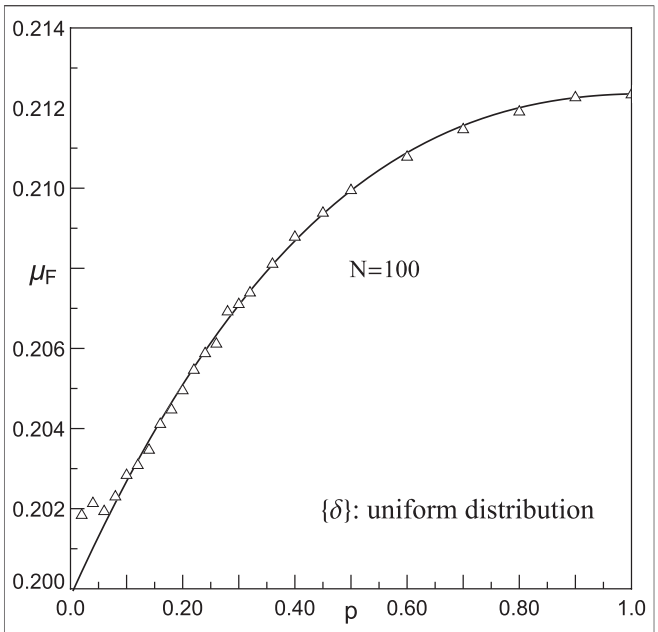

FIGURE 3 | Estimated functional dependence of μ_F on rewiring probability p: $\mu_F = a + b(1 - c \cdot p)^3$, with $a = 0.2128 \pm 0.0006$, $b = 0.01228 \pm 0.005$ and $c = 0.741 \pm 0.079$ for $N = 100$. Each data point corresponds to averaging over 10^6 samples.

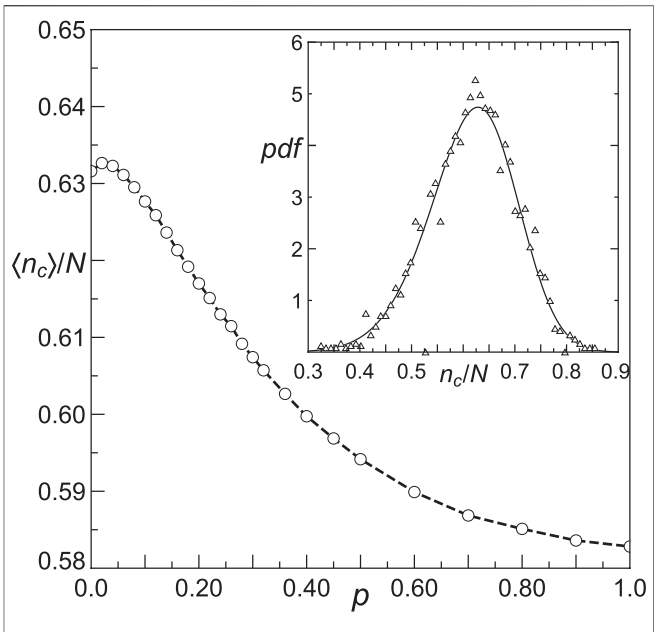

FIGURE 4 | Scaled mean critical number of reliable units $\langle n_c \rangle / N$ for $N = 100$. The sample size equals 10^6. The Inset shows empirical distribution of n_c/N computed from 2,500 uniform distributions of load thresholds for an exemplary Watts-Strogatz graph with $p = 0.2$.

with small world connectivity can significantly enhance their robustness against different attack by simultaneous increase of the rewiring probability and average degree [33].

RESULTS AND DISCUSSION

In order to acquire data necessary to build reliable empirical distributions, we have adopted two computational schemes that correspond to small and large numbers of units. In the first scheme, for each N, an ensemble of M_δ load-threshold distributions $\{\delta_i\}_{i \in \{1,\ldots N\}}$ is generated. Then, for each selected value of $p \in [0, 1]$ a separate ensemble $\{\mathcal{G}^{(s)}(N,p)\}_{s=1,\ldots,M_\mathcal{G}}$ of Watts-Strogatz graphs $\mathcal{G}(N,p)$ is formed and stored. This means that for each chosen pair (N,p), two corresponding ensembles $\{\delta_i\}_{i=1,\ldots,N}$ and $\mathcal{G}(N,p)$ allow us to probe $M_\delta \cdot M_\mathcal{G}$ different realizations of failure evolution for the uniform as well as for the Weibull distributions of $\{\delta\}$. To study networks with $N \leq 10^3$, we employ the first scheme with $M_\delta = 2500$ and $M_\mathcal{G} = 400$. The second scheme involves systems with $1,200 \leq N \leq 21,600$. For each chosen values of (N,p), a set consisting of 10^4 pairs $(\{\delta_i\}_{i=1,\ldots,N}, \mathcal{G}(N,p))$ is generated. The two computational schemes allow us to probe 10^6 or 10^4 different realizations of failure evolution for a small or large N regime, respectively.

We use both computational schemes for uniformly distributed load thresholds. In simulations with the Weibull distribution we consider $\rho = 2, 3, 5$ and 8. For all these ρ we conduct simulation following the first computational scheme. In the large N limit, we restrict ourselves to distributions with $\rho = 2$ only.

Subsequently, when averaging a quantity Y over either $\{\delta\}$ or $\{\mathcal{G}\}$ alone, we denote the respective mean by $\overline{Y}^{\delta}$ and $\overline{Y}^{\mathcal{G}}$, whereas the symbol $\langle Y \rangle$ refers to averaging Y over both ensembles.

Maximal Supported Load and Minimal Number of Reliable Units

Following the described computational schemes, we have collected large data sets containing detailed information about how the maximal load, together with the minimal number of units, vary when we pass through all pairs $\{\delta_i\}_{i=1,\ldots,N}, \mathcal{G}(N,p)$ of stored ensembles.

The gathered data turn out to be skewed independently of what distribution governs $\{\delta\}$. Specifically, the data pointed to F_c are positively skewed whereas the data related to n_c reveal negative skewness. This can be seen in **Figure 2** for chosen values of N and $p = 0.2$. Interestingly, we were able to fit all data by one family of probability distributions (p.d.), namely by the three-parameter skew-normal p.d. [34] defined as:

$$\phi(x) = \frac{\mathrm{erfc}\left(-\alpha \frac{x-\mu}{\sqrt{2}\,\sigma}\right)}{\sqrt{2\pi}\sigma} \exp\left[-\left(\frac{x-\mu}{\sqrt{2}\sigma}\right)^2\right], \tag{5}$$

where μ, σ and α are the location, scale and shape parameters, respectively.

We have rigorously examined the data sets employing a number of goodness of fit tests, including the Cramer-von Mises and Anderson-Darling tests [35] and have accepted $\phi(\cdot)$, **Eq. 5**, as the distribution that best fits the empirical distributions of F_c/N and n_c/N. A selection of correct distribution for gathered data sets is an important task.

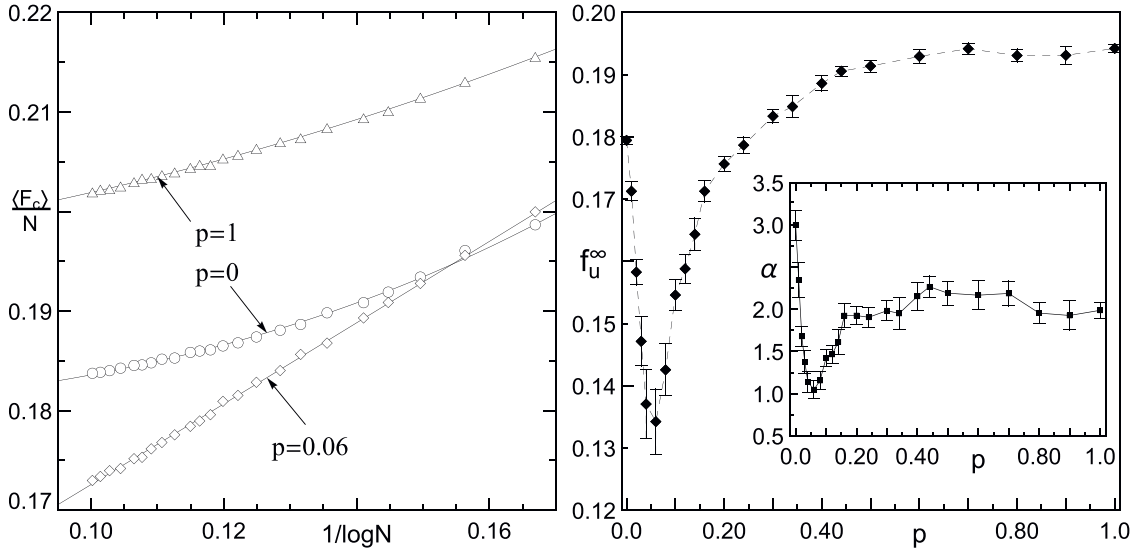

FIGURE 5 | Left panel: The logarithmic size dependence of system strength for networks that: are ordered (p = 0), disordered (p = 1) and correspond to the weakest system (p = 0.06). The lines are drawn following **Eq. 7** with coefficients shown in the right panel. Right panel: The ultimate system strength f_u^{∞} and exponent α (Inset) computed for different values of p according to the best fit given in **Eq. 7**. Black marks represent the best fit to data of which some examples are shown in the left panel. The error bars indicate 95% confidence intervals. Data in both panels refers to $\{\delta\}$ distributed uniformly over $(0, 1)$.

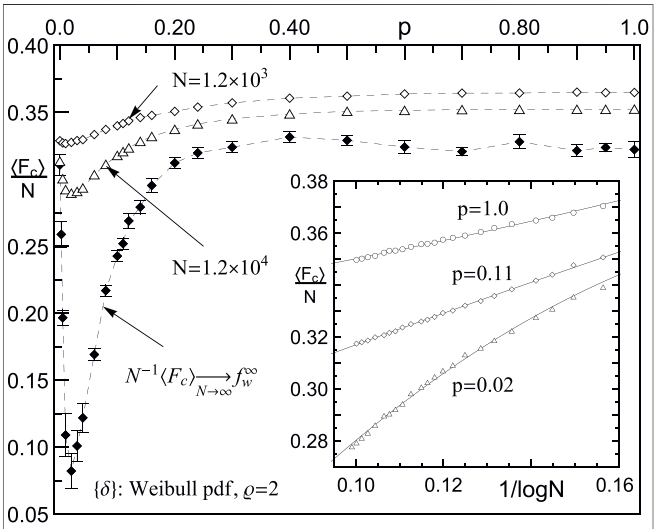

FIGURE 6 | The system's strength scaled by size in the large N limit. Inset: the logarithmic dependence of scaled system strength for: p = 0.02 (minimum of f_w^{∞}), p = 0.11 ($B_w \sim 0 \Rightarrow f_w^{\infty} \sim 1/\log(N)$, see **Eq. 8** and **Figure 7**) and p = 1 (maximally disordered network). Data correspond to the Weibull distribution of $\{\delta\}$ with ρ = 2. The sample size is equal to 10^4 for each data point.

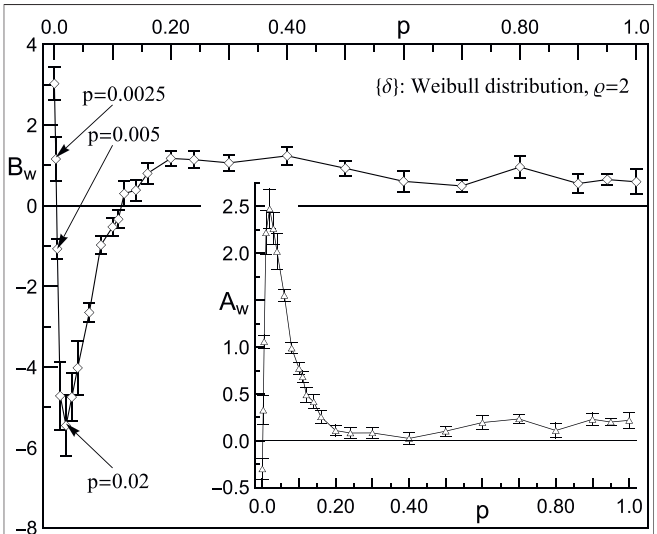

FIGURE 7 | Amplitudes A_w (Inset) and B_w of f_c in the large N limit for systems with $\{\delta\}$ governed by the Weibull p.d., see **Eq. 8**. Each data point results from an averaging of over 10^4 samples.

Appropriate methods exist to establish confidence sets and perform hypothesis tests, including an universal procedure [36]. In this regard we should mention that a substantial portion of our data sets is satisfactorily modeled by the three-parameter Weibull p.d. also. We opt, however, for representing all data by **Eq. 5** because the skew-normal p.d. works correctly for almost all data sets and for those when both models are acceptable, the skew-normal p.d. returns higher values of maximized likelihood function and greater p-values than the Weibull p.d.

We have also estimated values of the parameters μ, σ and α. The gathered data yield estimate functional dependences of μ, σ and α on model parameters N, p and ρ. As an example, consider empirical p.d. of F_c/N related to different values of rewiring probability $p \in [0, 1]$. The corresponding skew-normal p.d. reads:

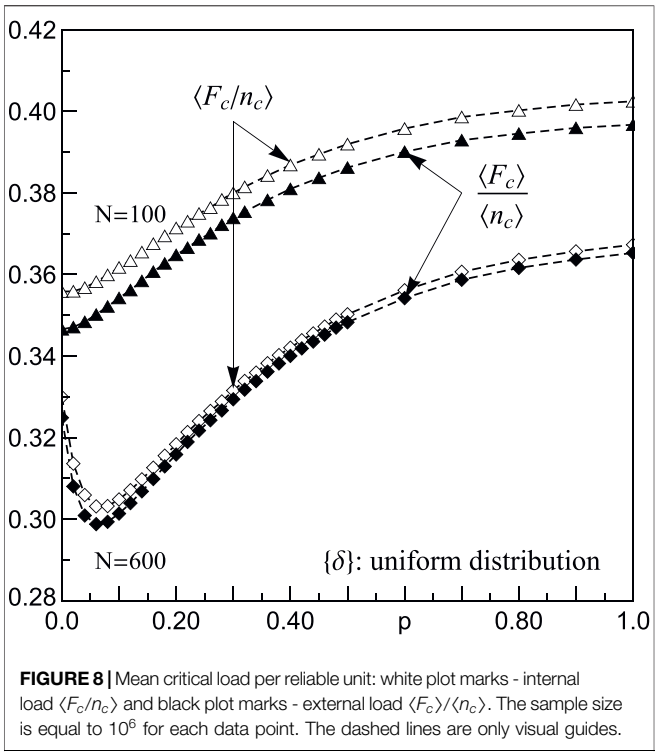

FIGURE 8 | Mean critical load per reliable unit: white plot marks - internal load $\langle F_c/n_c\rangle$ and black plot marks - external load $\langle F_c\rangle/\langle n_c\rangle$. The sample size is equal to 10^6 for each data point. The dashed lines are only visual guides.

$$\phi\left(F_c/N,\,N,\,p\right)=\frac{\operatorname{erfc}\left(-\alpha_F\left(N,p\right)\frac{F_c/N-\mu_F\left(N,p\right)}{\sqrt{2}\,\sigma_F\left(N,p\right)}\right)}{\sqrt{2\pi}\sigma_F\left(N,p\right)}\exp\left[-\left(\frac{F_c/N-\mu_F\left(N,p\right)}{\sqrt{2}\sigma_F\left(N,p\right)}\right)^2\right]. \tag{6}$$

We have directly written that μ, σ and α are functions of N and p whereas parameters characterizing distributions of $\{\delta\}$ are omitted. We have estimated the functional dependences of these coefficients on model parameters. For instance, in **Figure 3**, we present how the location parameter μ varies with p, while keeping constant values of N. The resulting fitting function turns out to be a polynomial of the third order in p.

Since the location parameter μ_F grows with p and F_c/N is positively skewed $(\alpha_F > 0)$ then the corresponding mean $\langle F\rangle_c/N$ increases. This is because $\langle F_c\rangle/N = \mu_F + \sqrt{2}\cdot\alpha_F\cdot\sigma_F/\sqrt{\pi(1+\alpha^2)}$. Similar calculations yield estimators related to n_c and F_c/n_c. As an example, an average critical number of units $\langle n_c\rangle/N$ is presented in **Figure 4** for uniformly distributed $\{\delta\}$. Data related to the Weibull distribution with exemplary values of ρ are displayed in **Figure 12**.

It should be pointed out that when p is growing, the resulting networks become more and more disordered and the probability that a given node has a low degree increases. Hence, the sLSG activates all the reliable units more frequently than it happens in networks generated with a small value of p.

Large N Limit

Even though the applications mentioned in **Section 2.4** refer to networks composed of about 10^2–10^4 units, it is worth addressing the questions on how the sLGS drives a very large system and how such the system converges to attain its ultimate strength. In the following we report relevant details.

It is known that the LLS model on a complex network behaves similarly to the GLS model giving rise to a non-vanishing critical strength f_c in the large N limit [5]. Formally, the family of Wats-Strogatz graphs covers the spectrum of networks ranging from the locally regular $(p = 0)$ to the maximally disordered $(p = 1)$ ones. The locally regular network is the only exception in this family because under the LLS the strength f_c decays as $\sim 1/\log(N)$. Is this thus obvious that, the sLGS, by switching between the LLS and the GLS, does the same?

Based on results of simulations of large-N systems, we have found that: i) $f_c \to f_c^{\infty} > 0$, ii) f_c^{∞} depends quantitatively on p and $\{\delta\}_{\mathcal{G}_0}$, and iii) f_c^{∞} depends qualitatively on probability distribution that generates $\{\delta\}_{\mathcal{G}_0}$. For the uniform p.d.

$$f_c^u\left(z=1/\log(N),p\right)\sim f_u^{\infty}(p)+A_u(p)\cdot z^{\alpha(p)} \tag{7}$$

while for the Weibull p.d. the best fit reads

$$f_c^w\left(z=1/\log(N),p,\rho\right)\sim f_w^{\infty}(p,\rho)+A_w(p,\rho)\cdot z+B_w(p,\rho)\cdot z^2, \tag{8}$$

where the subscripts u and w stand for the uniform and Weibull distributions, respectively. The estimated system's strength f_u^{∞} and the exponent α are displayed in **Figure 5**. Correspondingly, for the Weibull p.d. f_w^{∞} is presented in **Figure 6** whereas the amplitudes A_w, B_w are shown in **Figure 7**.

These plots illustrate a variety of ways in which f_c converges toward f_c^{∞}. For both distributions of $\{\delta\}$, the locally regular network $(p = 0)$ sustains $f_c^{\infty} > 0$. For small values of p the ultimate system strength rapidly decreases, attains its minimum and then increases. Until $p \sim 0.2$ the growth of f_c is fast, then moderate, until $p \sim 0.5$. For $p > 0.5$ the strength varies a little and saturates around value $0.77 \times f_c^{\infty}(GLS)$, where $f_c^{\infty}(GLS)$ is the ultimate strength for the GLS rule, i.e., $f_c^{\infty}(GLS) = 0.25$ for uniformly distributed $\{\delta\}$ and $f_c^{\infty}(GLS) = (\rho\cdot e)^{-1/\rho}$ for the Weibull distribution. As shown in **Figure 7**, except for $p \lesssim 0.003$, the amplitude B_w is negative up to $0.11 < p^* < 0.12$, then becomes positive. This means that $f_c^w(1/\log(N))$ is concave down for $p < p^*$. Therefore, the speed of convergence of $f_c^w(1/\log(N))$ grows when $1/\log(N)$ tends to zero. Passing p^*, the function f_c^w becomes concave up and the speed of its convergence toward f_w^{∞} slows down.

A deep minimum of f_u^{∞} at $p \sim 0.06$, seen in **Figure 5**, and correspondingly that of f_w^{∞} at $p \sim 0.02$, displayed in **Figure 6**, result from an interplay between a slightly perturbed order of the locally regular network and the activity of the GLS-component of the sLGS rule. This can be qualitatively explained by adopting arguments formulated in [5]: (i) when a complex network is progressively loaded, the FBM with the LLS rule behaves as the GLS model because clusters of failed units appear, continuously grow and glue into a DLC, (ii) due to the small-world effect,

TABLE 1 | Estimated coefficients in **Eq. 9**: $\langle Y\rangle = u + w \cdot (1 - \xi \cdot p)^3$, for systems with $N = 100$ units and uniformly distributed δs.

$\langle Y\rangle$	u	w	ξ
$\langle F_c\rangle/N$	0.2309 ± 0.002	–0.0120 ± 0.02	1.039 ± 0.032
$\langle n_c\rangle/N$	0.5802 ± 0.004	0.0569 ± 0.002	0.707 ± 0.078
$\langle F_c/n_c\rangle$	0.4042 ± 0.002	–0.0519 ± 0.0015	0.734 ± 0.061
$\overline{C}^{\mathcal{G}}$	0.0358 ± 0.0004	0.4605 ± 0.0008	1.099 ± 0.007

reliable units remain closely to each other and to the DLC and thus, the system resembles the GLS model, (iii) on an ordered network which is spatially uniform, clusters of failed units originate and extend in an equal condition and the DLC emerges abruptly. Now consider the argument (iii) in conjunction with the sLGS rule engaged on a network with $p \sim 0$. Since the network is almost regular and highly clustered the LLS component prevails over the GLS one in the early stages of the loading process. The sLGS rule with its frequently activated LLS component continues operating until the network becomes fragmented. Then, the GLS component starts to allocate terminal loads from failed fragments to units that are still reliable. From there, the process behaves similarly to that with the GLS rule. Contrary to the case of the LLS rule, the resulting system strength does not vanish. It is, however, smaller than that corresponding to the GLS rule. When p increases, the arguments (i) and (ii) come into the picture. First, for $0.01 \lesssim p \lesssim 0.1$, the average path length begins to decrease whereas networks are still highly clustered albeit no more locally ordered. Even that such conditions support a gradual DLC emergence, the average path length is not sufficiently small to facilitate the DLC growth. This, combined with the lack of local ordering favor the LLS component activity on clusters bigger than those appearing within an almost ordered network. In consequence, the system strength passes through its minimum. Networks with p roughly bigger than 0.1 enter a scenario characterized by the argument (i). The sLGS differs from the LLS, however. As it was already stated in the beginning of **Section 2**, whenever an island of reliable units appears its

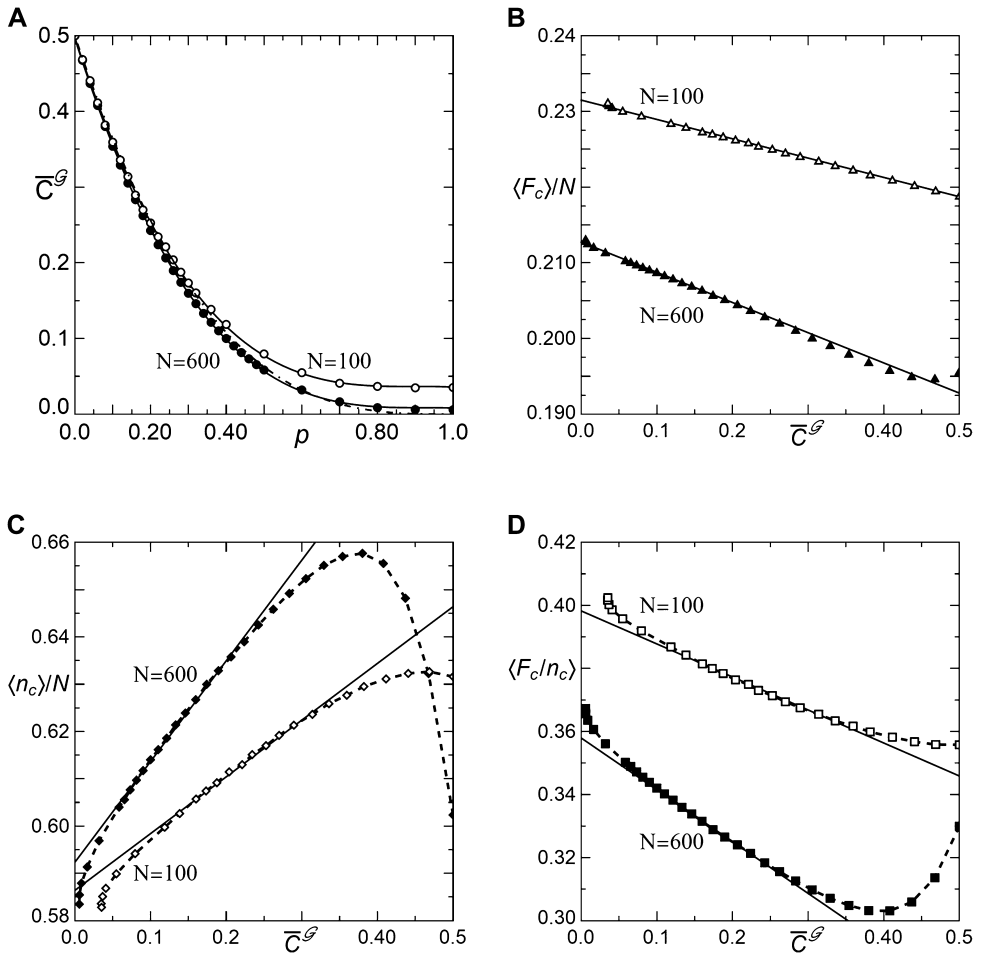

FIGURE 9 | (A) Calculated mean empirical global clustering coefficient $\overline{C}^{\mathcal{G}}$ as a function of p for employed sets of 400 Watts-Strogatz graphs, each with connectivity $k = 4$. The solid line is given by **Eq. 9** with: $u = 0.0358 \pm 0.0004, w = 0.4605 \pm 0.0008, \xi = 1.1 \pm 0.007$, for $N = 100$ and $u = 0.0085 \pm 0.0017, w = 0.488 \pm 0.001, \xi = 1.076 \pm 0.001$ for $N = 600$). The dash-dotted line represents $C_\infty(p) = C(0)(1-p)^3$, valid in the limit $N \to \infty$, where $C(0) = (3/4)(k-2)/(k-1)$ [37]. The diagrams **(B–D)** refer to: $\langle F_c/N\rangle$, $\langle n_c/N\rangle$, and $\langle F_c/n_c\rangle$, respectively on a linear scale for the $\overline{C}^{\mathcal{G}}$. Straight lines represent **Eq. 10** and are drawn in accordance with parameters presented in **Table 2**. The dashed lines are visual guides. The sample size is equal to 10^6 for each data point. Load thresholds are distributed uniformly.

TABLE 2 | Estimated coefficients in **Eq. 10**: $\langle Y\rangle = a_N + b_N \cdot \overline{C}_N^{\mathcal{G}}$, N = 100 and 600, $\{\delta\}$: distributed uniformly over (0, 1).

$\langle \boldsymbol{Y}\rangle$	$\boldsymbol{a}_{100}$	$\boldsymbol{b}_{100}$	$(\boldsymbol{p}^-, \boldsymbol{p}^+)_{100}$	$\boldsymbol{a}_{600}$	$\boldsymbol{b}_{600}$	$(\boldsymbol{p}^-, \boldsymbol{p}^+)_{600}$
$\langle F_c\rangle/N$	$0.232^{+0.001}_{-0.001}$	$-0.0255^{+0.0003}_{-0.0003}$	(0.02, 0.60)	$0.2127^{+0.0004}_{-0.0004}$	$-0.0395^{+0.0005}_{-0.0005}$	(0.10, 0.38)
$\langle n_c\rangle/N$	$0.586^{+0.001}_{-0.001}$	$0.120^{+0.005}_{-0.005}$	(0.12, 0.40)	$0.5924^{+0.0008}_{-0.0008}$	$0.2130^{+0.006}_{-0.006}$	(0.10, 0.38)
$\langle F_c/n_c\rangle$	$0.398^{+0.001}_{-0.001}$	$-0.105^{+0.005}_{-0.005}$	(0.12, 0.50)	$0.3579^{+0.0008}_{-0.0008}$	$-0.1640^{+0.005}_{-0.005}$	(0.24, 0.40)

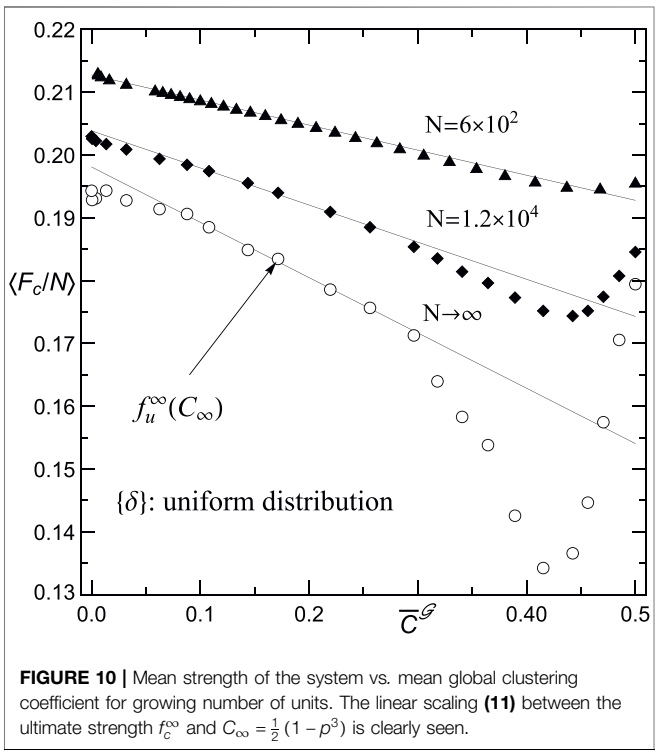

FIGURE 10 | Mean strength of the system vs. mean global clustering coefficient for growing number of units. The linear scaling **(11)** between the ultimate strength f_c^{∞} and $C_{\infty} = \frac{1}{2}(1-p^3)$ is clearly seen.

terminal load is transferred by the sLGS to all other reliable units and not to the closest ones. This inhibits the DLC growth and increases the system strength correspondingly.

Within our numerical approach, it is difficult to precisely estimate $f_c^{u,w}$ in the very close vicinity of $p = 0$. For this reason, we were unable to analyze the continuity of $f_{u,w}^{\infty}$ when $p \to 0$. Therefore the question arises whether $f_{u,w}^{\infty}(p = 0)$ is an isolated point of the ultimate system strength.

Internal vs. External Load From a Reliable-Unit's Point of View

When considering its future reliability, a prospective unit behaves as an outer observer whose forecast is limited to the external load F. When entering the system, the unit is confronted with an internal-load impact. It is thus worth discussing to what extent these two points of view differ.

We have assumed that during the evolution, the external load F is distributed identically on reliable units and is growing stepwise along the rule that was discussed in Sub**section 2.3**.

Having initially $\mathcal{G}_0 \neq \varnothing, F_0 = 0, \{f(0)\}_{\mathcal{G}_0} = \{0\}_{\mathcal{G}_0}$, the rule yields consecutive F_t:

if $\mathcal{G}(F_t) \neq \varnothing$ then

$$F_{t+1} = F_t + \min\left[\{\delta - f(F_t)\}_{\mathrm{G}(F_t)}\right] \wedge \mathrm{G}(F_t) \to \mathrm{G}(F_{t+1}) \subset \mathrm{G}(F_t)$$

else

$$F_c = F_t \wedge n_c = |\mathrm{G}(F_c)|$$

end if

This iterative chain involves successive patterns of local load $\{f(F_t)\}_{\mathcal{G}(F_t)}$ that are strongly affected by the load-sharing rule, i.e., the mLGS in our case.

Now, consider n_t units that are reliable at the stage t of the evolution. Let us choose one of them, say the i-th unit. This means that $\delta_i > f_i$, where f_i is the local load at node i. When $F_t \to F_{t+1} > F_t$ then $n_t \to n_{t+1} < n_t$ and the pattern of local load becomes $\{f(F_{t+1})\}_{\mathcal{G}(F_{t+1})}$. The state of our chosen unit is now determined by the difference between the quenched value of δ_i and the updated $\tilde{f}_i$. While δ_i remains unchanged, the updated $\tilde{f}_i$ increases because of a growing $F_{t+1}/n_{t+1} > F_t/n_t$ and new shared loads, possibly assigned to the unit at the stage t. Clearly, internal-load distributions are subject to non-trivial variations that can be observed during the evolution.

It is important to make a distinction between impacts of external and internal loads on units. To obtain a closer look at these different impacts, we compare F_t/n_t with $\{f(F_t)\}_{\mathcal{G}(F_t)}$ for a given network $\mathcal{G}(F_t)$ in the course of evolution. As an illustrative example, we compare the impacts at critical configuration resulting from averaging over 10^6 samples. **Figure 8** displays $\langle F_c\rangle/\langle n_c\rangle$ and $\langle\{f(F_c)\}_{\mathcal{G}_c}\rangle = \langle F_c/n_c\rangle$.

Analyzing computed values, we detect that the mean internal load prevails over the mean external one for all values of p. In networks with $N \sim 10^2$, the relative difference is of the order of 0.01 and thus, is relevant to a prospective unit. Such a difference should be taken into account when forecasting long-term reliability, especially when considering units with low values of their δs.

Small-World Properties at Critical Configuration

When the sLGS rule is in operation, a load is assigned according to accessibility of reliable units, i.e., either locally or globally. If the hosting network reveals a relatively strong local connectivity, then the sLGS looks like the LLS.

A lasting presence of reliable nearest-neighbours depends on a connectivity of an underlying network. Independently of the value of rewiring probability p, random graphs generated by the Watts-Strogatz model preserve the number of edges and mean-node degree. This means that when p grows, we pass from ordered to disordered networks, keeping the numbers of nodes and edges unchanged. For intermediate values of p, the resulting networks turn out to be locally clustered, whereas randomly

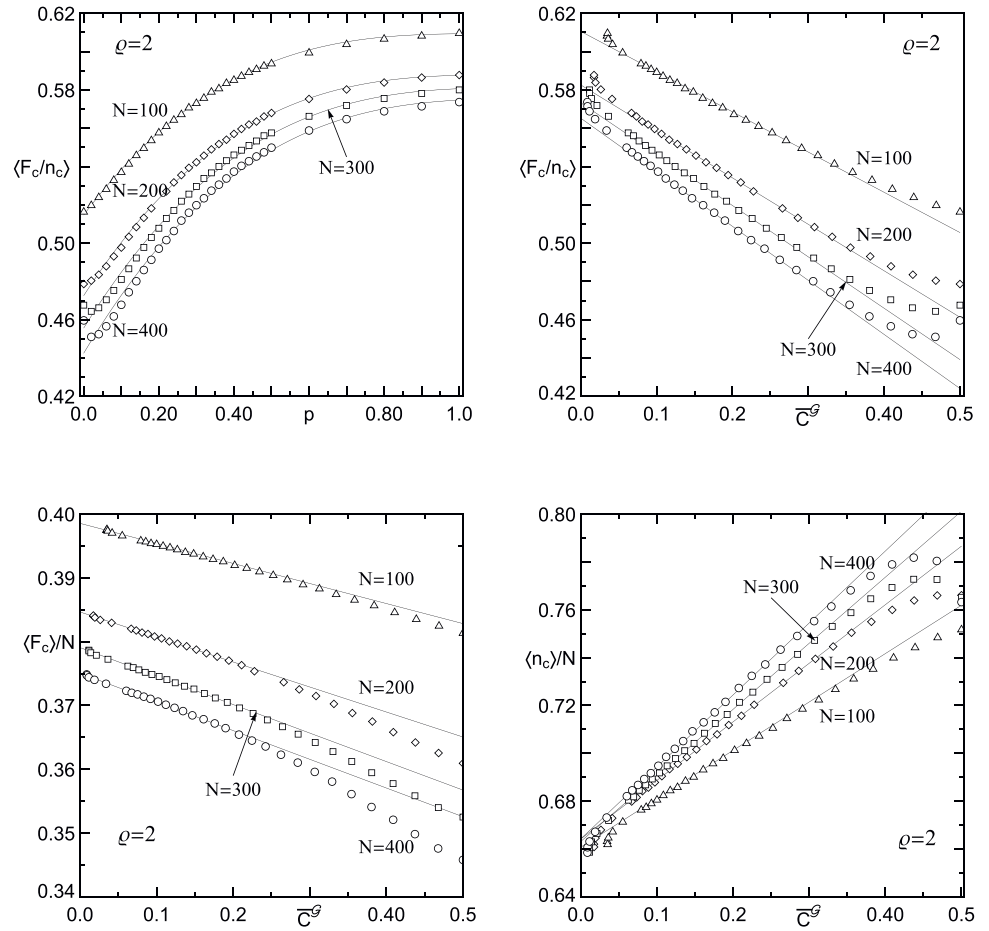

FIGURE 11 | Upper panels: Mean system's strength per reliable unit at critical configuration: **(left)** as function of p with solid lines drawn according to 9 and **(right)** on a linear scale for the respective mean $\overline{C}^{\mathcal{G}}$. Bottom panels: Mean system's strength and mean number of reliable units at critical configuration, scaled by systems size N, as functions of mean empirical clustering coefficient calculated for corresponding networks. Results were obtained from 10^6 samples with the Weibull distribution of $\{\delta\}$ for each data point.

rewired edges reduce the mean path lengths. Thus, there exists a range of p, where networks belonging to $\{\mathcal{G}_0(N,p)\}$ resemble a so-called "small-world" environment, i.e., they reveal a relatively strong clustering and a short mean path length.

We thus expect that the "small-world" properties would mark their presence in data sets related to F_c, n_c and F_c/n_c. When analyzing the data together with values of the global clustering coefficient C, defined by the **Eq. 2** and computed for corresponding networks, we notice that for a given value of N, formula

$$\langle Y\rangle(p) = u + w\cdot\left(1-\xi\cdot p\right)^3 \tag{9}$$

best fits the quantity $\langle Y\rangle$ that represents the following mean: $\langle F_c/n_c\rangle, \langle F_c\rangle$ and $\langle n_c\rangle$. Detailed information is presented in **Table 1**. Because the same fit **(9)** also holds for $\overline{C}^{\mathcal{G}}(N,p)$ we can relate $\langle Y\rangle$ directly to $\overline{C}^{\mathcal{G}}$. Interestingly, it appears that the corresponding relation is linear for a range $p\in\{p_N^-, p_N^+\}$ that depends on N, namely:

$$\langle Y\rangle = a + b\cdot\overline{C}^{\mathcal{G}} \tag{10}$$

Figure 9 displays respective relations for systems with uniformly distributed $\{\delta\}$. Appropriate coefficients are presented in **Table 2**. In the large N limit, the relation **(10)** is valid for uniformly distributed $\{\delta\}_{\mathcal{G}}$. An example of such persistence is shown in **Figure 10** where for $p\in(0.14, 0.44)$ the ultimate strength scales linearly as:

$$f_u^{\infty} = (0.1982\pm 0.0013) - (0.089\pm 0.007)\cdot C_{\infty}, \tag{11}$$

with $C_{\infty} = (1/2)\cdot(1-p)^3$ [37]

When sets $\{\delta\}_{\mathcal{G}}$ are drawn from the Weibull distribution the relations **(9) and (10)** are present in systems with $N\sim 10^2$, see **Figure 11**. When $\rho\gtrsim 5$ the relation **(10)** disappears gradually with an increase in N, as it is shown in **Figure 12**. This indicates that when ρ grows an ascending degree of order among load thresholds homogenizes the system and suppresses the linear relation between network's clustering and system's strength.

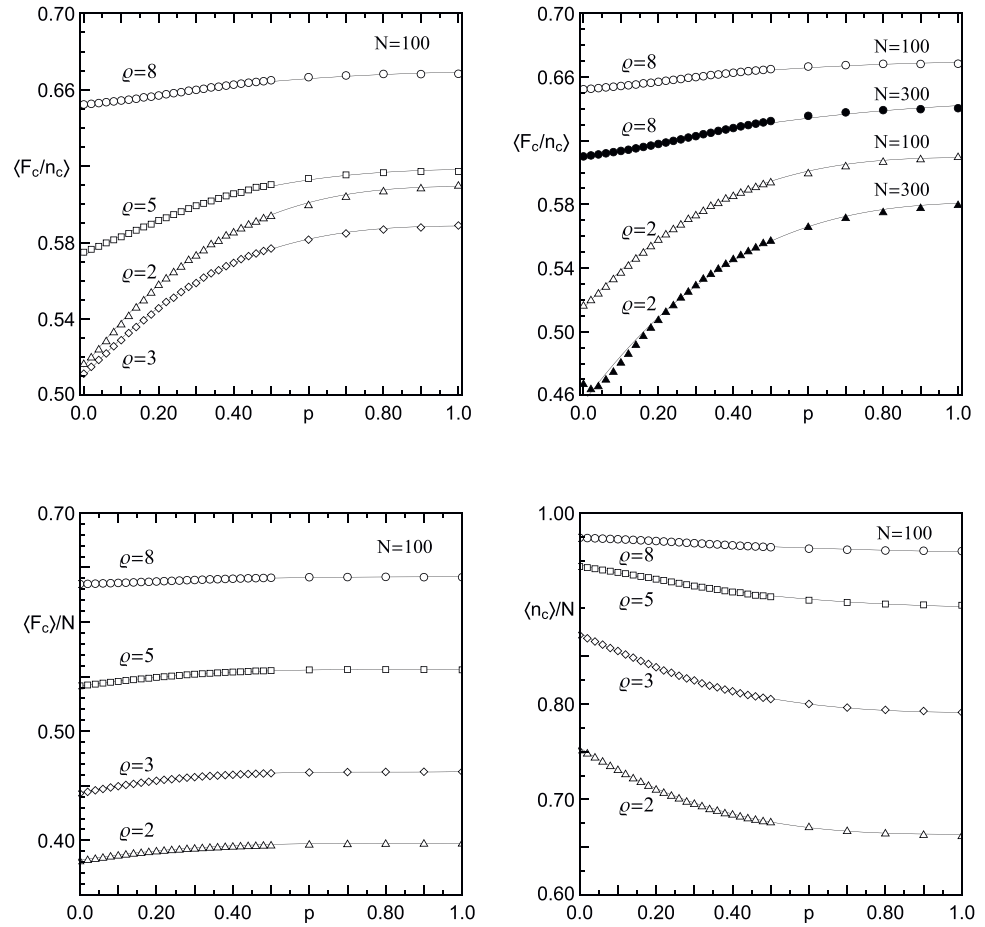

FIGURE 12 | Scaled mean critical quantities: $\langle F_c/n_c\rangle$, $\langle F_c\rangle/N$ and $\langle n_c\rangle/N$ for different values of Weibull shape parameter ρ and system size N as functions of p. The solid lines represent **Eq. 9** with coefficients estimated from data. The sample size equals 10^6.

It should be noticed that the expressibility of $\langle\cdot\rangle$ in $\overline{C}^{\mathcal{G}}(N,p)$ is not due to a kind of approximation or simplification that come from beyond the model but reflects a role that the small world structure of networks plays in maintaining functionalities of systems with strong to moderate load-threshold-disorder. It is also worth mentioning that the presented scaling results from: (i) the sLSG rule that allocates loads and (ii) the quasi-static method of load's growth. It remains to be verified whether the scaling **(10)** is valid for other loading schemes.

SUMMARY

We have investigated the evolution of failure among units that live at nodes of "small-world" networks and are exposed to a growing load. By introducing the sLGS rule of load transfer, which switches between the LLS and GLS rules depending on the accessibility of local interdependent nodes, we were able to mimic unit failures, and thus follow the evolution of the system toward the limit of its functionality. In particular, by employing the Watts-Strogatz random graphs to simulate the networks, we have collected data sufficient to form empirical distributions of the maximal load F_c, that would be safely supported by the minimal number n_c of reliable units. These quantities have turned out to be skewed and adequately fitted by appropriate skew-normal distributions. The obtained distributions reflect: i) how F_c, n_c and F_c/n_c depend on number of units, and ii) how strongly they are affected by an amount of a network's disorder, which is controlled by the rewiring probability p with which the links among interdependent nodes are modified.

The simulations show that if p is within the range of values given in **Table 2** then $\langle F_c\rangle$, $\langle n_c\rangle$ and $\langle F_c/n_c\rangle$ are linearly related to the global clustering coefficient averaged over the set of employed graphs. It should be noted, however, that even though our model sits on the Watts-Strogatz "small-world" networks, the obtained results are insensitive to the mean shortest path between pairs of nodes. This due to the sLGS rule that engages either the nearest-neighbouring nodes of a given node or all the other ones. Therefore, no distribution of distances appears in the presented results.

We are conscious of the fact that our simplified model of failure evolution involves some less realistic assumptions. Among the most serious is that we have considered each link between a pair of units as a reciprocally profitable relation. The other less strict assumption is that we allow the load thresholds be identically distributed. Our model can be tailored to fit a particular realistic scenario, e.g., by employing directed graphs, we would prevent some less reliable units from being interdependent.

DATA AVAILABILITY STATEMENT

The raw data supporting the conclusions of this article will be made available by the author, without undue reservation.

AUTHOR CONTRIBUTIONS

ZD performed the research and wrote the manuscript.

REFERENCES

1. Lorenz J, Battiston S, Schweitzer F. Systemic risk in a unifying framework for cascading processes on networks. *Eur Phys J B* (2009) **71**:441. doi:10.1140/epjb/e2009-00347-4
2. Capelli A, Reiweger I, Lehmann P, Schweizer J. Fiber-bundle model with time-dependent healing mechanisms to simulate progressive failure of snow. *Phys Rev E* (2018) **98**:023002. doi:10.1103/PhysRevE.98.023002
3. Domanski Z. Damage statistics in progressively compressed arrays of nano-pillars. *Eng Lett* (2019a) **27**:18–23.
4. Hemmer PC, Pradhan S. Failure avalanches in fiber bundles for discrete load increase. *Phys Rev E* (2007) **75**:046101. doi:10.1103/PhysRevE.75.046101
5. Kim D-H, Kim BJ, Jeong H. Universality class of the fiber bundle model on complex networks. *Phys Rev Lett* (2005) **94**:025501. doi:10.1103/PhysRevLett.94.025501
6. Kun F, Raischel F, Hidalgo R, Herrmann H. Extensions of fibre bundle models. In: P Bhattacharyya BK Chakrabarti, editors *Modelling critical and catastrophic phenomena in geoscience*. Berlin, Heidelberg: Springer (2006) p 57–92.
7. Pradhan S, Hansen A, Chakrabarti BK. Failure processes in elastic fiber bundles. *Rev Mod Phys* (2010) **82**:499–555. doi:10.1103/RevModPhys.82.499
8. Pugno NM, Bosia F, Abdalrahman T. Hierarchical fiber bundle model to investigate the complex architectures of biological materials. *Phys Rev E* (2012) **85**:011903. doi:10.1103/PhysRevE.85.011903
9. Hidalgo RC, Zapperi S, Herrmann HJ. Discrete fracture model with anisotropic load sharing. *J Stat Mech Theor Exp* (2008b) **2008**:P01004. doi:10.1088/1742-5468/2008/01/P01004
10. Hidalgo RC, Kovács K, Pagonabarraga I, Kun F. Universality class of fiber bundles with strong heterogeneities. *EPL* (2008a) **81**:54005. doi:10.1209/0295-5075/81/54005
11. Sbiaai H, Hader A, Boufass S, Achik I, Bakir R, Boughaleb Y. The effect of the substitution on the failure process in heterogeneous materials: fiber bundle model study. *Eur Phys J Plus* (2019) **134**:148. doi:10.1140/epjp/i2019-12475-7
12. Wang D, Jiang C, Park C. Reliability analysis of load-sharing systems with memory. *Lifetime Data Anal* (2017) **25**:341–60. doi:10.1007s10985-018-9425-8
13. Zhao X, Liu B, Liu Y. Reliability modeling and analysis of load-sharing systems with continuously degrading components. *IEEE Trans Reliab* (2018) **67**:1096–110. doi:10.1109/TR.2018.2846649
14. Hansen A, Hemmer P, Pradhan S. *The fiber bundle model: modeling failure in materials*. Weinheim, Germany: Viley-VCH (2015)
15. Watts D, Strogatz S. Collective dynamics of 'small-world' networks. *Nature* (1998) **393**:440–2. doi:10.1038/30918
16. Jackson MO. An overview of social networks and economic applications. In: Benhabib J, Bisin A, Jackson M, editors. *Handbook of social economics*. **Vol. 1A**. North Holland, Netherlands: Elsevier (2012) p. 511–85.
17. Newman M. The structure and function of complex networks. *SIAM Rev* (2003) **45**:167–256. doi:10.1137/S003614450342480
18. Burkholz R, Schweitzer F. Framework for cascade size calculations on random networks. *Phys Rev E* (2018) **97**:042312. doi:10.1103/PhysRevE.97.042312
19. Pradhan S, Chakrabarti BK, Hansen A. Crossover behavior in a mixed-mode fiber bundle model. *Phys Rev E* (2005) **71**:036149. doi:10.1103/PhysRevE.71.036149
20. Biswas S, Chakrabarti BK. Crossover behaviors in one and two dimensional heterogeneous load sharing fiber bundle models. *Eur Phys J B* (2013) **86**:160. doi:10.1140/epjb/e2013-40017-4
21. Kim BJ. Phase transition in the modified fiber bundle model. *Europhys Lett* (2004) **66**:819–25. doi:10.1209/epl/i2004-10038-4
22. La Rocca CE, Stanley HE, Braunstein LA. Strategy for stopping failure cascades in interdependent networks. *Phys Stat Mech Appl* (2018) **508**:577–83. doi:10.1016/j.physa.2018.05.154
23. Domanski Z. Statistics of flow through a multichannel supply system with random channel capacitances. *IAENG J Appl Math* (2019b) **43**:18–23.
24. Allen F, Gale D. Financial contagion. *J Polit Econ* (2000) **108**:1–33. doi:10.1086/262109
25. Boss M, Elsinger H, Summer M, Thurner S. Network topology of the interbank market. *Quant Finance* (2004) **4**, 677–84. doi:10.1080/14697680400020325
26. Cuadra L, Salcedo-Sanz S, Del Ser J, Jiménez-Fernández S, Geem Z. A critical review of robustness in power grids using complex networks concepts. *Energies* (2015) **8**:9211–65. doi:10.3390/en8099211
27. Pagani GA, Aiello M. The power grid as a complex network: a survey. *Phys Stat Mech Appl* (2013) **392**:2688–700. doi:10.1016/j.physa.2013.01.023
28. Rosas-Casals M, Valverde S, Solé RV. Topological vulnerability of the european power grid under errors and attacks. *Int J Bifurc Chaos* (2007) **17**:2465–75. doi:10.1142/S0218127407018531
29. Pagani GA, Aiello M. Towards decentralization: a topological investigation of the medium and low voltage grids. *IEEE Trans Smart Grid* (2011) **2**:538–47. doi:10.1109/TSG.2011.2147810
30. Saniee Monfared MA, Jalili M, Alipour Z. Topology and vulnerability of the iranian power grid. *Phys Stat Mech Appl* (2014) **406**:24–33. doi:10.1016/j.physa.2014.03.031
31. Cuadra L, Pino M, Nieto-Borge J, Salcedo-Sanz S. Optimizing the structure of distribution smart grids with renewable generation against abnormal conditions: a complex networks approach with evolutionary algorithms. *Energies* (2017) **10**:1097. doi:10.3390/en10081097
32. Sun Y, Tang X, Zhang G, Miao F, Wang P. Dynamic power flow cascading failure analysis of wind power integration with complex network theory. *Energies* (2017) **11**:63. doi:10.3390/en11010063
33. Zhang Z-Z, Xu W-J, Zeng S-Y, Lin J-R. An effective method to improve the robustness of small-world networks under attack. *Chin Phys B* (2014) **23**:088902. doi:10.1088/1674-1056/23/8/088902
34. Azzalini A. *The skew-normal and related families*. Cambridge, UK: Institute of Mathematical Statistics Monographs (Cambridge University Press) (2013)
35. Arnold T, Emerson J. Nonparametric goodness-of-fit tests for discrete null distributions. *R J* (2011) **3**:34–9. doi:10.32614/RJ-2011-016
36. Wasserman L, Ramdas A, Balakrishnan S. Universal inference. *Proc Natl Acad Sci USA* (2020) **117**:16880–90. doi:10.1073/pnas.1922664117
37. Barrat A, Weigt M. On the properties of small-world network models. *Eur Phys J B* (2000) **13**:547–60. doi:10.1007/s100510050067

Conflict of Interest: The author declares that the research was conducted in the absence of any commercial or financial relationships that could be construed as a potential conflict of interest.

frontiers in Physics

REVIEW
published: 10 December 2020
doi: 10.3389/fphy.2020.604053

The Three Extreme Value Distributions: An Introductory Review

Alex Hansen *

PoreLab, Department of Physics, Norwegian University of Science and Technology, Trondheim, Norway

The statistical distribution of the largest value drawn from a sample of a given size has only three possible shapes: it is either a Weibull, a Fréchet or a Gumbel extreme value distributions. I describe in this short review how to relate the statistical distribution followed by the numbers in the sample to the associate extreme value distribution followed by the largest value within the sample. Nothing I present here is new. However, from experience, I have found that a simple, short and compact guide on this matter written for the physics community is missing.

Keywords: extreme value statistics, statistical analysis, Weibull analysis, Gumbel distribution, Frechet distribution, Weibull distribution

OPEN ACCESS

Edited by:
Matjaž Perc,
University of Maribor, Slovenia

Reviewed by:
Arnab Pal,
Tel Aviv University, Israel
Haroldo V. Ribeiro,
State University of Maringá, Brazil

***Correspondence:**
Alex Hansen
Alex.Hansen@ntnu.no

Specialty section:
This article was submitted to Interdisciplinary Physics, a section of the journal Frontiers in Physics

Received: *08 September 2020*
Accepted: *22 October 2020*
Published: *10 December 2020*

Citation:
Hansen A (2020) The Three Extreme Value Distributions: An Introductory Review. Front. Phys. 8:604053. doi: 10.3389/fphy.2020.604053

1 INTRODUCTION

Extreme value statistics offers a powerful tool box for the theoretical physicist. But it is the kind of tool box that is not missed before one has been introduced to it—perhaps a little like the smart phone. It concerns the statistics of extreme events and it aims to answer questions like "if the strongest signal I have observed over the last hour had the value x, what would the strongest signal expected to be if measured over hundred hours?" Furthermore, if I divide up this hundred-hour interval into a hundred 1-h intervals, what would be the statistical distribution of strongest signal in each 1-h interval?

It is the latter question which is the focus of this mini-review.

There is no lack of literature on extreme value statistics, see e.g., [1–5] or simply *google* the term. We find it used in connection with spin glasses and disordered systems [6], in connection with $1/f$ noise [7], in connection with optics [8], in connection with fracture [9] or the fiber bundle model [10], in diffusion processes [11] etc. There are plenty of examples from diverse fields of physics.

So, there is no lack of material for the novice that has seen a need for this tool. The problem is that it is not so easy to penetrate the literature, which is often cast in a rather mathematical language which takes work to penetrate. The aim of this mini-review is to present the theory behind and the main results concerning the extreme value distributions in a simple and compact way. We will present nothing new. For a longer, wider and more detailed review of extreme value statistics, Fortin and Clusel [12] or Majumdar et al. present exactly that [13].We have a statistical distribution $p(x)$ and its associated cumulative probability

$$P(x) = \int_{-\infty}^{x} p(x')dx', \tag{1}$$

which is the probability to find a number smaller than or equal to x. We draw N numbers from this distribution and record the largest of the N numbers. We repeat this procedure M times and thereby obtain M largest numbers, one for each sequence. What is the distribution of these M largest numbers in the limit when $M \to \infty$, which then defines the *extreme value distribution*?

It turns out that depending on $p(x)$, the extreme value distribution will have one of three functional forms:

- The *Weibull* cumulative probability

$$\Phi(u) = \begin{cases} e^{-(-u)^{\alpha}} & \text{for } u < 0, \\ 1 & \text{for } u \geq 0, \end{cases} \tag{2}$$

where we assume $\alpha > 0$. Note that $\Phi(-\infty) = 0$. The corresponding Weibull extreme value distribution is

$$\phi(u) = \begin{cases} \alpha(-u)^{\alpha-1} e^{-(-u)^{\alpha}} & \text{for } u < 0, \\ 0 & \text{for } u \geq 0. \end{cases} \tag{3}$$

- The *Fréchet* cumulative probability

$$\Phi(u) = \begin{cases} 0 & \text{for } u \leq 0, \\ e^{-u^{-\alpha}} & \text{for } u > 0. \end{cases} \tag{4}$$

Also here we assume $\alpha > 0$. Note that $\Phi(\infty) = 1$. The Fréchet extreme value distribution is

$$\phi(u) = \begin{cases} 0 & \text{for } u \leq 0, \\ \alpha u^{-\alpha-1} e^{-u^{-\alpha}} & \text{for } u > 0. \end{cases} \tag{5}$$

- The *Gumbel* cumulative probability

$$\Phi(u) = e^{-e^{-u}}, \tag{6}$$

where $-\infty < u < \infty$, so that $\Phi(-\infty) = 0$ and $\Phi(\infty) = 1$. The corresponding Gumbel extreme value distribution is given by

$$\phi(u) = e^{-u-e^{-u}}. \tag{7}$$

The questions are 1. which classes of distributions $p(x)$ lead to which of the three extreme value distributions and 2. what is the connection between x and u in each case? It turns out that.

- distributions where $p(x) = 0$ for $x > x_0$ and $p(x) \sim (x_0 - x)^{\alpha-1}$ as $x \to x_0^-$, see **Eq. 10**, lead to the *Weibull extreme value distribution,*
- distributions where $p(x) \sim x^{-\alpha-1}$ as $x \to \infty$, see **Eq. 24** lead to the *Fréchet extreme value distribution,*
- and distributions where $p(x)$ falls of faster than any power law as $x \to \infty$, see **Eq. 53** lead to the *Gumbel extreme value distribution.*

Furthermore, we will find that.

- for the *Weibull extreme value distribution, u* is given in terms of x in **Eq. 13**,
- for the Fréchet extreme value distribution, u given in terms of x in **Eq. 27**,
- for the Gumbel extreme value distribution, u is given in terms of x in **Eqs 51** and **43**.

We summarize these results in **Table I**.

The discussion that will now follow, will be built on the following relation. We draw N numbers from the probability distribution $p(x)$: $x_1, x_2, \cdots, x_N$. The probability that all the N numbers are smaller than or equal to a value x is

$$\text{Prob}[x_1 \leq x, x_2 \leq x, \cdots, x_N \leq x] = \left[\int_{-\infty}^{x} p(x')dx' \right]^N = P(x)^N, \tag{8}$$

where $P(x)$ is the cumulative probability **1**. Our task is to figure out the limit $\text{Prob}[x_1 \leq x, x_2 \leq x, \cdots, x_N \leq x] = P(x)^N \to \Phi(u)$ as $N \to \infty$, and what is $u = u(x)$ as we approach this limit.

Rather than the conventional approach (see e.g., [10]) to this subject based on the Fréchet, Fisher and Tippett stability criterion [1], I will base the entire discussion on the relation

$$\lim_{N \to \infty} \left(1 + \frac{x}{N}\right) = e^x. \tag{9}$$

I believe this to be the simpler and more intuitive way.

2 WEIBULL CLASS

We consider here probability distributions $p(x)$ having the form

$$p(x) = \begin{cases} b\alpha(x_0 - x)^{\alpha-1} & \text{for } x \to x_0^-, \\ 0 & \text{for } x > x_0, \end{cases} \tag{10}$$

where b is positive. We note that $0 < \alpha < 1$ leads to a diverging probability density as $x \to x_0^-$. We furthermore note that $\alpha = 1$ implies that $p(x)$ approach a constant when $x \to x_0^-$ — which for example is the case when the distribution is uniform. The corresponding cumulative probability is given by

$$P(x) = \begin{cases} 1 & \text{for } x \geq x_0, \\ 1 - b(x_0 - x)^{\alpha} & \text{for } x \to x_0^-. \end{cases} \tag{11}$$

The extreme value cumulative probability for N samplings is given by

$$P(x)^N = [1 - b(x_0 - x)^{\alpha}]^N, \tag{12}$$

for $x \to x_0^-$. We introduce the variable change

$$x - x_0 = \frac{u}{(bN)^{1/\alpha}}, \tag{13}$$

where the reader should note that b is defined by the original distribution **10**. **Equation 12** then becomes

$$P(x)^N = \left[1 - \frac{(-u)^{\alpha}}{N}\right]^N. \tag{14}$$

In the limit of $N \to \infty$, this becomes

TABLE 1 | Summary of main results.

	$\mathbf{p(x)}$	$\phi(\mathbf{u})$	$\mathbf{u = u(x)}$
Weibull	$b\alpha(x_0 - x)^{\alpha-1}$ for $x \to x_0^-$ 0 for $x \geq x_0$	$\alpha(-u)^{\alpha-1}e^{-(-u)^\alpha}$ for $u \leq 0$ 0 for $u > 0$	$u = (bN)^{1/\alpha}(x - x_0)$
Fréchet	$b\alpha x^{-\alpha-1}$ for $x \to \infty$	$\alpha u^{-\alpha-1}e^{-u^{-\alpha}}$ for $u \geq 0$ 0 for $u < 0$	$u = (bN)^{-1/\alpha}x$
Gumbel	$f'(x)\exp[-f(x)]$ for $x \to \infty$ where $d[1/f'(x)]/dx \to 0$	$\exp[-u - e^{-u}]$ for $-\infty < u < \infty$	$u = Np(x_N)(x - x_N)$ where $P(x_N) = 1 - 1/N$

$$\Phi(u) = \lim_{N\to\infty} P(x)^N = e^{-(-u)^\alpha}, \tag{15}$$

for negative u. Hence, we have that

$$\Phi(u) = \begin{cases} e^{-(-u)^\alpha} & \text{for } u < 0, \\ 1 & \text{for } u \geq 0, \end{cases} \tag{16}$$

which is the *Weibull cumulative probability,* valid for *all* values of u even though we only know the behavior of $p(x)$ close to x_0. The Weibull probability density is given by

$$\phi(u) = \frac{d\Phi(u)}{du} = \begin{cases} \alpha(-u)^{\alpha-1}e^{-(-u)^\alpha} & \text{for } u < 0, \\ 0 & \text{for } u \geq 0. \end{cases} \tag{17}$$

We note that the Weibull distribution resembles a stretched exponential. This is correct for $\alpha < 1$. However, $\alpha \geq 1$ is much more common in the wild.

We express the Weibull cumulative probability in terms of the original variable x using **Eq. 13**,

$$\Phi(u) = \Phi\Big((bN)^{1/\alpha}(x - x_0)\Big) = e^{-Nb(x_0-x)^\alpha} = \tilde{\Phi}(x). \tag{18}$$

Hence, in terms of the original variable x, the Weibull extreme value distribution becomes

$$\tilde{\phi}(x) = \frac{d\tilde{\Phi}(x)}{dx} = Nb\alpha(-x)^{\alpha-1}e^{-Nb(x_0-x)^\alpha}. \tag{19}$$

2.1 Weibull: An Example

We now work out a concrete example. Let us assume that $p(x)$ is given by

$$p(x) = \begin{cases} 0 & \text{for } x < 0, \\ \alpha(1 - x)^{\alpha-1} & \text{for } 0 \leq x \leq 1, \\ 0 & \text{for } x > 1, \end{cases} \tag{20}$$

i.e., $b = 1$ and $x_0 = 1$ in **Eq. 10**. The cumulative probability is then

$$P(x) = \begin{cases} 0 & \text{for } x < 0, \\ 1 - (1 - x)^\alpha & \text{for } 0 \leq x \leq 1, \\ 1 & \text{for } x > 1. \end{cases} \tag{21}$$

From **Eq. 19** and we have that

$$\tilde{\phi}(x) = N\alpha(1 - x)^{\alpha-1}e^{-N(1-x)^\alpha}. \tag{22}$$

We show the distribution **20** with $\alpha = 3$ together with the corresponding extreme value distributions for $N = 100$ and $N = 1,000$, **Eq. 19** in **Figure 1A**.

Using a random number generator producing IID numbers[1] r uniformly distributed on the unit interval, we may stochastically generate numbers that are distributed according to the probability density $p(x)$ given in **20**. We do this by inverting the expression $P(x) = r$, where the cumulative probability is given by **21**. Hence, we have

$$x = 1 - r^{1/\alpha}, \tag{23}$$

where we have also used that r may be substituted for $1 - r$ in **21**. We generate a sequence of sequences of numbers using this algorithm, each sequence having length N. We then identify the largest value within each sequence. We chose $N = 100$ and $N = 1,000$, in each case generating 10^7 such sequences. The histograms based on the random numbers themselves, and of the extreme values for each sequence of length either 100 or 1,000 we show in **Figure 1B**. This figure should be compared to **Figure 1A**.

The Weibull distribution, **Eq. 17** is much used in connection with material strength [15]. This is no coincidence. Consider a chain. Each link in the chain can sustain a load up to a certain value, above which it fails. This maximum value is distributed according to some probability distribution. When the chain is loaded, it will be the link with the *smallest* failure threshold that will break first causing the chain as a whole to fail. Hence, the strength distribution of an ensemble of chains is an extreme value distribution, but with respect to the smallest rather than the largest value. The link strength must a positive number. Hence, the link strength distribution is cut off at zero or some positive value. The distribution close to this cutoff value must behave as a power law in the distance to the cutoff, e.g., due to a Taylor expansion around the cutoff. The corresponding extreme value distribution, which is the chain strength distribution, must then be a Weibull distribution.

3 FRÉCHET CLASS

We now assume that the probability distribution $p(x)$ behaves as

$$p(x) = b\alpha x^{-\alpha-1} \text{ for } x \to \infty, \tag{24}$$

[1]IID variables. Independent and identically distributed random variables, a terminology used in some communities.

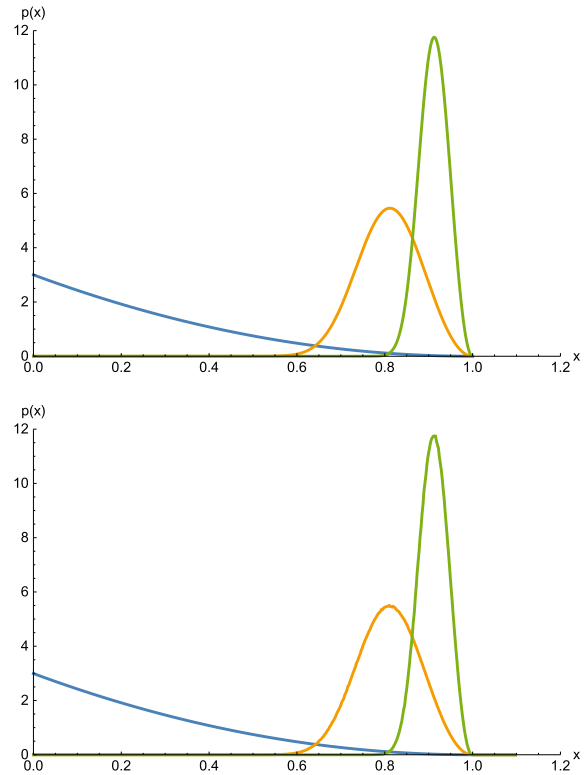

FIGURE 1 | (A) The curve that has its maximum at $x = 0$ is the probability distribution **20** with $\alpha = 3$. The curve that has its maximum in the middle is $\tilde{\phi}(x)$, **Eq. 22** with $N = 100$ and the curve that has its maximum to the right is $\tilde{\phi}(x)$ with $N = 1,000$. **(B)** The histograms shown here are based on data according to the probability distribution 20 with $\alpha = 3$. The histogram having its maximum to the left shows all the generated data. The histogram having its maximum in the middle shows the largest number among each sequence of numbers of length 100, and the histogram having its maximum to the right shows the largest number among each sequence of numbers of length 1,000. We generated 10^7 sequences for both cases.

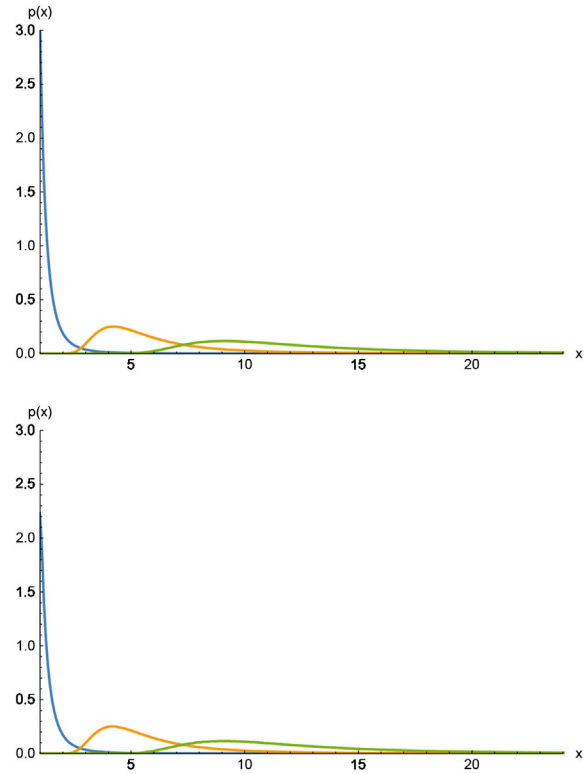

FIGURE 2 | (A) The curve that has its maximum at $x = 1$ is the probability distribution **34** with $\alpha = 3$. The curve that has its maximum in the middle is $\tilde{\phi}(x)$, **Eq. 36** with $N = 100$ and the curve that has its maximum to the right is $\tilde{\phi}(x)$ with $N = 1,000$. **(B)** The histograms shown here are based on data according to the probability distribution **34** with $\alpha = 3$. The histogram having its maximum to the left shows all the generated data. The histogram having its maximum in the middle shows the largest number among each sequence of numbers of length 100, and the histogram having its maximum to the right shows the largest number among each sequence of numbers of length 1,000. For each sequence length, 10^7 such sequences were generated.

and the corresponding cumulative probability behaves as

$$P(x) = 1 - bx^{-\alpha} \text{ for } x \to \infty. \tag{25}$$

The extreme value cumulative probability for N samplings is given by

$$P(x)^N = [1 - bx^{-\alpha}]^N, \tag{26}$$

for $x \to \infty$. We introduce the variable change

$$x = (bN)^{1/\alpha} u, \tag{27}$$

where b comes from the original distribution **24**. We now plug this change of variables into **Eq. 26** to find

$$P(x)^N = \left[1 - b\left((bN)^{1/\alpha} u\right)^{-\alpha}\right]^N = \left[1 - \frac{u^{-\alpha}}{N}\right]^N. \tag{28}$$

In the limit of $N \to \infty$, this becomes

$$\Phi(u) = \lim_{N \to \infty} P(x)^N = e^{-u^{-\alpha}}, \tag{29}$$

where $u \geq 0$ is given by **Eq. 27**. We see that $\Phi(u) \to 0$ as $u \to 0^+$. Furthermore, for $u < 0$, the function is no longer real. Hence, we define $\Phi(u) = 0$ for $u < 0$. The ensuing extreme value cumulative probability is then given by

$$\Phi(u) = \begin{cases} 0 & \text{for } u \leq 0, \\ e^{-u^{-\alpha}} & \text{for } u > 0, \end{cases} \tag{30}$$

which is the *Fréchet cumulative probability*. The Fréchet probability density is given by

$$\phi(u) = \frac{d\Phi(u)}{du} = \begin{cases} 0 & \text{for } u \leq 0. \\ \alpha u^{-\alpha-1} e^{-u^{-\alpha}} & \text{for } u > 0. \end{cases} \tag{31}$$

We express the Fréchet cumulative probability in terms of the original variable x using **Eq. 27**,

$$\Phi(u) = \Phi\left(\frac{x}{(bN)^{1/\alpha}}\right) = e^{-Nx^{-\alpha}} = \tilde{\Phi}(x). \tag{32}$$

Hence, in terms of the original variable x, the Fréchet extreme value distribution becomes

$$\tilde{\phi}(x) = \frac{d\tilde{\Phi}(x)}{dx} = N\alpha x^{-\alpha-1} e^{-Nx^{-\alpha}}. \tag{33}$$

3.1 Fréchet: An Example

We consider the distribution

$$p(x) = \begin{cases} 0 & \text{for } x \le 1, \\ \alpha x^{-\alpha-1} & \text{for } x > 1, \end{cases} \tag{34}$$

The corresponding cumulative probability is given by

$$P(x) = \begin{cases} 0 & \text{for } x \le 1, \\ 1 - x^{-\alpha} & \text{for } x > 1. \end{cases} \tag{35}$$

Using **Eq. 33**, we find the corresponding Fréchet extreme value distribution to be

$$\tilde{\phi}(x) = N\alpha x^{-\alpha-1} e^{-Nx^{-\alpha}}, \tag{36}$$

valid for all $x > 1$. We show $p(x)$ and the corresponding $\tilde{\phi}(x)$ for $\alpha = 3$ and $N = 100$ and $N = 1,000$ in **Figure 2A**.

In order to compare with numerical results, we generate numbers distributed according to **34** by solving the equation $P(x) = r$ where r is drawn from a uniform distribution on the unit interval. From **Eq. 35**, we get

$$x = r^{-1/\alpha}. \tag{37}$$

We generate a sequence of numbers using this algorithm, grouping them together in sequences of $N = 100$ or $N = 1,000$. We generate 10^7 such sequences. The histograms based on the random numbers themselves generated with **Eq. 37**, and of the extreme values for each sequence of length either 100 or 1,000 we show in **Figure 2B**. This figure should be compared to **Figure 2A**.

4 GUMBEL CLASS

We now assume we have a probability distribution that takes the form

$$p(x) = f'(x) e^{-f(x)} \quad \text{for } x > x_0, \tag{38}$$

where $f'(x) = df(x)/dx$. We have that x_0 is any number, positive or negative, and $f(x)$ is an increasing function of x. We will later on introduce a sufficient criterion imposed on $p(x)$ to produce the Gumbel distribution, see **Eq. 53**. This criterion is equivalent to $f(x)$ fulfilling

$$\lim_{x\to\infty} \frac{d}{dx}\left(\frac{1}{f'(x)}\right) = 0. \tag{39}$$

This criterion is e.g., fulfilled by any polynomial $f(x)$.

The cumulative probability is

$$P(x) = 1 - e^{-f(x)} \quad \text{for } x > x_0. \tag{40}$$

We do not care about the form of $p(x)$ or $P(x)$ for $x \le x_0$.

The extreme value cumulative probability for N samplings is given by

$$P(x)^N = \left[1 - e^{-f(x)}\right]^N, \tag{41}$$

for $x > x_0$. We introduce the variable change

$$\tilde{u} = f(x) - f(x_N), \tag{42}$$

where x_N is given by

$$P(x_N) = 1 - \frac{1}{N}. \tag{43}$$

Even though x_N is defined by **43**, we may interpret its meaning. We do so in the conclusion, see **Eq. 71**. From **Eq. 40** we then have that

$$f(x_N) = \ln N. \tag{44}$$

Let us now define

$$\Delta x = x - x_N. \tag{45}$$

We then expand $f(x)$ around x_N,

$$f(x) = f(x_N + \Delta x) = \sum_{n=0}^{\infty} \frac{f^{(n)}(x_N)}{n!} \Delta x^n, \tag{46}$$

where $f^{(n)}(x) = d^n f(x)/dx^n$. If we now set

$$\Delta x = \frac{1}{f'(x_N)}, \tag{47}$$

so that the first order term in the expansion becomes constant as N increases, we will have that

$$f'(x_N)\Delta x + \sum_{n=2}^{\infty} \frac{f^{(n)}(x_N)}{n!} \Delta x^n = 1 + \sum_{n=2}^{\infty} \frac{f^{(n)}(x_N)}{n!\, f'(x_N)^n}. \tag{48}$$

Hence, if we have that

$$\lim_{N\to\infty} \frac{f^{(n)}(x_N)}{f'(x_N)^n} = 0, \tag{49}$$

for $n \ge 2$, then in this limit, we will find

$$f(x) = f(x_N) + f'(x_N)\Delta x = f(x_N) + u, \tag{50}$$

where we define

$$u = f'(x_N)\Delta x = Np(x_N)(x - x_N). \tag{51}$$

Here we have used **Eqs (40)** and **(44)**.

4.1 Sufficient Criterion for the Gumbel Class

If we combine **Eq. 49** for $n = 2$ with **Eqs 38** and **40**, we find

$$\lim_{N\to\infty} \frac{f''(x_N)}{f'(x_N)^2} = \lim_{N\to\infty} \frac{d}{dx}\left[\frac{1 - P(x)}{p(x)}\right]_{x=x_N} = 0, \tag{52}$$

which is equivalent to

$$\lim_{x\to\infty}\frac{d}{dx}\left[\frac{1-P(x)}{p(x)}\right]=0. \tag{53}$$

Equation 53, which is equivalent to **Eq. 39**, is in fact a *sufficient condition* for **49** to hold for all $n>1$. We may show this through induction. We have that

$$\frac{f^{(n+1)}(x)}{f'(x)^{n+1}}=\frac{1}{f'(x)}\frac{d}{dx}\left(\frac{f^{(n)}(x)}{f'(x)^{n}}\right)+\frac{f^{(n)}(x)}{f'(x)^{n+2}}. \tag{54}$$

If condition **52** is fulfilled, that is when the expression above is zero in the limit $x\to\infty$ for $n=2$, we also have that

$$\lim_{N\to\infty}\frac{f^{(3)}(x)}{f'(x)^{3}}=0, \tag{55}$$

since both terms on the right hand side of **Eq. 54** are zero in this limit. We now assume **Eq. 49** to be true for some $n>3$. We then have that

$$\lim_{N\to\infty}\frac{f^{(n+1)}(x_N)}{f'(x_N)^{n+1}}=0, \tag{56}$$

again due to both terms on the right hand side of **Eq. 54** are zero in this limit. This completes the proof.

4.2 Return to the Derivation

We now combine **Eq. 42** with **Eq. 41** to find

$$P(x)^N=\left[1-e^{-u-f(x_N)}\right]^N=\left[1-e^{-u-\ln N}\right]^N=\left[1-\frac{e^{-u}}{N}\right]^N. \tag{57}$$

In the limit of $N\to\infty$, this becomes

$$\Phi(u)=\lim_{N\to\infty}P(x)^N=e^{-e^{-u}}, \tag{58}$$

which is the *Gumbel cumulative probability*. Here $-\infty<u<\infty$. The Gumbel probability density is given by

$$\phi(u)=\frac{d\Phi(u)}{du}=e^{-u-e^{-u}}. \tag{59}$$

We express the Gumbel cumulative probability in terms of the original variable x using **Eq. 51**,

$$\Phi(u)=\Phi\left(Np(x_N)(x-x_N)\right)=e^{-e^{-Np(x_N)(x-x_N)}}=\tilde{\Phi}(x). \tag{60}$$

Hence, in terms of the original variable x, the Gumbel extreme value distribution becomes

$$\tilde{\phi}(x)=\frac{d\tilde{\Phi}(x)}{dx}=Np(x_N)e^{-Np(x_N)(x-x_N)-e^{-Np(x_N)(x-x_N)}}. \tag{61}$$

4.3 An Example: The Gaussian

Here is an example: the Gaussian. The Gaussian probability density is given by

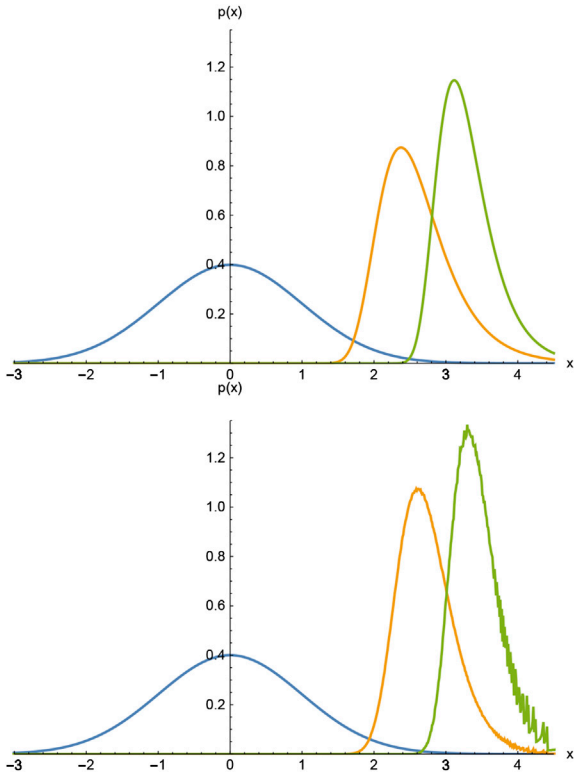

FIGURE 3 | (A) The Gaussian and the corresponding Gumbel distributions for $\sigma=1$ and $N=100$ and $N=1,000$. **(B)** The histograms shown here are based on data generated using the Box-Müller algorithm which produces numbers distributed according to a Gaussian. Here $\sigma=1$. The histogram with the maximum to the left shows all the generated data. The histogram with its maximum in the middle shows the largest number among each sequence of numbers of length 100, and the histogram with the rightmost maximum shows the largest number among each sequence of numbers of length 1,000. For each sequence length, 10^7 such sequences were generated.

$$p(x)=\frac{e^{-x^2/2\sigma}}{\sqrt{2\pi\sigma}}, \tag{62}$$

where σ is the square of the standard deviation. The cumulative probability is

$$P(x)=\frac{1}{2}\left[1+\mathrm{erf}\left(\frac{x}{\sqrt{2\sigma}}\right)\right], \tag{63}$$

where $\mathrm{erf}(z)$ is the error function. In order to verify that the Gaussian generates the Gumbel extreme distribution, we use the sufficient condition **53**,

$$\lim_{x\to\infty}\frac{d}{dx}\left[\frac{1-P(x)}{p(x)}\right]=\lim_{x\to\infty}\sqrt{\frac{\pi}{2\sigma}}e^{x^2/2\sigma}x\left[1-\mathrm{erf}\left(\frac{x}{\sqrt{2\sigma}}\right)\right]=0. \tag{64}$$

The Gaussian cumulative probability in **Eq. 63** has the asymptotic form

$$P(x) = 1 - \sqrt{\frac{\sigma}{2\pi}}\,\frac{e^{-x^2/2\sigma}}{x}, \tag{65}$$

for large x. We determine x_N solving **Eq. 43** using this asymptotic form. We find

$$x_N = \sqrt{\sigma W\left(\frac{N^2}{2\pi}\right)}, \tag{66}$$

where $W(z)$ is the Lambert W function, also known as the product logarithm, which is the solution to the equation $W(z)\exp[W(z)] = z$. For large arguments, it approaches the natural logarithm, $W(z) \to \log(z)$ as $z \to \infty$ [16]. This gives us

$$Np(x_N) = \sqrt{\frac{1}{\sigma} W\left(\frac{N^2}{2\pi}\right)}, \tag{67}$$

when inserting the expression for $x = x_N$, **Eq. 66** into **Eq. 62**. Thus we may now express the variable u in the Gumbel cumulative probability **57** in terms of the variables x, σ and N using **Eq. 51**,

$$u = x\sqrt{\frac{1}{\sigma} W\left(\frac{N^2}{2\pi}\right)} - W\left(\frac{N^2}{2\pi}\right). \tag{68}$$

We show in **Figure 3A** the Gaussian and the corresponding Gumbel distributions for $\sigma = 1$ and $N = 100$ and $N = 1,000$. We find that $x_{100} = 2.375$ and $x_{1000} = 3.115$. These are the confidence intervals for 99% and 99.9%.

We show in **Figure 3B** a histogram based on numbers distributed according to a Gaussian distribution using the Box-Müller algorithm [14]. These numbers were grouped together in sets of either $N = 100$ or $N = 1,000$ elements. I generated 10^7 such sets. The figure displays the two extreme distributions for the two set sizes. This figure should be compared to **Figure 3A**. In contrast to the two other extreme value distributions, we see that there are visible discrepancies between the calculated Gumbel distributions in **Figure 3A** and the extreme value histograms in **Figure 3B**. We see furthermore that the histogram for $N = 1,000$ is closer to the calculated Gumbel distribution than the histogram for $N = 100$. This is due to the very slow convergence induced by the Lambert W functions. Slow convergence is typical for the Gumbel extreme value distributions. This slow convergence has been analyzed and recently and through clever use of scaling methods remedied [17].

5 CONCLUDING REMARKS

We summarize the main results presented in this mini-review in **Table I**.

We have only discussed the distributions associated with the *largest* values of x except for the Weibull extreme value distribution, **Section 2**. It is, however, easy to work out: *just transform* $x \to -x$. Otherwise, the story presented here is rather complete.

There is one remark that needs to be made, though. In the derivation of the Gumbel extreme value distribution, **Section 4**, we defined a variable x_N in **Eq. 43**. First of all, x_N defined in **Eq. 43** may be calculated for *any* cumulative probability $P(x)$ and it has an interpretation making it very useful.

The probability density for the largest among N numbers drawn using the probability distribution $p(x)$ is given by

$$p_N(x) = \frac{dP(x)^N}{dx} = NP(x)^{N-1}p(x). \tag{69}$$

We calculate the average of the cumulative probability $P(x)$ for the extreme value based on N samples,

$$\langle P(x)\rangle = \int_{-\infty}^{\infty} P(x)p_N(x)dx = \int_0^1 P^N dP = \frac{N}{N+1} = 1 - \frac{1}{N+1}. \tag{70}$$

For large N, we may write this as

$$\langle P(x)\rangle = P(x_N) = 1 - \frac{1}{N}, \tag{71}$$

using here **Eq. 43**. Hence, we may interpret x_N as the x value corresponding to the average confidence interval of the largest observed value in sequences of N numbers. It is essentially the typical size of the extreme value for a sample of size N.

AUTHOR CONTRIBUTIONS

The author confirms being the sole contributor of this work and has approved it for publication.

FUNDING

This work was partly supported by the Research Council of Norway through its Centers of Excellence funding scheme, project number 262644.

ACKNOWLEDGMENTS

I thank Eivind Bering, Astrid de Wijn, H. George, E. Hentschel, Srutarshi Pradhan, and Itamar Procaccia for numerous interesting discussions on this topic.

REFERENCES

1. Gumbel EJ. *Statistics of extremes*. New York: Columbia University Press (1958)
2. David HA. *Order statistics*. 2nd ed. New York: Wiley (1981)
3. Galambos J. *The asymptotic theory of extreme order statistics*. Malabar, FL: Krieger(1987)
4. Embrechts P, Klüppelberg C, Mikosh T. *Modeling extreme events for insurance and finance*. Berlin: Springer (1997)
5. Coles S. *An introduction to statistical modeling of extreme events*. Berlin: Springer (2001)

6. Bouchaud J-P, Mézard M. Universality classes for extreme-value statistics. *J Phys Math Gen* (1997) 30:7997. doi:10.1088/0305-4470/30/23/004
7. Antal T, Droz M, Györgyi G, Rácz Z. 1/f noise and extreme value statistics. *Phys Rev Lett* (2001) 87:240601. doi:10.1103/physrevlett.87.240601
8. Randoux S, Suret P. Experimental evidence of extreme value statistics in Raman fiber lasers. *Opt Lett* (2012) 37:500. doi:10.1364/OL.37.000500
9. Taloni A, Vodret M, Costantini G, Zapperi S. Size effects on the fracture of microscale and nanoscale materials. *Nat Rev Mater* (2018) 3:211–24. doi:10.1038/s41578-018-0029-4
10. Hansen A, Hemmer PC, Pradhan S. *The fiber bundle model*. Berlin: Wiley VCH (2015)
11. Pal A, Eliazar I, Reuveni S. First passage under restart with branching. *Phys Rev Lett* (2019) 122:020602. doi:10.1103/PhysRevLett.122.020602
12. Fortin J-Y, Clusel M. Applications of extreme value statistics in physics. *J Phys Math Theor* (2015) 48:183001. doi:10.1088/1751-8113/48/18/183001
13. Majumdar SN, Pal A, Schehr G. Extreme value statistics of correlated random variables: a pedagogical review. *Phys Rep* (2020) 840:1. doi:10.1016/j.physrep.2019.10.005
14. Press WH, Teukolsky SA, Vetterling WT, Flannery BP. *Numerical recipes*. 3rd ed. Cambridge: Cambridge University Press (2007)
15. Rinne H. *The Weibull distribution*. Boca Raton: CRC Press (2008).
16. Corless RM, Gonnet GH, Hare DEG, Jeffrey DJ, Knuth DE. On the LambertW function. *Adv Comput Math* (1996) 5:329–59. doi:10.1007/BF02124750
17. Zarfaty L, Barkai E, Kessler DA. Accurately approximating extreme value statistics (2020) arXiv:2006.13677.

Conflict of Interest: The author declares that the research was conducted in the absence of any commercial or financial relationships that could be constructed as a potential conflict of interest.

frontiers in Physics

REVIEW
published: 15 February 2021
doi: 10.3389/fphy.2020.613392

Cooperative Dynamics in the Fiber Bundle Model

Bikas K. Chakrabarti[1,2], *Soumyajyoti Biswas*[3] *and Srutarshi Pradhan*[4]*

[1]*Saha Institute of Nuclear Physics, Kolkata, India,* [2]*S. N. Bose National Centre for Basic Sciences, Kolkata, India,* [3]*SRM University-AP, Andhra Pradesh, India,* [4]*PoreLab, Department of Physics, Norwegian University of Science and Technology, Trondheim, Norway*

We discuss the cooperative failure dynamics in the fiber bundle model where the individual elements or fibers are Hookean springs that have identical spring constants but different breaking strengths. When the bundle is stressed or strained, especially in the equal-load-sharing scheme, the load supported by the failed fiber gets shared equally by the rest of the surviving fibers. This mean-field-type statistical feature (absence of fluctuations) in the load-sharing mechanism helped major analytical developments in the study of breaking dynamics in the model and precise comparisons with simulation results. We intend to present a brief review on these developments.

Keywords: fiber bundle model, dynamic cooperation, fixed-point solution, Universality, noise-induced failure dynamics, self-organization

OPEN ACCESS

Edited by:
Subhrangshu Sekhar Manna, S.N. Bose National Centre for Basic Sciences, India

Reviewed by:
Ferenc Kun, University of Debrecen, Hungary
Federico Bosia, Politecnico di Torin, Italy
Stepan Lomov, KU Leuven, Belgium

***Correspondence:**
Srutarshi Pradhan
srutarshi.pradhan@ntnu.no

Specialty section:
This article was submitted to Interdisciplinary Physics, a section of the journal Frontiers in Physics

Received: *02 October 2020*
Accepted: *23 December 2020*
Published: *15 February 2021*

Citation:
Chakrabarti BK, Biswas S and Pradhan S (2021) Cooperative Dynamics in the Fiber Bundle Model. Front. Phys. 8:613392. doi: 10.3389/fphy.2020.613392

1 INTRODUCTION

Fiber bundle model (FBM) has been used widely for studying the fracture and failure [1] of composite materials under external loading. The simplicity of the model allows us to achieve analytic solutions [2–4] to an extent that is not possible in any other fracture models. For these very reasons, FBM is widely used as a model of breakdown that extends beyond disordered solids. In fact, FBM was first introduced in connection with textile engineering [5]. Physicists took interest in it recently to explore the critical failure dynamics and avalanche phenomena during such stress-induced failures [6–9]. Apart from the classical fracture–failure in composites, FBM has been used successfully for studying noise-induced (creep/fatigue) failure [10–14] where a fixed load is applied on the system and external noise triggers the failure of elements. Furthermore, it was used as a model for other geophysical phenomena, such as snow avalanche [15], land slides [16, 17], biological materials [18], or even earthquakes [19]. In this review article, we concentrate only on the cooperative dynamical aspects in FBM.

F. T. Peirce, a textile engineer, introduced the fiber bundle model [5] in 1926 to study the strength of cotton yarn. Later, in 1945, Daniels discussed some static behavior of such a bundle [20] and the model was brought to the attention of physicists in 1989 by Sornette [21] who started analyzing the failure process. Even though FBM was designed initially as a model for the fracture or failure of a set of parallel elements (fibers), having different breaking thresholds, with a collective load-sharing scheme, the failure dynamics in the model shows all the attributes of the critical phenomena and the associated phase transition. It seems, due to the usefulness and richness, FBM plays the same role (in the field of fracture) as the Ising model in magnetism [22].

In FBM, a number of parallel Hookean springs or fibers are clamped between two horizontal platforms (**Figure 1**). The breaking strengths of the springs or fibers are different. When the load per fiber (stress) exceeds a fiber's own threshold, it fails. The load it carries has to be shared by the surviving fibers. If the lower platform deforms under loading while the upper platform remains rigid, fibers in the neighborhood of the just-failed fiber will absorb more of the load compared to fibers

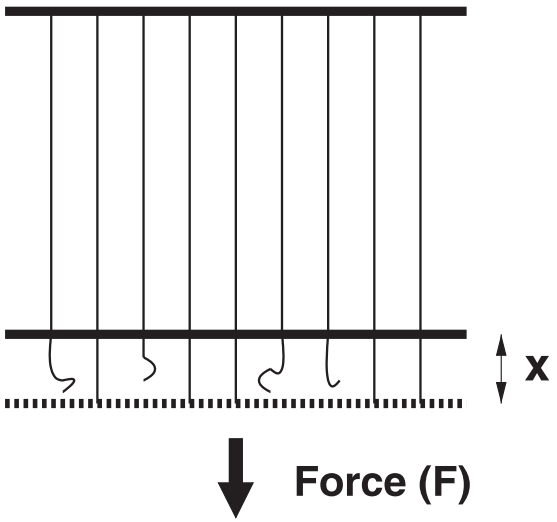

FIGURE 1 | A cartoon of the fiber bundle model where a macroscopically large number (*N*) of Hookean springs, with identical spring constants but different breaking thresholds, hang parallelly from an upper rigid bar and a load/force *F* is applied at the lower horizontal rigid bar (not allowing any local deformation of the bar and consequent local stress concentration). If any spring fails at any time, the (extra) load is shared by the surviving fibers at that time. In the equal-load-sharing scheme, considered here, this extra load is shared equally by all the surviving fibers (*x* denoting the strain of the surviving fibers).

sitting further away, and this arrangement is called the local-load-sharing (LLS) scheme [23, 24]. If both the platforms are rigid, the load has to be equally distributed among all the surviving fibers, which is called the equal-load-sharing (ELS) scheme. Intermediate load redistribution schemes are also studied (see, e.g., [25]), where a part of the load is shared locally within a few fibers and the rest is shared globally among all the fibers.

How does cooperative dynamics set in? In the case of ELS, all the intact fibers carry the load equally. When a fiber fails, the stress level increases on the remaining fibers and that can trigger more fiber failures (successive failure). As long as the initial load is low, the successive failures of the fibers remain small, and though the strain (stretch) of the bundle grows with increasing stress (load), the bundle as a whole does not fail. Once the initial load reaches a "critical" value, determined by the fiber strength distribution, the successive failures become global (catastrophic) and the bundle collapses.

We arrange this review article as follows: In the short introduction (**Section 1**), we elaborate the concept of the fiber bundle model and its evolution as a fracture model. **Section 2** deals with the equal-load-sharing FBM where we demonstrate the dynamic behavior of FBM with evolution dynamics and their solutions. Analytic results are compared with numerical simulations in this section. In **Section 3**, we discuss noise-induced failure dynamics in FBM through theory, simulation, and real data analysis. The self-organizing mechanism in FBM is discussed in **Section 4**. We reserve **Section 5** for discussions on some works that would help to understand the cooperative dynamics in FBM. Finally, we have a short Summary and Conclusion section (**Section 6**) at the end.

2 EQUAL LOAD SHARING FBM

We consider an FBM having N parallel fibers placed between two rigid bars. Each fiber follows Hook's law with a force f to the stretch value x as $f = \kappa x$, where κ is the spring constant. To make things simpler, we consider $\kappa = 1$ for all the fibers. Each fiber has a particular strength threshold value and if the stretch x exceeds this threshold, the fiber fails irreversibly. We are interested in the equal-load-sharing (ELS) mode (the bars are rigid), and by construction of the model, the applied load has to be shared equally by the intact fibers.

Other than the analytical treatment of the model, several aspects of the model are also explored numerically. The implementation of the model, particularly in the equal load sharing version we discuss here, is straightforward. The load is initially applied to each fiber equally. The fibers having failure thresholds less than the applied load are irreversibly broken. The load carried by those fibers is redistributed equally among the remaining fibers, which can cause further breaking. The redistribution continues until no new fibers are breaking. The external load is held constant during the whole redistribution process. This is due to the separation of time scales of externally applied loading rate and the internal (elastic) relaxation processes within materials. After the end of each redistribution cycle, the external load is further increased to continue the dynamics. This process continues until the entire system is broken. The critical strength, avalanche statistics, and other critical exponents are calculated from this dynamics, which, as we will see, match well with the analytical results.

2.1 Fiber Strength Distributions

The fiber strength thresholds are drawn from a probability density of $p(x)$. The corresponding cumulative probability is

$$P(x) = \int_0^x p(y)dy. \tag{1}$$

The most used threshold distributions are uniform and Weibull distributions (see **Figure 2**) in the FBM literature.

For a uniform distribution, we can write

$$p(x) = 1; P(x) = x, \tag{2}$$

where, the range of function is between 0 and 1. The cumulative Weibull distribution has the form:

$$P(x) = 1 - \exp\left(-x^k\right), \tag{3}$$

where, k is the shape parameter or the Weibull index. The corresponding probability distribution takes the form:

$$p(x) = kx^{k-1}\exp\left(-x^k\right). \tag{4}$$

The shapes of the uniform and Weibull distributions are shown in **Figure 2**. The range of definition is between 0 and ∞.

2.2 The Critical Values

When we stretch the bundle by applying a force, the fibers fail according to their thresholds, the weakest first, then the next

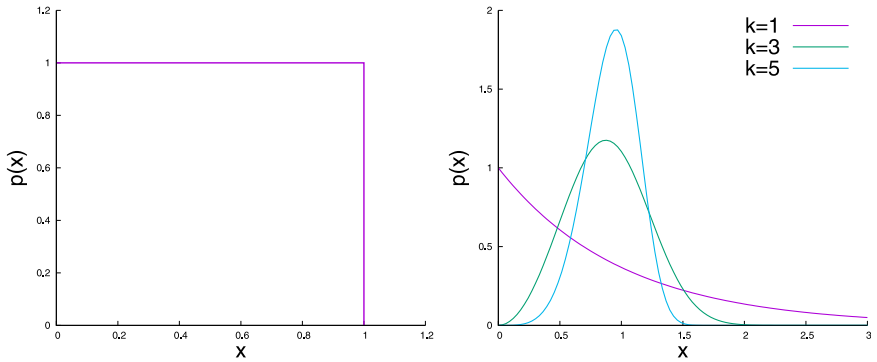

FIGURE 2 | The uniform and Weibull distributions of fiber strengths (thresholds).

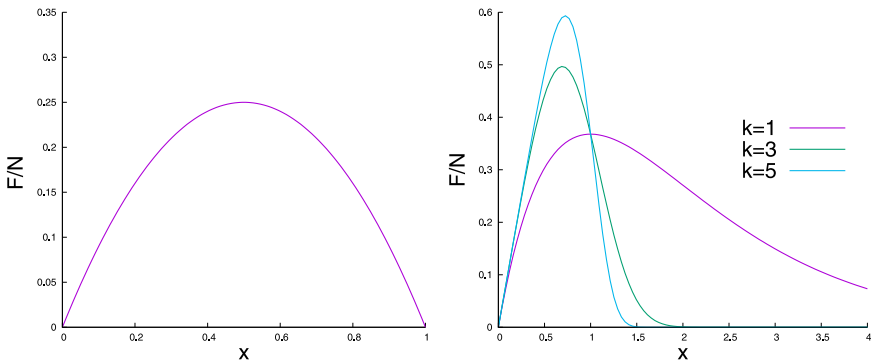

FIGURE 3 | Normalized force (F/N) against extension x for a fiber bundle with uniform ($x_c = 0.5$) and Weibull $x_c = 1, (1/3)^{1/3}, (1/5)^{1/5}$ for $k = 1, 3, 5$, respectively, distributions of strengths (thresholds).

weakest, and so on. If N_f fibers have failed at a stretch value of x, the force on the bundle is

$$F = \left(N - N_f\right)x = N\left(1 - P\left(x\right)\right)x, \tag{5}$$

as $\kappa = 1$. The normalized force (F/N) versus the stretch x curve looks like a parabola (**Figure 3**).

It is obvious that the maximum of the force value is the strength of the bundle, and the corresponding stretch value (x_c) is called the critical stretch beyond which the bundle collapses. Therefore, we can define two distinct phases of the system: stable phase for $0 < x \leq x_c$ and unstable phase for $x > x_c$.

The critical stretch value can be obtained easily by setting $\mathrm{d}F\left(x\right)/\mathrm{d}x = 0$:

$$1 - x_c p\left(x_c\right) - P\left(x_c\right) = 0. \tag{6}$$

1. Uniform threshold distribution

Substituting the $p\left(x_c\right)$ and $P\left(x_c\right)$ values for uniform distribution, we obtain

$$x_c = \left(\frac{1}{2}\right). \tag{7}$$

Now inserting the x_c value in the force expression (**Eq. 5**), we get

$$\frac{F_c}{N} = \frac{1}{4}; \tag{8}$$

which is the critical strength of the bundle (**Figure 3**).

2. Weibull threshold distribution

In the case of Weibull distribution, at the force-maximum, by inserting the $P\left(x\right)$ and $p\left(x\right)$ values into the expression (**Eq. 6**), we obtain

$$\exp\left(-x_c^k\right) - \left(x_c k x_c^{k-1} \exp\left(-x_c^k\right)\right) = 0. \tag{9}$$

One can get the critical stretch value

$$x_c = k^{-1/k}; \tag{10}$$

and the corresponding critical force value

$$\frac{F_c}{N} = k^{-1/k} \exp\left(-\frac{1}{k}\right). \tag{11}$$

For $k = 1$, $x_c = 1.0$ and $(F_c/N) = (1/e)$ (**Figure 3**).

2.3 Different Ways of Loading

Now, we will discuss how the load or stress can be applied on the bundle. In the FBM literature, the most common loading mechanism discussed [26, 27] is the -weakest-link-failure mechanism of loading. This loading process ensures a separation in time scales between external loading and internal stress redistribution. This is equivalent to a quasi-static approach, and noise/fluctuation in the threshold distribution influences the breaking dynamics as well as the avalanche statistics.

A fiber bundle can also be loaded in a different way by applying a fixed amount of load at a time. In that case, all fibers having a failure threshold below the applied load, fail. The stress on the surviving fibers then increases due to load redistribution. The increased stress may drive further failures, and so on. This iterative breaking process continues until an equilibrium is reached where the intact fibers (those who can support the load) is reached. One can also study the failure dynamics of the bundle when the external load on the bundle is then increased infinitesimally, but by a fixed amount (irrespective of the fluctuations in the fiber strength distribution as discussed above). Indeed, as shown recently in Biswas and Chakrabarti [28], the universality class of the dynamics of such fixed loading (even for the same ELS mode of load redistribution after individual fiber failure) will be different from that for the quasi-static (or weakest link failure type) loading discussed above and is given by the Flory statistics [29] for linear polymers, accommodating the Kolmogorov-type dispersion in turbulence [30].

2.4 The Cooperative Dynamics

We are going to discuss the cooperative dynamical behavior of the breaking processes for the bundle loaded by fixed amount per step (following the formulations in the References [1, 2, 4, 8, 26, 27, 31]).

Let us assume that an external force F is applied to the fiber bundle. The stress on the bundle (the external load per fiber) is

$$\sigma = F/N. \tag{12}$$

Let us call N_t to be the number of surviving fibers after t steps in the stress redistribution cycle, with $N_0 = N$.

Now, the effective stress becomes

$$\sigma_t = N\sigma/N_t. \tag{13}$$

Therefore, $NP(N\sigma/N_t)$ of fibers will fail in the first stress redistribution cycle. The number of intact fibers in the next cycle will be

$$N_{t+1} = N - NP(N\sigma/N_t). \tag{14}$$

Using $n_t = N_t/N$, **Eq. (14)** takes the form of a recursion relation,

$$n_{t+1} = 1 - P(\sigma/n_t), \tag{15}$$

with σ as the control parameter and $n_0 = 1$ as the start value.

The character of an iterative dynamics is determined by its *fixed points* (denoted by *) where a dynamical variable remains exactly at the same value it had in the previous step of the dynamics. In other words, a fixed point is a value (of a dynamical variable) that is mapped onto itself by the iteration. The dynamics stops or it becomes locked at the fixed point.

One can find out the possible fixed points $n^\star$ of **(15)**, which satisfy

$$n^* = 1 - P(\sigma/n^*), \tag{16}$$

and the solutions of the breaking dynamics at the fixed point.

2.5 The Critical Exponents

If we consider that the fiber strengths follow uniform distribution, the recursion relation can be written as

$$n_{t+1} = 1 - \sigma/n_t, \tag{17}$$

Consequently, at the fixed point, the relation assumes a simple form

$$(n^*)^2 - n^* + \sigma = 0, \tag{18}$$

with solution

$$n^\star = \frac{1}{2} \pm (\sigma_c - \sigma)^{1/2.} \tag{19}$$

Here the critical stress value is $\sigma_c = (1/4)$, beyond which the bundle collapses completely. In **Eq. 19**, the upper sign gives $n^* > n_c$, which corresponds to a stable fixed point. From this solution, it is easy to derive the order parameter, susceptibility, and relaxation time (all defined below).

The fixed-point solution gives the critical value $(\sigma = \sigma_c)$.

$$n_c^* = \frac{1}{2}. \tag{20}$$

Therefore, the fixed-point solution can be presented as

$$n^*(\sigma) - n_c^* \propto (\sigma_c - \sigma)^\beta, \quad \beta = \frac{1}{2}. \tag{21}$$

Clearly, $n^\star(\sigma) - \mathrm{n}_\mathrm{c}^*$ can be considered like an order parameter, which shows a clear transition from nonzero to zero value at σ_c.

The susceptibility is defined as $\chi = -dn^*/\mathrm{d}\sigma$ and the fixed-point solution gives

$$\chi \propto (\sigma_c - \sigma)^{-\gamma}, \quad \gamma = \frac{1}{2}; \tag{22}$$

which follows a power law and diverges at the critical point σ_c.

The dynamical approach very near a fixed point is very interesting, and this can be investigated by expanding the differences $n_t - n^\star$ around the fixed point. In the case of uniform distribution, the recursion relation (**Eq. 17**), gives

$$n_{t+1} - n^* = \frac{\sigma}{n^*} - \frac{\sigma}{n_t} = \frac{\sigma}{n_t n^*}(n_t - n^*) \simeq \frac{\sigma}{n^{*2}}(n_t - n^*). \tag{23}$$

Clearly, the fixed point is approached with exponentially decreasing steps:

$$n_t - n^\star \propto \mathrm{e}^{-t/\tau,} \tag{24}$$

where τ is a relaxation parameter, dependent on stress value:

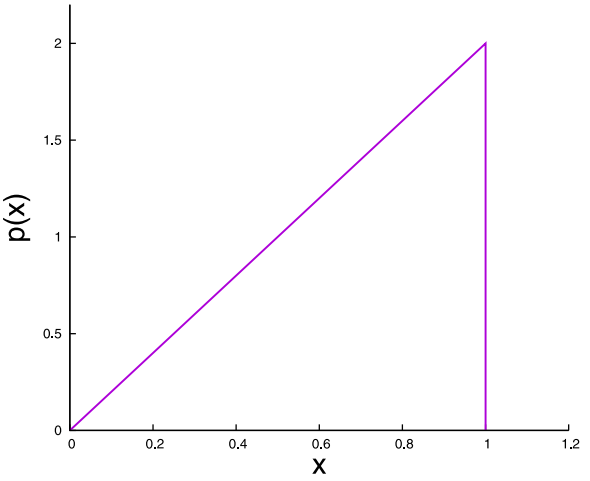

FIGURE 4 | The linearly increasing fiber strength distribution.

$$\tau = 1\Big/\ln\left(n^{*2}/\sigma\right) = 1\Big/\ln\left[\left(\frac{1}{2}+\sqrt{\frac{1}{4}-\sigma}\right)^2\Big/\sigma\right]. \tag{25}$$

At the critical stress, $\sigma = \sigma_c = 1/4$, the argument of the logarithm is 1 and apparently τ is infinite. As the critical stress is approached for $\sigma \to \sigma_c$.

$$\tau \simeq \frac{1}{4}(\sigma_c - \sigma)^{-\theta} \quad \text{with } \theta = \frac{1}{2}. \tag{26}$$

This divergence clearly shows the character of the breaking dynamics, that is, it becomes very slow at the critical point.

2.6 Universal Behavior

The recursion relation and the fixed point solutions demonstrated the dynamic critical behavior for the uniform distribution of the breaking thresholds. Now the question arises—how general the results are? The universality of the cooperative breaking dynamics can be verified by considering a different distribution of fiber strengths. We are now going to examine the situation for a linearly increasing distribution (**Figure 4**) within the interval $(0, 1)$,

$$p(x) = \begin{cases} 2x, & 0 \le x \le 1, \\ 0, & x > 1. \end{cases} \tag{27}$$

From the force–stretch relationship, the average force per fiber is

$$F(x)\Big/N = \begin{cases} x\left(1-x^2\right), & 0 \le x \le 1, \\ 0, & x > 1. \end{cases} \tag{28}$$

Therefore, the critical point is

$$\sigma_c = \frac{2}{3\sqrt{3}}. \tag{29}$$

In this case, the breaking dynamics can be written as a recursion relation:

$$n_{t+1} = 1 - (\sigma/n_t)^2, \tag{30}$$

and the fixed-point equation is

$$(n^*)^3 - (n^*)^2 + \sigma^2 = 0, \tag{31}$$

that is, a cubic equation in n^*. Clearly, there are three solutions of n^* for a value of σ. At the critical stress value, $\sigma_c = 2/3\sqrt{3}$, the only acceptable solution of **Eq. 31** is

$$n_c^* = \frac{2}{3}. \tag{32}$$

We want to investigate the breaking dynamics in the neighborhood of the critical point. Therefore, we insert $n = 2/3 + (n - n_c)$ into (**Eq. 30**), with the result

$$\frac{4}{27} - (n-n_c)^2 - (n-n_c)^3 = \sigma^2 = \left(\frac{2}{3\sqrt{3}} + \sigma - \sigma_c\right)^2 = \frac{4}{27} + \frac{4}{3\sqrt{3}}(\sigma - \sigma_c) + (\sigma - \sigma_c)^2. \tag{33}$$

We get (to leading order)

$$(n - n_c)^2 = \frac{4}{3\sqrt{3}}(\sigma_c - \sigma). \tag{34}$$

Obviously, for $\sigma \le \sigma_c$ the order parameter behaves as

$$n(\sigma) - n_c \propto (\sigma_c - \sigma)^{\beta}, \quad \beta = \frac{1}{2}, \tag{35}$$

in accordance with (**Eq. 21**). The susceptibility $\chi = -dn/\mathrm{d}\sigma$ gives

$$\chi \propto (\sigma_c - \sigma)^{-\gamma}, \quad \gamma = \frac{1}{2}. \tag{36}$$

We can also discuss how the stable fixed point is approached from below. From **Eq. 30**, one can write, around the fixed point,

$$n_{t+1} - n^* = \frac{\sigma^2}{n^{*2}} - \frac{\sigma^2}{n_t^2} = \frac{\sigma^2}{n^{*2} n_t^2}\left(n_t^2 - n^{*2}\right) \simeq (n_t - n^*)\frac{2\sigma^2}{n^{*3}}. \tag{37}$$

The approach is clearly exponential,

$$n_t - n^* \propto e^{-t/\tau} \quad \text{with } \tau = \frac{1}{\ln\left(n^{*3}/2\sigma^2\right)}. \tag{38}$$

The argument of the logarithm becomes 1 exactly at the critical point; therefore, τ diverges when the critical state is approached. The nature of such divergence assumes the same form,

$$\tau \propto (\sigma_c - \sigma)^{-\theta}, \quad \theta = \frac{1}{2}, \tag{39}$$

which is similar to the model with a uniform fiber strength distribution, **Eq. 26**.

We can now conclude that the ELS FBM with a linearly increasing fiber strength distribution possesses the same critical power laws as the ELS FBM with a uniform fiber strength distribution. This confirms that the critical properties

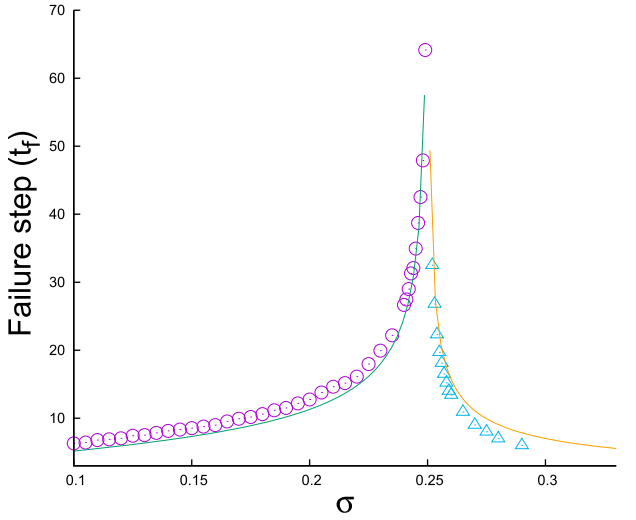

FIGURE 5 | Postcritical and precritical relaxation: Numerical data are for a bundle with $N = 10^6$ fibers having uniform threshold distribution and averages are taken over 10^5 samples. Lines are showing theoretical estimates.

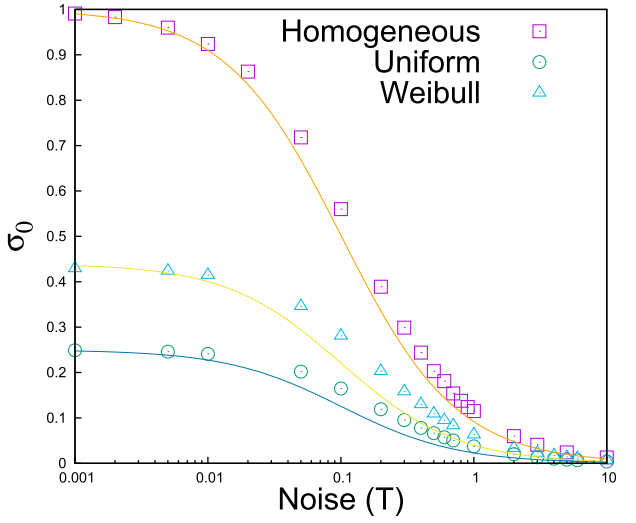

FIGURE 6 | Phase boundary (σ_0 vs. T plot) for three different types of fiber strength distributions with $N = 20000$. Data points are simulation results and solid lines are analytic estimates (**Eq. 50**) based on mean-field arguments.

of cooperative breaking dynamics are universal. A general treatment for verifying universality in ELS FBM can be found in Reference [26].

2.7 Two-Sided Critical Divergence

When a fixed amount of load is applied on the system, the iterative breaking process ends with one of the two possible end results. Either the whole bundle collapses, or an equilibrium situation is reached where intact fibers can hold/support the applied load/stress. Thus, the final fate of the bundle depends on whether the external stress σ on the bundle is postcritical ($\sigma > \sigma_c$), precritical ($\sigma < \sigma_c$), or critical ($\sigma = \sigma_c$). It is interesting to know how the breaking dynamics is approaching the critical point (failure point) from below (precritical) and above (postcritical) stress values.

In the case of uniform fiber strength distribution when the external stress approaches the critical value of $\sigma_c = 1/4$ from a higher value, that is, in the postcritical region, the number of necessary iterations needed for the whole system to break increases as the critical point is approached. Close to the critical point, the number of iterations shows a square root divergence [8]:

$$t_f \simeq \frac{1}{2}\pi(\sigma - \sigma_c)^{-1/2}. \tag{40}$$

Similarly, in the precritical region, when the external stress approaches the critical value of $\sigma_c = 1/4$ from below, the number of iterations has again a square root divergence [8] (for uniform distribution) close to the critical point:

$$t_f = \frac{1}{4}\ln(N)(\sigma_c - \sigma)^{-1/2}. \tag{41}$$

The only difference is that, in precritical case, the amplitude of the square root divergence has a system-size-dependence, which is absent in the postcritical case.

We can conclude that in ELS FBM, the breaking dynamics shows a two-sided critical divergence in terms of the number of iteration steps needed to reach critical points from below (precritical) and above (postcritical) (**Figure 5**). The theoretical details of the exact solutions can be found in References [8, 26].

2.8 Avalanche Dynamics With Fixed Amount Loading

The number of fibers (S) breaking between two successive stable conditions of the fiber bundle is called an avalanche. The distribution of the avalanche sizes $P(S)$ shows a power-law tail for the large S limit [6], which is a sign of the criticality discussed above. This is experimentally widely observed for driven disordered systems in general [31] and for quasi-brittle/ductile fracture in particular. While the details of the avalanche dynamics seen in the fiber bundle model with quasi-static load increase has been discussed elsewhere in this special issue [32], here we briefly describe the avalanche dynamics for fixed amount load increase, that is, when the system is in a stable condition, a fixed amount of load δ is added, which restarts the dynamics. As before, the number of fibers breaking until the system reaches the next stable state constitutes an avalanche. Clearly, this type of avalanche is a result of the cooperative breaking dynamics, and it is not arising due to any fluctuations in stress levels or in fiber strength distribution. We will describe below how to calculate theoretically the distribution of such avalanches.

The load curve, in terms of the threshold values, can be written as

$$F(x) = Nx(1 - x). \tag{42}$$

For the uniform threshold distribution in $(0, 1)$ (see **Eq. 5**). The load increases between 0 and $N/4$ with an increment of δ. Therefore, the values of the load are $m\delta$, with

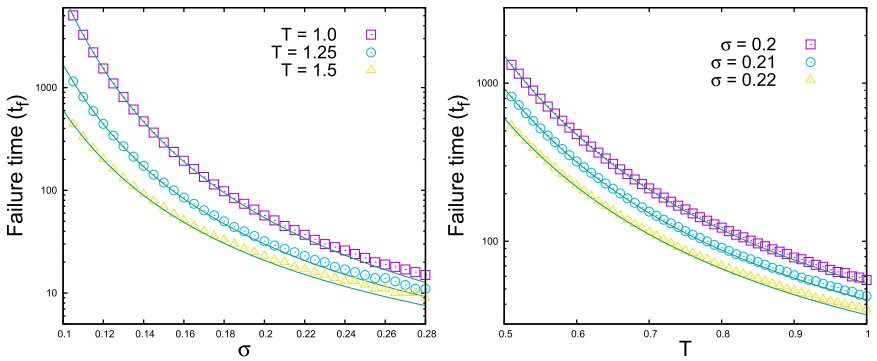

FIGURE 7 | Failure time versus σ (left) and versus T (right) for a homogeneous bundle having identical fibers with a strength of 1 (σ_c = 1 as well). The data are for simulations over a single realization with a system size of N = 1000000, and the solid lines are the theoretical estimates following (**Eq. 55**).

$m = 0, 1, 2, \ldots, N/4\delta$. The threshold value for load $m\delta$ can be obtained from (**Eq. 4**) as

$$x_m = \frac{1}{2}\left(1 - \sqrt{1 - 4m\delta/N}\right). \tag{43}$$

The average number of fibers broken due to the increase of load from $m\delta$ to $(m+1)\delta$ is

$$S = N\frac{\mathrm{d}x_m}{\mathrm{d}m} = \frac{\delta}{\sqrt{1 - 4m\delta/N}}. \tag{44}$$

The number of avalanches of size between S and $S + \mathrm{d}S$ is obtained from the corresponding interval of the variable m, that is, $P(S)\mathrm{d}S = \mathrm{d}m$. From the equation above, we have

$$\frac{\mathrm{d}S}{\mathrm{d}m} = \frac{2S^3}{(N\delta)}. \tag{45}$$

Therefore, the avalanche size distribution is given by

$$P(S) = \frac{dm}{dS} = \frac{1}{2}N\delta S^{-3}, \quad \text{for} \quad S \geq \delta. \tag{46}$$

Indeed, it is possible to show [26] that for an arbitrary threshold distribution, $p(x)$, the large S asymptotic limits of the avalanche size distribution is

$$P(S) \sim CS^{-3}, \tag{47}$$

with $C = (N\delta p(x_c)^2/2p(x) + x_c p'(x_c))$, with the mild assumption that the load curve has a generic parabolic form with a critical point.

3 NOISE-INDUCED FAILURE IN FBM

So far we have discussed the classical stress-induced failure of fibers without the presence of noise. A noise-induced failure scheme for the fiber bundle model can be formulated [13, 14, 33] for which the cooperative failure dynamics can be solved analytically.

As in the previous sections, we consider a bundle of N parallel fibers clamped between two rigid bars. A load or force $(F = \sigma N)$ is applied on the bundle. The fibers have different strength thresholds (x), and there is a critical strength σ_c [1] for the whole bundle, so that the bundle does not fail completely for stress $\sigma \leq \sigma_c$, but it fails immediately for $\sigma > \sigma_c$. Now we introduce noise (T) in the system and assume that each fiber having the strength of x_i has a finite probability $P_f(\sigma, T)$ of failure at any stress σ induced by a noise T:

$$P_f(\sigma, T) = \begin{cases} C\exp\left[-\frac{1}{T}\left(\frac{x_i}{\sigma} - 1\right)\right], & 0 \leq \sigma \leq x_i, \\ 1, & \sigma > x_i. \end{cases} \tag{48}$$

Here C is a prefactor. $P_f(\sigma, T)$ increases as T increases and for a fixed value of T and σ_c, as we increase σ, the bundle breaks more rapidly. The motivation behind (**Eq. 48**) comes from the time-dependent behavior or the so-called creep behavior of materials, observed in real systems [10, 26]. It is obvious that the strength of elements/fibers degrades in time due to external influences like moisture, temperature, etc.

Such a noise-induced failure scheme will produce two different failure regimes depending on the stress and noise levels—continuous breaking regime and intermittent breaking regime. In the continuous breaking regime, we can calculate the failure time (step) as a function of stress and noise values. However, in the intermittent breaking regime, one can define the waiting time between two consecutive failure phases.

The phase boundary can be determined through a mean-field argument that at $\sigma = \sigma_0$, at least one fiber must break to trigger the continuous fracturing process. After this single failure, the applied load has to be redistributed on the intact fibers (due to ELS) and the effective stress will surely increase (more than σ_0), which in turn enhances failure probability for all the intact fibers. Following this logic, in the case of a homogeneous bundle where all the fibers have identical strength, $x_i = 1$ (and $\sigma_c = 1$), at the phase boundary $NP_f(\sigma_0, T) \geq 1$ giving

$$N\exp\left[-\frac{1}{T}\left(\frac{1}{\sigma_0} - 1\right)\right] \geq 1. \tag{49}$$

which finally gives

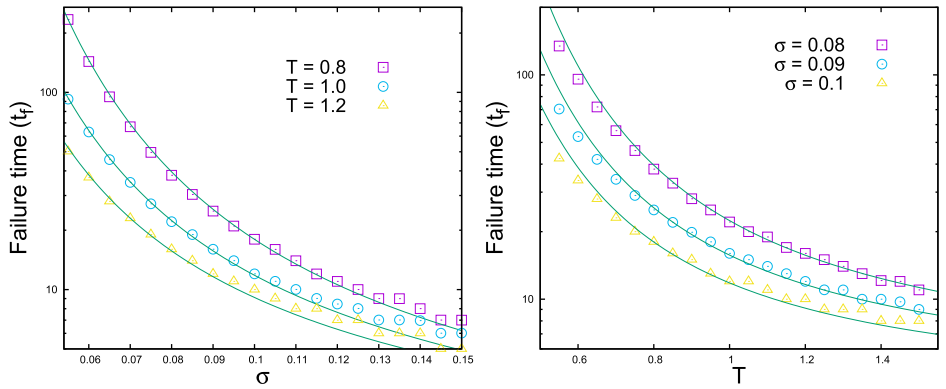

FIGURE 8 | Failure time versus σ (left) and versus T (right) for bundles having uniform strength distributions. The data are for simulations over 1000 realizations with a system size of $N = 10^6$, and the solid lines are the theoretical estimates following (**Eq. 56**).

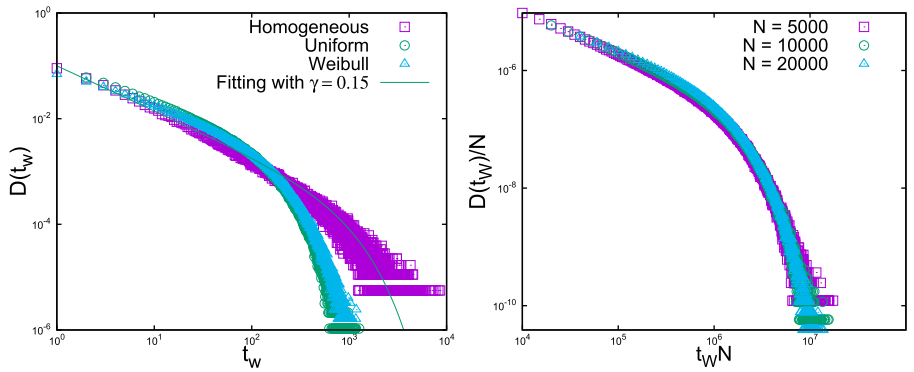

FIGURE 9 | Left: The simulation results for the waiting time distributions for three different types of fiber strength distributions, with $N = 20000$. All the curves can be fitted with the Gamma form $\exp(-t_W/a)/t_W^{1-\gamma}$, where $\gamma = 0.15$ is for the homogeneous case and $\gamma = 0.26$ is for uniform and Weibull distributions. **Right:** we show the data collapse of the waiting time distributions with system sizes for uniform fiber strength distribution.

$$\sigma_0 \geq \frac{1}{1 - T\log(1/N)}. \tag{50}$$

In absence of noise, when $T = 0$, the above equation gives $\sigma_0 = 1 = \sigma_c$, which is consistent with the static FBM results [1]. This analytic estimate overlaps with the data obtained from simulation (**Figure 6**). It shows that the continuous and intermittent fracturing regimes are separated by a well-defined phase boundary, which depends on both the stress level and the noise level [33].

In the case of heterogeneous FBMs where fibers have different strength thresholds, keeping in mind that in absence of noise T, we should always get $\sigma_0 = \sigma_c$, one can make a conjecture that

$$\sigma_0 \geq \frac{\sigma_c}{1 - T\log(1/N)}. \tag{51}$$

The numerical data for the heterogeneous cases (**Figure 6**) having uniform and Weibull-type fiber strength distributions supports the conjecture well [33].

Identification of such a phase boundary has important consequences in material-fracturing and in other similar fracture-breakdown phenomena. During material/rock fracturing, acoustic emission (AE) measurements can record the burst or avalanche events in terms of AE amplitude and AE energy [34]. Therefore, AE data could reveal the correct rupture-phase of a material body under stress. Once a system enters into continuous rupture phase, the system collapse must be imminent. Thus, identification of the rupture phase can guide us to visualize the final fate of a system. It can also help to stop system collapse, if it is possible to withdraw external stress in time before the system enters into continuous rupture phase.

We will now discuss cooperative dynamics in both these regimes in the following sub-sections.

3.1 Continuous Breaking Regime

In the continuous breaking regime, one can describe the breaking dynamics in an FBM through a recursion relation [14]. Let us consider a homogeneous bundle having N fibers with exactly the

same strength thresholds of 1; therefore, critical (or failure) strength of the bundle is $\sigma_c = 1$. Now, we consider a noise-induced failure probability for breaking of each fiber in the continuous regime:

$$P_f(\sigma, T) = \begin{cases} \frac{\sigma}{\sigma_c}\exp\left[-\frac{1}{T}\left(\frac{x_i}{\sigma}-1\right)\right], & 0 \le \sigma \le x_i, \\ 1, & \sigma > x_i. \end{cases} \quad (52)$$

As all the fibers are identical, $x_i = 1 = \sigma_c$. The prefactor is a function of stress level σ, and this is a careful choice to get a solution of the recursive dynamics, which we will describe below.

We denote the fraction of total fibers that remain intact at time (step) t by n_t and the breaking dynamics can be written as

$$n_{t+1} = n_t\left[1 - P_f\left(\frac{\sigma}{n_t}, T\right)\right]. \quad (53)$$

In the continuum limit, the above recursion relation can be presented in a differential form

$$-\frac{dn}{dt} = \frac{\sigma}{\sigma_c}\exp\left[-\frac{1}{T}\left(\frac{\sigma_c}{\sigma}n - 1\right)\right]. \quad (54)$$

Giving the failure time

$$t_f = T\exp\left(-\frac{1}{T}\right)\left[\exp\left(\frac{\sigma_c}{\sigma T}\right) - 1\right]. \quad (55)$$

The simulation result shows (**Figure 7**) the exact agreement with this theoretical estimate.

In the case of heterogeneous bundles where fibers have distributed strengths, the failure times seem to follow another form [14]:

$$t_f = T\exp\left(-\frac{1}{T}\right)\left[\exp\left(\frac{\sigma_c}{\sigma T} + \frac{1}{T}\right) - 1\right]. \quad (56)$$

This form was obtained through a trial and error approach. It is extremely difficult (as of now) to write the recursion relation for noise-induced failure dynamics in the case of heterogeneous systems. The simulation results have been compared with the formula above, and the agreement (**Figure 8**) is quite satisfactory [14].

3.2 Intermittent Regime

As we discussed before, in the intermittent fracturing phase, simultaneous breaking events (avalanches) are separated by waiting times (t_W) of different magnitudes. The waiting time distribution can be fitted with a Gamma distribution [33] for both homogeneous and heterogeneous bundles

$$D(t_W) \propto \exp(-t_W/a)/t_W^{1-\gamma} \quad (57)$$

where $\gamma = 0.15$ for homogeneous case and $\gamma = 0.26$ for heterogeneous cases (**Figure 9**). Here a is a measure of the extent of the power law regime, and it seems that the power law exponent does not change with the variation of σ, T, and N [33].

In the waiting time distributions, the power law part dominates for small t_W values and exponential law dominates for bigger t_W values. The inherent global load sharing nature is responsible for the power law part of the Gamma distribution, as power law usually comes from a long range cooperative mechanism [6, 35, 36]. The exponential part of the Gamma distribution is contributed by the noise-induced failure factor $P_f(\sigma, T)$. For large t_W values, one can eventually treat the failures to be independent. If P indicates the noise-induced failure probability within t_W, then the probability $D(t_W) = A(1-P)^{t_W N} \sim \exp(-P t_W N)$, where A is a constant. The normalization of $D(t_W)$ requires $A \sim N$. Though for smaller values of t_W, one cannot ignore the correlations between successive failures (responsible for the power law part in $D(t_W)$), the exponential scaling behavior for $D(t_W)$ can be easily obtained from the above. As shown in the inset of **Figure 9**, the plot of $D(t_W)/N$ against $t_W N$ gives good data collapse for different N values. Such a data collapse indicates the robustness of the Gamma function form. It is not clear yet whether the Gamma-type distribution is a direct consequence of the failure probability function (**Eq. 48**). It needs more investigations with various other types of possibilities for **Eq. 48**.

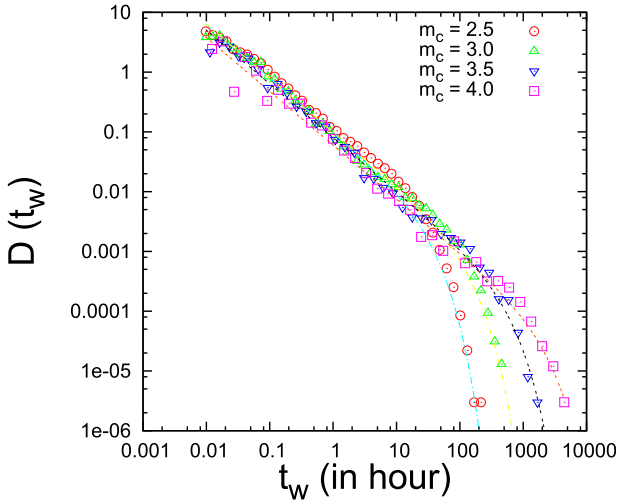

FIGURE 10 | Gamma-fitting (dotted lines) to the waiting time distributions in California catalog (1984–2002).

Apparently, the modeling scheme for noise-induced rupture process is not limited to any particular system, rather it is a general approach and perhaps it can model more complex situations like rupture-driven earthquakes. In literature, we can find evidences of stress-localization around fracture/fault lines in an active seismic-zone. Also, there are several factors that can help rupture evolution, like friction, plasticity, fluid migration, spatial heterogeneities, chemical reactions, etc. To some extent, such stress redistribution/localization can be taken into account through a proper load sharing scheme and a noise term (T) can in principle represent the combined effect of all other factors.

To compare the waiting time results of the model system with real data, the California earthquake catalog from 1984 to 2002 [37] has been analyzed [33] to study the statistics of waiting times

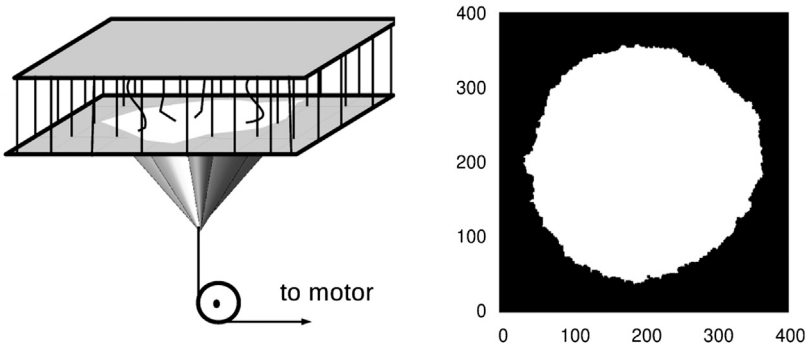

FIGURE 11 | A schematic representation of locally loaded fiber bundle model and the resulting interface propagation. From [44].

[38–40] between earthquake events. First, a cutoff (m_c) has been set in the earthquake magnitude, so that all earthquake events above this cutoff magnitude will be considered for the analysis. The distribution of waiting times shows similar variation for different cutoff values. It seems [33] waiting time distributions for all the data sets follow a Gamma distribution [38]:

$$D(t_W) \propto \exp(-t_W/a) \Big/ t_W^{(1-\gamma)}; \tag{58}$$

with same γ ($\simeq$ 0.1) and different a values for different cutoff levels: a = 30, 120, 500, 2000, respectively, for m_c = 2.5, 3.0, 3.5, 4.0 (see **Figure 10**).

The similarities in waiting time statistics and scaling forms suggest that slowly driven (noise-induced) fracturing process and earthquake dynamics (stick-slip mechanism) perhaps have some common origin.

4 INTERFACE PROPAGATION IN THE FIBER BUNDLES: SELF-ORGANIZATION AND DEPINNING TRANSITION

So far we have considered FBM versions that are globally loaded, that is, all the fibers in the system are loaded equally from the initial time, and the load remains equal on each surviving fiber, given that the load sharing is equal. This necessarily implies that the damage or failures in the system could occur at any point; indeed, there is no notion of distance in this form of the model.

However, in fracture dynamics, particularly in the mode-1 variant of it, a front could propagate in the direction transverse to that of the loading. A fracture front necessarily implies damage localization within a region with a lower dimension than that of the system, that is, a front-line in two dimensions or a front surface in a three-dimensional system. Indeed, front propagation driven through a disordered medium is not limited to fracture; it also happens in the vortex lines in superconductors [41], magnetic domain walls in magnetic materials with impurities [42], contact line dynamics in wetting [43], and so on.

In the context of FBM, it is possible to capture the dynamics of a front propagating through a disordered medium by considering a localized loading of the system (when the fibers are arranged in a square lattice and the load is applied at an arbitrarily chosen central site; see **Figure 11**) in dimension higher than one (in one dimension, the damage interface is a point and hence cannot increase). The external load is increased at a low and constant rate (maintaining the separation of time scales between applied loading rate and redistribution process) [44]. Initially, the system is not loaded anywhere except for the one fiber at an arbitrarily chosen central site. As the external load increased beyond the failure threshold of the said central fiber, it breaks and the load carried by that fiber is redistributed among the fibers that are in the damage boundary (in the beginning just the four nearest neighbors). Therefore, the fibers that are newly exposed to the load after an avalanche carry a lower load compared to those accumulating loads from the earlier avalanches. This process keeps a compact structure of the cluster of the broken fibers. The localized nature of the load redistribution is justified from the fact that the newly exposed fibers are further away from the point of loading and therefore carry a smaller fraction of the load at the original central site.

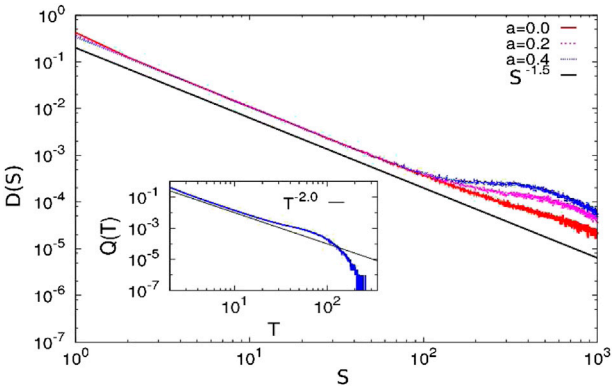

FIGURE 12 | The avalanche size distributions are plotted for zero and finite lower cutoffs for Model II. The distribution function is a power law with an exponent value of 1.50 ± 0.01, which is also our estimate from scaling arguments. Inset: The distribution of avalanche duration is plotted for Model II. This also shows a power law decay with an exponent value of 2.00 ± 0.01. From [44].

As the damage perimeter increases, so does the number of fibers on that perimeter. This implies that for an avalanche, the load per fiber will decrease along the damage boundary. But due to a further increase in the load, this value will subsequently increase, initiating another avalanche. In the steady state, the load per fiber value will fluctuate around a constant and the system is said to have reached a self-organized state. In this state, the failure of fibers in the process of avalanches has a scale-free size distribution, which suggests that it is a self-organized critical (SOC) state (where external drive and dissipation balance and the critical point becomes an attractive fixed point [31]).

The steady-state value of the load per fiber and the corresponding avalanche size distribution can be calculated for a variant of this model where the load redistribution is uniform along the entire damage boundary, that is, every fiber along the damage boundary gets the same fraction of load in a redistribution process. We discuss this for the Weibull distribution below, but this is true for other distributions as well.

The Weibull distribution in its general form can be written as

$$W_{\alpha,\beta}(x) = \alpha\beta x^{\alpha-1} e^{-\beta x^{\alpha}}, \tag{59}$$

where α and β are the two parameters. We can consider the particular case when $\alpha = 2$ and $\beta = 1$. The failure threshold of a fiber is greater than x with a probability that is proportional to $\int_x^{\infty} x_l e^{-x_l^2} \mathrm{d}x_l \sim e^{-x^2}$. Given that the probability density function for force is uniform, the probability of a fiber having a load between x and $x + \mathrm{d}x$ is $e^{-x^2} P(x)\mathrm{d}x$, with $P(x) = c$ (unnormalized). The normalization gives $c\int_0^{\infty} e^{-x^2}\mathrm{d}x = 1$, implying $c = 2/\sqrt{\pi}$. Hence, the normalized probability density function for the load on the surviving fibers is

$$D_{\sigma}(x) = \frac{2}{\sqrt{\pi}} e^{-x^2}. \tag{60}$$

Similarly, the probability that the load is lower than x is proportional to x. Using the form for threshold distribution ($\sim xe^{-x^2}$), the probability density function for the threshold distribution of the survived fibers becomes

$$D_{th}(x) = \frac{4}{\sqrt{\pi}} x^2 e^{-x^2}. \tag{61}$$

Both of these functions are in good agreement with numerical simulations. Also, the saturation value of the average load per fiber can be calculated as

$$\int_0^{\infty} x D_{\sigma}(x)\mathrm{d}x = \frac{2}{\sqrt{\pi}} \int_0^{\infty} x e^{-x^2}\mathrm{d}x = \frac{1}{\sqrt{\pi}}, \tag{62}$$

which is again in good agreement with simulations.

The size distribution of avalanches is a power law with the exponent value close to 3/2 (see **Figure 12**), which is in agreement with the scaling prediction of avalanche size distributions in SOC models for the mean field. The distribution of the avalanche duration, that is, the number of redistribution steps for an avalanche, is a power law with an exponent value close to 2.00 ± 0.01, which is again in agreement with the scaling predictions of the SOC models in mean field.

For estimating the avalanche size exponent, it can be assumed that the average load per fiber on the damage boundary has a distribution, which is Gaussian around its mean: $P(\sigma) \sim e^{-(\sigma-\sigma_c)^2/\delta\sigma}$. Hence, from a dimensional analysis, mean-squared fluctuation is $\delta\sigma \sim (\sigma - \sigma_c)^2$. Also, the avalanche size S scales as $(\delta\sigma)^{-1}$, as it may be viewed as the number of broken fibers after a load increase of $\delta\sigma$. This gives

$$(\sigma - \sigma_c) \sim S^{-1/2.} \tag{63}$$

The probability of an avalanche being of the size between S and $S + \mathrm{d}S$ is $D(S)\mathrm{d}S$. Now, the deviation from the critical point scales [1] with the cumulative size of all avalanches up to that point; giving $(\sigma - \sigma_c) \sim \int_S^{\infty} D(S)\mathrm{d}S$. If we take $D(S) \sim S^{-\gamma}$, then

$$(\sigma - \sigma_c) \sim S^{1-\gamma}. \tag{64}$$

By comparing **Eqs. 63** and **64**, we have $\gamma = 3/2$. So, the probability density function for the avalanche size becomes $D(S) \sim S^{-3/2}$, which fits well with simulation results (**Figure 12**).

5 SOME RELATED WORKS ON THE DYNAMICS OF FBM

In this section, we would like to bring attention to some related works on the dynamics of FBM which, we believe, may be regarded as essential reading in this field.

As we have discussed in detail in the earlier sections, there has been considerable progress in characterizing the failure dynamics in the fiber bundle model through tools describing critical phenomena. One crucial step toward that direction is to identify the universality class of the model. That often needs a coarse grained description of the model, writing down the free energy form suited for the dynamics and then identifying the symmetries and consequently the universality class. One such step was done in Ref. [45] by writing down a mesoscopic description of the ELS-FBM. By specifically, writing the time evolution of the order parameter $n(\sigma) - n_c = \eta$ and the driving field (stress increase) as $J = \sigma_c - \sigma$, the dynamics is described by

$$\frac{\partial \eta}{\partial t} = -\eta^2 + J. \tag{65}$$

Writing in terms of the density of intact fibers n,

$$\frac{\partial n}{\partial t} = \lambda n(1 - n) - \sigma, \tag{66}$$

with $\lambda = 1$. This equation has a particle-hole symmetry for zero external field $\sigma = 0$; hence, it is generally expected to be in the CDP or compact domain growth universality class of non-equilibrium phase transition [46]. Although done for the ELS version, this approach of relating fiber bundle model dynamics to nonequilibrium critical phenomena through a Langevin equation could provide useful insights into more realistic versions.

Among other attempts to relate fracture and in particular FBM dynamics with different universality classes, a relatively less explored route is that of the hydrodynamics of turbulence. The analogy between the velocity fluctuation in turbulence

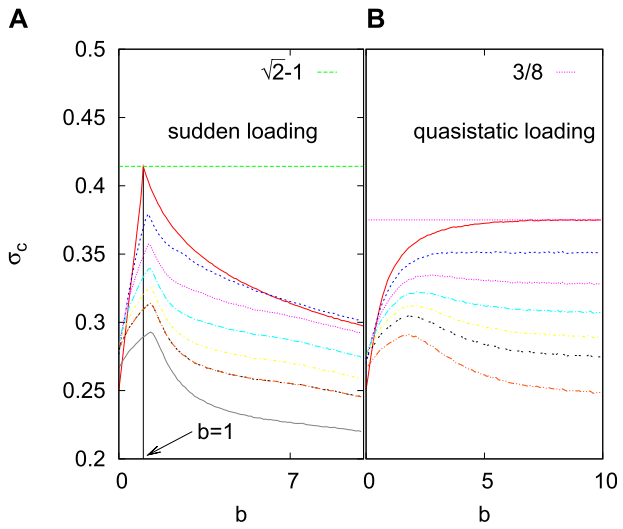

FIGURE 13 | The phase diagram in the $b - \sigma_c$ plane (b represents the anisotropy in the load redistribution process) is shown for (a) discrete step and (b) quasi-static loading for various fractional errors in the knowledge of the threshold values of the individual fibers (curves from top to below are for $e = 0.0, 0.1, 0.2, 0.3, 0.4, 0.5, 0.75$). The upper bounds for both cases are shown, which are reached for $b = 1$ (a) and $b \to \infty$ (b). From [51].

and surface roughness due to fracture have been explored before [47]. However, given that FBM is able to provide a reasonably consistent picture for fracture dynamics, its association with hydrodynamics of fracture is a crucial question. In Ref. [28], the relation between the Kolmogorov energy dispersion in turbulence and avalanche dynamics in the FBM was explored. Specifically, the vortex lines in a fully developed turbulence can be mapped to self-avoiding walk (SAW) picture of polymers [48]. Then, following Flory's theory [29], the Kolmogorov energy dispersion becomes

$$E_q \sim q^{-1/\nu_F}, \tag{67}$$

where q is the wave number, ν_F is the Flory exponent, and d is the spatial dimension. Then, drawing the parallel with the energy dispersion in avalanche dynamics in the FBM (see **Eq. 47**), we get $E_q \sim q^{-d/3}$ for the mean field case (i.e., $d = d_u$, the upper critical dimension). By taking $d_u = 6$, which is consistent for the FBM [49], we get back the Flory mean field result $E_q \sim q^{-2}$. In parallel, by taking the correlation length as inverse of the wave number q, and using finite size-scaling arguments, one can show that $\nu d = 2/3$ in the mean field limit, where ν is the correlation length exponent. Again using $d = 6$ as the upper critical dimension, one gets $\nu = 1/4$.

It may be noted that there is also a gratifying consistency in the main results discussed above. In the ELS FBM, the critical exponents β, γ and ν for the order parameter, breakdown susceptibility and correlation length respectively satisfy the Rushbrooke scaling relation (incorporating the hyperscaling relation) [50] : $2\beta + \gamma = d\nu$, with $\beta = 1/2 = \gamma$ along with the value of the upper critical dimension $d = 6$ and $\nu = 1/4$.

Given that the fiber bundle is essentially an ensemble of discrete elements having finite failure thresholds, under the condition of conserved load, it can serve as a generic model for intermittent progress toward catastrophic failure in a wide variety of systems. Such systems can be roads carrying traffic, power grids, or redundant computer circuitry. In several of such cases, the load redistribution following the failure of an individual element (say, traffic jam along one road, failure of one power station, etc.) is controllable to some extent–a freedom lacking in the case of stressed disordered solids. Under such circumstances, it is useful to ask the question as to how the total load-carrying capacity of the system could be maximized by a suitable load redistribution rule [51].

It is rather straightforward to establish that the maximum limit of σ_c would be achieved when the maximum number of fibers carry loads to their fullest capacity. For a uniform distribution of the failure thresholds in (0, 1), it is possible to show that for loading in a discrete step the limiting value for the critical load is $\sqrt{2} - 1$ and for quasi-static loading, it is 3/8. The remaining question, therefore, is to find the rule of load transfer following a local failure that can achieve the global failure threshold in the closest proximity to the abovementioned limits.

Intuitively, it is clear that a higher share of load should be transferred to the fibers with higher capacity. Generally, it is useful to assume that the transfer rule would be of the form $A\,(f_i - \sigma_i)^b$, where f_i and σ_i are, respectively, the failure threshold and load of the i-th element; A is an appropriate constant to ensure load conservation and b is a parameter.

The dynamics, as discussed before, depends on whether the load is applied in a discrete step or gradually. The maximization of the strength of the system would also, therefore, depend on the loading protocol. The only parameter to tune here is b. It is possible to calculate analytically that the maximum strength is indeed achieved with this redistribution rule for $b = 1$ for the

discrete step loading and $b \to \infty$ (practically achieved for $b \approx 10$) for quasi-static loading (see **Figure 13**).

An important information in implementing the redistribution rule is the exact knowledge of the failure thresholds of all the surviving elements. This requirement may not be always fulfilled. Assuming that there is a (fractional) error e in the knowledge of the failure thresholds, numerical simulations show (see **Figure 13**) that the redistribution rule still gives better results than a uniform redistribution. Therefore, in situations where the load redistribution is controllable, the redistribution rule mentioned above gives the best possible outcome.

We would like to mention that cooperative dynamics appears in another class of fiber bundle models where fibers are treated as viscoelastic elements [52–54]. The readers can go through [55] (appearing in the same research topic: The fiber bundle) for a review on viscoelastic fiber bundle models.

6 SUMMARY AND CONCLUSION

One can easily see that the fiber bundle model (FBM) introduced by Peirce [5] in 1926 as a model to understand the strength of composite materials is extremely elegant. As mentioned before, the model consists of a macroscopically large number of parallel fibers/springs with linear elastic behavior and of identical length. The breaking thresholds, however, are different for each fiber and are drawn from a probability distribution. All these fibers/springs hang from a rigid horizontal platform. The load on the bundle is applied at the lower horizontal platform. This lower platform has been assumed here to be rigid, implying that the stress or load share per surviving fibers/springs is equal, irrespective of how many fibers or springs might have broken (equal load sharing or ELS scheme). It may be mentioned that we have not discussed here the extensive studies on fiber bundle models with local load sharing (LLS) schemes, for which the readers may be advised to consult Refs. [1, 26], and the "impregnated fiber bundle" models for which the readers may be referred to Refs. [56, 57].

As discussed in this review, the failure dynamics of the FBM under the ELS scheme of load sharing have been analyzed for long, both analytically as well as numerically by several distinguished groups of investigators from engineering, physics, and applied mathematics. The results may be briefly summarized as follows: After introducing the model, we have described the dynamics of the equal load sharing (ELS) fiber bundle model in **Section 2**. Specifically, in this section, we discuss and summarize works (Refs. [1, 2, 4, 8, 28], see also [26, 40, 41]) related to the cooperative failure dynamics in the ELS fiber bundle model having a large number of fibers with different strength thresholds. We start this section by describing the force displacement relation (load curve) when the bundle is stretched by an amount x. The maximum point of this curve gives the strength of the whole bundle. One can easily derive the strength of the bundle for different fiber threshold distributions. We have chosen uniform and Weibull distributions as examples and derive bundles' strength as critical displacement (x_c) and critical force (F_c). Next, we describe how to formulate the dynamics of failure through a recursion relation in case of loading by discrete steps when fiber thresholds are uniformly distributed. The solution of the recursion relation at the fixed point gives some important information of the failure dynamics: Order parameter goes to zero following a power law as the applied stress values approach a critical value and both susceptibility and relaxation time diverge at the critical stress following well-defined power laws (see [4, 8, 42]). To check the universality of the failure dynamics, we choose different types of fiber strength distributions (linearly increasing) and derive the fixed-point solutions. The exponent values of the power laws for order parameter, susceptibility, and relaxation time variations are exactly the same as the model with a uniform distribution and therefore the failure dynamics in ELS fiber bundle model is universal. In addition, we present the exact solutions for pre- and post-critical relaxation behavior which we believe is one of the most important theoretical developments in this field. In the last part of this section, we present an analysis on the avalanche statistics for loading by a fixed amount. Such a loading scheme introduces a different mechanism for the avalanche sizes of simultaneous breaking of fibers. We discuss using analytical calculations that the exponent of the avalanche size distribution ($P(S)$) for discrete loading would be −3, which is different (−5/2) from the same in the case of quasi-static loading situation [6].

In **Section 3**, we summarize some recent developments (Refs. [11–16, 47, 49, 56]) in the cooperative dynamics of noise-induced failure in ELS fiber bundle models. In addition to applied stress, the noise factor plays a crucial role in triggering the failure of individual fibers. The trick here is how to define the failure probability of individual fibers as a function of applied/effective stress and the noise level. Normally, noise-level remains constant during the entire failure process, but the stress level increases gradually due to stress redistribution mechanism. The choice of the probability function should satisfy the fact that without the noise factor the noise-induced failure model must reproduce the classical failure scenario (discussed in **Section 2**). We start this section by presenting a noise-induced failure probability for individual fiber failure. The choice of stress and noise level dictates whether the system is in continuous breaking regime or in intermittent breaking regime. Through a mean-field argument, one can easily find out the phase diagram separating these two regimes (**Eq. 50**; **Figure 6**). Apparently, the continuous breaking regime is easy to analyze. For a homogeneous bundle, where all the fibers are identical (strengths are the same), one can write down the failure dynamics as a recursion relation (**Eq. 53**). The solution gives an exact estimate for the failure time (steps) as a function of applied stress (σ) and noise level (T) (**Eq. 55**). Simulation results show perfect agreement with the theoretical estimates (**Figure 7**). When we consider a strength distribution among the fibers in the model, it becomes extremely difficult to construct the recursion relation for the failure dynamics. One reason could be that during the failure process the strength distribution gets changed with time. However, the simulation results (**Figure 8**) for the failure time of heterogeneous bundles follow similar variation with applied stress and noise level with an extra noise factor (**Eq. 56**). Next,

we discuss the other regime, that is, the intermittent failure regime where there is waiting time between the two failure phases. The distribution of the waiting time is the most important aspect in this regime. Simulation results on homogeneous and heterogeneous bundles show that the waiting time distribution follows a Gamma distribution (**Eq. 57**) and a data collapse confirms the universal nature of such distribution function (**Figure 9**). Surprisingly, waiting time distribution from earthquake time series (California catalog) seems to follow a similar Gamma distribution (**Figure 10**).

In **Section 4**, we have considered self-organized fracture front propagation in a fiber bundle model where the fracture front adjusts its size in a self-organized way to meet the increasing load on the bundle and several features of the self-organized dynamics can still be analyzed in a mean field way; see, for example, **Figure 12** for the avalanche size distribution, which fits well with $D(S) \sim S^{-3/2}$.

As already mentioned (in **Section 2**), the universality class of the dynamics of fixed load increment during the ongoing dynamics of failure in the bundle (until its complete failure) will be different from that for the quasi-static (or weakest link failure type) loading during its dynamics. And, as discussed in **Section 5**, it is given by the Flory statistics for linear polymers, when fracture dynamics in the bundle is mapped to turbulence and one utilizes the Kolmogorov-type dispersion energy cascades [28]. In particular, we already obtained ([3]; see **Eqs. 35** and **36**) the order parameter exponent, $\beta = 1/2 = \gamma$, the susceptibility exponent. Employing the Rushbrooke scaling $2\beta + \gamma = \mathrm{d}\nu$ (where ν denotes the correlation length exponent), we get $\mathrm{d}\nu = 3/2$ here in conformity with finite-size scaling results. As discussed in [28] (see also the discussions in **Section 5**), by mapping the avalanche size distribution (**Eq. 47**) to the Kolmogorov energy dispersion in turbulence (**Eq. 67**) and identifying S with the energy and inverse correlation length as the wave vector q, we got the upper critical dimension d_u for FBM in the ELS scheme to be 6. This suggests that the correlation length exponent ν value here is 1/4.

As discussed in this review, the absence of stress concentrations or fluctuations around the broken fibers allows mean-field-type statistical analysis in such equal load sharing fiber bundle models. This feature of the models helped major analytical studies for the breaking dynamics and also allowed precise comparisons with computer simulation results.

AUTHOR CONTRIBUTIONS

BKC made the initial plan for the review article. All the authors contributed equally in discussions and in the writing of the manuscript.

FUNDING

This work was partly supported by the Research Council of Norway through its Centers of Excellence funding scheme, project number 262644.

ACKNOWLEDGMENTS

BKC is grateful to J. C. Bose Fellowship Grant for support.

REFERENCES

1. Pradhan S, Hansen A, Chakrabarti BK. Failure processes in elastic fiber bundles. *Rev Mod Phys* (2010) 82:499. doi:10.1103/RevModPhys.82.499
2. Pradhan S, Chakrabarti BK. Precursors of catastrophe in the Bak-Tang-Wiesenfeld, Manna, and random-fiber-bundle models of failure. *Phys Rev E-Stat Nonlinear Soft Matter Phys* (2002) 65:016113. doi:10.1103/PhysRevE.65.016113
3. Pradhan S, Bhattacharyya P, Chakrabarti BK. Dynamic critical behavior of failure and plastic deformation in the random fiber bundle model. *Phys Rev E-Stat Nonlinear Soft Matter Phys* (2002) 66:016116. doi:10.1103/PhysRevE.66.016116
4. Bhattacharyya P, Pradhan S, Chakrabarti BK. Phase transition in fiber bundle models with recursive dynamics. *Phys Rev E-Stat Nonlinear Soft Matter Phys* (2003) 67:046122. doi:10.1103/PhysRevE.67.046122
5. Peirce FT. Tensile tests for cottom yarns. "The weakest link" theorems on the strength of long and composite specimens. *J Text Ind* (1926) 17:355. doi:10.1080/19447027.1926.10599953
6. Hemmer PC, Hansen A. The distribution of simultaneous fiber failures in fiber bundles. *ASME J Appl Mech* (1992) 59:909. doi:10.1115/1.2894060
7. Pradhan S, Hansen A, Hemmer PC. Crossover behavior in burst avalanches: signature of imminent failure. *Phys Rev Lett* (2005) 95:125501. doi:10.1103/PhysRevLett.95.125501
8. Pradhan S, Hemmer PC. Relaxation dynamics in strained fiber bundles. *Phys Rev E-Stat Nonlinear Soft Matter Phys* (2007) 75:056112. doi:10.1103/PhysRevE.75.056112
9. Divakaran U, Dutta A. Effect of discontinuity in the threshold distribution on the critical behavior of a random fiber bundle. *Phys Rev E-Stat Nonlinear Soft Matter Phys* (2007) 75:011117. doi:10.1103/PhysRevE.75.011117
10. Lawn BR. *Fracture of brittle solids*. Cambridge, United Kingdom: Cambridge University Press (1993).
11. Coleman BD. Statistics and time dependence of mechanical breakdown in fibers. *J Appl Phys* (1958) 29:968. doi:10.1063/1.1723343
12. Scorretti R, Guarino A, Ciliberto S. Disorder enhances the effects of thermal noise in the fiber bundle model. *Europhys Lett* (2001) 55:626. doi:10.1209/epl/i2001-00462-x
13. Roux S. Thermally activated breakdown in the fiber-bundle model. *Phys Rev E* (2000) 62:6164. doi:10.1103/physreve.62.6164
14. Pradhan S, Chakrabarti BK. Failure due to fatigue in fiber bundles and solids. *Phys Rev E - Stat Nonlinear Soft Matter Phys* (2003) 67:046124. doi:10.1103/PhysRevE.67.046124
15. Reiweger I, Schweizer J, Dual J, Herrmann HJ. Modelling snow failure with a fibre bundle model. *J Glaciol* (2009) 55:997. doi:10.3189/002214309790794869
16. Cohen D, Lehmann P, Or D. Fiber bundle model for multiscale modeling of hydromechanical triggering of shallow landslides. *Water Resour Res* (2009) 45:W10436. doi:10.1029/2009WR007889
17. Pollen N, Simon A. Estimating the mechanical effects of riparian vegetation on stream bank stability using a fiber bundle model. *Water Resour Res* (2005) 41:W07025. doi:10.1029/2004WR003801
18. Pugno NM, Bosia F, Abdalrahman T. Hierarchical fiber bundle model to investigate the complex architectures of biological materials. *Phys Rev E-Stat Nonlinear Soft Matter Phys* (2012) 85:011903. doi:10.1103/PhysRevE.85.011903
19. Sornette D. Mean-field solution of a block-spring model of earthquakes. *J Phys I France* (1992) 2:2089. doi:10.1051/jp1:1992269
20. Daniels HE. The statistical theory of the strength of bundles of threads. *Proc Roy Soc Ser A* (1945) 183:243. doi:10.1098/rspa.1945.0011

21. Sornette D. Elasticity and failure of a set of elements loaded in parallel. *J Phys Math Gen* (1989) 22:L243.
22. Ising E. Beitrag zur theorie des ferromagnetismus. *Z Phys* (1925) 31:253. doi:10.1007/BF02980577
23. Harlow DG, Phoenix SL. Approximations for the strength distribution and size effect in an idealized lattice model of material breakdown. *J Mech Phys Solid* (1991) 39:173. doi:10.1016/0022-5096(91)90002-6
24. Gómez J, Iñiguez DAF, Pacheco AF. Solvable fracture model with local load transfer. *Phys Rev Lett* (1993) 71:380. doi:10.1103/PhysRevLett.71.380
25. Hidalgo RC, Kun YF, Herrmann HJ. Fracture model with variable range of interaction. *Phys Rev E - Stat Nonlinear Soft Matter Phys* (2002) 65:046148. doi:10.1103/PhysRevE.65.046148
26. Hansen A, Hemmer PC, Pradhan S. *The fiber bundle model*. Berlin, Germany: WileyVCH (2015).
27. Pradhan S, Chakrabarti BK. Introduction to critical phenomena through the fiber bundle model of fracture. *Eur J Phys* (2019) 40:014004. doi:10.1088/1361-6404/aaeb53
28. Biswas S, Chakrabarti BK. Flory-like statistics of fracture in the fiber bundle model as obtained via Kolmogorov dispersion for turbulence: a conjecture. *Phys Rev E* (2020) 102:012113. doi:10.1103/PhysRevE.102.012113
29. Flory PJ. *Statistical mechanics of chain molecules*. Hoboken, NJ: Wiley (1969)
30. Kolmogorov AN. Local structure of turbulence in an incompressible fluid at very high Renolds number. *Dokl Akad Nauk SSSR* (1941) 30:299. doi:10.1098/rspa.1991.0075
31. Biswas S, Ray P, Chakrabarti BK. *Statistical physics of fracture, breakdown, and earthquake*. Berlin, Germany: Wiley VCH (2015)
32. Kjellstadli JT. Burst distribution by asymptotic expansion in the equal load sharing fiber bundle model. *Front Physiol* (2019) 7:201. doi:10.3389/fphy.2019.00201
33. Pradhan S, Chandra A, Chakrabarti BK. Noise-induced rupture process: phase boundary and scaling of waiting time distribution. *Phys Rev E - Stat Nonlinear Soft Matter Phys* (2013) 88:012123. doi:10.1103/PhysRevE.88.012123
34. Petri A, Paparo G, Vespignani A, Alippi A, Costantini M. Experimental evidence for critical dynamics in microfracturing processes. *Phys Rev Lett* (1994) 73:3423. doi:10.1103/PhysRevLett.73.3423
35. Chakrabarti BK, Benguigui LG. *Statistical physics of fracture and breakdown in disordered systems*. Oxford, United Kingdom: Oxford University Press (1997)
36. Herrmann HJ, Roux S. *Statistical models for the fracture of disordered media*. Amsterdam, Netherlands: North-Holland (1990).
37. http://www.data.scec.org/ftp/catalogs/SHLK (Accessed February 1, 2005).
38. Corral A. Universal earthquake-occurrence jumps, correlations with time, and anomalous diffusion. *Phys Rev Lett* (2006) 97:178501. doi:10.1103/PhysRevLett.97.178501
39. Corral A. Local distributions and rate fluctuations in a unified scaling law for earthquakes. *Phys Rev E - Stat Nonlinear Soft Matter Phys* (2003) 68:035102. doi:10.1103/PhysRevE.68.035102
40. Bak P, Christensen K, Danon L, Scanlon T. Unified scaling law for earthquakes. *Phys Rev Lett* (2002) 88:178501. doi:10.1103/PhysRevLett.88.178501
41. Larkin AI, Ovchinnikov YN. Pinning in type II superconductors. *J Low Temp Phys* (1979) 34:409. doi:10.1007/BF00117160
42. Zapperi S, Cizeau P, Durin G, Stanley HE. Dynamics of a ferromagnetic domain wall: avalanches, depinning transition, and the Barkhausen effect. *Phys Rev B* (1998) 58:6353. doi:10.1103/PhysRevB.58.6353
43. Chevalier T, Talon L. Moving line model and avalanche statistics of Bingham fluid flow in porous media. *Eur Phys J E Soft Matter* (2015) 38:76. doi:10.1140/epje/i2015-15076-5
44. Biswas S, Chakrabarti BK. Self-organized dynamics in local load-sharing fiber bundle models. *Phys Rev E-Stat Nonlinear Soft Matter Phys* (2013) 88:042112. doi:10.1103/PhysRevE.88.042112
45. Hendrick M, Pradhan S, Hansen A. Mesoscopic description of the equal-load-sharing fiber bundle model. *Phys Rev E* (2018) 98:032117. doi:10.1103/PhysRevE.98.032117
46. Henkel M, Hinrichsen H, Lübeck S. Non-equilibrium phase transitions. In: *Absorbing phase transitions*, Vol. 1. Berlin, Germany: Springer (2008).
47. Basu A, Chakrabarti BK. Hydrodynamic descriptions for surface roughness in fracture front propagation. *Philos Trans A Math Phys Eng Sci* (2018) 377:20170387. doi:10.1098/rsta.2017.0387
48. Huang K. *Lectures on statistical physics and protein folding*. Singapore: World Scientific (2005).
49. Sinha S, Kjellstadli JT, Hansen A. Local load-sharing fiber bundle model in higher dimensions. *Phys Rev E-Stat Nonlinear Soft Matter Phys* (2015) 92:020401. doi:10.1103/PhysRevE.92.020401
50. Ma SK. *Modern theory of critical phenomena*. New York, NY: Taylor & Francis (1976).
51. Biswas S, Sen P. Maximizing the strength of fiber bundles under uniform loading. *Phys Rev Lett* (2015) 115:155501. doi:10.1103/PhysRevLett.115.155501
52. Hidalgo RC, Kun F, Herrmann HJ. Creep rupture of viscoelastic fiber bundles. *Phys Rev E-Stat Nonlinear Soft Matter Phys* (2002) 65:032502. doi:10.1103/PhysRevE.65.032502
53. Jagala EA. Creep rupture of materials: insights from a fiber bundle model with relaxation. *Phys Rev E-Stat Nonlinear Soft Matter Phys* (2011) 83:046119. doi:10.1103/PhysRevE.83.046119
54. Baxevanis T, Katsaounis T. Load capacity and rupture displacement in viscoelastic fiber bundles. *Phys Rev E-Stat Nonlinear Soft Matter Phys* (2007) 75:046104. doi:10.1103/PhysRevE.75.046104
55. Capelli A, Reiweger I, Schweizer J, Studying snow failure with fiber bundle models, *Front Phys* (2020) 8:236. doi:10.3389/fphy.2020.00236
56. Bunsell A, Gorbatikh L, Morton H, Pimenta S, Sinclair I, Spearing M, et al. Benchmarking of strength models for unidirectional composites under longitudinal tension. *Composite A: Appl Sci Manufacturing* (2018) 111:138. doi:10.1016/j.compositesa.2018.03.016
57. Breite C, Melnikov A, de Morais AB, Otero F, Mesquita F, Costa J, et al. Blind benchmarking of seven longitudinal tensile failure models for two virtual unidirectional composites. *Compos Sci Technol* (2021) 202:108555. doi:10.1016/j.compscitech.2020.108555
58. Pradhan S, Chakrabarti BK, Hansen A. Crossover behavior in a mixed-mode fiber bundle model. *Phys Rev E - Stat Nonlinear Soft Matter Phys* (2005) 71:036149. doi:10.1103/PhysRevE.71.036149
59. Roy S, Ray P. Critical behavior in fiber bundle model: a study on brittle to quasi-brittle transition. *Europhys Lett* (2015) 112:26004. doi:10.1209/0295-5075/112/26004
60. Roy C, Kundu S, Manna SS. Scaling forms for relaxation times of the fiber bundle model. *Phys Rev E-Stat Nonlinear Soft Matter Phys* (2013) 87:062137. doi:10.1103/PhysRevE.87.062137
61. Chakrabarti BK. A fiber bundle model of traffic jams. *Physica A* (2006) 377:162–166. doi:10.1016/j.physa.2006.05.003
62. Pahwa S, Scoglio C, Scala A. Abruptness of cascade failures in power grids. *Sci Rep* (2014) 4:3694. doi:10.1038/srep03694
63. Petri A, Pontuale G. Morphology and dynamics in SOC universality classes. *J Stat Mech Theor Exp* (2018) 6:063201. doi:10.1088/1742-5468/aac138
64. Pradhan S, Hansen A, Ray P. A renormalization group procedure for fiber bundle models. *Front Physiol* (2018) 6:65. doi:10.3389/fphy.2018.00065
65. Biswas S, Goehring L. Interface propagation in fiber bundles: local, mean-field and intermediate range dependent statistics. *New J Phys* (2016) 18:103048. doi:10.1088/1367-2630/18/10/103048

Conflict of Interest: The authors declare that the research was conducted in the absence of any commercial or financial relationships that could be construed as a potential conflict of interest.

frontiers in Physics

ORIGINAL RESEARCH
published: 04 March 2021
doi: 10.3389/fphy.2021.613493

Stick-Slip Dynamics in Fiber Bundle Models with Variable Stiffness and Slip Number

Zoltán Halász[1,2]*, *Imre Kállai*[3] *and Ferenc Kun*[1,2]

[1]Institute for Nuclear Research (Atomki), Debrecen, Hungary, [2]Department of Theoretical Physics, Doctoral School of Physics, Faculty of Science and Technology, University of Debrecen, Debrecen, Hungary, [3]Diehl Aviation Hungary Kft, Debrecen, Hungary

We present an extension of fiber bundle models to describe the mechanical response of systems which undergo a sequence of stick-slip cycles taking into account the changing stiffness and the fluctuating number of slip events of local material elements. After completing all stick-slip cycles allowed, fibers can either ultimately break or can keep their final stiffness leading to softening or hardening of the bundle, respectively. Under the assumption of global load sharing we derive analytic expressions for the constitutive response of the bundle with both quenched and annealed disorder of the failure thresholds where consecutive slips occur. Our calculations revealed that on the macro-scale the bundle exhibits a plastic behavior, which gets more pronounced when fibers undergo a higher number of stick-slip cycles with a gradually degrading stiffness. Releasing the load a permanent deformation remains, which increases monotonically for hardening bundles with the maximum deformation reached before unloading starts, however, in the softening case a non-monotonous behavior is obtained. We found that the macroscopic response of hardening bundles is more sensitive to fluctuations of the number of stick-slip cycles allowed than of the softening ones. The quenched and annealed disorder of failure thresholds gives rise to the same qualitative macro-scale behavior, however, the plastic response is found to be stronger in the annealed case.

Keywords: fiber bundle, stick-slip, plastic behaviour, varying stiffness, fluctuating slip number

OPEN ACCESS

Edited by:
Subhrangshu Sekhar Manna, S.N. Bose National Centre for Basic Sciences, India

Reviewed by:
Soumyajyoti Biswas, SRM University, India
Sumanta Kundu, Osaka University, Japan

***Correspondence:**
Zoltán Halász
zoltan.halasz@atomki.hu

Specialty section:
This article was submitted to Interdisciplinary Physics, a section of the journal Frontiers in Physics

Received: *02 October 2020*
Accepted: *04 January 2021*
Published: *04 March 2021*

Citation:
Halász Z, Kállai I and Kun F (2021) Stick-Slip Dynamics in Fiber Bundle Models with Variable Stiffness and Slip Number. Front. Phys. 9:613493. doi: 10.3389/fphy.2021.613493

1 INTRODUCTION

Fibre bundle models (FBM) are one of the most important theoretical approaches to the damage and fracture of disordered materials [1]. In the framework of FBMs, the specimen is discretized as a bundle of parallel fibers which are subject to an external load along the fibers' direction [2, 3]. The Young modulus of fibers is typically assumed to be constant so that materials' heterogeneity is entirely represented by the randomness of the strength of fibers. Even in their simplest form, FBMs provided a deep insight into the process of damaging of heterogeneous materials [2, 4, 5] making also possible to embed fracture processes into the general framework of statistical physics [1, 6, 7] and to clarify its analogy to phase transitions and critical phenomena [8–13].

Soon after the introduction of the basic concept of FBMs by Peires in 1927 [14], the model had been extended to capture time dependence and fatigue effects [15]. During the past decades subsequent developments of the model have demonstrated that varying the mechanical response [16] (brittle, plastic) and rheological (visco-elastic) behavior [17–20] of individual fibers, furthermore, the degree of strength disorder [21–23], range of load sharing (local, global) [11,

24, 25] following breaking events, and the way of loading [19, 20, 26] (quasi-static, creep, fatigue) the model is able to capture a broad spectrum of materials' behavior. Due to this flexibility, the model has gained a wide variety of applications from the fracture of fiber reinforced composites [25, 27], through granular materials, where force chains were treated as load bearing fibers [28, 29], to the rupture of biological materials [30].

Recently, we have proposed an extension of FBMs [31, 32] to describe the mechanical response of systems with a complex micro-structure which respond to external loading by local rearrangements, for instance, of particles like in granular materials [28, 33] and in agglomerates of dipolar particles [34], or by an activation of internal stored length such as spider silk [35]. A special area where stick-slip dynamics can be exploited for technological applications, is the development of nanocomposites, in particular carbon nanotube (CNT) composites, where CNTs are embedded in a polymeric matrix. One of the interesting properties of CNT nanocomposites is the ability to absorb vibrational energy which, together with high strength and fatigue tolerance, makes them perfect candidates for new multifunctional composite structures [36]. Recent experimental studies have revealed that the damping enhancement can be attributed to the CNT-matrix stick-slip caused by the severe elastic mismatch which leads to shear stress localization at the interfaces [37]. To represent the microscale complexity underlying stick-slip dynamics, fibers of our model were assumed to undergo a sequence of stick-slip events: when the local load reaches a failure threshold the fiber does not break, instead its load drops down to zero but the fiber has the ability of support load again. The model has been successfully applied to analyze the mechanical response of sheared granular materials [33] and the effect of root reinforcement on the stability of soils [29]. Complementing the stick-slip FBM with a healing mechanism it proved to be capable to describe the failure process of snow [38, 39].

In the basic setup of the model it is assumed that fibers keep their original stiffness during their entire damage history [31, 32], which is a crude simplification. It is reasonable to assume that restructuring events give rise to a degradation of the local stiffness or to hardening, e.g., due to damage or activating stored length inside the material, respectively. Additionally, fibers of the bundle are allowed to undergo the same number of slip events although in an extended sample the number of possible restructurings may have a spatial variation. To make the stick-slip FBM more realistic, in the present paper we resolve these limitations by allowing for the change of the stiffness of fibers as a result of slip events, and we capture the fluctuations of the number of stick-slip cycles allowed for fibers. Under the assumption of global load sharing, we derive analytic expressions for the macroscopic constitutive response of the bundle both for quenched and annealed disorder of failure thresholds where slip is activated. The stiffness change is treated in a multiplicative way which allows for a unified framework of stiffness degradation and stiffening. We demonstrate that the stick-slip dynamics results in a plastic behavior on the macro-scale and explore consequences of the new degrees of freedom of the model.

2 STICK-SLIP DYNAMICS WITH VARYING STIFFNESS

The model consists of N parallel fibers which are characterized by the same initial stiffness value $E = 1$. Under an increasing external load σ fibers have a linearly elastic behavior up to a threshold load σ_{th}. When the load on a fiber exceeds the failure threshold we assume that the fiber does not break, instead it slips and gets extended by increasing its equilibrium length until the load drops down to zero. Heterogeneity of the material is represented by the randomness of the slip thresholds, which are sampled from a probability distribution $p(\sigma_{th})$. The slip event is instantaneous in the sense that it does not take time, however, after slipping has been completed the fiber can support load again. As an important step of generalization of the model we let the fibers' stiffness change after slipping in a multiplicative way, i.e. the stiffness is updated as

$$E' = aE, \tag{1}$$

where $a \geq 0$ is the stiffness parameter of the model. Note that the special case $a = 0$ captures the immediate irreversible failure of the fiber right at the first slip which essentially results into the same dynamics as the classical fiber bundle model [2, 4, 40]. The parameter choice $a = 1$ recovers the original stick-slip model where stiffness does not change during the loading history of fibers [31, 32]. In our present study we focus on the parameter ranges $0 < a < 1$ and $a > 1$, which represent stiffness degradation and stiffening of fibers following slipping, respectively. For practical applications of the model, stiffness degradation $(a < 1)$ is typically caused by internal damage of material units represented by fibers. Stiffness increase $(a < 1)$ occurs, for instance, in granular materials under compression where the restructuring of force chains may be accompanied by stiffening [28], and in biological materials like spider silk which respond to an increasing load by the activation of stored length [41].

After the slip has been completed, the fiber gets sticked so that it can support load again described by the constitutive law

$$\sigma = aE(\varepsilon - \varepsilon_{th}), \tag{2}$$

where ε denotes the strain of the fiber. **Eq. 2** takes into account that the relaxed length of the fiber is extended with the strain threshold $\varepsilon_{th} = \sigma_{th}/E$ of slipping. This dynamics has the consequence that fibers may fulfill again the slipping condition and can eventually undergo a stick-slip sequence representing the gradual restructuring of the material. In order to describe such sequences we set the number of allowed slip events $K \geq 1$, which is first assumed to have a fixed value for all the fibers of the bundle. It follows from **Eq. 1** that after k stick-slip cycles the stiffness E_f of the fiber has the value

$$E_f = a^k E, \tag{3}$$

which can be greater or lower than the initial value E, for $a > 1$ and $a < 1$, respectively. It is a crucial question at which threshold loads the subsequent slip events occur. In the simplest case we can assume that the threshold value σ_{th} is fixed for the entire history of a fiber which provides a representation of the quenched

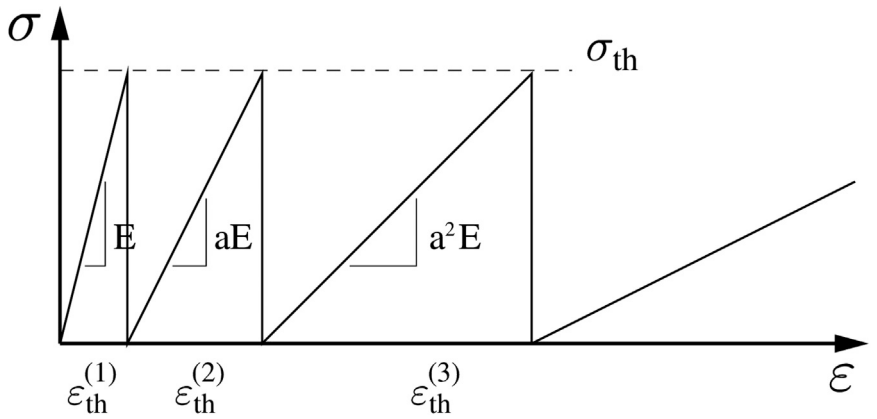

FIGURE 1 | Mechanical response of a single fiber in the case of quenched disorder when the slipping threshold σ_{th} is fixed for the entire damage history of the fiber. The value of a is set to $a = 0.8$ so that gradual stiffness degradation occurs through the subsequent stick-slip periods. Since the stiffness is changing, the threshold strains of slipping are increasing $\varepsilon_{th}^{(1)} < \varepsilon_{th}^{(2)} < \varepsilon_{th}^{(3)}$, in spite of the fixed stress threshold σ_{th} of the fiber.

disorder of the materials' micro-structure. It can also occur that after restructuring events the local physical properties of the system change which can be captured by assigning a new threshold value to the fiber from the same probability distribution $p(\sigma_{th})$ each time a slipping occurred (annealed disorder).

For the interaction of fibers we assume global load sharing in such a way that fibers are stretched between two hard loading plates which ensure a global response of the entire system following local slipping events. However, global load sharing does not imply equal load of fibers in our stick-slip system since fibers which suffered a different number of slips have different stiffnesses and relaxed lengths, hence, they keep different loads. After fixing the type of disorder the threshold strains of slips can be determined from the corresponding stress thresholds. A fiber which has slipped k times at the consecutive strain thresholds $\varepsilon_{th}^{(1)}, \varepsilon_{th}^{(2)}, \ldots, \varepsilon_{th}^{(k)}$ up to the externally imposed strain ε, keeps the load

$$\sigma = a^k E\left(\varepsilon - \varepsilon_{th}^{(1)} - \varepsilon_{th}^{(2)} - \cdots \varepsilon_{th}^{(k)}\right), \tag{4}$$

where the sum of failure thresholds $\varepsilon_0^k = \sum_{j=1}^{k} \varepsilon_{th}^{(j)}$ determines the relaxed length ε_0^k of the fiber. In the following we derive the macroscopic constitutive relation of the bundle for the cases of quenched and annealed disorder of slipping thresholds with global load sharing. Our main goal is to explore the consequences of the changing stiffness and of the fluctuations of the number of slip events fibers can experience.

2.1 Quenched Disorder of Failure Thresholds

Quenched disorder means that slips of a fiber always occur at the same stress threshold σ_{th}, assigned to it in the initial state of the system. However, the corresponding threshold strains are not constant, which is illustrated in **Figure 1**, where the damage history of a single fiber is presented with a stiffness parameter $a < 1$. It can be observed that in spite of the constant threshold load σ_{th}, the strain values $\varepsilon_{th}^{(1)}, \varepsilon_{th}^{(2)}, \varepsilon_{th}^{(3)}, \ldots$ where slips occur, gradually increase due to the degrading stiffness. It follows from **Eq. 4** that the threshold strains $\varepsilon_{th}^{(k)}$ $(k = 1, \ldots, K)$ of consecutive slips of a fiber are determined by its initial strain threshold $\varepsilon_{th}^{(1)}$ and by the stiffness parameter a of the model as

$$\varepsilon_{th}^{(k)} = \frac{\varepsilon_{th}^{(1)}}{a^{k-1}}. \tag{5}$$

The relaxed length $\varepsilon_0^{(k)}$ of the fiber after the kth slip is the sum of all previous threshold strains which yields

$$\varepsilon_0^{(k)} = \varepsilon_{th}^{(1)}\left(1 + \frac{1}{a} + \frac{1}{a^2} + \cdots + \frac{1}{a^{k-1}}\right). \tag{6}$$

For the sum of the geometric series inside the brackets we introduce the shorthand notation $S(a, k)$ so that **Eq. 6** simplifies to $\varepsilon_0^{(k)} = \varepsilon_{th}^{(1)} S(a, k)$. Here the value of $S(a, k)$ can be cast into the closed form $S(a, k) = (a^{-k} - 1)/(a^{-1} - 1)$ for $a \neq 1$. The above expressions are valid both for gradual degradation $a < 1$ and stiffening $a > 1$, resulting in an increasing and decreasing sequence of strain thresholds of slip events, respectively. Note that in the particular case of the original stick-slip model with $a = 1$, the sum $S(a, k)$ takes the value $S(a, k) = k$.

2.1.1 Derivation of the Constitutive Equation With Varying Stiffness

To obtain a closed analytic form for the constitutive equation, we assume strain controlled loading of the bundle between two hard plates. At a given strain ε during the loading process, the bundle is a mixture of subsets of fibers which are either intact (no slip), or have suffered different number of slip events k, where $1 \leq k \leq K$ holds. Based on **Eqs 4–6** the failure index k of fibers can be expressed in terms of their initial failure thresholds $\varepsilon_{th}^{(1)}$ and the externally imposed strain ε as

$$\varepsilon_{th}^{(1)} < \varepsilon, \quad k = 0, \tag{7}$$

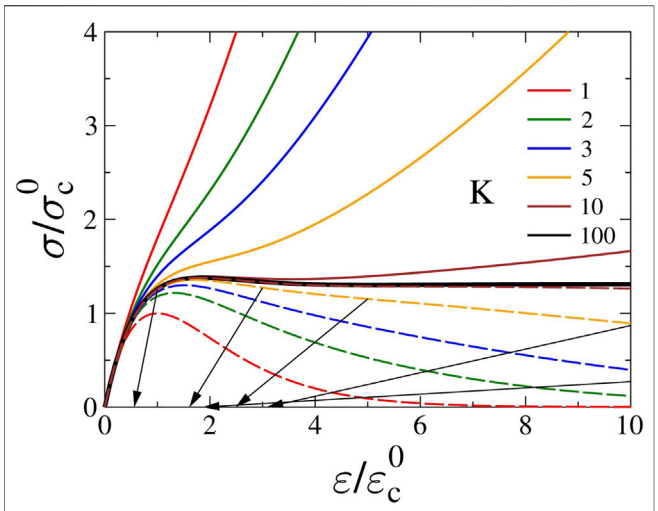

FIGURE 2 | Constitutive behavior of the stick-slip bundle with quenched disorder of the sliding thresholds according to **Eq. 8** including both cases of remaining stiffness (continuous lines) and ultimate failure of fibers (dashed lines) after completing K slip events. The arrows highlight unloading curves, which start at different strains ε_m of the constitutive curve of the softening bundle of $K = 5$. The value of the stiffness parameter is $a = 0.8$.

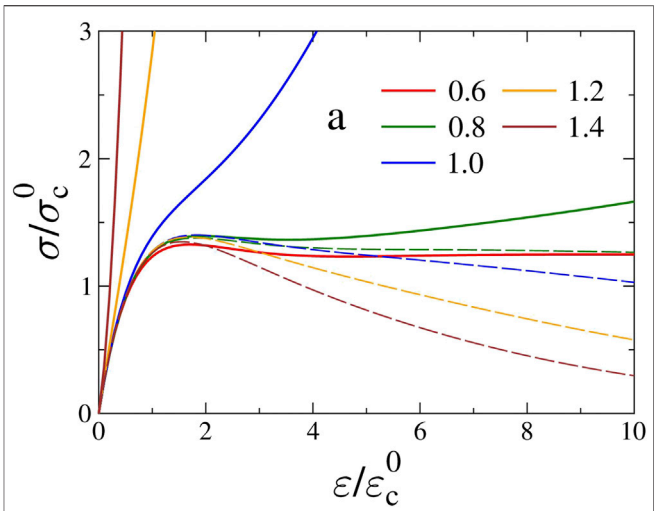

FIGURE 3 | The effect of the value of the stiffness parameter a on the macroscopic behavior of a bundle where all fibers are allowed to perform $K = 10$ stick-slip cycles. Constitutive curves of hardening (continuous lines) and softening (dashed lines) bundles are also included. The slip thresholds are exponentially distributed. Fibers keep their final stiffness so that all bundles are hardening even if the asymptotic regimes are not visible for the lowest a.

$$\frac{\varepsilon}{S(a,k)} < \varepsilon_{th}^{(1)} < \frac{\varepsilon}{S(a,k+1)}, \quad 1 \le k < K,$$
$$\frac{\varepsilon}{S(a,K)} < \varepsilon_{th}^{(1)}, \quad k = K,$$

where the failure index $k = 0$ stands for intact fibers.

The macroscopic constitutive response of the system can be obtained by summing up the load $\sigma_k(\varepsilon)$ kept by the subsets of fibers which suffered exactly k slip events

$$\sigma(\varepsilon) = \sum_{k=0}^{K} \sigma_k(\varepsilon). \tag{8}$$

The partial loads $\sigma_k(\varepsilon)$ can be expressed in terms of the disorder distribution as

$$\sigma_0(\varepsilon) = E\varepsilon[1 - P(\varepsilon)] \quad \text{for} \quad k = 0, \tag{9}$$

$$\sigma_k(\varepsilon) = a^k E \int_{\varepsilon/S(a,k+1)}^{\varepsilon/S(a,k)} [\varepsilon - \varepsilon_1 S(a,k)] p(\varepsilon_1) d\varepsilon_1 \quad \text{for} \quad 1 \le k < K, \tag{10}$$

$$\sigma_K(\varepsilon) = a^K E \int_{\varepsilon_{th}^{min}}^{\varepsilon/S(a,K)} [\varepsilon - \varepsilon_1 S(a,K)] p(\varepsilon_1) d\varepsilon_1 \quad \text{for} \quad k = K, \tag{11}$$

where the first, second, and third terms provide the contribution of intact fibers, of the fibers which have suffered exactly $1 \le k < K$ slip events, and of the fibers which have completed all the K stick-slip cycles, respectively. Note that the integration limits capture the separation of the subsets of fibers given by **Eq. 7**. In the limiting case of small deformation $\varepsilon \to 0$ only the first term **Eq. 9** has a finite contribution recovering the expected linear behavior $\sigma(\varepsilon) \approx E\varepsilon$ with the initial stiffness. In the opposite limit $\varepsilon \to +\infty$ only the last term **Eq. 11** survives which expresses that after the number K of allowed slip events the fibers still keep load and a linear behavior emerges

$$\sigma(\varepsilon) \approx a^K E\left(\varepsilon - S(a,k)\langle\varepsilon_{th}^{(1)}\rangle\right) \tag{12}$$

With the asymptotic stiffness $E_a = a^K E$. On the right hand side $\langle\varepsilon_{th}^{(1)}\rangle$ denotes the average slip threshold in the initial state of the bundle. Between the two limits, at intermediate strains the second term **Eq. 10** controls the macroscopic response as fibers gradually undergo more and more slip events.

The constitutive behavior of the stick-slip bundle is illustrated in **Figure 2** for several values of the maximum number K of slip events at a fixed value of the stiffness parameter $a = 0.8$. For the explicit calculations we considered exponentially distributed slip thresholds with the probability density function

$$p(\sigma_{th}) = \lambda e^{-\lambda\sigma_{th}}, \tag{13}$$

where the parameter λ is set to $\lambda = 1$. This disorder distribution has the advantage that all the expressions of **Eqs 9–11** can be obtained analytically. When presenting the results we rescale the stress σ and strain ε with the fracture strength σ_c^0 and ε_c^0 of a simple equal load sharing FBM of the same threshold distribution where fibers break when the load exceeds their strength. Note that the constitutive equation of this classical FBM coincides with $\sigma_0(\varepsilon)$ of **Eq. 9**. It can be seen that at intermediate strains a plastic behavior emerges which gets more pronounced for higher values of K, i.e. the hardening curves tend to asymptotic straight lines according to **Eq. 12** which are preceded by longer and longer plateau regimes in spite of the degrading stiffness. The model can also account for the ultimate breaking of fibers after completing

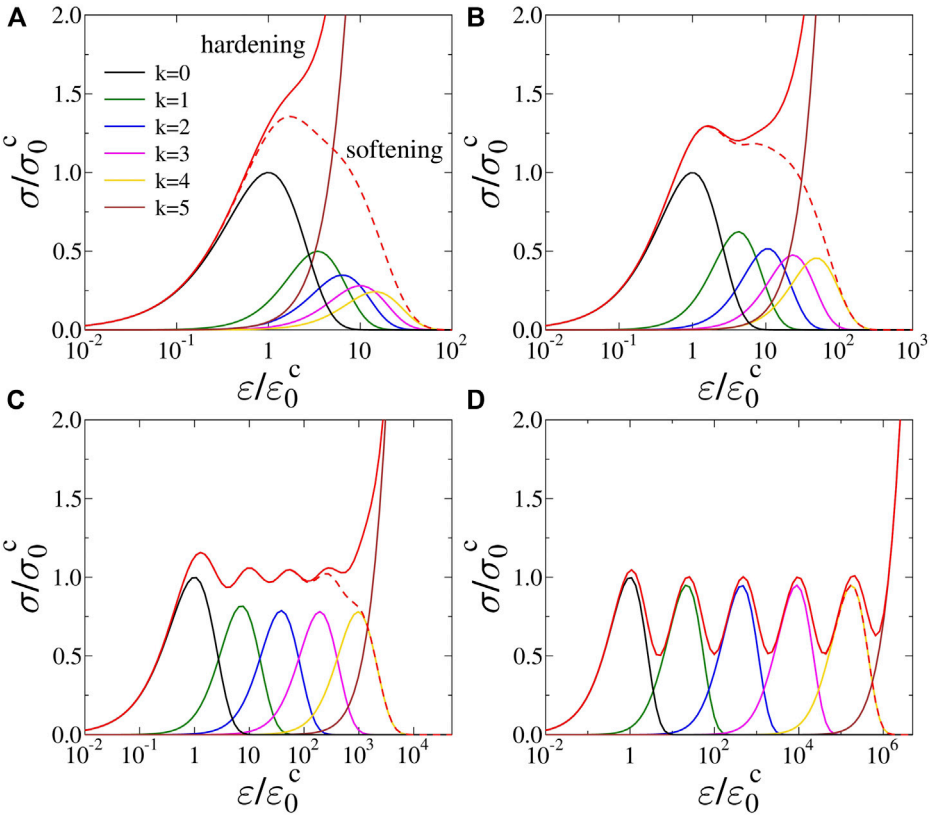

FIGURE 4 | Emergence of the plateau regime as the stiffness parameter a decreases at a fixed value of the maximum number $K = 5$ of stick-slip cycles allowed for fibers. The partial loads $\sigma_k(\varepsilon)$ **Eqs 9–11** kept by the subsets of fibers which have suffered exactly k slip events are also shown for $k = 0, 1, 2, 3, 4, 5$ for four different values of the stiffness parameter a: **(A)** 0.8, **(B)** 0.5, **(C)** 0.2, and **(D)** 0.05. The constitutive curve of the entire bundle $\sigma(\varepsilon)$ is also presented for both hardening (continuous red line), and softening (dashed red line). On the horizontal axis logarithmic scale is used due to the large strains involved at low a.

the allowed number K of stick-slip cycles by omitting the term of $\sigma_K(\varepsilon)$ in **Eq. 8**. Fiber breaking implies that in the limit $\varepsilon \to \infty$ the load bearing capacity of the bundle gradually diminishes so that $\sigma(\varepsilon) \to 0$ follows, however, increasing the number of slip events K a broader plastic plateau emerges similar to the hardening bundles (see **Figure 2**).

2.1.2 Effect of the Varying Fiber Stiffness on the Macroscopic Response of Stick-Slip Bundles

The value of the stiffness parameter a has an important effect on the overall behaviour of the system. It can be inferred from **Eqs 5**, **6** that for the stiffening case $a > 1$ consecutive slip events rapidly follow each other so that the asymptotic regime **Eq. 12** is reached at a relatively low strain. Decreasing a at a constant value of K, the plastic regime preceding hardening gets more-and-more extended (see **Figure 3** for illustration). For the lowest values of the stiffness parameter a the hardening regime is approached only at very high strains which hinders the precise structure of the $\sigma(\varepsilon)$ curves in **Figure 3**. That's why we further analyze the emergence of the plateau regime at low a values in **Figure 4** using logarithmic scale on the horizontal axis presenting also the partial loads $\sigma_k(\varepsilon)$ of the subsets of fibers of different failure indices. It can be observed that lowering the stiffness parameter, the plastic plateau develops as a steady regime decorated with some oscillations. It can be seen that for higher a values, where the stiffness slowly degrades, the curves of $\sigma_k(\varepsilon)$ strongly overlap each other and their peak load rapidly decreases with k. As a decreases the steady state emerges because the $\sigma_k(\varepsilon)$ curves get more-and-more separated while their peak load increases approaching σ_c of the classical FBM, which coincides with $\sigma_{k=1}(\varepsilon)$. In the limit of $a \to 0$ the steady stress regime disappears because the $\sigma_k(\varepsilon)$ functions become almost completely separated (see **Figure 4D**).

The separation of the $\sigma_k(\varepsilon)$ curves in the low a limit also reveals that their functional form is essentially the same, determined by the constitutive equation of the classical fiber bundle model $\sigma_{k=0}(\varepsilon)$. The overall shape of the constitutive curve of FBMs has a high degree of robustness for a broad class of disorder distributions [2], which implies the robustness of the macroscopic behaviour of the stick-slip FBM presented above, against the distribution of slip thresholds $p(\varepsilon_{th}^{(1)})$.

It is a very important consequence of the stick-slip dynamics that upon unloading $\sigma \to 0$ the bundle a permanent deformation ε_r remains which depends on the maximum deformation ε_m reached before unloading sets on. If fibers keep their last stiffness value after K stick-slip cycles, the permanent deformation

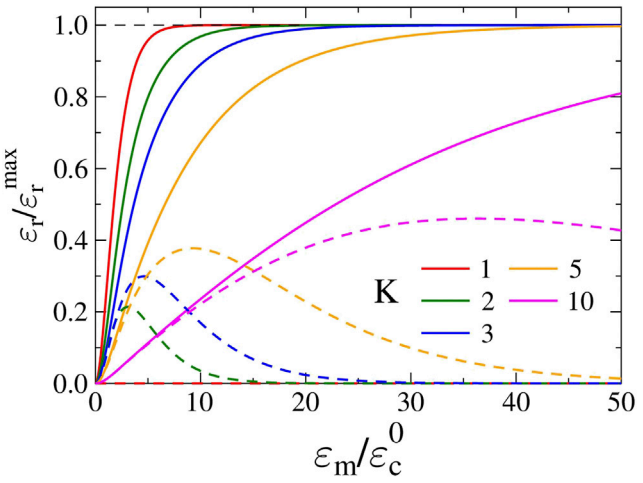

FIGURE 5 | Permanent deformation ε_r of hardening (continuous lines) and softening (dashed lines) stick-slip bundles as function of the maximum deformation ε_m reached before unloading started for different values of the slip number K at the stiffness parameter $a = 0.8$. The remaining deformation ε_r is scaled with the corresponding maximum value ε_r^{max} of the hardening case given by **Eq. 14**. For softening bundles a non-monotonous behavior is obtained. Additionally, even the maximum values of the $\varepsilon_r(\varepsilon_m)$ curves fall below the corresponding curves of hardening bundles.

monotonically increases and it has an upper limit ε_r^{max}, which can be realized if the unloading starts along the asymptotic linear regime of a hardening bundle. The value of ε_r^{max} can be obtained from **Eq. 12** using the condition $\sigma(\varepsilon_r^{max}) = 0$, which yields

$$\varepsilon_r^{max} = S(a,K)\langle\varepsilon_{th}^{(1)}\rangle. \tag{14}$$

For intermediate starting points ε_m, the remaining deformation ε_r can be determined by applying the condition $\sigma(\varepsilon_r) = 0$ in the constitutive equation **Eq. 8** taking also into account that along the unloading curve no slip events occur. This leads to the final form

$$\varepsilon_r = \frac{\sum_{k=1}^{K-1} a^k S(a,k)\int_{\varepsilon_m/S(a,k+1)}^{\varepsilon_m/S(a,k)} \varepsilon_1 p(\varepsilon_1)d\varepsilon_1 + a^K S(a,K)\int_{\varepsilon_{th}^{min}}^{\varepsilon_m/S(a,K)} \varepsilon_1 p(\varepsilon_1)d\varepsilon_1}{1 - P(\varepsilon_m) + \sum_{k=1}^{K-1} a^k \int_{\varepsilon_m/S(a,k+1)}^{\varepsilon_m/S(a,k)} p(\varepsilon_1 d\varepsilon_1) + a^K \int_{\varepsilon_{th}^{min}}^{\varepsilon_m/S(a,K)} p(\varepsilon_1)d\varepsilon_1}, \tag{15}$$

which converges to ε_r^{max} in the limit $\varepsilon_m \to \infty$. Note that the starting point of unloading ε_m appears in the upper bound of the integrals. The permanent deformation ε_r of hardening bundles is presented in **Figure 5** for several values of the maximum slip number K. It follows from **Eqs 14**, **15** that for increasing the number of slip events K and decreasing the stiffness parameter a, hardening bundles store a higher plastic deformation, which is also supported by the numerical results of the figure.

Examples of unloading curves are presented in **Figure 2** for the case of softening bundles, where fibers break after K slips. Since no slip can occur under a decreasing load, the unloading curves are always straight lines and their slope, i.e. the unloading modulus decreases with increasing ε_m. The analytic expression of the unloading modulus E_u coincides with the denominator of **Eq. 15** multiplied by the initial stiffness E of fibers

$$E_u = E\left[1 - P(\varepsilon_m) + \sum_{k=1}^{K-1} a^k \int_{\varepsilon_m/S(a,k+1)}^{\varepsilon_m/S(a,k)} p(\varepsilon_1)d\varepsilon_1 + a^K \int_{\varepsilon_{th}^{min}}^{\varepsilon_m/S(a,K)} p(\varepsilon_1)d\varepsilon_1\right]. \tag{16}$$

The expression shows that the unloading modulus E_u at a given ε_m is the weighted average of the moduli Ea^k of the subsets of fibers with slip numbers $k = 0, 1, \ldots, K$, where the weights are determined by the distribution $p(\varepsilon_1)$ of the slip thresholds. In the limit $\varepsilon_m \to \infty$, the unloading modulus E_u converges to the asymptotic value $E_u \to E_a = Ea^K$.

For the unloading modulus of softening bundles the last term inside the brackets has to be skipped to take into account the ultimate breaking of fibers. It can also be inferred from **Figure 2** that the permanent deformation of softening bundles is not monotonous, i.e. the $\varepsilon_r(\varepsilon_m)$ function has a maximum and decreases when unloading along the tail of the softening regime of the constitutive curve $\sigma(\varepsilon)$. This behavior can be realized in **Figure 2** by the changing order of the end points of the unloading curves. **Figure 5** demonstrates that even the maximum value of the remaining deformation of softening bundles is significantly smaller than the corresponding maximum permanent deformation ε_r^{max} of the hardening ones.

It follows from **Figure 4** that once a plastique plateau can be identified, its extension is practically the same for hardening (no breaking) and softening (breaking after K slips) bundles. At a given parameter set a, K, the extension of the plateau can be characterized by the asymptotic value ε_r^{max} of the remaining deformation **Eq. 14** of hardening bundles. It is interesting to note that in the case of $a > 1$ the value of $S(a,K)$ in **Eq. 14** converges to $S \approx 1/(1 - a^{-1})$ for $K \to \infty$, which implies a finite limit of the permanent deformation

$$\varepsilon_r^{max} \to \frac{1}{1 - a^{-1}}\langle\varepsilon_{th}^{(1)}\rangle, \tag{17}$$

and hence, of the extension of the plateau, when fibers get stiffer after slip events. However, for the case of stiffness degradation $a < 1$, the sum $S(a,K)$ does not have a finite limit for large K values giving rise to a monotonically broadening plateau as the maximum slip number K increases.

3 FLUCTUATING MAXIMUM NUMBER OF SLIP EVENTS

Fiber bundle models with stick-slip dynamics can be applied to understand damage accumulation and fracture in a large variety of systems where micro-scale restructuring plays a dominating role. However, in the present form of the model the maximum number of allowed stick-slip cycles is fixed for all the fibers, which is a very strong constraint and limits the applicability of the model under realistic conditions. In this section we extend the model to capture the effect of the fluctuating slip number K.

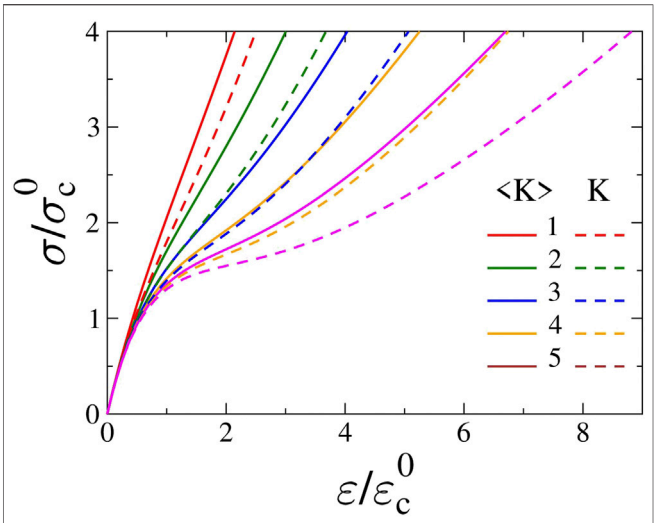

FIGURE 6 | Comparison of the constitutive curves of stick-slip bundles with constant (*dashed lines*) and fluctuating (*continuous lines*) maximum number of slip events for the case of hardening at the stiffness parameter $a = 0.8$. The constant K values are set to be equal to the average $\langle K\rangle$ of the Poissonian distribution. A natural choice for $g(K)$ is the Poisson distribution.

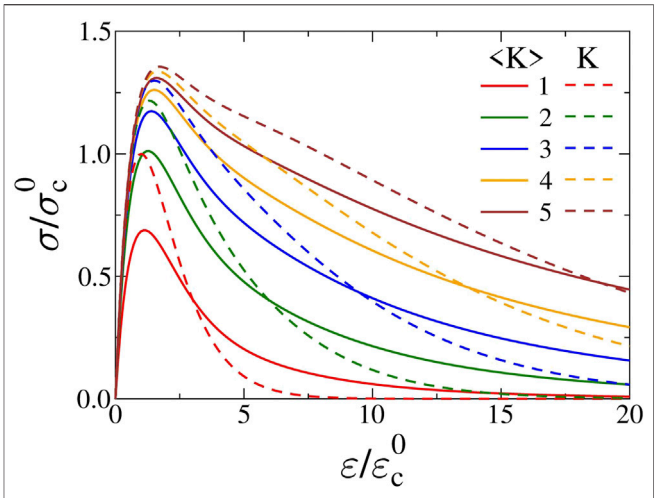

FIGURE 7 | Comparison of the constitutive curves of stick-slip bundles with constant (*dashed lines*) and fluctuating (*continuous lines*) maximum number of slip events for the case of softening at the stiffness parameter $a = 0.8$. The constant K values are set to be equal to the average $\langle K\rangle$ of the Poissonian distribution.

We assume that K is a random variable which is sampled from a probability density function $g(K)$ defined over the range $0 \le K < \infty$ with the normalization condition

$$\sum_{K=0}^{\infty} g(K) = 1. \tag{18}$$

Note that the possibility of fibers with $K = 0$ is included, which implies that some fibers remain always intact during the loading process.

The constitutive equation $\sigma(\varepsilon)$ of the stick-slip fiber bundle with fluctuating maximum number of slip events K can be obtained by averaging the contributions of subsets of fibers of constant K **Eqs 9–11** with the distribution $g(K)$

$$\begin{aligned}\sigma(\varepsilon) = {} & \big(g(0) + [1 - g(0)][1 - P(\varepsilon)]\big)E\varepsilon + \\ & \sum_{K=1}^{\infty} g(K) \sum_{k=1}^{K-1} Ea^k \int_{\varepsilon/S(a,k+1)}^{\varepsilon/S(a,k)} [\varepsilon - S(a,k)\varepsilon_1]p(\varepsilon_1)d\varepsilon_1 + \\ & \sum_{K=1}^{\infty} g(K)Ea^K \int_{\varepsilon_{th}^{min}}^{\varepsilon/S(a,k)} [\varepsilon - S(a,k)\varepsilon_1]p(\varepsilon_1)d\varepsilon_1.\end{aligned} \tag{19}$$

The first term of the right hand side of **Eq. 3** represents the load kept by intact fibers taking into account that a fiber can be intact either because it can never slip $K = 0$, or because it is damageable $K > 0$ but at the current strain it has not experienced any slip $k = 0$. The second term stands for those fibers which have slipped exactly k times and still can undergo further stick-slip cycles $k < K$ with the same maximum value K, while the last one is the contribution of the fibers which have completed all allowed stick-slip cycles and still support load with their final stiffness.

$$g(K) = \frac{\langle K\rangle^K e^{-\langle K\rangle}}{K!}, \tag{20}$$

which we use for explicit calculations to demonstrate the outcomes of the generic derivations. Here the parameter $\langle K\rangle$ denotes the average of the slip number K inside the bundle. Assuming that flaws responsible for slip events occur in an uncorrelated manner along fibers, the Poissonian distribution controlled by the average $\langle K\rangle$ gives an adequate description of the statistics of the maximum slip number K [42]. **Figure 6** presents a comparison of the constitutive curves of the stick-slip bundle with constant and Poisson distributed maximum number of slip events in such a way that the constant Ks are set to be equal to the average $\langle K\rangle$ of the Poissonian. It can be seen that the functional form of the two sets of constitutive curves is practically the same. For low values of $K = \langle K\rangle$ the corresponding curves fall relatively close to each other, however, deviations increase with increasing $\langle K\rangle$. The reason is that the standard deviation of the Poissonian distribution growth as the square root of the average $\sqrt{\langle K\rangle}$ so that at higher $\langle K\rangle$ the distribution **Eq. 20** gets broader and the fluctuations of K become more relevant. The fluctuating K affects also the asymptotic form of $\sigma(\varepsilon)$ of hardening bundles

$$\sigma(\varepsilon) \approx E\varepsilon\left[g(0) + \sum_{K=1}^{\infty} g(K)a^K\right] - E\langle\varepsilon_{th}^{(1)}\rangle \sum_{K=1}^{\infty} g(K)a^K S(a,K), \tag{21}$$

which yields

$$E_a = E\left[g(0) + \sum_{K=1}^{\infty} g(K)a^K\right] = E\langle a^K\rangle, \tag{22}$$

and

$$\varepsilon_r^{max} = \langle \varepsilon_{th}^{(1)} \rangle \frac{\sum_{K=1}^{\infty} g(K) a^K S(a,K)}{\langle a^K \rangle}, \tag{23}$$

for the asymptotic Young modulus E_a and for the maximum value of the permanent deformation ε_r^{max}, respectively. Note that the average value $\langle a^K \rangle$ is calculated with the distribution $g(K)$ of the maximum slip number K, while the average threshold $\langle \varepsilon_{th}^{(1)} \rangle$ is determined by the disordered strength of fibers $p(\varepsilon_{th})$.

The constitutive response of softening bundles with fluctuating maximum slip number can also be obtained from **Eq. 3** by skipping the last term, which represents the contribution of fibers with failure index $k = K$. **Figure 7** compares the behavior of softening stick-slip bundles with constant and fluctuating maximum slip numbers where the average $\langle K \rangle$ was set to be equal to the fixed K values of the corresponding bundles. It is interesting to note that contrary to the hardening case, deviations of the corresponding constitutive curves are more pronounced for small deformations. The position of the maxima of the corresponding $\sigma(\varepsilon)$ curves nearly coincide, however, bundles of fluctuating K keep a lower load than their constant K counterpart. As the deformation ε increases the curves cross each other indicating the higher load bearing capacity of bundles with fluctuating K. For large deformation $\varepsilon \to \infty$ the stress must converge to zero with a constant maximum slip number, however, the final stiffness of bundles with fluctuating K is not zero. This is the effect of those fibers which are not allowed to slide $K = 0$, resulting in a finite asymptotic stiffness $E_a = g(0)E = e^{-\langle K \rangle}E$. Increasing the average slip number $\langle K \rangle$ the fraction of unbreakable fibers exponentially goes to zero making the difference of constant and fluctuating K bundles larger for low values of K (see **Figure 7**).

4 ANNEALED DISORDER OF FAILURE THRESHOLDS

In materials with a complex micro-structure slip events may be followed by a change of the local material properties. In our fiber bundle model this behavior can be captured up to some extent by assigning a new threshold value to the fiber after each slip event from the same probability distribution $p(\sigma_{th})$. This type of annealed disorder leads to a constitutive behavior qualitatively similar to the case of the quenched one, however, with a more complicated dynamics. After k slip events the load σ kept by a fiber is given by **Eq. 4** of the general model construction, however, now the stress threshold σ_{th} is not fixed for the fiber, instead after each consecutive slip event a new threshold is generated $\sigma_{th}^{(i)}$ from the same distribution $p(\sigma_{th})$. It has the consequence that the threshold strains $\varepsilon_{th}^{(1)}, \varepsilon_{th}^{(2)}, \ldots, \varepsilon_{th}^{k}$ of consecutive slips events can be obtained as

$$\varepsilon_{th}^{(k)} = \frac{\sigma_{th}^{(k)}}{a^k E} = \frac{\varepsilon_k}{a^k}, \tag{24}$$

where $\varepsilon_k = \sigma_{th}^{(k)}/E$ are strain values which have the same distribution $p(\varepsilon_{th})$ for the entire history of the fiber. **Eq. 24** shows that although the stress thresholds $\sigma_{th}^{(k)}$ are generated with the same distribution, the corresponding strain values ε_k still have to be transformed to obtain the strain thresholds, where fiber slips occur. The constitutive behavior of a single fiber and the relation of the variables $\varepsilon_{th}^{(k)}$ and $\sigma_{th}^{(k)}$ are illustrated in **Figure 8**.

Based on the above expressions the constitutive equation $\sigma(\varepsilon)$ of the entire bundle with a fixed number of allowed slip events K can be cast into the form

$$\sigma = E\varepsilon[1 - P(\varepsilon)] + E\sum_{k=1}^{K-1} a^k \int_{\varepsilon_{th}^{min}}^{\varepsilon} \int_{\varepsilon_{th}^{min}}^{\varepsilon-\varepsilon_0} \cdots \int_{\varepsilon_{th}^{min}}^{\varepsilon-\sum_{j=0}^{k}\varepsilon_j/a^j} \prod_{j=1}^{k} d\varepsilon_j p\left(\varepsilon_j/a^j\right) \left[1 - P\left(\varepsilon - \sum_{j=0}^{k}\varepsilon_j/a^j\right)\right] \left(\varepsilon - \sum_{j=0}^{k}\varepsilon_j/a^j\right) + Ea^K \int_{\varepsilon_{th}^{min}}^{\varepsilon} \cdots \int_{\varepsilon_{th}^{min}}^{\varepsilon-\sum_{j=0}^{k}\varepsilon_j/a^j} \prod_{j=1}^{k} d\varepsilon_j p\left(\varepsilon_j/a^j\right) \left(\varepsilon - \sum_{j=0}^{k}\varepsilon_j/a^j\right). \tag{25}$$

where again the load bearing contributions of the subsets of fibers of different slip numbers $k = 0, \quad 1, \ldots, K$ are summed up: the first term represents the load kept by fibers which are intact $k = 0$ at the deformation ε; the second one is the sum of the contributions of fibers which have undergone exactly $1 \le k < K$ slip events, and the last term captures the load bearing capacity of fibers after completing all the allowed K slip events. Note that the products of probability density functions occur due to the independence of consecutive slip events, additionally, the upper bounds of the integrals have also complex dependencies.

The constitutive responses of stick-slip bundles with quenched and annealed disorder are compared in **Figure 9** for the case of hardening with fixed values of the number of slip events K. It can be observed that the two sets of curves have a qualitatively similar behavior. For $K = 1$ there is no difference between the two types of disorder so that the corresponding curves must coincide, however, larger quantitative differences of quenched and annealed responses are observed for higher K values. The sequence of independent identically distributed failure thresholds of annealed disorder gives rise to broader plateau regimes with a higher value of the mean stress along the plateau. For large deformation both sets of curves converge to asymptotic straight lines whose slope $E_a = a^K E$ does not depend on the type of disorder. Due to the qualitative similarities of the macroscopic responses of quenched and annealed disorder stick-slip bundles, we skip the details of further comparisons.

5 DISCUSSION

We presented an extension of fiber bundle models of stick-slip dynamics incorporating the effect of stiffness change of the fibers after slip events, and the fluctuations of the number of stick-slip cycles fibers can experience under an increasing external load. Stick-slip dynamics implies that when the load of a fiber exceeds its local strength the fiber does not break, instead it slips which increases its relaxed length. As a consequence, the load of the fiber drops down to zero, however, the fiber retains its load bearing capacity. The stick-slip FBM has a high degree of complexity making it flexible to describe various materials' behaviors. In order to enhance the applicability of the model, we introduced a parameter which controls the change of fibers' stiffness after slip events in a multiplicative way allowing for both gradual degradation and stiffening. During their loading history fibers

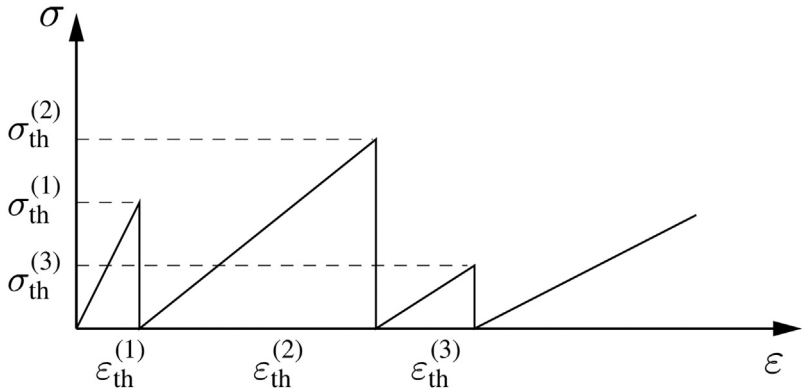

FIGURE 8 | Constitutive behavior of a single fiber with annealed disorder of the slip thresholds. The value of the stiffness parameter is $a = 0.8$ so that the fiber stiffness gradually decreases (compare to **Figure 1**). The consecutive thresholds $\sigma_{th}^{(k)}$ are drawn from the same probability distribution $p(\sigma_{th})$, then the corresponding strain thresholds $\varepsilon_{th}^{(k)}$ are obtained from **Eq. 24**.

can undergo a sequence of stick-slip cycles. In our model construction the failure thresholds where slip is activated can be either fixed for the entire failure process of the fiber (quenched disorder), or it can be sampled from a probability distribution (annealed disorder) representing fixed structural disorder of materials and the effect of the local change of the material's behavior after slip events, respectively. As another novel element of our study, the maximum number of slip events is treated as a random variable inside the bundle sampled from a probability distribution. The total number of slip events allowed and the threshold loads where slip is activated are independent random variables. After completing all the stick-slip cycles a fiber can either keep its final stiffness or it can suffer ultimate breaking, which result in global hardening and softening of the bundle in the limit of high deformation, respectively.

We analyzed the model in the mean field limit, i.e. global load sharing (GLS) was assumed. However, in stick-slip FBMs GLS does not imply equal load on fibers, because at a given strain fibers of the bundle can have different relaxed lengths and stiffness values. We derived closed analytic forms for the macroscopic constitutive response of the bundle both for quenched and annealed disorder of the slip thresholds. These results showed that on the macro-scale the bundle exhibits a plastic behavior, i.e. the $\sigma(\varepsilon)$ curves develop a plateau regime which becomes broader with increasing number of slips. We analyzed in details the role of the changing stiffness of fibers in the emergence of the plastic plateau. Our calculations revealed that the stiffness parameter controls the degree of overlap of the contributions of fiber subsets of different failure index. In the limit of low stiffness parameter $a \ll 1$, the plastic plateau is decorated with well separated maxima, while for slowly degrading stiffness $a \lesssim 1$ and high values of the slip number K a smooth horizontal plateau is obtained.

Releasing the load on the bundle, a permanent deformations remains, which increases monotonically with the maximum deformation reached before unloading started for hardening bundles, while in the softening case a non-monotonous behavior is obtained. The permanent deformation of softening bundles proved to be smaller than that of their hardening counterpart. The asymptotic value of the permanent deformation of hardening bundles can be used to characterize the extension of the plateau regime at different stiffness parameters a. Our calculations revealed that increasing the number of allowed slips K the extension of the plateau has a finite limit for stiffening bundles $a > 1$, while it diverges for stiffness degradation $a < 1$.

We showed that fluctuations of the number of stick-slip cycles allowed for fibers affect the behavior of both hardening and softening bundles. Comparing hardening bundles of constant and fluctuating slip numbers with the same average value revealed that larger fluctuations result in a narrower plastic regime affecting also the asymptotic stiffness and the permanent deformation of the bundle. For softening bundles the

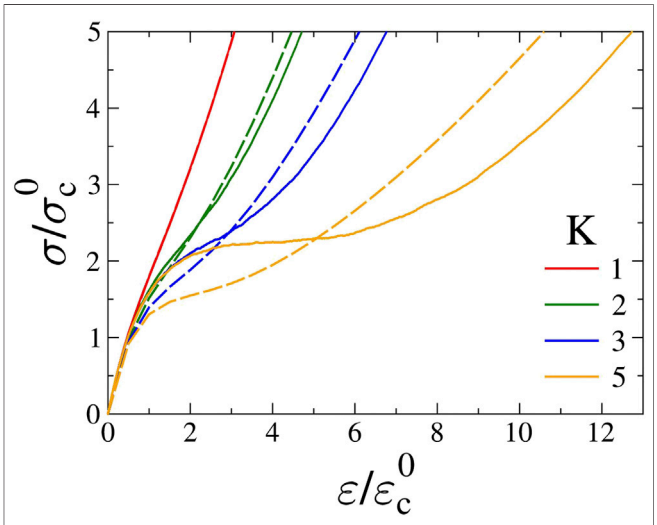

FIGURE 9 | Comparison of the constitutive curves of hardening stick-slip bundles with quenched (*dashed lines*) and annealed (*continuous lines*) failure thresholds for several values of the fixed number of allowed slip events K at the stiffness parameter $a = 0.8$.

fluctuations of the slip number result in lower and higher load bearing capacities at small and large deformations, respectively, compared to their constant slip number counterparts.

Annealed disorder of slip thresholds results in a qualitatively similar macroscopic response to quenched disorder, however, its description involves a higher mathematical complexity.

Here we focused on the effect of the changing stiffness and fluctuating slip number of fibers on the macroscopic behavior of a stick-slip FBM, and demonstrated that varying its parameters the model is capable to capture several aspects of the macro-scale consequences of stick-slip dynamics. The constitutive curves with the softening regimes and oscillations along the plateau can only be realized in strain controlled experiments. Under stress controlled loading slip events are followed by a load redistribution inside the bundle which can induce further slips and eventually can trigger an entire avalanche of slipping fibers until the bundle gets stabilized. As to the next, we are going to explore the effect of the varying stiffness and fluctuating slip number on dynamics and statistics of slip avalanches, which can have a relevance for the understanding of restructuring avalanches of granular materials and of earthquakes.

Although, the model is complex, still it could be further extended to fit to specific applications. For instance, when consecutive slip events result in the accumulation of internal damage of fibers, the degradation of fibers' stiffness may be accompanied by the reduction of fibers' strength. This correlation of local strength and stiffness can be captured by the model in such a way that at slip events fibers get a new failure threshold (annealed disorder) from a distribution which has the same functional form as the original one, however, its average is gradually reduced. Due to its flexibility, the model can serve as a starting point to develop more realistic micro-mechanical models of carbon nanotube reinforced polimeric composites where the high damping ability of the material originates from the stick-slip occurring at the CNT-matrix interface. Our approach can complement recently developed micro-mechanical models of CNT nanocomposites [43–45] providing an efficient framework for the representation of two sources of disorder (local strength and slip number), degradation and stiffening after slip events, and softening or hardening after the maximum slip number is reached. Work in this direction is in progress.

DATA AVAILABILITY STATEMENT

The raw data supporting the conclusions of this article will be made available by the authors, without undue reservation.

AUTHOR CONTRIBUTIONS

ZH, IK, and FK carried out analytical derivations, ZH performed computer simulations. ZH and FK performed the data analysis, conceived and designed the study and drafted the manuscript. All authors read and approved the manuscript.

FUNDING

The project is co-financed by the European Union and the European Social Fund. This research was supported by the National Research, Development and Innovation Fund of Hungary, financed under the K-16 funding scheme Project no. K 119967. The research was financed by the Thematic Excellence Programme of the Ministry for Innovation and Technology in Hungary (ED_18-1-2019-0028), within the framework of the Vehicle Industry thematic programme of the University of Debrecen.

ACKNOWLEDGMENTS

The authors are grateful for discussions with Gergő Pál.

REFERENCES

1. Herrmann HJ Roux S eds. Statistical models for the fracture of disordered media In: *Random materials and processes*. Amsterdam, Netherlands: Elsevier (1990).
2. Hansen A, Hemmer P, Pradhan S. The fiber bundle model: modeling failure in materials. In: *Statistical physics of fracture and breakdown*. Hoboken, New Jersey: Wiley (2015).
3. Kun F, Raischel F, Hidalgo RC, Herrmann HJ. Extensions of fiber bundle models. In: Bhattacharyya P Chakrabarti BK, editors. *Modelling critical and catastrophic phenomena in geoscience: a statistical physics approach. Lecture notes in physics*. Berlin, Germany: Springer-Verlag Berlin Heidelberg New York (2006). p. 57–92.
4. Hidalgo RC, Kun F, Kovács K, Pagonabarraga I. Avalanche dynamics of fiber bundle models. *Phys Rev E—Stat Nonlinear Soft Matter Phys* (2009) 80:051108. doi:10.1103/PhysRevE.80.051108
5. Danku Z, Kun F. Temporal and spacial evolution of bursts in creep rupture. *Phys Rev Lett* (2013) 111:084302. doi:10.1103/PhysRevLett.111.084302
6. Sinha S, Kjellstadli JT, Hansen A. Local load-sharing fiber bundle model in higher dimensions. *Phys Rev E—Stat Nonlinear Soft Matter Phys* (2015) 92: 020401. doi:10.1103/PhysRevE.92.020401
7. Danku Z, Ódor G, Kun F. Avalanche dynamics in higher-dimensional fiber bundle models. *Phys Rev E* (2018) 98:042126. doi:10.1103/physreve.98.042126
8. Andersen JV, Sornette D, Leung K. Tricritical behavior in rupture induced by disorder. *Phys Rev Lett* (1997) 78:2140–3. doi:10.1103/physrevlett.78.2140
9. Yoshioka N, Kun F, Ito N. Kertész line of thermally activated breakdown phenomena. *Phys Rev E—Stat Nonlinear Soft Matter Phys* (2010) 82:055102. doi:10.1103/PhysRevE.82.055102
10. Karpas E, Kun F. Disorder-induced brittle-to-quasi-brittle transition in fiber bundles. *Epl* (2011) 95:16004. doi:10.1209/0295-5075/95/16004
11. Roy S, Biswas S, Ray P. Modes of failure in disordered solids. *Phys Rev E* (2017) 96:063003. doi:10.1103/PhysRevE.96.063003
12. Roy S, Ray P. Critical behavior in fiber bundle model: a study on brittle to quasi-brittle transition. *Epl* (2015) 112:26004. doi:10.1209/0295-5075/112/26004
13. Roy C, Manna SS. Brittle to quasibrittle transition in a compound fiber bundle. *Phys Rev E* (2019) 100:012107. doi:10.1103/PhysRevE.100.012107
14. Peires FT. Tensile tests for cotton yarns. V.-"The weakest link," theorems on the strength of long composite specimens. *J Textil Inst* (1926) 17:T355–368.
15. Coleman BD. Time dependence of mechanical breakdown in bundles of fibers. III. The power law breakdown rule. *Trans Soc Rheol* (1958) 2:195–218. doi:10.1122/1.548830

16. Raischel F, Kun F, Herrmann HJ. Failure process of a bundle of plastic fibers. *Phys Rev E—Stat Nonlinear Soft Matter Phys* (2006) 73:066101. doi:10.1103/PhysRevE.73.066101
17. Nechad H, Helmstetter A, Guerjouma RE, Sornette D. Andrade and critical time-to-failure laws in fiber-matrix composites: experiments and model. *J Mech Phys Solid* (2005a) 53:1099. doi:10.1016/j.jmps.2004.12.001
18. Nechad H, Helmstetter A, Guerjouma RE, Sornette D. Creep ruptures in heterogeneous materials. *Phys Rev Lett* (2005b) 94:045501. doi:10.1103/PhysRevLett.94.045501
19. Kun F, Moreno Y, Hidalgo RC, Herrmann HJ. Creep rupture has two universality classes. *Europhys Lett* (2003) 63:347–53. doi:10.1209/epl/i2003-00469-9
20. Hidalgo RC, Kun F, Herrmann HJ. Creep rupture of viscoelastic fiber bundles. *Phys Rev E—Stat Nonlinear Soft Matter Phys* (2002a) 65:032502. doi:10.1103/PhysRevE.65.032502
21. Hidalgo RC, Kovács K, Pagonabarraga I, Kun F. Universality class of fiber bundles with strong heterogeneities. *Europhys Lett* (2008) 81:54005. doi:10.1209/0295-5075/81/54005
22. Roy C, Kundu S, Manna SS. Fiber bundle model with highly disordered breaking thresholds. *Phys Rev E—Stat Nonlinear Soft Matter Phys* (2015) 91:032103. doi:10.1103/PhysRevE.91.032103
23. Danku Z, Kun F. Fracture process of a fiber bundle with strong disorder. *J Stat Mech* (2016) 2016:073211. doi:10.1088/1742-5468/2016/07/073211
24. Hidalgo RC, Moreno Y, Kun F, Herrmann HJ. Fracture model with variable range of interaction. *Phys Rev E—Stat Nonlinear Soft Matter Phys* (2002b) 65:046148. doi:10.1103/PhysRevE.65.046148
25. Phoenix SL, Newman WI. Time-dependent fiber bundles with local load sharing. ii. general weibull fibers. *Phys Rev E—Stat Nonlinear Soft Matter Phys* (2009) 80:066115. doi:10.1103/PhysRevE.80.066115
26. Bhattacharyya P, Pradhan S, Chakrabarti BK. Phase transition in fiber bundle models with recursive dynamics. *Phys Rev E—Stat Nonlinear Soft Matter Phys* (2003) 67:046122. doi:10.1103/PhysRevE.67.046122
27. Curtin WA. Size scaling of strength in heterogeneous materials. *Phys Rev Lett* (1998) 80:1445. doi:10.1103/physrevlett.80.1445
28. Hidalgo RC, Grosse CU, Kun F, Reinhardt HW, Herrmann HJ. Evolution of percolating force chains in compressed granular media. *Phys Rev Lett* (2002c) 89:205501. doi:10.1103/PhysRevLett.89.205501
29. Michlmayr G, Or D, Cohen D. Fiber bundle models for stress release and energy bursts during granular shearing. *Phys Rev E—Stat Nonlinear Soft Matter Phys* (2012) 86:061307. doi:10.1103/PhysRevE.86.061307
30. Layton BE, Sastry AM. Equal and local-load-sharing micromechanical models for collagens: quantitative comparisons in response of non-diabetic and diabetic rat tissue. *Acta Biomater* (2006) 2:595. doi:10.1016/j.actbio.2006.05.013
31. Halász Z, Kun F. Fiber bundle model with stick-slip dynamics. *Phys Rev E—Stat Nonlinear Soft Matter Phys* (2009) 80:027102. doi:10.1103/PhysRevE.80.027102
32. Halász Z, Kun F. Slip avalanches in a fiber bundle model. *Europhys Lett* (2010) 89:26008. doi:10.1209/0295-5075/89/26008
33. Michlmayr G, Chalari A, Clarke A, Or D. Fiber-optic high-resolution acoustic emission (AE) monitoring of slope failure. *Landslides* (2017) 14:1139–46. doi:10.1007/s10346-016-0776-5
34. Furst EM, Gast AP. Micromechanics of dipolar chains using optical tweezers. *Phys Rev Lett* (1999) 82:4130. doi:10.1103/physrevlett.82.4130
35. Emile O, Foch AL, Vollrath F. Time-resolved torsional relaxation of spider draglines by an optical technique. *Phys Rev Lett* (2007) 98:167402. doi:10.1103/PhysRevLett.98.167402
36. Suhr J, Koratkar NA. Energy dissipation in carbon nanotube composites: a review. *J Mater Sci* (2008) 43:4370–82. doi:10.1007/s10853-007-2440-x
37. Zhou X, Shin E, Wang K, Bakis C. Interfacial damping characteristics of carbon nanotube-based composites. *Compos Sci Technol* (2004) 64:2425–37. doi:10.1016/j.compscitech.2004.06.001
38. Capelli A, Reiweger I, Lehmann P, Schweizer J. Fiber-bundle model with time-dependent healing mechanisms to simulate progressive failure of snow. *Phys Rev E* (2018) 98:023002. doi:10.1103/PhysRevE.98.023002
39. Capelli A, Reiweger I, Schweizer J. Studying snow failure with fiber bundle models. *Front Phys* (2020) 8:236. doi:10.3389/fphy.2020.00236
40. Pradhan S, Hansen A, Chakrabarti BK. Failure processes in elastic fiber bundles. *Rev Mod Phys* (2010) 82:499. doi:10.1103/revmodphys.82.499
41. Vollrath F, Porter D. Spider silk as archetypal protein elastomer. *Soft Matter* (2006) 2:377–85. doi:10.1039/b600098n
42. Yates R, Goodman D. *Probability and stochastic processes: a friendly introduction for electrical and computer engineers*. Hoboken, NJ: John Wiley & Sons (2005).
43. Huang Y, Tangpong X. A distributed friction model for energy dissipation in carbon nanotube-based composites. *Commun Nonlinear Sci Numer Simulat* (2010) 15:4171–80. doi:10.1016/j.cnsns.2010.01.017
44. Wang TY, Liu SC, Tsai JL. Micromechanical stick-slip model for characterizing damping responses of single-walled carbon nanotube nanocomposites. *J Compos Mater* (2016) 50:57–73. doi:10.1177/0021998315570371
45. Formica G, Lacarbonara W. Three-dimensional modeling of interfacial stick-slip in carbon nanotube nanocomposites. *Int J Plast* (2017) 88:204–17. doi:10.1016/j.ijplas.2016.10.012

Conflict of Interest: The authors declare that the research was conducted in the absence of any commercial or financial relationships that could be construed as a potential conflict of interest.

frontiers in Physics

ORIGINAL RESEARCH
published: 29 March 2021
doi: 10.3389/fphy.2021.644815

A Stochastic Model Based on Fiber Breakage and Matrix Creep for the Stress-Rupture Failure of Unidirectional Continuous Fiber Composites 2. Non-linear Matrix Creep Effects

Amy Engelbrecht-Wiggans[1]* *and Stuart Leigh Phoenix*[2]

[1] Theiss Research, La Jolla, CA, United States, [2] Sibley School of Mechanical and Aerospace Engineering, Cornell University, Ithaca, NY, United States

OPEN ACCESS

Edited by:
Ferenc Kun,
University of Debrecen, Hungary

Reviewed by:
Purusattam Ray,
Institute of Mathematical Sciences, India
Srutarshi Pradhan,
Norwegian University of Science and Technology, Norway

***Correspondence:**
Amy Engelbrecht-Wiggans
aee52@cornell.edu

Specialty section:
This article was submitted to Interdisciplinary Physics, a section of the journal Frontiers in Physics

Received: 21 December 2020
Accepted: 26 February 2021
Published: 29 March 2021

Citation:
Engelbrecht-Wiggans A and Phoenix SL (2021) A Stochastic Model Based on Fiber Breakage and Matrix Creep for the Stress-Rupture Failure of Unidirectional Continuous Fiber Composites 2. Non-linear Matrix Creep Effects. Front. Phys. 9:644815. doi: 10.3389/fphy.2021.644815

Stress rupture (sometimes called creep-rupture) is a time-dependent failure mode occurring in unidirectional fiber composites under high tensile loads sustained over long times (e. g., many years), resulting in highly variable lifetimes and where failure has catastrophic consequences. Stress-rupture is of particular concern in such structures as composite overwrapped pressure vessels (COPVs), tension members in infrastructure applications (suspended roofs, post-tensioned bridge cables) and high angular velocity rotors (e.g., flywheels, centrifuges, and propellers). At the micromechanical level, stress rupture begins with the failure of some individual fibers at random flaws, followed by local load-transfer to neighboring intact fibers through shear stresses in the matrix. Over time, the matrix between the fibers creeps in shear, which causes lengthening of local fiber overload zones around previous fiber breaks, resulting in even more fiber breaks, and eventually, formation clusters of fiber breaks of various sizes, one of which eventually grows to a catastrophically unstable size. Most previous models are direct extension of classic stochastic breakdown models for a single fiber, and do not reflect the micromechanical detail, particularly in terms of the creep behavior of the matrix. These models may be adequate for interpreting experimental, composite stress rupture data under a constant load in service; however, they are of highly questionable accuracy under more complex loading profiles, especially ones that initially include a brief "proof test" at a "proof load" of up to 1.5 times the chosen service load. Such models typically predict an improved reliability for proof-test survivors that is higher than the reliability without such a proof test. In our previous work relevant to carbon fiber/epoxy composite structures we showed that damage occurs in the form of a large number of fiber breaks that would not otherwise occur, and in many important circumstances the net effect is reduced reliability over time, if the proof stress is too high. The current paper continues our previous work by revising the model for matrix creep to include non-linear creep whereby power-law creep behavior occurs not only in time but also in shear stress level and with differing

exponents. This model, thus, admits two additional parameters, one determining the sensitivity of shear creep rate to shear stress level, and another that acts as a threshold shear stress level reminiscent of a yield stress in the plastic limit, which the model also admits. The new model predicts very similar behavior to that seen in the previous model under linear viscoelastic behavior of the matrix, except that it allows for a threshold shear stress. This threshold allows consideration of behavior under near plastic matrix yielding or even matrix shear failure, the consequence of which is a large increase in the length-scale of load transfer around fiber breaks, and thus, a significant reduction in composite strength and increase in variability. Derivations of length-scales resulting from non-linear matrix creep are provided as Appendices in the Supplementary Material.

Keywords: failure probabilities, stress rupture behavior, proof testing, composite overwrapped pressure vessels, local load sharing model, Weibull distribution, non-linear viscoealsticity

INTRODUCTION

From a materials engineering perspective, stress rupture (sometimes called creep-rupture) is a time-dependent failure mode in unidirectional, continuous fiber composites that are primarily loaded in tension over long time periods and whose failure is typically catastrophic. Such composites, often consisting of carbon fibers in an epoxy matrix, operate at either ambient temperatures, or temperatures well below the matrix glass transition temperature. Examples of such structures include composite overwrapped pressure vessels (COPVs), tension members in infrastructure applications such as cables in suspended roofs, post-tensioned bridge platform cables, and rotors spinning at high angular velocity such flywheels, centrifuges and propellers, where hoop and radial stresses become very large. In such cases, stress rupture failure is explosive resulting in sudden release of potential and/or kinetic energy and in the case of COPVs the stored contents can also be combustible. Typically, stress-rupture occurs with little or no warning, and its unpredictable nature necessitates large safety factors even when a considerable experimental data base exists to support various life prediction methodologies.

In engineering applications, which are often subject to life-safety requirements, much of the concern stems from the fact that reliabilities in such structures must be extremely high (e.g., probability of failure $<10^{-8}$) over a specified lifetime (typically many years) under a specified service load. No amount of brute-force testing can directly demonstrate such reliabilities, especially when test objects in the laboratory necessarily differ from actual service components in key respects, such as being much smaller in overall material volume under load. Thus, size effects are a key issue, and predicting stress-rupture lifetime, and particularly the lower tail of the lifetime distribution for a given load, inevitably requires sophisticated modeling in light of any previous, or simultaneously generated, test data.

The general experimental approach to characterizing the stress-rupture behavior of such a carbon fiber/epoxy structures in applications is to first determine the strength distribution of subscale artifacts, such as epoxy-impregnated strands, or small laboratory scale pressure vessels, which have been filament wound using the same materials. Typically, a Weibull strength distribution is observed, and the Weibull scale and shape parameter values are estimated. Then several fixed stress levels are selected, and for each level multiple test artifacts are placed under test and failures recorded over time, which in many cases requires many months and sometime years to gather sufficient lifetime data for prediction purposes. Typically, the lifetime data is also found to be of Weibull form, but with extremely high variability (low Weibull shape parameter value typically less than unity). Furthermore, statistical estimation techniques, such as maximum likelihood, must be used to deal with censored test samples, since at lower stress levels, only a few of the test samples may have failed.

While methods vary for analyzing and presenting such strength and stress-rupture data, the general approach is often to plot the mean lifetime (or Weibull lifetime scale parameter) vs. fixed stress level on log-stress vs. log-lifetime coordinates, and to fit a power law, i.e., lifetime varies as stress level to a negative power, which is often of the order of 100 in magnitude. Some effort may also be made to estimate the shape parameter for Weibull lifetime at each stress level, hopefully the same for each, and from the results, to determine a stress level that results in the desired high reliability, i.e., low probability of failure over the chosen structural component lifetime.

The previously mentioned approaches to modeling stress-rupture lifetime are discussed in detail in [1–4] where it is shown that such a lifetime estimation approach is fraught with many serious difficulties some of which are as follows: First, there are serious practical limitations in sample sizes that can be tested at each stress level. Second, since the variability in lifetime is very high, the uncertainty in any reliability estimate is also very high to the point of resulting in unusable reliability bounds (much less providing the ability to select between competing models, which are typically phenomenological). Third, the typically used "proof test" approach to screen out weaker, and presumably, lower reliability specimens is fraught with difficulties, such as what proof stress level to use, and whether damage is caused to the structure in the act of proof testing that cancels any potential benefit, perhaps even making the structure even less reliable. Thus there is

a need for the development of sophisticated models that consider the micromechanics and statistics of fiber load-sharing and failure, and which are reasonably tractable and whose predictions can be defended. Since we are most interested in the high reliability (low probability of failure) region of various distributions, we are able to take advantage of various power-law approximations to the lower tails of various Weibull distributions to construct reliability estimates. This is seen throughout the derivations.

Before developing the model, and in view of the broad audience, we provide some context regarding the breadth of fiber bundle models that have played a key role in the study of failure processes in a heterogeneous materials, as conducted in statistical physics, materials, and mechanics communities. Some excellent reviews from various perspectives are provided in [5–10]. The simplest versions focus on material strength in response to an applied load, and where individual fibers are assumed to have variability in their strengths following some probability distribution, such as uniform or Weibull, the latter being common to engineering applications [9, 10]. Under a tensile bundle load some fibers fail, and their loads are transferred to their survivors, some of which may also fail due to their increased loads, leading to more load redistribution, and so on. Depending on applied bundle load, the bundle may either reach a stable state where some smaller group of surviving fibers are strong enough to support the bundle load, or, all survivors are exhausted and the bundle collapses. As discussed below, details on the evolution of this failure process depend on the bundle load magnitude, the fiber strength distribution, the bundle size (number of fibers), and critically on the mechanism by which fibers share and redistribute load.

In the simplest bundle models, load-sharing mechanisms fall between two extremes: (i) equal load-sharing (ELS) where the loads of failed fibers are redistributed equally onto all survivors, and (ii) local load sharing (LLS), where the loads of failed fibers are transferred onto their closest surviving neighbors, as expanded upon in [5–10]. Under ELS fiber failure patterns tend to be diffuse and percolation-like, whereas under LLS, clusters of breaks nucleate and grow reminiscent of catastrophic cracks. The contrast in the two pattern types depends on the variability in fiber strength. Larger variability results in increasingly similar failure patterns across the load redistribution range from ELS and LLS, however, that the bundle strength statistics ultimately differ as bundle size grows indefinitely, as shown in [9, 10].

In statistical physics, various aspects are of interest, such as critical behavior, recursive failure dynamics, universality classes, burst distributions and avalanches, precursors (warnings) of global failure, cross-over behavior, and localization in terms of forming of critical clusters vs. mean field analysis [5–8]. In both the physics and engineering communities size effects are a key issue [9–13] because the size scales of multiple laboratory test samples are necessarily orders of magnitude smaller than their monolithic structural counterparts in applications. Approaches to the study of such models vary from being purely analytical (requiring various simplifying assumptions but yielding profound insight) to numerical Monte Carlo methods where fiber strengths and load redistribution for evolving failure configurations are directly calculated. Numerical simulation has limitations, however, because bundle structures of interest can have more than 10^8 fiber elements (e.g., carbon fiber/epoxy composite overwrapped pressure vessels) whereas eventual scaling behavior may be inconclusive in bundles of 10^4 to 10^5fiber elements, and require 10^3replications to obtain accurate statistics. Additionally, while some researchers use mean field approaches, attempting to calculate the limiting strength of bundles approaching infinite size, others focus on obtaining distributions for strength of finite-size bundles especially deep into their lower tails particularly when high reliability is of concern. For instance finding a particular bundle load for which the failure probability is $<10^{-\aleph}$ may be of interest, where $\aleph \geq 8$ (sometimes referred to as the "number of nines" of the reliability, $1-10^{-\aleph}$) would require at least $10^{\aleph+1} = 10^9$ replications, currently a computationally prohibitive number. How to extend to such low probability levels for large-scale structures such as carbon-fiber/epoxy pressure vessels is a key challenge and is where theoretical modeling and scaling arguments become powerful tools, as is addressed in this paper.

Generalizations of simple fiber bundle models for material strength, particularly for longer structures, typically assume fiber flaw occurrence along an individual fiber following a compound Poisson point process in distance and flaw strength (local failure stress). When the flaw strength follows a power law, the result is a Weibull distribution for fiber strength vs. length that satisfies weakest link statistics. We call this a Weibull-Poisson (WP) fiber strength model. For long bundles with fibers bonded together in a flexible matrix, or in a stiff matrix but where the matrix has a low yield strength or the fiber-matrix interface is weak and slip occurs, ELS generalizes to global load-sharing (GLS). Under GLS a fiber can fail at multiple locations along its length, however, at any cross-sectional composite plane, a locally failed fiber may still carry some load depending on the distance from the plane to its closest break. In cases where LLS still applies at a cross-section, behavior also depends on whether the bundle is planar (i.e., each fiber has only two flanking neighbors) or the fibers are packed in a square, hexagonal or random array in which case failing fibers have many neighbors onto which to redistribute their loads. Thus, milder versions of LLS emerge at a plane where some load is transferred to next-nearest and even further neighbors following some power-law decay in lateral distance. In both GLS and LLS failure tends to concentrate in transverse planes whereby material failure is well-described using a chain-of-bundles approach [9, 13], which means that size effects become important [11–13].

The failure of heterogeneous materials typically involves time-dependence of some form, and in accommodating such features, fiber bundle models become more complex, but also richer in features, as can be seen in [14–55]. Time dependence can enter into the bundle failure process in various ways: First, the fiber breakdown process may be thermally activated as for instance in [14–29], or may involve time-dependent kinetics of

flaw growth in the fiber as in [30, 31]. On the other hand, the matrix may creep, or the fiber/matrix interface may slip over time, thus causing relaxation in broken fibers and overloading of others [32–55], thus altering the length scale of fiber-to-fiber load transfer.

In the case of the former where fiber load-sharing, ranging from ELS to LLS, is by itself time independent, many models for time-dependent fiber failure involve a breakdown rule with the fiber failure rate depending on fiber stress level raised to a power, or as an exponential in fiber stress level. These rules are often tied to activation energy ideas of molecular bond failure, depending on the absolute temperature. In such cases, the fiber lifetime distribution under fixed load may be taken as exponential (constant hazard rate over time) and in others, a memory integral of past stress history is involved. This integral then becomes the argument of a second function controlling the shape of the lifetime distribution, and when of power form and the fiber is under a constant stress, Weibull fiber lifetime results. Several works specifically focus on such time-dependent fiber bundles as well as more elaborate network and lattice extensions, a sampling of which are discussed in [14–29]. In papers involving varying ranges of lateral load transfer somewhere between the ELS and LLS extremes, crossovers from mean-field to short range behavior are seen where break clusters form and instability is seen. To span ELS to LLS, the degree of localization also depends on the magnitude of the power-law breakdown exponent. Even in LLS bundles, one may see ELS-like diffuse fiber failure when the power-paw exponent approaches two and especially below 1 as shown in [24–27].

The works [14–29], which span the last 25 years of research, reveal surprising consistency in the overall behavior observed, in terms of size effects, localization in cluster growth and the types of lifetime distributions obtained, especially in the lower tails. Numerical Monte Carlo methods have become more efficient and computational power has increased, for a bundle with a given geometric and load-sharing complexity, by two to three orders of magnitude in size, which has been critical to providing insight into ultimate convergent (or divergent) behavior as the size scale increases. Fortunately, analytical models with various idealizations based on LLS and GLS modeling approaches have proven very effective in uncovering characteristics of bundle lifetime distributions deep into their lower tails. In cases where a clear choice between an LLS vs. a GLS modeling approach is ambiguous, it often happens that the two approaches result in surprisingly similar lifetime distribution shapes.

Other bundle models with time-dependent fibers (or analogs at the molecular scale) involve unique approaches [32–34] to specialized circumstances. For instance [32], which models a metal-matrix composite, involves a creeping, elasto-plastic matrix, and fibers that have some mix of strength behavior and time dependent degradation, all treated in a finite-element framework. Another approaches fiber behavior using a kinetic Monte-Carlo algorithm based directly on thermal fluctuations [33]. In another, fibers constitute a molecular network and a molecular dynamics approach is used [34].

Yet another group of models [35–37], involve fibers that are essentially elastic but upon failure undergo slow relaxation behaving as Maxwell elements. In [35], the fiber strength follows a uniform distribution and the modeling is purely GLS with broken fibers slowly shedding load to their survivors. In [36] fiber strengths are assumed Weibull a with shape parameter of two, whereupon bundle lifetime was found to be lognormal. In [37] the load-sharing ranged between GLS and LLS using a power-law, variable range of interaction rule, and again Weibull fiber strength. The two universality classes associated with GLS vs. LLS extremes appeared robust.

The focus in the current paper is on time-dependent bundle models where the fibers are brittle, initially continuous, time-independent, and that are aligned in a polymer matrix that itself supports negligible tensile load. The fibers have WP strength properties and time dependence enters through matrix shear creep around fiber breaks, which over time increases the length-scale of fiber load transfer at breaks. Examples of models in an ELS-GLS framework are described in [38–41], where in [38–40] plots of stress level vs. the logarithm of the mean lifetime is of interest, whereas in [41] the interest is on the residual composite strength after considerable time spent under constant load. These models do not focus on the nature of the lifetime distribution over time given the applied stress level. Of particular interest are such bundle models under LLS, several of which are discussed in [42–55]. The first two models [42, 43] are predecessors to the model we develop later and involve both theory and experiments on the strength and creep-rupture of seven-fiber, micro-composites of carbon fibers in an epoxy. They demonstrate various features of interest in the current paper, including Weibull fiber strength, distributions for micro-composite strength with Weibull "envelopes" having segments predicted by LLS theory, Weibull lifetime distributions also having Weibull envelope segments, and lastly, plots of log-load vs. log-lifetime behavior whose slopes depend on the shape parameter for fiber strength and the power-law creep exponent in time. Also, [44] contains a supporting analytical/numerical model for composite creep-rupture involving Weibull fibers with planar and hexagonal fiber packing in a linearly viscoelastic matrix.

Two related works [45, 46], present both theory and experimental results on the strength and lifetime of epoxy-impregnated carbon fiber strands. The models, however, are largely phenomenological and do not directly build on micromechanical LLS behavior with matrix creep. Nonetheless, such microstructural behavior arguably underlies the behavior observed. Time-dependence is reflected in the epoxy creep compliance, including time-temperature shift factors. This framework provides coherence to both the strength and the lifetime distributions obtained, respectively, at various strain rates and fixed stress levels, and at temperatures from 298°K to 443°K. Strand strength followed a Weibull distribution, and lifetime distributions were shown where the scale parameter had log-log dependence through a function of normalized time based on the matrix creep response. Overall, the experimental behavior seen is consistent with the model results we develop later.

In a sequence of papers by Bunsell et al. [47–55], a model has been developed that considers the lifetime of unidirectional carbon fiber-epoxy composites under sustained loads, and where

the main application is filament wound pressure vessels. In [47] the work begins with numerical modeling of the micro-mechanisms of fiber-to-fiber load transfer resulting from WP fiber failures. In [48], the load-transfer mechanism over time is altered by relaxation due to the viscoelastic and plastic behavior of the matrix, also causing locally increasing loads on neighboring fibers. In larger scale structures, these processes are used in [49] to model fiber break progression in a multi-scale framework, involving representative volume elements (RVEs) applicable to both strength and lifetime testing. In the latter, delayed fiber failures occur as new flaws are exposed thus leading to growing fiber break clusters and their coalescence into a critical damage state causing composite failure. Their model is applied in [50] to carbon fiber-epoxy matrix pressure vessels where the issue of proof testing is raised, and where the authors comment as follows:

> *"At present, there are no proof testing techniques or in-service reliability assessments techniques, which are mentioned in standards that are suitable or based on the failure processes known to control lifetimes of composite structures."*

Later in the same paragraph, the authors say:

> "*A hydraulic [proof] test on a composite pressure vessel has only* one *clear outcome, which is that fibers, which ordinarily would not have broken, fail during the test and the vessel is closer to failure than it was before the test, as is illustrated in Figure 2.*"

Much of their work in [50] is directed at determining an appropriate proof test level, for both new pressure vessels and pressure vessels that have seen pressurized service over long time periods. Investigating the issue of proof-testing is also a primary focus in the model we develop later.

In later works [51–55], these authors extend their RVE modeling in terms of the formation and evolution of small clusters of breaks called of *i*-plets of various sizes (e.g., two-plets, four-plets, eight-plets, 16-plets, 32-plets, …). The focus is on critical damage states in tension testing [51], sustained loading over time [52], and laminated structures [53]. The work in [54, 55] looks deeper into critical damage states in terms of *i*-plets as precursors to imminent failure and on the possibility of determining a lower threshold for applied composite stress below which the lifetime becomes infinite [55]. Overall, the impressive multi-scale model developed in [47–55] is computationally intensive so that Monte Carlo replications beyond a few 100 samples are currently impractical. Except in [55] where 100 replications were performed, the focus was largely on mean lifetime behavior, rather than the form of lifetime distributions, particularly in their lower tails. Nonetheless the overall failure process is qualitatively very similar to that which we develop later, and thus, some of our results may be of use in extending their models in [47–55].

As with many models described previously, a key assumption in the model we develop later is that individual carbon fibers are time independent, that is, essentially immune from creep rupture at typical temperatures of interest. This has been established in the work of Farquhar et al. [56]. A second assumption is that the mechanics of fiber stress-relaxation and load transfer around fiber breaks is accurately described by a non-linear matrix creep law, including a matrix plastic-like yielding effect. Over the past two decades there have been many papers [57–62], that have used micro-Raman spectroscopy and other techniques to measure time-dependent stress-relaxation and load transfer around fiber breaks in arrays of carbon fibers in an epoxy matrix. These experiments have been interpreted using sophisticated shear-lag modeling in [59–62] assuming elastic fibers and a linearly viscoelastic matrix, and which reveal the occurrence of varying degrees of shear yielding and debonding at the fiber-matrix interface, particularly at fiber strains approaching fiber failure. Thus, the assumption of a linearly elastic-perfectly bonded matrix requires revision, as will be key in our modeling approach in later sections. Indeed, there are several theoretical works [63–67] that allow us to make such revisions.

Our model involves the growth of clusters of fiber breaks to critical size. The concept of critical cluster formation under LLS has been a feature of various models discussed earlier. In this work we draw heavily on the mechanics of fiber load transfer around breaks as pioneered in the work of Hedgepeth and NASA associates [68–70]. The clusters in our model are idealized as growing in a planar fashion, whereas one might expect fiber breaks to be staggered out of plane. However, near planar cluster growth is often seen [71], and in effect clusters act as though they are increasingly planar as the length scale of load transfer increases over time [44]. We especially note a body of work [9, 10, 44, 72–76] specifically devoted to growth of clusters of fiber breaks to critical size, and the associated probability calculations through analysis and Monte Carlo simulation. Actual clusters seen in Monte Carlo simulations over time often have a far more random shape than the idealized clusters we consider. However, despite their differing appearance, upon reaching catastrophic instability the resulting failure distributions are remarkably similar to the point where only a small scaling adjustment is necessary to create congruence deep into the lower distribution tails. This behavior holds up even for Weibull shape parameters in the range of 2 or 3, which is below those for carbon fibers of interest in this paper. A group of recent papers [74–76] is very insightful regarding the nature of the critical cluster concept in LLS, and the limited role played by local ELS behavior within small groups of fiber failures but embedded within an overall LLS framework, and resulting distributions shapes and size scaling. These findings are remarkable and when experiment does not match theory, one may better focus more broadly on variability introduced in fabrication of a structure, rather than just on shortcomings in modeling assumptions. For instance, in [77] various fiber packings were considered including square, hexagonal and random, and yet the results proved surprisingly robust. Similar robust behavior was noted in [26, 27] working with distorted triangular lattices. Such details are less important that might first be suspected, which perhaps explains why fiber bundle models, with all their idealizations, work so well in the first place.

The focus of this paper, therefore, is to revisit and further develop our previous model [78] that took into account not

only the statistical failure of individual fiber elements in the composite, but also linearly viscoelastic matrix behavior in shear as the matrix locally transfers loads from broken fibers elements to neighboring intact fiber elements over a length-scale that increases over time.

As was described above in the context of a wide range of fiber bundle models, stress rupture is caused by fiber breakage occurring over time, where individual fiber breaks ultimately form clusters that increase in size until one becomes unstable and the composite fails catastrophically. A key aspect is that the load once carried by a broken fiber is locally transferred to its neighboring fibers through shear in the matrix, thus creating stress concentrations in these neighbors, which then grow in time especially as fiber breaks form in clusters that grow. A key driver of the failure process is that the local length-scale of these overloads increases over time as the matrix creeps in shear so that, over time, more and more fiber flaws are exposed to stresses that cause them to fail, despite having survived the applied service load absent any stress-concentrations, or even loads from a proof test. Thus, a critical aspect of this stress-rupture process occurring in the composite over time, is that it occurs even if the fibers themselves are immune to stress-rupture, which is essentially the case for carbon fibers.

The stress rupture failure process described above is the basis for the stochastic fiber breakage (SFB) model [78], which accounts for the relevant micromechanics of fiber-to-fiber load transfer in the presence of matrix creep, and the statistics of fiber strength and flaw occurrence in determining the overall lifetime distribution. Several other models have been applied to describe stress-rupture composite lifetimes; however, these models have largely been phenomenologically based on single fibers, as described in [14–19, 79], some of which are compared in [1]. In developing the micro-mechanically based SFB model in [78], many simplifying assumptions were necessary.

One key assumption was that the matrix is linearly viscoelastic, and creeps in shear following a power-law in time. This assumption has been used in shear-lag modeling [63–65] and mathematically builds on models assuming elastic fibers and an elastic matrix. Associated with this assumption, however, is that the matrix and the fiber/matrix interface are immune to failure in shear, which may be an unrealistic assumption when fiber breaks first occur, or clusters become large. Of course, over time, matrix creep relaxes these initially high shear stresses, however, it is known that in many circumstances of high fiber volume fraction and fiber strength the initial shear stresses around fiber breaks exceed the matrix yield strength or interfacial shear strength for fiber-matrix debonding. The SFB model in [78] does not accommodate such non-linear matrix phenomena, although qualitatively and using rough approximations, their consequences can be appreciated as significant when they occur. Thus, to accommodate such non-linear matrix behavior in shear, Mason et al. [66] investigated the case where the matrix undergoes non-linear creep in shear, both in stress and time. The current paper extends the SFB by incorporating the non-linear results in [66] into our previous model in [78].

Lastly, we discuss the effect of proof testing on composite lifetime in this revised version of the SFB model with non-linear matrix behavior, and how the additional parameters that arise allow us to accommodate non-linear matrix behavior such as plastic-like matrix yielding, yet preserve the overall character of the results.

Section Overview of Context of the Stochastic Fiber Breakage Model and Forms of Key Results provides a brief overview of the context of the SFB model in applications as well as various distribution forms that will expanded upon in subsequent sections. Section Modeling the Instantaneous Composite Strength and Determining its Distribution provides a derivation of the distribution for "short-term" composite strength, in circumstances where the timescale for matrix creep is assumed too short to affect the strength behavior, as was the case in [78]. However, certain parameters will be defined in anticipation of non-linear matrix effects that will require revisions to the model of [78].

Section Modeling Composite Lifetime in Stress Rupture and Determining its Distribution derives the distribution for composite lifetime, building on the methods used in Section Modeling the Instantaneous Composite Strength and Determining its Distribution and previously in [78], but also incorporating non-linear viscoelastic behavior to the matrix, using a variation of the load transfer length explored in [66] and expanded upon in **Appendices A–D** (All Appendices are provided in the Supplementary Material linked to the paper). In **Appendix A**, context is provided for how various parameters arise and the roles they play, particularly with respect to the growth in time of the characteristic load-transfer length. **Appendices B,C** derive results accommodating shear-driven increases in the length scale of load-transfer on surviving fibers around a growing cluster of fiber breaks. In **Appendix D** we discuss a simpler version of the non-linear creep model in [66], which is analytically solvable for all the 3-fiber cases in **Appendix A**, including those where the exponent on time is not unity. The behavior of crucial quantities, such as the length scale of fiber load transfer over time, turn out to be virtually identical.

Section Lifetime Distribution of a Composite Component that has Survived a Proof Test derives the distribution for lifetime of a composite component that has survived an initial proof-test up to some fraction of its initial strength (or has been overloaded by some multiplier of its ultimate service stress). Section Results and Discussion summarizes the influence of non-linear matrix creep on various parameters governing the distributions for composite strength and lifetime, and illustrates various results and non-linear effects in graphical form where the effects of varying certain key parameters are discussed, paying special attention to more subtle volume effects.

Section Conclusions concludes with some comments on key distinguishing features of the model that result from extending into the non-linear range the viscoelastic matrix creep behavior in our previous work [78]. We also provide some additional context on the overall stress-rupture problem in unidirectional composite structures that goes beyond the task of developing a model, as was done in this paper.

OVERVIEW OF CONTEXT OF THE STOCHASTIC FIBER BREAKAGE MODEL AND FORMS OF KEY RESULTS

Load Profiles Applied to the Composite and Desired Strength and Lifetime Distributions

Ramp Loading to Determine Composite Strength

The first load history of interest is the ramp loading for determining the composite strength. This is given by:

$$\sigma(t) = Rt, \quad t \geq 0 \tag{1}$$

where t is time and the parameter, $R > 0$, is the loading rate or stress rate. Typically, R is sufficiently fast to cause failure in 20–200 s, and where such failure times are shorter than a particular characteristic time, t_c, for matrix creep in shear, especially the fraction of time spent closer the failure load where most fiber breakage occurs. As such, the time-dependence of the matrix is typically ignored when modeling composite strength behavior, and we can treat the matrix as though it is purely elastic (though there will be exceptions and subtleties worthy of discussion).

In this case, the goal is to calculate the distribution function, $H_V(\sigma)$, for the strength of the composite, in terms of applied stress level, $\sigma > 0$, which will turn out to be approximately of Weibull form with scale and shape parameters, $\hat{\sigma}_V$ and $\hat{\alpha}$, respectively, that are to be determined from the model and where V is the composite volume expressed as the total number of fiber elements it contains, each with characteristic length, δ_c. Note that applied stress is to be interpreted as applied force divided by some overall fiber material cross-sectional area of the structure, and will not the same as the elevated local stress on a particular fiber element that happens to be next to a newly broken fiber element, and thus, is also supporting part of that fiber element's original load.

Constant Load in the Study of Composite Stress-Rupture Lifetime

The second load history of interest is that used in modeling composite lifetime in stress rupture. In this case, applied stress is assumed to be constant over all time, i.e.,

$$\sigma(t) = \bar{\sigma}, \quad t \geq 0 \tag{2}$$

where $\bar{\sigma} > 0$ is the applied stress level (fiber force over overall fiber material cross-sectional area of the loaded structure), and in practice, is typically only a fraction of the Weibull scale parameter for composite strength measured using the ramp loading (1), that is, $\bar{\sigma} < \hat{\sigma}_V$. In reality, the initial loading of the composite up to stress level, $\bar{\sigma}$, cannot be performed instantaneously and typically requires an initial ramp loading following load-history (1), where R is sufficiently rapid. However, time-dependence of the matrix under such initial loading rates, typically has a negligible effect on the resulting lifetime distribution at times of interest well-beyond the characteristic time, t_c, mentioned above. Note that this applied stress can only be supported as long as the elevated local fiber stresses near some growing cluster of fiber breaks in the material, have not reached the point where cluster growth becomes unstable and catastrophic.

In this case, the goal is to calculate the distribution function, $H_V(t;\bar{\sigma})$, for the lifetime of the composite, for times, $t \gg t_c$, which will also be of the Weibull form with scale and shape parameters, $\hat{t}_V$ and $\hat{\beta}$, respectively, and where V is the previously defined composite volume. We will find that $\hat{t}_V = t_c\left(\bar{\sigma}/\hat{\sigma}_V\right)^{-\hat{\rho}}$ where $\hat{\rho}$ is a power-law exponent that will characterize the dependence of the lifetime on the inverse of the applied stress level, $\bar{\sigma}$.

Stress-Rupture Lifetime of a Composite Following a Brief Proof Test at Higher Load

Typically manufactured composite structural components, prior to being put into service, are subjected to a "proof test" where a ramp loading (1), is applied up to proof stress level, σ_p, which may be significantly higher than the ultimate service stress, $\bar{\sigma}$, and which is maintained for some proof hold time, t_p, typically several minutes, after which the applied stress is lowered to the service stress level, $\bar{\sigma} \leq \sigma_p$, which is kept constant thereafter (Here we admit the possibility that the proof test is minimal, i.e., the stress level is simply the ultimate service stress). There can be variations to this loading profile whereby after time, t_p, the applied stress is lowered from σ_p to near zero and the component is stored for some time before later being put into service at constant stress $\bar{\sigma}$. For the purposes of this paper, however, it suffices to use the simplified load profile:

$$\sigma(t) = \begin{cases} \sigma_p, & 0 \leq t < t_p \\ \bar{\sigma}, & t \geq t_p \end{cases} \tag{3}$$

The rationale for this practice is that applying a proof test to stress level, $\sigma_p \geq \bar{\sigma}$, will "weed out" inferior composite structural components, thus improving the overall reliability of components that pass the proof test and are put in service. As is discussed later, classic models used for composite lifetime in stress rupture typically support this strategy, and the higher the proof stress, the better. We shall show, however, that the more detailed model developed in this paper does not universally support such a strategy, since proof-testing inflicts damage in the form of broken fibers that otherwise would have remained intact. This can negatively influence composite reliability at much longer times. This is a critical issue raised by Bunsell and Thionnet [50], as previously mentioned.

In this case we are interested in the conditional distribution for lifetime, $H_V\left(t|\, t \geq t_p, \sigma_p, \bar{\sigma}\right)$, given $t \geq t_p$, that is, given the component survived the proof test loading under stress σ_p up to time $t = t_p$, which means $H_V\left(t|\, t \geq t_p, \sigma_p, \bar{\sigma}\right) = 0$ when $t = t_p$. The resulting lifetime distribution has a complex but insightful structure, though it does not neatly collapse to a Weibull form, even when $\sigma_p = \bar{\sigma}$.

MODELING THE INSTANTANEOUS COMPOSITE STRENGTH AND DETERMINING ITS DISTRIBUTION

Distribution for Fiber Strength in Tension and Size (Length) Effect

Fibers in the composite are initially continuous having diameter, d, and Young's modulus, E. We assume the WP fiber strength model applies, such that a fiber element of length, δ, follows a Weibull distribution for tensile strength, σ, of the form:

$$F_\delta(\sigma) = 1 - \exp\left(-\frac{\delta}{\delta_c}\left(\frac{\sigma}{\sigma_{\delta_c}}\right)^\zeta\right),\ \sigma \geq 0 \tag{4}$$

where δ_c is a characteristic length mentioned earlier and described in more detail below, and σ_{δ_c} and ζ are the fiber Weibull scale and shape parameters, respectively, corresponding to length δ_c. A critical feature of (4) is that increasing the element length, δ, increases the probability of element failure at stress level, σ, since more strength limiting and randomly occurring flaws are exposed. Note also that the Weibull scale parameter for fiber strength at length, δ, is simply:

$$\sigma_\delta = \sigma_{\delta_c}(\delta_c/\delta)^{1/\zeta} \tag{5}$$

which reveals the inverse dependence of fiber strength on length, δ, and its sensitivity to ζ. This becomes a key component of the stress-rupture model for lifetime since matrix creep in shear has the effect of increasing over time, t, the effective overload lengths on fiber segments adjacent growing clusters of fiber breaks. However, the fibers and their randomly occurring flaws are themselves time independent, and segments of fixed length and under a fixed load do not undergo stress rupture.

A Taylor series expansion of (4) results in a convenient lower tail approximation, namely:

$$F_\delta(\sigma) \approx \frac{\delta}{\delta_c}\left(\frac{\sigma}{\sigma_{\delta_c}}\right)^\zeta,\ 0 \leq \sigma < \sigma_\delta, \tag{6}$$

which is of power-law form. This approximation happens to be extremely accurate for typical values of ζ, since fiber stress levels, σ, in the composite failure model typically satisfy $0 \leq \sigma \ll \sigma_{\delta_c}$. Later the composite stress-rupture model will involve the formation and growth of clusters of fiber breaks that have formed under an applied composite stress level, σ. Intact neighbors next to a cluster of i fiber breaks will thus be subject to stress $K_i\sigma > 1$, where K_i is the fiber stress concentration induced by the cluster (as will be described in more detail in sub-section Stress Concentrations and Break Cluster Growth Parameters for Failing Fiber Elements below). If the cluster grows in size such that [[Mathtype-mtef1-eqn-77.mtf]], then under (6), $F_\delta(K_i\sigma) \to 1$, whereas under (4), $F_\delta(K_i\sigma) \to 0.632 > 1/2$. Either way, the fiber break cluster has reached instability and catastrophic failure results. However, (6) greatly simplifies the calculations.

Characteristic Elastic and Statistical Length Scales for Fiber Load Redistribution Near Breaks

Using the classic shear-lag model [68, 69], Hedgepeth et al. described the load transfer process from broken to intact fibers in a composite where fibers are arranged in either a planar, square or hexagonal array within a flexible matrix. Fundamentally, a characteristic elastic length, δ_e, emerges that depends on various mechanical and geometric parameters of the fiber and matrix and their spacing, these being the fiber Young's modulus, E, fiber cross-sectional area, A, fiber diameter, d, matrix instantaneous elastic shear modulus, G_e, effective width, w, of matrix between two fiber surfaces, and the effective matrix thickness, which is also taken as d.

For fully elastic behavior, δ_e is typically expressed in terms of these parameters as [9, 63–65]:

$$\delta_e = d\sqrt{\frac{E}{G_e}\frac{A}{d^2}\frac{w}{d}} \approx d\sqrt{\frac{E}{G_e}\frac{w}{d}} \tag{7}$$

the latter assuming the approximation $A \approx d^2$, The dominating influences on δ_e are the fiber diameter, d, the square root of the fiber to matrix stiffness ratio, $\sqrt{E/G_e}$, and the square root of the matrix width between the fibers divided by its thickness $\sqrt{w/d}$. In simple terms, the ratio w/d is related to the fiber volume fraction, V_f, and whether the fibers are arranged as a planar tape (planar fiber array) or as a hexagonal array, whereby $V_f \approx 1/(1+\kappa w/d)$ where $\kappa \approx 2$ for a planar fiber array and $\kappa \approx 3$ for a hexagonal array. Thus, for a given fiber volume fraction, the ratio w/d will be smaller for a hexagonal vs. a planar array, however, the effect is mitigated by the square-root since $\sqrt{2/3} = 0.816$, and thus, for a given V_f the effect on δ_e is no more than 20%.

Along a neighboring fiber close to a fiber break, its overload profile in terms of fiber stress is roughly triangular with the peak stress occurring adjacent to the break. However, the effect of the triangular stress profile, in terms of determining its probability of failure can be modeled using an "effective, rectangular overload profile" at peak stress, but over some shorter length depending on the Weibull shape parameter, ζ, for fiber strength. This calculation requires accounting for the statistical rate of occurrence along the fiber of flaws of varying strength, as characterized by the WP fiber strength model [9, 10]. In our earlier work [78], this characteristic length, called δ_c in (4) through (6), was chosen as $\hat{\delta}_c$, which in our current notation and under linear viscoelastic behavior in [78] is:

$$\hat{\delta}_c \equiv \frac{4}{\zeta+1}\delta_e. \tag{8}$$

One factor of "2" arises because the overload profile extends over length $2\delta_e$ spanning the break. The other factor, $2/(\zeta+1)$, arises from triangular nature of the over-stress profile and its integration within the WP fiber model over length $2\delta_e$ [For more details see Equations (85–88) in [9] and associated discussion there]. The scaling factor, which is inversely proportional to $\zeta+1$,

results from the fact that the higher the value of ζ, the lower the variability in fiber strength, which means there is a sparser distribution of weaker flaws along the fiber. Thus, only the higher stresses near the peak of the triangular overload region are likely to cause fiber failure. Overall, the overloaded region is shortened for larger values of ζ [We caution that the notation used here is different from that in [78], since $2\delta_e$ here is $\hat{\delta}_e$ in the previous paper where both sides of the break were included. The definition of δ_e in (7) is more in line with that in the literature, [9, 10, 68, 69], and will simplify later comparisons].

In the current work the introduction of non-linear creep, and in particular, effects associated with the applied composite stress level, will require modification of δ_c, and we will find that taking $\delta_c = \hat{\delta}_c \equiv 4\delta_e/(\zeta+1)$, as in [78], does not account for the matrix yielding effect that will need to be incorporated. A new form of δ_c will be developed in Section Modeling Composite Lifetime in Stress Rupture and Determining its Distribution Fiber-to-Fiber Load Transfer at Fiber Breaks Under Linear and Non-linear Matrix Creep in Shear and in **Appendix A** in the Supplementary Material once the non-linear matrix creep model has been introduced, and a scale parameter for composite strength has been formulated; however, in this section δ_c needs no further characterization.

Stress Concentrations and Break Cluster Growth Parameters for Failing Fiber Elements

In the absence of time dependence of the matrix, the failure process in the composite involves the growth of clusters of fiber breaks resulting from local stress local concentrations on intact neighbors that are candidates for the next fibers to fail. Thus, in accordance with the definitions in both [10] and [78], we let:

$$K_i = \begin{cases} \sqrt{1+i\pi/4}\,, \text{ planar fiber array,} \\ \sqrt{1+\sqrt{4i/\pi}\,/\pi}\,, \text{ hexagonal fiber array,} \end{cases} i = 0, 1, 2, \ldots \tag{9}$$

be the stress concentration on a fiber next to a cluster of i broken fibers, where we note that $\sqrt{4i/\pi} = D$, is the diameter (dimensionless) of an approximately disc-shaped cluster containing i tightly-packed fiber breaks (That is, the actual cluster diameter is of order Dd). Also,

$$c_k = \prod_{j=0}^{k-1} N_j,\ k = 1, 2, 3, \cdots \tag{10}$$

is approximately the number of ways a cluster of k breaks can grow one break at a time from a single triggering break, where $N_0 \equiv 1$ and N_j is the effective number of overloaded neighbors next to a cluster of size j, one of which becomes the next fiber failure. The number, N_j, is given in [10, 44, 78] as approximately,

$$N_j = \begin{cases} 2, \text{ planar fiber array} \\ \phi j^{\gamma}, \text{ hexagonal fiber array} \end{cases}, j = 1,\ 2,\ 3, \ldots \tag{11}$$

where in a hexagonal array, ϕ and γ are parameters having the respective ranges, $2.5 \le \phi \le 6$ and $0 \le \gamma \le 0.5$ depending on subtleties of the fiber packing geometry and other factors. These all apply to the case of a linearly viscoelastic matrix.

In **Appendix C** in the Supplementary Material we consider the effects of non-linear matrix creep behavior of the matrix in shear on the overload lengths of fibers next to a cluster of breaks of size j, and find that the definitions of N_j change in both cases, and in a hexagonal array γ can increase by as much as 1/2 depending on the degree of non-linearity in shear stress level. These aspects will be explored in terms of determining N_j in (11) and calculating c_k in (10) when applying the model in Section Results and Discussion.

Distribution Function for Composite Strength

In determining the probability of composite failure as a function of stress level, σ, under a ramp loading as described in (1), we first focus on a quantity $W_k(\sigma)$, which is the probability of a cluster of k fiber breaks forming at a particular location in the composite under arbitrary stress, σ, starting with a single fiber break, and where $k \ge 1$is an arbitrary integer. These results are used later in connection with a specific value of $k = \hat{k}$, called the critical cluster size for instability. Any group of k adjacent fiber elements has the potential to become a cluster of k breaks, despite being a rare event for a given group of k fibers. However, the probability of obtaining at least one cluster of size k somewhere in the composite is much larger, and the overall probability of occurrence takes the weakest link form:

$$H_{V,k}(\sigma) = 1 - [1 - W_k(\sigma)]^V,\ \sigma \ge 0,\ k = 1,\ 2,\ 3, \ldots \tag{12}$$

where V is the dimensionless volume of the composite in terms of number of fiber elements of length δ_c, That is, V, is the total length of fiber in the composite, Λ, divided by δ_c. Note that (12) holds even though two nearby groups of k fiber elements can overlap each other and might ostensibly be viewed as statistically dependent. In reality, they satisfy the concept of k-dependence and essentially act independently (see Smith et al. for theorems on the concept of k-dependence associated with rare events [72]].

Since V is large (12), is well-approximated by the exponential form:

$$H_{V,k}(\sigma) \approx 1 - \exp[-VW_k(\sigma)], \quad \sigma \ge 0, \tag{13}$$

reminiscent of the Weibull form, as described by Smith et al. [72]. The general expression for the strength of a cluster of k fibers, $W_k(\sigma)$, as described in [9, 10, 78], is well-approximated by:

$$W_k(\sigma) \approx c_k \left[\prod_{i=0}^{k-1} F_{\delta_c}(K_i\sigma) \right],\ k = 1,\ 2,\ 3, \ldots,\ \sigma \ge 0. \tag{14}$$

where $F_{\delta_c}(\sigma)$, K_i and $c_k$were given previously by (6) and (9–11), respectively.

Using the lower tail approximation in (6), we can rewrite (14) as:

$$W_k(\sigma) \approx c_k\left(K_0K_1K_2\cdots K_{k-1}\right)^{\zeta}\left(\frac{\sigma}{\sigma_{\delta_c}}\right)^{k\zeta},\ k = 1, 2, 3, 4, \ldots. \tag{15}$$

Combining Equations (13) and (15), and taking $k = \hat{k}$, which is the critical cluster size whose value is determined below, we obtain an approximation for the failure probability of the composite, $H_V(\sigma)$, at a stress level σ, where:

$$H_V(\sigma) \equiv H_{V,k}(\sigma)\big|_{k=\hat{k}} \tag{16}$$

This can be rearranged into the Weibull form:

$$H_V(\sigma) \approx 1 - \exp\left(-\left(\frac{\sigma}{\hat{\sigma}_V}\right)^{\hat{\alpha}}\right),\ \sigma \geq 0, \tag{17}$$

Where,

$$\hat{\sigma}_V = \sigma_{\delta_c}\left(Vc_{\hat{k}}\right)^{-1/\left(\hat{k}\zeta\right)}\left(\prod_{i=0}^{\hat{k}-1} K_i\right)^{-1/\hat{k}},\ \hat{k} \geq 1, \tag{18}$$

is the effective Weibull scale parameter for strength and

$$\hat{\alpha} = \hat{k}\zeta,\quad \hat{k} \geq 1, \tag{19}$$

is the corresponding effective Weibull shape parameter.

In [78], we defined the critical cluster size, $\hat{k}$, as the value $\bar{k}$ satisfying $K_{\bar{k}-1}\hat{\sigma}_V < \sigma_{\delta_c} \leq K_{\bar{k}}\hat{\sigma}_V$. The idea there is that at such composite stress level $\sigma = \hat{\sigma}_V$, the probability of failure of an adjacent element to a cluster of size, of size $\bar{k}-1$ is approaching $1-e^{-1} = 0.632$ and adding one more break to increase the cluster to size $\bar{k}$ pushes the failure probability to the point of instability, and thus, catastrophic cluster growth with any further breaks.

For typical values of ζ, this choice works well in the case of a planar array, since there only two neighboring fibers to a growing cluster. However, in the case of a hexagonal array, the number of overloaded neighbors, N_j, to a cluster of size, j, grows large, especially for smaller ζ values. Thus, a point of instability for a given stress value σ, will likely occur at a smaller cluster size, $\hat{k}$, than the $\bar{k}$ value above, that is, the true $\hat{k}$ would be overestimated by the definition given in [78].

To address this issue, a more refined approach to determining the $\hat{k}$ associated with the onset of cluster instability is to first seek stress values, $\sigma = \sigma_k$, for integer values, $k \geq 1$, where $W_{k-1}(\sigma)$ happens to intersect with $W_k(\sigma)$ when σ is locally varied; that is, where $W_k(\sigma_k) = W_{k+1}(\sigma_k)$. These intersections result in a set of stress values satisfying $\cdots < \sigma_k < \sigma_{k-1} < \cdots < \sigma_2 < \sigma_1 < \sigma_{\delta_c}$, thus placing the focus on the probabilities of instability and failure associated with a given stress level, σ, that happens to fall between two successive values, say, $\sigma_k \leq \sigma < \sigma_{k-1}$. Thus, using (15) in the equality $W_k(\sigma_k) = W_{k+1}(\sigma_k)$ and canceling common factors leads simply to $K_k\sigma_k = \sigma_{\delta_c}/N_k^{1/\zeta}$. Then for $\hat{\sigma}_V$ satisfying $\sigma_k < \hat{\sigma}_V \leq \sigma_{k-1}$ for a particular k value that we call critical cluster size, $\hat{k}$, we find that:

$$K_{\hat{k}-1}\hat{\sigma}_V < \frac{\sigma_{\delta_c}}{N_{\hat{k}}^{1/\zeta}} \leq K_{\hat{k}}\hat{\sigma}_V. \tag{20}$$

Thus, this result adjusts for the increased probability of instability and failure resulting from a growing number, $N_{\hat{k}}$, of overloaded neighbors to a cluster, any one of which could break and trigger unstable cluster growth before the stress on such neighbors has reached σ_{δ_c} (The exponent, $1/\zeta$ arises from an equiprobability tradeoff of increasing N_k vs. decreasing stress level, σ, so that $N_k\sigma^{\zeta}$ remains fixed).

From (9), (18), and (20) we find that solving for the correct value of $\hat{k}$ requires satisfying:

$$\hat{k} = \begin{cases} \left\lceil \frac{4}{\pi}\left\{\left(2^{-1/\zeta}\,\sigma_{\delta_c}/\hat{\sigma}_V\right)^2 - 1\right\}\right\rceil, & \text{planar fiber array} \\ \left\lceil \frac{\pi^3}{4}\left\{\left(N_{\hat{k}}^{-1/\zeta}\,\sigma_{\delta_c}/\hat{\sigma}_V\right)^2 - 1\right\}^2\right\rceil, & \text{hexagonal fiber array} \end{cases} \tag{21}$$

where "$\lceil . \rceil$" corresponds to the ceiling function, i.e., rounding up the value of the argument to the next integer, since instability requires growing to the next highest cluster size. While this change in definition decreases $\hat{k}$ as compared to that calculated in [78], it has a negligible effect in the planar case for typical values of ζ. However, it results in a major improvement in the hexagonal case for smaller values of ζ, particularly since $N_{\hat{k}}$ also rapidly decreases with decreasing $\hat{k}$.

Note that the approach in the current paper results in a single Weibull distribution for strength for all stress levels and associated probabilities of failure, whereas a more refined analysis, as in [9, 10], leads to a strength distribution with a more concave shape in stress level noticeable over probability levels decreasing by many orders of magnitude (Later on, the same will be true of the distribution for lifetime given the applied load level). However, apart from greatly complicating the analysis, such refinements make little if any practical difference to the predictions for the material volumes and range of failure probabilities of interest.

MODELING COMPOSITE LIFETIME IN STRESS RUPTURE AND DETERMINING ITS DISTRIBUTION

The fiber breakage model for stress-rupture of a unidirectional composite relies not only on the elastic stiffness properties of the fibers in tension, but also on the elastic stiffness and creep properties of the matrix in shear. The fiber and matrix viscoelastic or viscoplastic properties and their dimensions with respect to their local packing geometry (e.g., 2D hexagonal, or 1D planar) determine the length scale, generally called $\delta(t)$, $t \geq 0$ (of with subscripts as appropriate), over which load is transferred from a broken fiber to its adjacent intact neighbors. It is the matrix creep behavior in shear, scaled by its elastic behavior, that determines how this length-scale of fiber load transfer grows over time, the consequence of which is the occurrence of additional fiber failures over time at newly exposed flaws. Thus, over time clusters of fiber breaks emerge and grow in both size and length of overloading until a point of instability is reached, and catastrophic failure is triggered. Below we explain how is determined in both the linear and non-linear matrix creep.

Length-Scales for Fiber Load Transfer Under Linear Viscoelastic Matrix Creep

Previously in [78] we considered the case where the matrix is linearly viscoelastic and that the matrix creeps in shear according to a creep compliance with the power-law form:

$$J(t) = J_e\left(1 + \left(\frac{t}{t_c}\right)^{\theta}\right),\ t \geq 0, \tag{22}$$

where $J_e \equiv 1/G_e$ is the instantaneous elastic creep compliance (being the inverse of, G_e, the instantaneous elastic shear modulus), t_c, is a characteristic time for creep, and θ is a power-law exponent, all being positive in value. Generally, under a time varying shear stress, $\tau(s)$, $t \geq 0$, the shear strain follows the convolution integral.

$$\begin{aligned}\gamma(t;\tau(\bullet)) &= \int_0^t J(t-s)\frac{d\tau(s)}{ds}ds \\ &= \frac{1}{G_e}\int_0^t \left(1 + \left(\frac{t-s}{t_c}\right)^{\theta}\right)\frac{d\tau(s)}{ds}ds\end{aligned} \tag{23}$$

Under a given fixed shear stress, $\bar{\tau}$, the matrix shear strain is $\gamma(t,\bar{\tau}) = \bar{\tau}J(t)$, and from (23) is,

$$\begin{aligned}\gamma(t,\bar{\tau}) &= \frac{\bar{\tau}}{G_e}\left(1 + \left(\frac{t}{t_c}\right)^{\theta}\right) \\ &\approx \frac{\bar{\tau}}{G_e}\left(\frac{t}{t_c}\right)^{\theta},\ t \gg t_c.\end{aligned} \tag{24}$$

Typically t_c is of the order seconds to minutes, whereas the ultimate failure time of the composite in stress-rupture applications is of the order of months to years, and even many decades. Also, a typical value for a polymer matrix is $\theta \sim 0.25$. In the case of a unidirectional composite with a large number of fibers, the stress redistribution from a broken fiber to its closest intact neighbors can be calculated using well-known shear-lag models, which assume the fibers primarily support tension and the much more flexible matrix primarily supports shear. In the case of the linear viscoelastic creep function for the matrix, and using the convolution (23), in an extensive analysis using Laplace transforms, Lagoudas et al. [63] showed that the length scale grows beyond the *elastic* length scale according to $\delta_e\sqrt{1 + (t/t_c)^{\theta}}$, $t > 0$, and thus the characteristic length scale is accurately described by:

$$\delta(t) = \delta_c\sqrt{1 + \left(\frac{t}{t_c}\right)^{\theta}},\ t > 0 \tag{25}$$

where δ_c is the characteristic statistical-elastic length scale for instantaneous fiber load transfer given previously by (8), that is, in this special case of linear viscoelasticity, $\delta_c = \hat{\delta}_c$. Furthermore, the fiber stress concentrations, K_i, near clusters of i fiber breaks still follow (9), and as time passes, transversely somewhat misaligned breaks in a cluster act as though they are increasingly aligned [58].

At much longer times, t, relative to the characteristic time for creep, $t = t_c$, and in keeping with the approximation in (23) we simplify (24) to,

$$\delta(t) \approx \delta_c\left(\frac{t}{t_c}\right)^{\theta/2},\ t_c \ll t,\ 0 < \theta \leq 1 \tag{26}$$

where we note that the exponent on normalized time has now become $\theta/2$. This reduction by one-half of the effect of the matrix creep exponent on time, i.e., from θ to $\theta/2$, occurs because matrix creep causes growth over time of the length-scale along a fiber over which stress-redistribution occurs as the fiber stress drops from the nominal far-field value, say σ, to zero at the break. Consequently, to maintain force balance in the fiber, the magnitude of the matrix shear stress necessarily diminishes with time, effectively slowing down the growth of matrix creep in shear compared to what one might deduce from (5).

Despite the reduction of the exponent, θ, in (24), to $\theta/2$ in (26), this approximation accurately describes the behavior of (25) for longer times, $t \gg t_c$, and at $t = t_c$ gives the same value, δ_c, as (25) does at $t = 0$. Thus, when considering probabilities of failure associated very short times, or even when measuring strength at times, $0 < t \ll t_c$, accurate predictions are obtained from lifetime probability calculations based on using the simpler (26), and taking $t = t_c$, as we discuss again later.

A key feature of matrix creep is ignored in simply using (25) and (26), but is potentially important when a composite has an isolated break or a small break cluster, and the applied composite tensile stress suddenly increases or decreases at certain times, or, when the composite stress is constant but a small break cluster induces additional neighboring breaks at times $t \gg t_c$, and grows in size, or some combination of the two. In such cases, the shear stress near fiber breaks can change substantially over time, and the amount of stress redistributed from broken to intact fibers, and the length scale over which it is applied, also changes over time in ways we model using (26) but not accounting for behavior implied by the stress history convolution (23). That said, the key elastic length-scale of load transfer, δ_e, for a single break or its counterpart for a small break cluster does not change (other than increasing slightly in a stepwise fashion as more breaks are added).

It turns out, however, that these result are surprisingly accurate even for the case of a viscous matrix where (26) applies exactly with $\theta = 1$, and where the matrix viscosity is interpreted as $t_c G_e$ [44, 64, 65]. Thus, despite these potential complications we are still able to use the forms (25) and (26) as well as the instantaneous load-redistribution factors, K_i, around fiber breaks obtained from elastic shear-lag analysis, as given in (9). That is, in the case of elastic fibers and a linearly viscoelastic matrix, these K_i happen to be determined from the elastic problem, via the so-called "correspondence principle."

Thus, for all breaks, we assume (25) and (26) apply irrespective of *when* new breaks occurred; that is, the time of occurrence for any new break is retroactively set to zero. Since θ is typically

small (and $\theta/2$ smaller still), the effect of retroactively assigning all break times to zero, once they occur, makes little practical difference to the model predictions, which if anything are slightly conservative. Such a simplification yields surprisingly accurate predictions in a stress-rupture setting, as was shown in [54] for the more demanding case of a viscous matrix, $\theta = 1$, especially when a composite is loaded under constant stress that is well below its breaking strength. Much of the reason for this is that the fiber breaking process, while rapid initially, becomes slower and slower as time progresses, and the spacing of breaks over time tends to become logarithmic, until catastrophic instability is reached. Consequently, log-scales in both time and stress level are typically used to describe the composite stress rupture process up to final failure.

Length Scales for Fiber Load Transfer Under Non-linear Matrix Creep of Mason et al. (1992)

In the case of non-linear matrix creep in shear, Mason et al. [66], formulated and solved certain shear lag problems involving a single broken fiber in the center of a planar composite under tension, and having three fibers and five fibers, respectively. The matrix creep law for shear strain, γ, was assumed to take the following power-law form in both time and shear stress, which we parameterize as:

$$\gamma\left(t;\tau\left(\bullet\right)\right) = \frac{\tau_y}{G_e}\left(\frac{1}{t_c}\int_0^t\left(\frac{\tau\left(s\right)}{\tau_y}\right)^{\varphi/\theta} ds\right)^{\theta},\ \tau \geq 0 \tag{27}$$

where$\tau\left(t\right)$, $t \geq 0$ is the applied shear stress that may vary with time, $0 < \theta \leq 1$ is again a fixed exponent reflecting the sensitivity of creep strain growth with time, the new parameter, $1 \leq \varphi < \infty$ is a fixed exponent reflecting the sensitivity of creep strain growth to shear stress level, and G_e is a reference stress reminiscent of the matrix elastic shear modulus. Also the other new parameter, τ_y, is a reference shear stress that in the limit of large $\varphi \to \infty$ will play the role of a perfectly plastic matrix yield stress in shear, but in the "linear" limit, $\varphi \to 1^+$, has no effect in (27) (Typically such creep laws are described in terms of creep rate, $\partial\gamma\left(t;\tau\left(\bullet\right)\right)/\partial t$, which is how they are used in the shear-lag model, however, this is easily calculated from 27).

Under constant shear stress, $\tau\left(s\right) = \bar{\tau}$, (27) reduces to,

$$\gamma\left(t,\bar{\tau}\right) = \frac{\bar{\tau}}{G_e}\left(\frac{\bar{\tau}}{\tau_y}\right)^{\varphi-1}\left(\frac{t}{t_c}\right)^{\theta},\ \bar{\tau} > 0,\ t \geq 0 \tag{28}$$

and when $\varphi \to 1^+$ we recover the approximation given in (24) for the case of a linearly viscoelastic matrix [As discussed in **Appendix D** in the Supplementary Material, there is a simpler version of (27) that leads to a creep-rate $\partial\gamma\left(t;\tau\left(\bullet\right)\right)/\partial t$, which avoids a memory integral inherited form (27) but otherwise results in (28). Fortunately, this simpler version yields results that are virtually identical to those developed in **Appendix C** in the Supplementary Material and used below].

While we have used an effective shear modulus, G_e, to normalize the shear stress, $\bar{\tau}$, the model in [66] does not explicitly reflect the initial instantaneous elastic shear behavior one might expect for a polymer matrix at time, $t = 0$, focusing instead on matrix creep over longer times, $t > 0$. However, initial elastic behavior may be important for determining the characteristic elastic length scale, δ_e, of (7) for elastic load transfer around a fiber break when determining the composite strength distribution, (17), using (4).

In **Appendix A** in the Supplementary Material we discuss solutions, based on (27), where we derive a characteristic length scale for load transfer, $\hat{\delta}_\varphi\left(t\right)$, given by (A41) through (A43) which covers both viscoelastic and viscoplastic cases. Recalling (8), whereby $\hat{\delta}_c \equiv 4\delta_e/(\zeta+1)$, reflecting both the elastic length scale δ_e and statistical effects through the Weibull shape parameter, we use $\hat{\delta}_\varphi\left(t\right)$ to obtain the key length scale, $\delta\left(t,\bar{\sigma}\right) = 4\hat{\delta}_\varphi\left(t\right)/(\zeta+1)$, i.e.,

$$\delta\left(t,\bar{\sigma}\right) = \frac{4}{\zeta+1}\delta_e\left(\frac{\bar{\sigma}}{\sigma_y}\right)^{(\varphi-1)/(\varphi+1)}\left(\frac{t}{t_c}\right)^{\theta/(\varphi+1)} \tag{29}$$

This can be written as,

$$\delta\left(t,\bar{\sigma}\right) = \delta_c\left(\frac{\bar{\sigma}}{\hat{\sigma}_V}\right)^{(\varphi-1)/(\varphi+1)}\left(\frac{t}{t_c}\right)^{\theta/(\varphi+1)} \tag{30}$$

where we have used the definition,

$$\delta_c \equiv \hat{\delta}_c\left(\frac{\hat{\sigma}_V}{\sigma_y}\right)^{(\varphi-1)/(\varphi+1)} \tag{31}$$

Where,

$$\sigma_y = 2\tau_y\delta_e\frac{d}{A} \approx 2\tau_y\frac{\delta_e}{d} \tag{32}$$

is a critical "yield" stress [see **Appendix A** in the Supplementary Material, and specifically, the discussion surrounding (A42), motivating the emergence of the length scale, δ_e in (32)].

This result is consistent with (26) in the case of viscoelastic creep at longer times. However, the length scale $\delta\left(t,\bar{\sigma}\right)$ of (30) reveals interesting effects in the case of non-linear creep: When $\varphi \to 1^+$, we see that $\delta\left(t,\bar{\sigma}\right)$ of (30) and (31) is consistent with $\delta\left(t\right)$ derived from (26) in the case of linear viscoelasticity. However, when $\varphi \to \infty$, time dependence disappears, and $\delta\left(t,\bar{\sigma}\right) = \hat{\delta}_c\hat{\sigma}_V/\sigma_y$ for all $t \geq 0$ reminiscent of plastic behavior. In general, $\hat{\sigma}_V > \sigma_y$ and thus, δ_c will be larger than $\hat{\delta}_c$ when $\varphi > 1$.

When deriving the distribution function (17), for composite strength where effectively the loading time is of order t_c or less, the appropriate length-scale for fiber-to-fiber load transfer is, δ_c. However, from (30) to (32), we see that when $t = t_c$, we obtain the length $\delta\left(t_c,\bar{\sigma}\right)$ which differs from δ_c when $\varphi > 1$ as reflected by the factor, $\left(\bar{\sigma}/\hat{\sigma}_V\right)^{(\varphi-1)/(\varphi+1)}$, whereas no such effect arose in the case of a linear viscoelasticity, since $\varphi = 1$. This leads to changes in (17) through (20) that must be accommodated.

As was done with the extension of (28) to (29) for non-linear matrix shear strain behavior to accommodate initial elastic effects, we also extend (30) to the form:

$$\delta\left(t,\bar{\sigma}\right)=\delta_{\mathrm{c}}\left(1+\left(\frac{\bar{\sigma}}{\hat{\sigma}_V}\right)^{\varphi-1}\left(\frac{t}{t_{\mathrm{c}}}\right)^{\theta}\right)^{1/(\varphi+1)}. \tag{33}$$

This has the correct asymptotic behavior of (30) as t/t_{c} grows large, and is consistent with the behavior of $\delta\left(t\right)$ derived from (25) when $\varphi=1$, as well as producing a fixed value, δ_{c}, when $t=0$, which also accommodates a yielding effect in (31).

As mentioned in the introduction, there are several experimental works that demonstrate the effects of non-linear matrix creep [57–62] on fiber stress relaxation and fiber-to-fiber load transfer around breaks. These include observations of matrix yielding and interface debonding and slip. The above results are consistent with the behavior seen, and in large part, were the motivation for revising this aspect of the previous model [78].

Distribution Function for Composite Lifetime in Stress Rupture

Next we model the occurrence of stress rupture in a composite structure that has been loaded according to (2) for some time period, and where the fixed applied stress level satisfies $\bar{\sigma}<\hat{\sigma}_V$. The lifetime distribution function, $H_V\left(t;\bar{\sigma}\right),\ t>0$, which gives the probability of stress-rupture failure occurring by time, t, can be derived in a manner similar to that used to derive the strength distribution (17), above. Using similar arguments, the distribution function for composite lifetime also follows:

$$H_V\left(t;\bar{\sigma}\right)\approx 1-\exp\left[-VW_{\hat{k}}\left(t;\bar{\sigma}\right)\right],\ t>0 \tag{34}$$

analogous to (13), where $W_{\hat{k}}\left(t;\bar{\sigma}\right)$ is a characteristic distribution function analogous to (14), but with an added time component:

$$W_{\hat{k}}\left(t;\bar{\sigma}\right)\approx c_{\hat{k}}F_{\delta_{\mathrm{c}}}\left(\bar{\sigma}\right)\left[\prod_{i=1}^{\hat{k}-1}F_{\delta_{\mathrm{c}}}\left(K_i\bar{\sigma},t\right)\right] \tag{35}$$

where $\hat{k}$ is again defined by (21) (where the actual values of $N_j$are later called $N_{j,\varphi}$ and specified in more detail). Also $F_{\delta_{\mathrm{c}}}\left(\bar{\sigma}\right)$ is as in (4), i.e., using (33) with $t=0$, and $F_{\delta_{\mathrm{c}}}\left(\bar{\sigma},t\right)$ in [78] is modified to give:

$$\begin{aligned}F_{\delta_{\mathrm{c}}}\left(\bar{\sigma},t\right)&=1-\exp\left(-\frac{\delta\left(t,\bar{\sigma}\right)}{\delta_{\mathrm{c}}}\left(\frac{\bar{\sigma}}{\sigma_{\delta_{\mathrm{c}}}}\right)^{\zeta}\right)\approx\frac{\delta\left(t,\bar{\sigma}\right)}{\delta_{\mathrm{c}}}\left(\frac{\bar{\sigma}}{\sigma_{\delta_{\mathrm{c}}}}\right)^{\zeta}\\&\approx\left(\frac{\bar{\sigma}}{\hat{\sigma}_V}\right)^{(\varphi-1)/(\varphi+1)}\left(\frac{\bar{\sigma}}{\sigma_{\delta_{\mathrm{c}}}}\right)^{\zeta}\left(\frac{t}{t_{\mathrm{c}}}\right)^{\theta/(\varphi+1)}\\&\approx\left(\frac{\sigma_{\delta_{\mathrm{c}}}}{\hat{\sigma}_V}\right)^{(\varphi-1)/(\varphi+1)}\left(\frac{\bar{\sigma}}{\sigma_{\delta_{\mathrm{c}}}}\right)^{\zeta+(\varphi-1)/(\varphi+1)}\\&\quad\left(\frac{t}{t_{\mathrm{c}}}\right)^{\theta/(\varphi+1)},\quad t\gg t_{\mathrm{c}}\end{aligned} \tag{36}$$

where $\delta\left(t,\bar{\sigma}\right)$ is given by (30), and the lower-tail approximation, using (6), is always sufficiently accurate in this setting, since $0<\bar{\sigma}\ll\sigma_{\delta_{\mathrm{c}}}$. Note that $F_{\delta_{\mathrm{c}}}\left(\bar{\sigma}\right)$, corresponding to $t=0$, is also given by (6). Thus, this added time component is based on the assumptions of linear or non-linear matrix creep and shear lag in a power law framework, as discussed below.

The key result used here for $\delta\left(t,\bar{\sigma}\right)$as derived from results in [66] was given earlier by (30) and (31). Upon substituting this into the lower-tail approximation for $F_{\delta_{\mathrm{c}}}\left(\bar{\sigma},t\right)$, given in (36), and then substituting the result into (35), we obtain after some rearrangement and factoring:

$$\begin{aligned}W_{\hat{k}}\left(t;\bar{\sigma}\right)&\approx c_{\hat{k}}\left(\frac{\sigma_{\delta_{\mathrm{c}}}}{\hat{\sigma}_V}\right)^{\left(\hat{k}-1\right)\frac{\varphi-1}{\varphi+1}}\left(\prod_{i=0}^{\hat{k}-1}K_i\right)^{\zeta+\frac{\varphi-1}{\varphi+1}}\left(\frac{\bar{\sigma}}{\sigma_{\delta_{\mathrm{c}}}}\right)^{\zeta}\\&\quad\left(\left(\frac{\bar{\sigma}}{\sigma_{\delta_{\mathrm{c}}}}\right)^{\zeta+\frac{\varphi-1}{\varphi+1}}\left(\frac{t}{t_{\mathrm{c}}}\right)^{\frac{\theta}{\varphi+1}}\right)^{\hat{k}-1}\\&\approx c_{\hat{k}}\left(\frac{\sigma_{\delta_{\mathrm{c}}}}{\hat{\sigma}_V}\right)^{\left(\hat{k}-1\right)\frac{\varphi-1}{\varphi+1}}\left(\prod_{i=0}^{\hat{k}-1}K_i\right)^{\zeta_\varphi}\left(\frac{\bar{\sigma}}{\sigma_{\delta_{\mathrm{c}}}}\right)^{\hat{k}\zeta_\varphi-\frac{\varphi-1}{\varphi+1}}\\&\quad\left(\frac{t}{t_{\mathrm{c}}}\right)^{\left(\hat{k}-1\right)\frac{\theta_\varphi}{2}},\quad t\gg t_{\mathrm{c}}\end{aligned} \tag{37}$$

where

$$\zeta_\varphi=\zeta+\frac{\varphi-1}{\varphi+1}. \tag{38}$$

and

$$\theta_\varphi=\frac{2\theta}{\varphi+1} \tag{39}$$

Substituting (37) into (34), we can write an expression for the composite lifetime in the form:

$$\begin{aligned}H_V\left(t;\bar{\sigma}\right)&\approx 1-\exp\left\{-Vc_{\hat{k}}\left(\frac{\sigma_{\delta_{\mathrm{c}}}}{\hat{\sigma}_V}\right)^{\left(\hat{k}-1\right)\frac{\varphi-1}{\varphi+1}}\left[\prod_{i=0}^{\hat{k}-1}K_i\right]^{\zeta_\varphi}\right.\\&\quad\left.\left(\frac{\bar{\sigma}}{\sigma_{\delta_{\mathrm{c}}}}\right)^{\hat{k}\zeta_\varphi-\frac{\varphi-1}{\varphi+1}}\left(\frac{t}{t_{\mathrm{c}}}\right)^{\left(\hat{k}-1\right)\frac{\theta_\varphi}{2}}\right\}\end{aligned} \tag{40}$$

This can also be written as:

$$H_V\left(t;\bar{\sigma}\right)\approx 1-\exp\left\{-\left(\left(\frac{\bar{\sigma}}{\hat{\sigma}_{V,\varphi}}\right)^{\hat{\rho}_\varphi}\frac{t}{t_{\mathrm{c}}}\right)^{\hat{\beta}_\varphi}\right\},\quad t\gg t_{\mathrm{c}} \tag{41}$$

where the lifetime shape parameter, $\hat{\beta}_\varphi$, is given by:

$$\hat{\beta}_\varphi=\left(\hat{k}-1\right)\theta_\varphi/2, \tag{42}$$

and the power-law exponent, $\hat{\rho}_\varphi$, is given by:

$$\hat{\rho}_\varphi = \left(\frac{\hat{k}}{\hat{k}-1}\right)\frac{2}{\theta_\varphi}\left(\zeta_\varphi - \frac{1}{\hat{k}}\frac{\varphi-1}{\varphi+1}\right), \tag{43}$$

and where the lifetime scale parameter, $\hat{\sigma}_{V,\varphi}$, is given by:

$$\begin{aligned}\hat{\sigma}_{V,\varphi} &= \sigma_{\delta_c}\left(Vc_{\hat{k}}\left(\frac{\sigma_{\delta_c}}{\hat{\sigma}_V}\right)^{\left(\hat{k}-1\right)(\varphi-1)/(\varphi+1)}\left(\prod_{i=0}^{\hat{k}-1}K_i\right)^{\zeta_\varphi}\right)^{\frac{-1}{\hat{k}\zeta_\varphi-(\varphi-1)/(\varphi+1)}} \\ &= \sigma_{\delta_c}\left(Vc_{\hat{k}}\right)^{\frac{-1}{\hat{k}\zeta_\varphi}\left(\frac{1}{1-(\varphi-1)/(\varphi+1)/\left(\hat{k}\zeta_\varphi\right)}\right)} \\ &\quad \left(\prod_{i=0}^{\hat{k}-1}K_i\right)^{\left(\frac{-1}{\hat{k}}\right)\left(\frac{1}{1-(\varphi-1)/(\varphi+1)/\left(\hat{k}\zeta_\varphi\right)}\right)}\Xi_\varphi\end{aligned} \tag{44}$$

This scale parameter can be reduced to:

$$\hat{\sigma}_{V,\varphi} = \sigma_{\delta_c}\left(\left(Vc_{\hat{k}}\right)^{-1/\left(\hat{k}\zeta_\varphi\right)}\left(\prod_{i=0}^{\hat{k}-1}K_i\right)^{-1/\hat{k}}\right)^{\frac{1}{1-(\varphi-1)/(\varphi+1)/\left(\hat{k}\zeta_\varphi\right)}}\Xi_\varphi \tag{45}$$

Where,

$$\Xi_\varphi = \left(\frac{\hat{\sigma}_V}{\sigma_{\delta_c}}\right)^{1/\left(\left(\frac{\hat{k}}{\hat{k}-1}\right)\left(\frac{\varphi+1}{\varphi-1}\right)\zeta+1\right)} \tag{46}$$

and we note that since $\hat{k} \gg 1$ we have approximately that:

$$\Xi_\varphi \to \begin{cases} 1, & \text{as } \varphi \to 1 \\ \left(\hat{\sigma}_V/\sigma_{\delta_c}\right)^{1/(\zeta+1)}, & \text{as } \varphi \to \infty \end{cases} \tag{47}$$

Also, the exponent $1/\left(1-(\varphi-1)/(\varphi+1)/\left(\hat{k}\zeta_\varphi\right)\right)$ in the first term of the right-hand side of (45) is typically very close to unity.

Thus, the difference between $\hat{\sigma}_{V,\varphi}$ of (45) and $\hat{\sigma}_V$ of (18) for the strength distribution is almost completely dominated by the factor, Ξ_φ, and the effect of φ on the first factor on the right-hand side of (45) is relatively small, since, ζ_φ typically differs little from ζ, which is the Weibull shape parameter for the fiber strength distribution.

Retrieving Results for Linear Matrix Viscoelasticity From the Non-linear Matrix Creep Results

The linear viscoelastic version of the lifetime distribution given in [78] is retrieved from the results above, simply by setting $\varphi = 1$, in which case:

$$\zeta_\varphi = \zeta, \tag{48}$$

$$\hat{\beta}_\varphi = \hat{\beta} \equiv \left(\hat{k}-1\right)\theta/2, \tag{49}$$

$$\hat{\rho}_\varphi = \hat{\rho} \equiv \left(\frac{\hat{k}}{\hat{k}-1}\right)\frac{2\zeta}{\theta}, \tag{50}$$

and

$$\hat{\sigma}_V = \sigma_{\delta_c}\left(Vc_{\hat{k}}\left(\prod_{i=0}^{\hat{k}-1}K_i\right)^{\zeta}\right)^{-\frac{1}{\hat{k}\zeta}} \tag{51}$$

since $\Xi_\varphi \to 1$ as $\varphi \to 1^+$ in (47). Thus, when $\varphi = 1$, the scale parameter, $\hat{\sigma}_V$, for stress level is identical to that given by (18) for the strength distribution and the shape parameter, $\hat{\alpha}$ of (19) is simply $\hat{\rho}\hat{\beta}$ from (49) to (50), which does not involve φ.

Interpreting the Strength Distribution in the Case of Non-linear Matrix Viscoelasticity

The assumption of non-linear viscoelastic behavior of the matrix does mean, however, that the strength distribution (17), and associated parameters require reinterpretation. In this case we use $\hat{\sigma}_{V,\varphi}$ of (45) in place of $\hat{\sigma}_V$ in (17) and replace $\hat{\alpha}$ by:

$$\hat{\alpha}_\varphi = \hat{\rho}_\varphi\hat{\beta}_\varphi \tag{52}$$

based on (49) and (50), which both involve φ. Furthermore, a practically meaningful strength distribution can be extracted from (41) by setting $t = t_c$.

While both parameters $\hat{\beta}_\varphi$ and $\hat{\rho}_\varphi$ see effects from $\varphi \gg 1$, the product $\hat{\rho}_\varphi\hat{\beta}_\varphi$, and thus the effective $\hat{\alpha}_\varphi$ on the strength distribution is little affected. Also, if we use (41) to calculate the probability of failure by a fixed time, $t \approx t_c$, associated with various stress levels, $\bar{\sigma}$, we see that the probability of failure vs. stress level, $\bar{\sigma}$, also follows a Weibull distribution, with scale parameter $\hat{\sigma}_{V,\varphi}$ of (55), but reduced in magnitude in comparison to $\hat{\sigma}_V$ of (18), because $\Xi_\varphi < 1$ since typically $\hat{\sigma}_V/\sigma_{\delta_c} < 1$. Also, the Weibull shape parameter now becomes:

$$\hat{\alpha}_\varphi = \hat{\rho}_\varphi\hat{\beta}_\varphi = \hat{k}\zeta_\varphi - \frac{\varphi-1}{\varphi+1} \tag{53}$$

By comparison, the Weibull distribution for composite strength (17), has scale parameter, $\hat{\sigma}_V$, given by (18), and shape parameter, $\hat{\alpha} = \hat{k}\zeta$, given by (19), where implicit to the derivation is that the timescale for the strength test is $0 < t \ll t_c$ whereby non-linear matrix creep effects do not have time not come into play, other than instantaneous plastic-like effects reflected in N_j in (20) used to calculate $\hat{k}$ (see later discussion where N_j becomes $N_{j,\varphi}$). Such a derivation requires thinking in terms of (33) rather than (30), the latter being the basis for the derivation of the lifetime distribution (41) and the extracted Weibull scale and shape parameters (45) and (53) for strength.

One effect on Weibull strength behavior, is a slight shift in the Weibull shape parameter for strength changing from $\hat{\alpha}$ at short

times $t \ll t_c$, to $\hat{\alpha}_\varphi$ at times $t \approx t_c$. However, this shift is relatively small since from (53) and (19) we have:

$$\hat{k}\zeta = \hat{\alpha} < \hat{\alpha}_\varphi < \hat{\alpha} + \left(\hat{k} - 1\right) = \hat{k}\,(\zeta + 1) - 1 \tag{54}$$

where the upper bound occurs when $\varphi \rightarrow \infty$. Thus, the difference in the Weibull shape parameter for composite strength is less than would occur by increasing the Weibull shape parameter for *fiber* strength from ζ to $\zeta + 1$.

In summary, the most important effect on Weibull strength is seen in comparing the scale parameter, $\hat{\sigma}_V$, in (18), which is also the scale parameter for stress level when modeling lifetime under linear viscoelasticity, to $\hat{\sigma}_{V,\varphi}$ of (45).

Effects of Non-linear Matrix Behavior of Determining the Effective Number of Overloaded Fiber Elements Surrounding a Break Cluster and Calculating the Critical Cluster Size

The key results in the paper, especially the calculation of $\hat{\sigma}_V$ in (18) and $\hat{\sigma}_{V,\varphi}$ in (45) and $\hat{k}$ itself in (20) require calculation of $c_{\hat{k}}$ in (10), which in turn requires calculating $N_j, j = 1, 2, \cdots, \hat{k} - 1$ of (11). In **Appendix A** in the Supplementary Material we have shown that in the case of non-linear matrix creep, the N_j values for under a linear viscoelastic matrix or in the absence of time dependence must be modified to

$$N_{j,\varphi} = \begin{cases} 2^{2/(\varphi+1)} j^{(\varphi-1)/(\varphi+1)}, \\ \qquad \text{planar fiber array} \\ \phi\pi^{(\varphi-1)/(\varphi+1)/2} j^{\gamma+(\varphi-1)/(\varphi+1)/2}, \\ \qquad \text{hexagonal fiber array} \end{cases}, \; j = 1,\ 2,\ 3, \ldots \tag{55}$$

and these values are used in (10) to calculate, $c_{\hat{k}}$. Clearly the resulting effect depends on the value of φ, and as $\varphi \rightarrow \infty$ results in proportionality to the number of breaks, j, in the planar case, and in the hexagonal case to $\sqrt{j}$ together with a change in ϕ to $\phi\sqrt{\pi}$. However, when $\varphi \rightarrow 1^+$ there is no effect compared to linear viscoelasticity.

For fiber Weibull shape parameter values, $\zeta \sim 5$, and using Monte Carlo failure simulations as a basis for comparison, Mahesh and Phoenix [44]. suggest the values $\phi = 2.5$ and $\gamma \approx 0.27$ using (55) with $\varphi \rightarrow 1^+$, i.e., for $N_j = N_{j,1}$. On the other hand, taking $\phi = \sqrt{4\pi} \approx 3.54$ and $\gamma = 1/2$ as in [5] has the interpretation that N_j is the number of neighbors surrounding a circular cluster of diameter$D$ and containing approximately $j \approx \pi D^2/4$ fiber breaks, as just noted. This results in:

$$N_{j,\varphi} = 2\left(\sqrt{\pi} j\right)^{1+(\varphi-1)/(\varphi+1)}, \text{hexagonal fiber array}, \quad j = 1,\ 2,\ 3, \ldots \tag{56}$$

However, this assumption effectively overcounts the number of severely overloaded neighbors to growing approximately hexagonal cluster that has incomplete rings, as some of the actual neighbors tend to be shielded and loaded significantly less than others, as discussed in [10, 72]. Nevertheless, non-linear matrix effects have a considerable effect when φ is larger by substantially increasing the effect of overloading of neighboring fibers to a break cluster.

Regarding (11), (55), and (56) we mention interesting analyses and Monte Carlo simulations in Mahesh and colleagues [74–76] on bundles up to size 10^6, and which show why values for γ and ϕ are difficult to establish, especially as the Weibull shape parameter, ζ, decreases below 5. They show that the fiber load-sharing during break cluster formation begins to have ELS-like behavior in terms of the failure of small ELS bundles as the cluster grows large. However, the eventual size effect and distribution shape into the lower tail robustly retains LLS features and weakest-volume scaling that is the basis for the model we develop in this paper, especially for ζ values of interest.

LIFETIME DISTRIBUTION OF A COMPOSITE COMPONENT THAT HAS SURVIVED A PROOF TEST

Proof testing consists of loading a composite structure to some proofing stress, $\sigma_p > \bar{\sigma}$, and holding that stress for at most a few minutes, and then lowering the stress to, $\bar{\sigma}$, which is the stress used in service. The idea is that applying a proof test will weed out inferior structural components thus improving the overall reliability of passing components put in service. Classic models used for composite stress rupture support this strategy. We shall determine whether this is true for the models considered in this paper.

We assume the simplified load profile given by (3) where we recall that $\sigma_p > \bar{\sigma}$ was the proof stress held for time $0 \le t < t_p$, where t_p was the proof hold time, after which the stress is reduced to $\bar{\sigma}$ for the life of the component. In studying the effects of a proof test a special fiber break cluster size becomes relevant, called $k_p = k_p(\bar{\sigma}/\sigma_p)$, and which satisfies $K_{k_p-1}\bar{\sigma} < \sigma_p \le K_{k_p}\bar{\sigma}$. From (19) we obtain:

$$k_p = \begin{cases} \left\lceil \frac{4}{\pi}\left\{\left(\sigma_p/\bar{\sigma}\right)^2 - 1\right\}\right\rceil, \text{ planar fiber array} \\ \left\lceil \frac{\pi^3}{4}\left\{\left(\sigma_p/\bar{\sigma}\right)^2 - 1\right\}^2\right\rceil, \text{ hexagonal fiber array} \end{cases} \tag{57}$$

And typically, $k_p \ll \hat{k}$. Clusters that form in the proof test that are smaller than size k_p will lead to overloads existing after time t_p, under stress $\bar{\sigma}$, that are smaller than the proof load itself, i.e., $K_{k_p-1}\bar{\sigma} < \sigma_p$. In contrast, clusters that form in the proof test that are larger than k_p will produce overloads, under stress $\bar{\sigma}$, after time t_p that are larger than the proof load itself, i.e., $\sigma_p \le K_{k_p}\bar{\sigma}$. These two conditions give rise to much of the complication in describing the probability of failure following a proof test, as given in [78] [Note that special circumstances arise where $\sigma_p < \hat{\sigma}_V$ but $\bar{\sigma}$ is so small that $\sigma_p/\bar{\sigma} > \sigma_{\delta_c}/\hat{\sigma}_V$, and thus, $k_p > \hat{k}$. This does not mean that a cluster of size k_p actually occurs, but rather it is one possible cluster size that was originally considered in the theory in [78]].

From Equation (72) in [78], the characteristic distribution function following a proof test is:

$$W_{\hat{k},\,k_{\mathrm{p}}}\left(t;\,\sigma_{\mathrm{p}},\bar{\sigma}\right)\approx c_{\hat{k}}F_{\delta_{\mathrm{c}}}\left(\sigma_{\mathrm{p}}\right)\left[\prod_{i=1}^{\hat{k}-1}F_{\delta_{\mathrm{c}}}\left(K_i\sigma_{\mathrm{p}},t_{\mathrm{p}}\right)\right]$$
$$+\sum_{k=1}^{\hat{k}-1}c_kF_{\delta_{\mathrm{c}}}\left(\sigma_{\mathrm{p}}\right)N_{k,\varphi}\left[\left[\prod_{i=1}^{k-1}F_{\delta_{\mathrm{c}}}\left(K_i\sigma_{\mathrm{p}},t_{\mathrm{p}}\right)\right]\right]\left(1-F_{\delta_{\mathrm{c}}}\left(K_k\sigma_{\mathrm{p}},t_{\mathrm{p}}\right)\right)^{N_{k,\varphi}}$$
$$\left\{\mathrm{H}\left(k-k_{\mathrm{p}}+1\right)\left(F_{\delta_{\mathrm{c}}}\left(K_k\bar{\sigma},t\right)-F_{\delta_{\mathrm{c}}}\left(K_k\bar{\sigma},t_{\mathrm{p}}\right)\right)\right.$$
$$\left[\left[\prod_{i=k+1}^{\hat{k}-1}N_{i,\varphi}F_{\delta_{\mathrm{c}}}\left(K_i\bar{\sigma},t-t_{\mathrm{p}}\right)\right]\right]+\mathrm{H}\left(k_{\mathrm{p}}-k\right)\left(F_{\delta_{\mathrm{c}}}\left(\sigma_{\mathrm{p}},t\right)-F_{\delta_{\mathrm{c}}}\left(\sigma_{\mathrm{p}},t_{\mathrm{p}}\right)\right)$$
$$\left.\left[\left[\prod_{i=k+1}^{\left(\hat{k}\vee k_{\mathrm{p}}\right)-1}N_{i\varphi}F_{\delta_{\mathrm{c}}}\left(\sigma_{\mathrm{p}},t-t_{\mathrm{p}}\right)\right]\right]\left[\left[\prod_{i=k_{\mathrm{p}}}^{\hat{k}-1}N_{i,\varphi}F_{\delta_{\mathrm{c}}}\left(K_i\bar{\sigma},t-t_{\mathrm{p}}\right)\right]\right]\right\},$$
$$t\geq t_{\mathrm{p}},\ t\gg t_{\mathrm{c}},\ \text{and}\ \hat{k}\geq 2 \tag{58}$$

where $F_{\delta_{\mathrm{c}}}\left(\bar{\sigma}\right)$ is as in (6), and $F_{\delta_{\mathrm{c}}}\left(\bar{\sigma},t\right)$ is as in (36), where (30) describes the change in overload length as a function of time, t, and stress, $\bar{\sigma}$, and where $c_{\hat{k}}$ is given by (10), and $N_{i,\varphi}$ by (55). Furthermore, for any function g_i, and any non-negative integers q, r and i we define:

$$\left[\left[\prod_{i=r}^{q}g_i\right]\right]\equiv\begin{cases}\prod_{i=r}^{q}g_i, & 1\leq r\leq q\\ 1, & 0\leq q<r\end{cases} \tag{59}$$

where the quantity in double-square parentheses is the usual product unless $q < r$ where it is unity. We also define a *left-continuous* version of the "Heaviside function," (i.e., $\mathrm{H}(0)\equiv 0$, instead of equaling "1"):

$$\mathrm{H}\left(\kappa\right)\equiv\begin{cases}0, & \kappa\leq 0\\ 1, & \kappa>0\end{cases} \tag{60}$$

and define:

$$k_1\vee k_2\equiv\min\left(k_1,k_2\right) \tag{61}$$

as the minimum of k_1 and k_2.

Substituting these into (58) and simplifying gives:

$$W_{\hat{k},\,k_{\mathrm{p}}}\left(t;\,\sigma_{\mathrm{p}},\bar{\sigma}\right)\approx c_{\hat{k}}\left(\frac{\sigma_{\delta_{\mathrm{c}}}}{\hat{\sigma}_V}\right)^{\left(\hat{k}-1\right)\frac{\varphi-1}{\varphi+1}}\left[\prod_{i=1}^{\hat{k}-1}K_i\right]^{\zeta_\varphi}\left(\frac{\sigma_{\mathrm{p}}}{\sigma_{\delta_{\mathrm{c}}}}\right)^{\hat{k}\zeta_\varphi-\frac{\varphi-1}{\varphi+1}}$$
$$\left(\frac{t_{\mathrm{p}}}{t_{\mathrm{c}}}\right)^{\left(\hat{k}-1\right)\theta_\varphi/2}\left[1+\sum_{k=1}^{\hat{k}-1}\left(\frac{t_{\mathrm{p}}}{t_{\mathrm{c}}}\right)^{\left(k-\hat{k}\right)\theta_\varphi/2}\left(\left(\frac{t}{t_{\mathrm{c}}}\right)^{\theta_\varphi/2}-\left(\frac{t_{\mathrm{p}}}{t_{\mathrm{c}}}\right)^{\theta_\varphi/2}\right)\right.$$
$$\left(\frac{t-t_{\mathrm{p}}}{t_{\mathrm{c}}}\right)^{\left(\hat{k}-k-1\right)\theta_\varphi/2}\left(1-\left(\frac{\sigma_{\delta_{\mathrm{c}}}}{\hat{\sigma}_V}\right)^{\frac{\varphi-1}{\varphi+1}}\left(\frac{K_k\sigma_{\mathrm{p}}}{\sigma_{\delta_{\mathrm{c}}}}\right)^{\zeta_\varphi}\left(\frac{t_{\mathrm{p}}}{t_{\mathrm{c}}}\right)^{\theta_\varphi/2}\right)^{N_{k,\varphi}}$$
$$\left\{\mathrm{H}\left(k-k_{\mathrm{p}}+1\right)\left(\frac{\bar{\sigma}}{\sigma_{\mathrm{p}}}\right)^{\left(\hat{k}-k\right)\zeta_\varphi}+\mathrm{H}\left(k_{\mathrm{p}}-k\right)\right.$$
$$\left.\left.\left[\left[\prod_{i=k}^{\left(\hat{k}\vee k_{\mathrm{p}}\right)-1}\frac{1}{K_i}\right]\right]^{\zeta_\varphi}\left(\frac{\bar{\sigma}}{\sigma_{\mathrm{p}}}\right)^{\left(\hat{k}-\left(\hat{k}\vee k_{\mathrm{p}}\right)\right)\zeta_\varphi}\right\}\right] \tag{62}$$

In the case where $\varphi = 1$ this reduces to Equation (75) from [78]. Using (62) we can then write an expression for the composite lifetime, following (34) and using (51) as:

$$H_V\left(t;\,\sigma_{\mathrm{p}},\bar{\sigma}\right)\approx 1-\exp\left\{-\left(\left(\frac{\sigma_{\mathrm{p}}}{\hat{\sigma}_{V,\varphi}}\right)^{\hat{\rho}_\varphi}\frac{t_{\mathrm{p}}}{t_{\mathrm{c}}}\right)^{\hat{\beta}_\varphi}\right.$$
$$\left[1+\sum_{k=1}^{\hat{k}-1}q_{k,\hat{k}}\left(t,\sigma_{\mathrm{p}}\right)\left(\frac{t_{\mathrm{p}}}{t_{\mathrm{c}}}\right)^{\left(k-\hat{k}\right)\theta_\varphi/2}\left\{\mathrm{H}\left(k-k_{\mathrm{p}}+1\right)\left(\frac{\bar{\sigma}}{\sigma_{\mathrm{p}}}\right)^{\left(\hat{k}-k\right)\zeta_\varphi}\right.\right.$$
$$\left.\left.\left.+\mathrm{H}\left(k_{\mathrm{p}}-k\right)\left[\left[\prod_{i=k}^{\left(\hat{k}\vee k_{\mathrm{p}}\right)-1}\frac{1}{K_i}\right]\right]^{\zeta_\varphi}\left(\frac{\bar{\sigma}}{\sigma_{\mathrm{p}}}\right)^{\left(\hat{k}-\left(\hat{k}\vee k_{\mathrm{p}}\right)\right)\zeta_\varphi}\right\}\right]\right\},\ t\geq t_{\mathrm{p}} \tag{63}$$

where

$$q_{k,\hat{k}}\left(t,\sigma_{\mathrm{p}}\right)=\left(\frac{t_{\mathrm{p}}}{t_{\mathrm{c}}}\right)^{\left(k-\hat{k}\right)\theta_\varphi/2}\left(\left(\frac{t}{t_{\mathrm{c}}}\right)^{\theta_\varphi/2}-\left(\frac{t_{\mathrm{p}}}{t_{\mathrm{c}}}\right)^{\theta_\varphi/2}\right)$$
$$\left(\frac{t-t_{\mathrm{p}}}{t_{\mathrm{c}}}\right)^{\left(\hat{k}-k-1\right)\theta_\varphi/2}\left(1-\left(\frac{\sigma_{\delta_{\mathrm{c}}}}{\hat{\sigma}_V}\right)^{\frac{\varphi-1}{\varphi+1}}\left(\frac{K_k\sigma_{\mathrm{p}}}{\sigma_{\delta_{\mathrm{c}}}}\right)^{\zeta_\varphi}\left(\frac{t_{\mathrm{p}}}{t_{\mathrm{c}}}\right)^{\theta_\varphi/2}\right)^{N_{k,\varphi}},$$
$$t\geq t_{\mathrm{p}} \tag{64}$$

Of special interest is the reliability of a structure, $R\left(t\,|\,t\geq t_{\mathrm{p}}\right)$, conditional on surviving a proof test. This is calculated in general terms using Bayes theorem:

$$R\left(t\,|\,t\geq t_{\mathrm{p}}\right)=\frac{R\left(t\right)}{R\left(t_{\mathrm{p}}\right)}=\frac{1-F\left(t\right)}{1-F\left(t_{\mathrm{p}}\right)}. \tag{65}$$

The conditional reliability for lifetime, $R_V\left(t|\,t\geq t_{\mathrm{p}},\sigma_{\mathrm{p}},\bar{\sigma}\right)$, under a sustained load, $\bar{\sigma}$, and for times $t\geq t_{\mathrm{p}}$, conditioned on survived an initial proof loading, $\sigma_{\mathrm{p}}\geq\bar{\sigma}$, up to time t_{p}, is given as:

$$R_V\left(t|\,t\geq t_{\mathrm{p}},\sigma_{\mathrm{p}},\bar{\sigma}\right)\approx\exp\left\{\left(\left(\frac{\sigma_{\mathrm{p}}}{\hat{\sigma}_{V,\varphi}}\right)^{\hat{\rho}_\varphi}\frac{t_{\mathrm{p}}}{t_{\mathrm{c}}}\right)^{\hat{\beta}_\varphi}\right.$$
$$\left(1-\left[1+\sum_{k=1}^{\hat{k}-1}q_{k,\hat{k}}\left(t,\sigma_{\mathrm{p}}\right)\left(\frac{\bar{\sigma}}{\sigma_{\mathrm{p}}}\right)^{\left(\hat{k}-k\right)\zeta_\varphi}\left(\mathrm{H}\left(k-k_{\mathrm{p}}+1\right)\right.\right.\right.$$
$$\left.\left.\left.+\mathrm{H}\left(k_{\mathrm{p}}-k\right)\left[\left[\prod_{i=k}^{\left(\hat{k}\vee k_{\mathrm{p}}\right)-1}\frac{1}{K_i}\right]\right]^{\zeta_\varphi}\left(\frac{\bar{\sigma}}{\sigma_{\mathrm{p}}}\right)^{\left(k-\left(\hat{k}\vee k_{\mathrm{p}}\right)\right)\zeta_\varphi}\right)\right]\right)\right\},\ t\geq t_{\mathrm{p}} \tag{66}$$

Thus, the conditional lifetime distribution following a proof test is $1 - R_V\left(t|\, t \geq t_\mathrm{p}, \sigma_\mathrm{p}, \bar{\sigma}\right)$, yielding:

$$H_V\left(t|\, t \geq t_\mathrm{p}, \sigma_\mathrm{p}, \bar{\sigma}\right) \approx 1 - \exp\left\{\left(\left(\frac{\sigma_\mathrm{p}}{\hat{\sigma}_{V,\varphi}}\right)^{\hat{\rho}_\varphi}\left(\frac{t_\mathrm{p}}{t_\mathrm{c}}\right)\right)^{\hat{\beta}_\varphi}\right.$$
$$\left(1 - \left[1 + \sum_{k=1}^{\hat{k}-1} q_{k,\hat{k}}\left(t, \sigma_\mathrm{p}\right) \times \left(\frac{\bar{\sigma}}{\sigma_\mathrm{p}}\right)^{\left(\hat{k}-k\right)\zeta_\varphi}\left(\mathrm{H}\left(k - k_\mathrm{p} + 1\right) + \mathrm{H}\left(k_\mathrm{p} - k\right)\right.\right.\right.$$
$$\left.\left.\left.\left[\left[\prod_{i=k}^{\left(\hat{k}\vee k_\mathrm{p}\right)-1} \frac{1}{K_i}\right]\right]^{\zeta_\varphi}\left(\frac{\bar{\sigma}}{\sigma_\mathrm{p}}\right)^{\left(k-\left(\hat{k}\vee k_\mathrm{p}\right)\right)\zeta_\varphi}\right)\right]\right)\Bigg\},\ t \geq t_\mathrm{p} \tag{67}$$

Composite Lifetime Distribution Following a Proof Test Under the Classic CPL-W Model

Historically stress rupture failure is most commonly described using the classic power law model in a Weibull framework (CPL-W model) [1]. For this model, the probability of failure for an arbitrary stress profile, $\sigma\left(t\right),\ t \geq 0$, is given by:

$$H_{V,\mathrm{CPL\text{-}W}}\left(t, \sigma\left(.\right)\right) = 1 - \exp\left\{-V\left[\int_0^t \left(\frac{\sigma\left(\tau\right)}{\sigma_\mathrm{ref}}\right)^{\tilde{\rho}} \frac{\mathrm{d}\tau}{t_\mathrm{c}}\right]^{\tilde{\beta}}\right\},$$
$$t \geq 0. \tag{68}$$

where the parameters have similar meanings as before, i.e., t_c is still a characteristic time constant and, σ_ref, is a reference stress scale parameter, $\tilde{\beta}$ is a lifetime shape parameter and $\tilde{\rho}$ is a power-law exponent relating lifetime to stress level. However, under the ramp loading (1), i.e., $\sigma\left(t\right) = Rt,\ t \geq 0$, where R is the loading rate, the strength distribution takes the form:

$$H_{V,\mathrm{CPL\text{-}W}}\left(\sigma; R\right) = 1 - \exp\left\{-V\left(\left(\frac{\sigma}{\sigma_\mathrm{ref}}\right)^{\tilde{\rho}} \frac{\sigma}{R\, t_\mathrm{c}\left(\tilde{\rho}+1\right)}\right)^{\tilde{\beta}}\right\},$$
$$\sigma \geq 0 \tag{69}$$

If σ_ref is chosen originally to satisfy $\sigma_\mathrm{ref} = R\, t_\mathrm{c}\left(\tilde{\rho}+1\right)$ then we can rewrite (69) as:

$$H_{V,\mathrm{CPL\text{-}W}}\left(\sigma; R\right) = 1 - \exp\left\{-\left(\frac{\sigma}{\tilde{\sigma}_V}\right)^{\tilde{\alpha}}\right\} \tag{70}$$

where

$$\tilde{\alpha} = \tilde{\beta}\left(\tilde{\rho}+1\right) \tag{71}$$

and

$$\tilde{\sigma}_V = V^{-1/\left(\tilde{\beta}\tilde{\rho}\right)}\sigma_\mathrm{ref} \tag{72}$$

Thus, the CPL-W model's strength distribution is a standard two parameter Weibull distribution, with a shape parameter of $\tilde{\alpha}$ and a scale parameter of $\tilde{\sigma}_V$.

In the case of stress-rupture testing, where the applied load is constant $\sigma\left(t\right) = \bar{\sigma},\ \ t \geq 0$ as in (2), then (69) yields the familiar form:

$$H_{V,\mathrm{CPL\text{-}W}}\left(\sigma, t\right) = 1 - \exp\left\{-\left(\left(\frac{\bar{\sigma}}{\tilde{\sigma}_V}\right)^{\tilde{\rho}} \frac{t}{t_\mathrm{ref}}\right)^{\tilde{\beta}}\right\},\ t \geq 0. \tag{73}$$

Thus, the CPL-W model for strength and lifetime is similar to that of current SFB model, but with a slightly different strength shape parameter, $\tilde{\beta}\left(\tilde{\rho}+1\right)$, in (69) vs. $\hat{\rho}_\varphi\hat{\beta}_\varphi$ from (42) and (43).

Using (67) in the CPL-W model, the lifetime distribution having survived the proof test is:

$$H_{V,\,\mathrm{CPL-W}}\left(t|\, t \geq t_\mathrm{p}, \sigma_\mathrm{p}, \bar{\sigma}\right) = 1 - \exp\left\{\left[\left(\frac{\sigma_\mathrm{p}}{\tilde{\sigma}_V}\right)^{\tilde{\rho}} \frac{t_\mathrm{p}}{t_\mathrm{ref}}\right]^{\tilde{\beta}}\right.$$
$$\left.\left[1 - \left(1 + \left(\frac{\bar{\sigma}}{\sigma_\mathrm{p}}\right)^{\tilde{\rho}} \frac{t - t_\mathrm{p}}{t_\mathrm{p}}\right)^{\tilde{\beta}}\right]\right\}, t \geq t_\mathrm{p} \tag{74}$$

and noting that $0 < \tilde{\beta} \ll 1$ we can expand the above to give:

$$H_{V,\,\mathrm{CPL-W}}\left(t|\, t \geq t_\mathrm{p}, \sigma_\mathrm{p}, \bar{\sigma}\right) \approx 1 - \exp\left\{\left[\left(\frac{\sigma_\mathrm{p}}{\tilde{\sigma}_V}\right)^{\tilde{\rho}} \frac{t_\mathrm{p}}{t_\mathrm{ref}}\right]^{\tilde{\beta}}\right.$$
$$\left.\left[1 - \left(1 + \tilde{\beta}\left(\frac{\bar{\sigma}}{\sigma_\mathrm{p}}\right)^{\tilde{\rho}} \frac{t - t_\mathrm{p}}{t_\mathrm{p}}\right)\right]\right\}, t \geq t_\mathrm{p} \tag{75}$$

which is accurate at least out to the time, $t = t_\mathrm{s}$ in (73) where the argument is unity and the failure probability is $H_{V,\,\mathrm{CPL\text{-}W}}\left(\sigma, t_\mathrm{s}\right) = 1 - \mathrm{e}^{-1} = 0.632$, so more than ½. For transparency, we have written (75) in a form for easy comparison to the corresponding result (67), from our model. For $\bar{\sigma} < \sigma_\mathrm{p} < \tilde{\sigma}_V$, inspection of (75) or (74) compared to (73) shows that, in the CPL-W model, proof testing will always reduce the probability of failure (increase the reliability) at any later time for specimens that "pass" (survive) the proof test.

Thus, despite these similarities in the strength and lifetime distributions in the model developed in the paper vs. the CPL-W model, for more complex loading profiles, such as a proof test, these models will have very different results, with the CPL-W model predicting an increased conditional reliability after a proof test and the current model predicting a decreased reliability [78].

RESULTS AND DISCUSSION

We have introduced a new model that builds on our previous model in [78] and involves two new parameters, φ and σ_y, which account for non-linear effects in matrix creep and matrix yielding in shear, respectively. In the limit of $\varphi \rightarrow 1^+$we recover the previous model based on a linearly viscoelastic matrix, whereupon the effects of σ_y also vanish. In this section we study the subtle effects of varying these two new parameters, beginning with their influence on characterizing the composite

volume in the model, and followed by how they also influence the distributions for composite strength and lifetime.

In such a complex model parametric studies are useful for understanding the effects of the various parameters and their combinations on overall behavior. In the examples below, we choose to vary model parameter values keeping in mind that, in practice, experimental values for several of these parameters may not be readily accessible. More often, statistical data sets are available from strength and lifetime tests on composite samples in multiple replications, where the lifetime tests have been replicated at several stress levels for various times (often months, and sometimes years). Thus, we vary certain model parameters governing fiber and matrix interactions at the microscale in order to observe their effects on parameters such as Weibull shape and scale parameters for strength and lifetime, that are typically obtained from fitting actual test data to models that are largely phenomenological [2]. This way the "practical" effects of various parameter choices will become more readily apparent.

Typical Parameter Values and Implications on Interpretation of Volume of Material in a Specimen or Component Being Loaded

This new model requires a more careful interpretation of the role of the "volume" parameter, V, which happens to be the number of material elements of length δ_c in the composite, rather than the physical composite volume under load expressed, for instance, as the total volume of fiber in the loaded composite. In our parametric study, we naturally desire to keep the physical composite volume constant for all cases. However, as both φ and σ_y change in the new model, so does the element length, δ_c, sometimes increasing by an order of magnitude, which means that the number of elements, V, must likewise decrease. Since δ_c, changes according to (31), we can see that, V, varies following the relation:

$$V \propto \left(\sigma_y/\hat{\sigma}_V\right)^{(\varphi-1)/(\varphi+1)}. \tag{76}$$

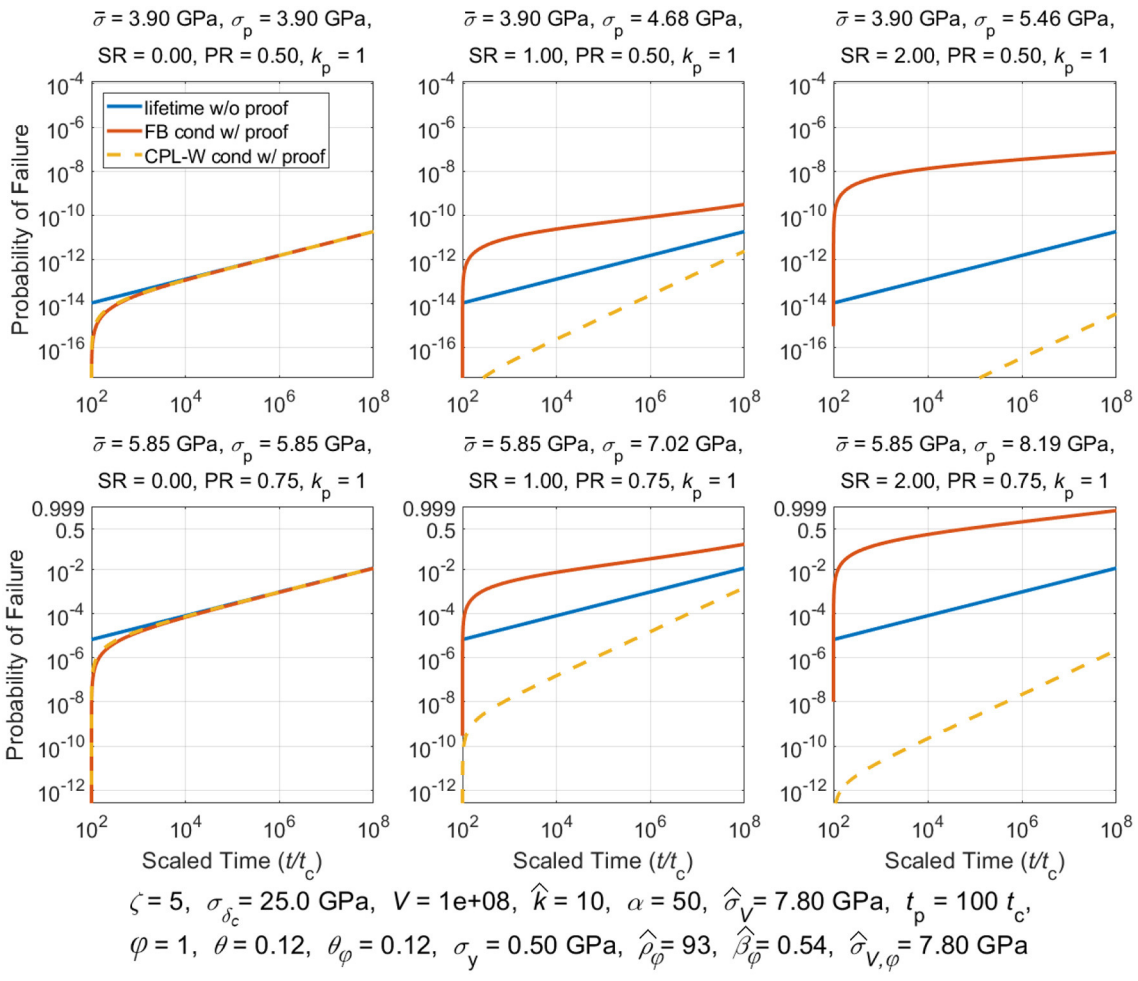

FIGURE 1 | Tows with fibers in a planar array and with matrix parameter, $\varphi = 1$.

The definition of δ_c in (31), also involves (7), (8), and (32), and thus, δ_c can also be written as:

$$\delta_c = \hat{\delta}_c \left(\frac{\hat{\sigma}_V}{\sigma_y}\right)^{(\varphi-1)/(\varphi+1)} = \frac{4}{\zeta+1}\delta_e \left(\frac{\hat{\sigma}_V}{\sigma_y}\right)^{(\varphi-1)/(\varphi+1)} \quad (77)$$

where $\delta_e \approx d\sqrt{(E/G_e)(w/d)}$ and $\sigma_y = 2\tau_y\delta_e/d$. Also, $\hat{\sigma}_V$, given by (18), depends on ζ, and on V itself, although, it is largely free of φ and σ_y except through minor effects on $\hat{k}$.

Typical Values of Various Micromechanical Parameters

Typically $w/d \sim 1/4$, $E/G_e \sim 200$, and $\tau_y \approx 35$ MPa, and thus, $\delta_e \approx d\sqrt{(1/4)(200)} = 7.07d$ and $\sigma_y \approx 2\,(35)\,(7.07) \approx 500$ MPa. This value of the tensile stress level σ_y, which is associated with driving matrix yielding shear around a fiber break, turns out to be an order of magnitude smaller than values typically obtained for $\hat{\sigma}_V$, hence the ratio, $\hat{\sigma}_V/\sigma_y$ will have a strong influence on the magnitude of the characteristic element length δ_c in (77), and thus on number fiber elements, V, in a given physical volume according to (76). Note that the effect on V in (76) can result in no effect at all when $\varphi = 1$, to a reduction in V by an order of magnitude when $\varphi \gg 1$.

The implications of (76) and (77) are thus twofold: First, the number of elements, V, changes in formulas such as (18) or (45) for determining the Weibull scale parameter for strength, and in (21) for determining the critical cluster size, $\hat{k}$. Second, the change in the volume parameter, V, in (76) is also associated with a change in the failure probability of a fiber element in (6) or (36), through the influence of δ_c on σ_{δ_c}. However, he effect of non-linear viscoplasticity is also seen in the difference between the Weibull scale parameters for strength, $\hat{\sigma}_V$ of (18), and $\hat{\sigma}_{V,\varphi}$ of (45), through the factor, Ξ_φ, of (46). For instance, in the case of a 2D array where $\hat{k} = 8$, $\varphi = 4$, $\zeta = 5$, and using (9) and (20), we obtain approximately $\hat{\sigma}_V/\sigma_{\delta_c} = 1/2.70 = 0.370$, and thus (46) gives:

$$\Xi_\varphi = (0.370)^{1/(1+(\frac{8}{7})(\frac{5}{3})5)} = (0.370)^{1/10.52} = 0.910 \quad (78)$$

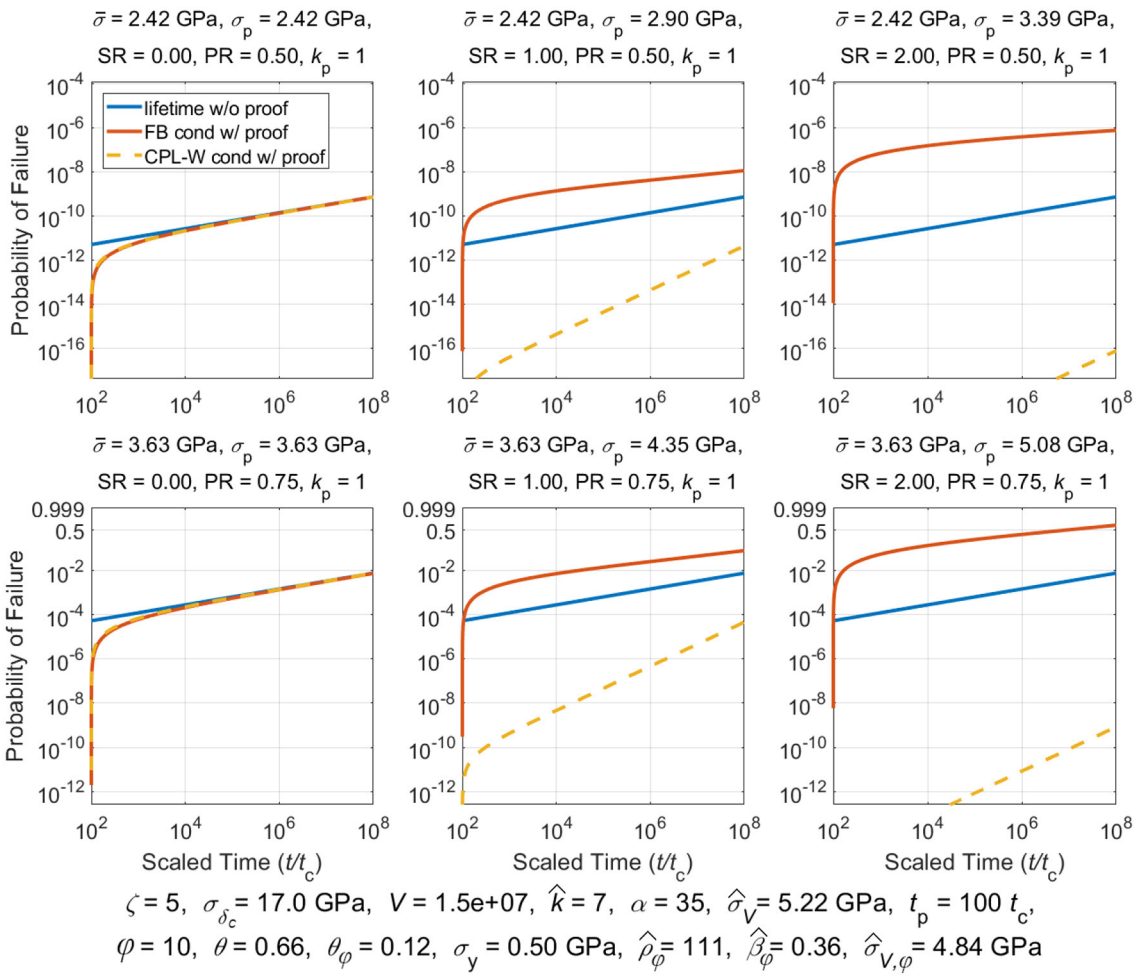

FIGURE 2 | Tows with fibers in a planar array and matrix parameters, $\varphi = 10$ and $\sigma_y = 0.5$ GPa.

Hence, the effect on composite strength, as viewed through the Weibull scale parameter, $\hat{\sigma}_{V,\varphi}$, compared to $\hat{\sigma}_V$ of the previous model in [78], also amounts to a strength reduction of about 9%, which is distinct from the ultimate effect of (76) and (77) in changing the number of fiber elements, V, despite assuming a fixed overall composite volume.

Parametric Study of Effects of φ and σ_y on Strength and Lifetime in Two Applications

To illustrate the implications of varying the two new parameters, φ and σ_y, we study two particular applications of the carbon fiber/epoxy matrix composites, namely: (i) the behavior of epoxy-impregnated, carbon fiber yarns (often called carbon/epoxy tows) building on fiber and matrix properties, and (ii) the behavior at a larger scale of composite overwrapped pressure vessels (COPVs) building on tow element and inter-tow interface properties. which govern the length-scale of tow element load-sharing over time. The values of various parameters for the cases of each application are listed at the bottom of each figure. This includes those parameters initially set in the model and those derived from the model itself. For simplicity, in all cases we set the characteristic matrix creep time as $t_c = 0.01$ hour and the proof-test time as, $t_p = 1$ hour, however, result will be presented in terms of scaled time, t/t_c .

Note that the value of θ_φ in (39) has been determined in each application so that the power law exponent, $\hat{\rho}_\varphi$ (or $\tilde{\rho}$), relating lifetime to stress level generally lies in the range 86–114. Such values are representative of carbon/epoxy composites (at ambient temperatures). They also allow for easy comparison among the cases as well as providing a more fruitful demonstration of certain model features. For all but one case, the resulting Weibull shape parameters for lifetime, $\hat{\beta}_\varphi$ or $\tilde{\beta}$, satisfy, $0 < \hat{\beta}_\varphi < 1$, however values vary considerably across the various cases, as do values for the Weibull scale parameters for strength and load level, $\hat{\sigma}_V$, $\hat{\sigma}_{V,\varphi}$ and $\tilde{\sigma}_V$. Investigation of changes in behavior of these Weibull strength and lifetime parameters with changes in φ and σ_y is a key aspect of the study. These values are all given for each case at the bottom of each figure.

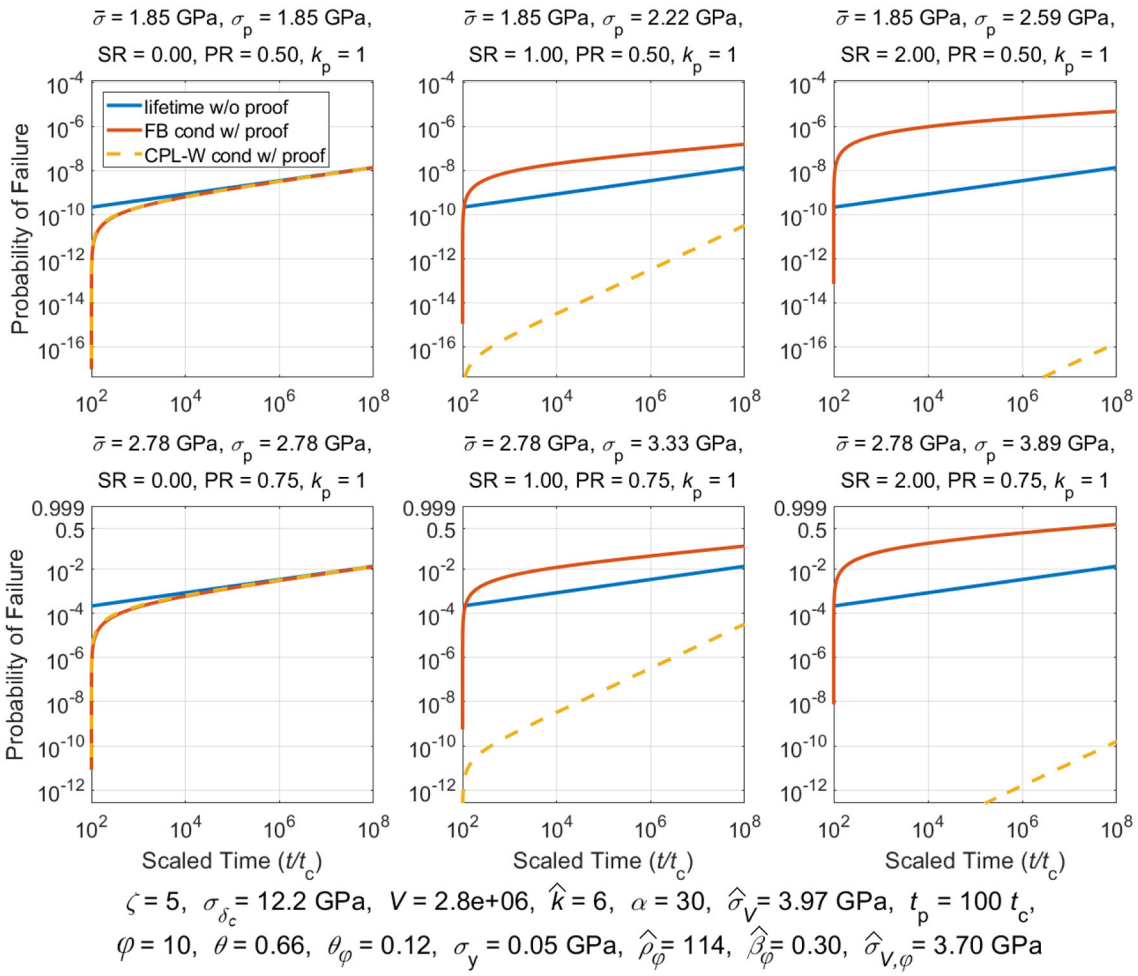

FIGURE 3 | Tows with fibers in a planar array and matrix parameters $\varphi = 10$ and $\sigma_y = 0.05$ GPa.

Additional Parametric Details in the Application to Carbon/Epoxy Tows

The first application involves predicting the strength and lifetime distributions of carbon/epoxy tows assuming the fibers follow a Weibull distribution for strength with shape parameter, $\zeta = 5$, and scale parameter $\sigma_{\hat{\delta}_c} = 25$ GPa. Here we note that $\hat{\delta}_c = \delta_c$ in the special case $\varphi = 1$, but not when $\varphi > 1$ and $\sigma_y < \hat{\sigma}_V$. In the latter case $\delta_c > \hat{\delta}_c$ from (31) and (32), and thus, $\sigma_{\delta_c} < 25$ GPa based on (77). In this application to tow behavior we consider both versions of fiber-to-fiber load-sharing: the first is a planar fiber array, and the second, a fiber array with hexagonal fiber packing and associated fiber stress redistribution, but also assuming two different versions of the number of overload fibers around a break cluster, i.e., (55) vs (56). Results are shown in **Figures 1**–**3** for a planar fiber array, and in **Figures 4**–**6**, for a hexagonal fiber array, where **Figures 4**, **5** are under (55) and **Figure 6** is under (56). Among all six figures, **Figures 1**, **4**, show results for the special case, $\varphi = 1$, which also happen to serve as results under the previous model [78] for a linearly viscoelastic matrix. Thus, these figures provide a basis for comparison of results from the previous model to the new model in **Figures 2**, **3**, **5**, **6**, where $\varphi > 1$ and σ_y play a major role.

Additional Parametric Details in the Application to COPVs

The second application involves predicting the strength of COPVs based on tow strength properties, as specified for the tow elements in the model, where by the Weibull shape parameter is $\zeta = 20$, and scale parameter is $\sigma_{\hat{\delta}_c} = 8.0$ GPa corresponding to the case $\varphi = 1$, where $\hat{\delta}_c = \delta_c$. In **Figure 7** we show results for a planar array of tows and associated load-sharing, and in **Figure 8** we show results for tows in a hexagonal array and sharing load accordingly with (56) governing the number of overloaded neighbors to a cluster. In both cases we assume $\varphi = 10$ and $\sigma_y = 0.25$ GPa for purposes of modeling interface creep or tow slippage in shear between tows (Results for $\varphi = 1$ are not shown).

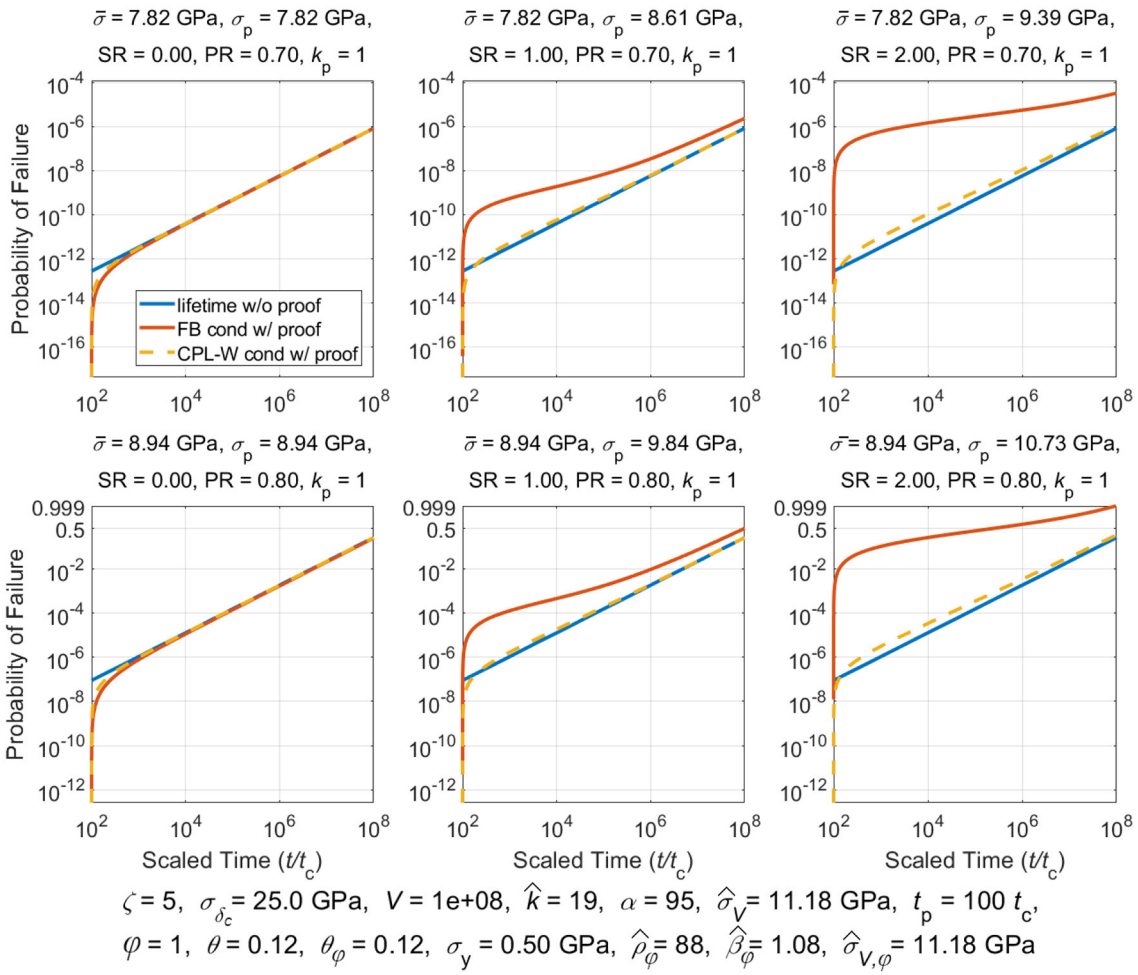

FIGURE 4 | Tows with fibers in a hexagonal array and matrix parameter, $\varphi = 1$, and with $\phi = 2.5$ and $\gamma = 0.27$ in (55) for calculating number of susceptible fibers around a cluster.

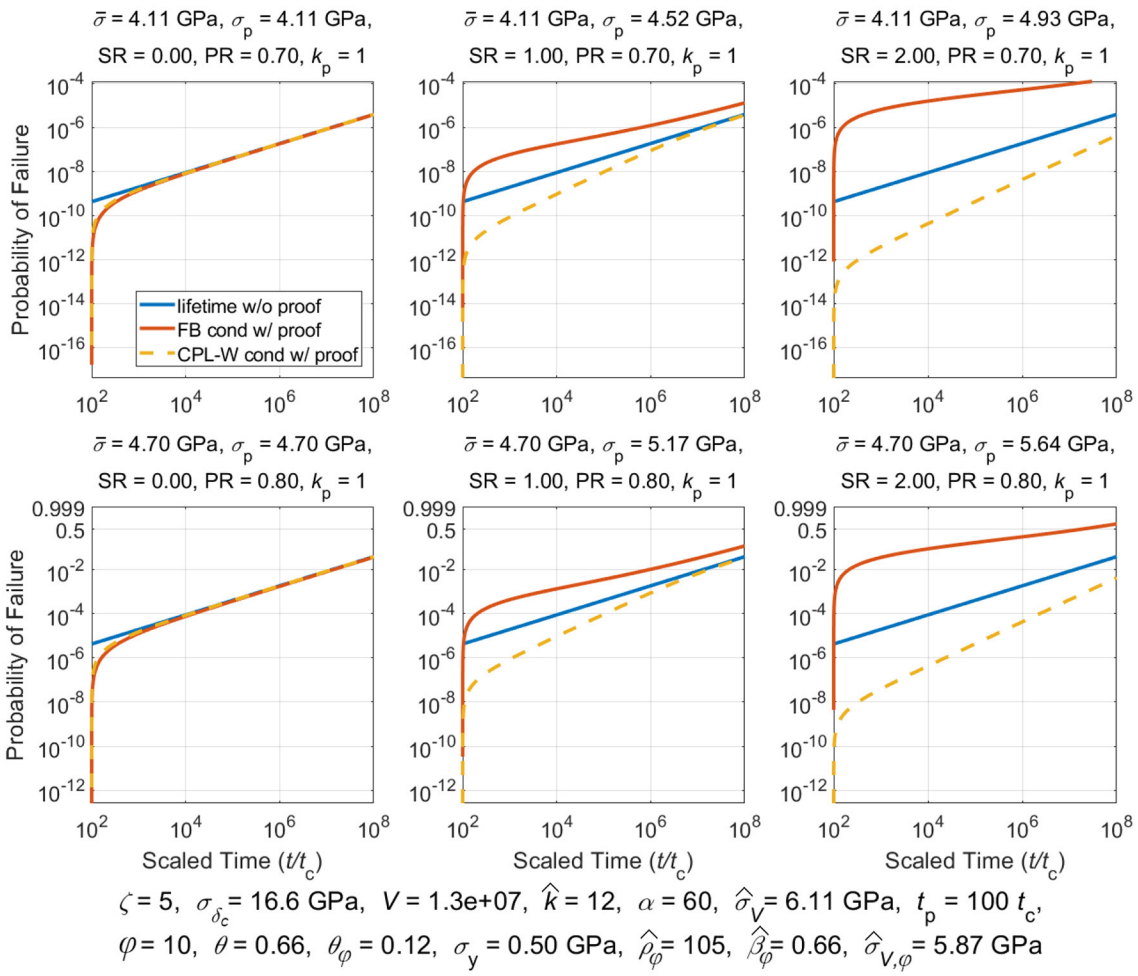

FIGURE 5 | Tows with fibers in a hexagonal array and matrix parameters $\varphi = 10$ and $\sigma_y = 0.50$ GPa, with $\phi = 2.5$ and $\gamma = 0.27$ in (55) used to calculate number of susceptible fibers around a cluster.

Plotted Quantities and Applied Loadings Used in Each Particular Application and Case

For all cases plotted in **Figure 1** through **Figure 8**, time begins at $t = 0$, though the horizontal axes and plotting of the graphs begins only at $t = t_p$. For this reason, a virgin specimen initially loaded at $t = 0$ can potentially fail before time t_p, which is why the failure probability at time, $t = t_p$is already distinctly non-zero. On the other hand, a proof-tested vessel sees its proof test applied over the time period, $0 \leq t < t_p$, and if it fails it is replaced by one that has survived the proof test, at which point time continues onward, i.e. $t_p \leq t$. Consequently, exactly at time $t = t_p$ the probability of failure of the proof-tested vessel, being a conditional probability of failure, is by definition zero. However, because of the proof test it will have many broken fiber elements that otherwise would not have occurred, had it been a virgin specimen that survived to time $t = t_p$. Thus, only a short time later at some time, [[Mathtype-mtef1-eqn-619.mtf]], its probability of failure shoots up beyond what occurs without the proof test. This "overshoot" after the proof test is a key feature of the model that generally does not occur for the classic CPL-W model or other models.

These effects are seen in all the figures, where the solid blue line represents the failure probability vs. time for a lifetime test under a constant loading (2), i.e., absent a proof test, both for the classic power-law (CPL-W) model and the current stochastic fiber breakage (SFB) model (which happen to be the same when parameter values in (73) and (41) are appropriately matched). In cases involving a proof test under loading (3), the conditional probability of failure vs. time following survival of the proof test is given as a solid orange line for the SFB model, and a dashed yellow line for the CPL-W model. Above each figure panel is the loading condition for that particular case, where the results presented for specific tow cases are in **Figures 1**–**6**, and specific COPV cases in **Figures 7**, **8**. The loading parameter "SR" in the various cases refers to the stress ratio used for that figure panel, which is the constant applied stress, $\bar{\sigma}$, in the lifetime test, divided by the Weibull stress scale parameter, $\hat{\sigma}_{V,\varphi}$, for that case. The parameter "PR" refers to the proof stress ratio used in a particular

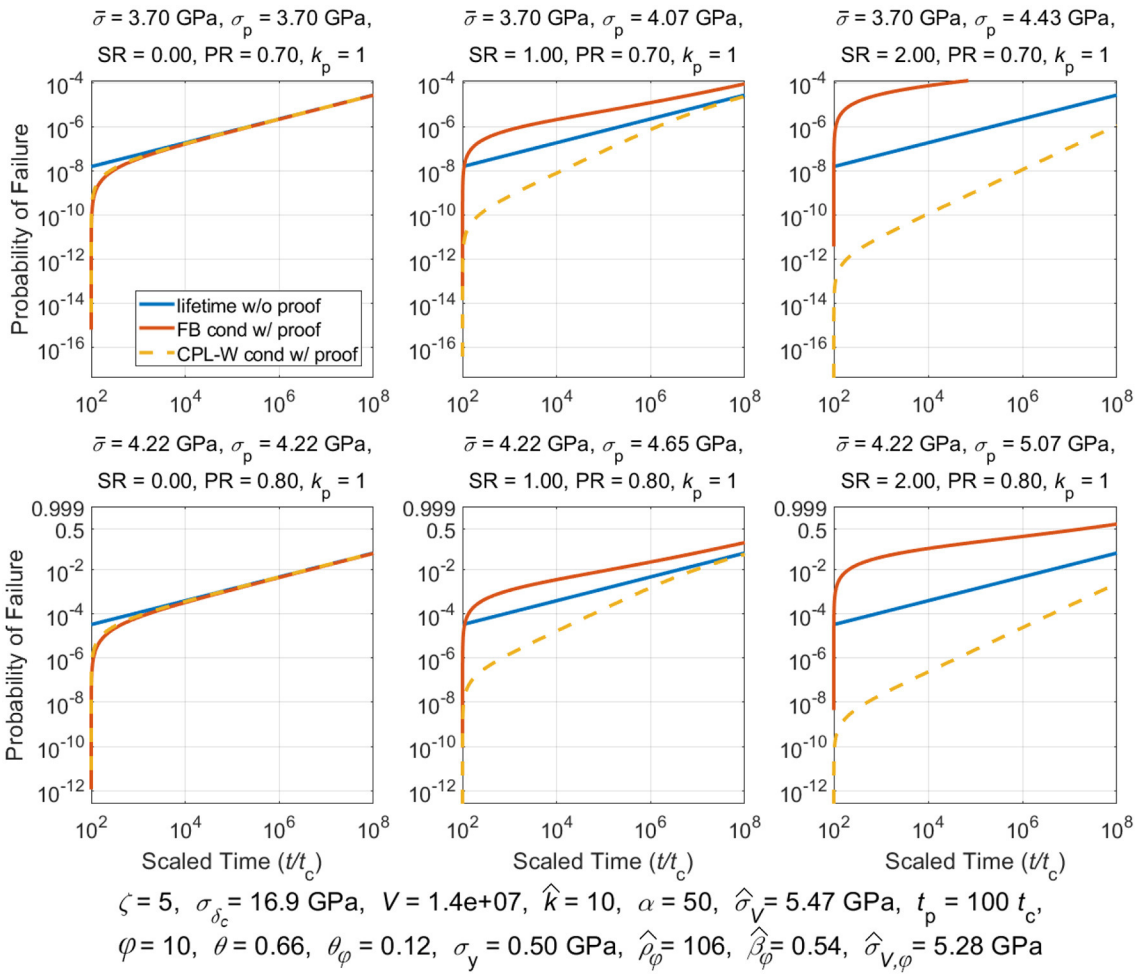

FIGURE 6 | Tow lifetime distribution with fibers arranged in a hexagonal array with number of overloaded neighbors following (56), and with matrix parameters $\varphi = 10$ and $\sigma_y = 0.50$ GPa.

case of a figure, being the ratio of the proof stress to the applied stress in the lifetime test, $\sigma_p/\bar{\sigma}$. Note that each figure presents plots for two different stress ratios and three different proof ratios in tows and two different proof ratios in COPVs. Also k_p refers to the special proof cluster size defined by (57).

Common Features of Plots Associated With a Proof Test, Whether for Tows or for COPVs

All figures show that when the stress in a proof test is the same as the lifetime stress level, i.e., $\sigma_p = \bar{\sigma}$, the SFB and CPL-W models predict the same results for probability of failure vs. time, although with failure probabilities that are initially lower than when no proof test is applied. However, when $\sigma_p > \bar{\sigma}$, the SFB model always predicts an *higher* probability of failure compared to a standard lifetime test without a proof test, which is sometimes higher by several orders of magnitude. In contrast, the CPL-W model predicts a *lower* probability of failure after a proof test in the typical case where $0 < \beta_\varphi < 1$, and typically by several orders of magnitude. However, in the CPL-W model a *higher* probability of failure does occur when $\beta_\varphi > 1$ (see **Figures 4**, **8**), though not of the magnitude seen in the SFP model. This is a critical difference between the two models, SFB vs CPL-W, also discussed extensively in [78] for the special case $\varphi = 1$.

Additional Features of Effects of φ and σ_y on the Strength Distribution of Tows

Figure 1 through **Figure 3** show the lifetime distribution of a carbon/epoxy tow assuming a planar fiber configuration and planar load-sharing. **Figures 1**, **2** showing the effects of changing φ from 1 to 10 when $\sigma_y = 0.5$ GPa, and **Figures 2**, **3** demonstrate the effect of further lowering σ_y by an order of magnitude to $\sigma_y = 0.05$ GPa, while maintaining $\varphi = 10$ (when $\varphi = 1$ there is no effect from changing σ_y). In **Figures 2**, **3**, choosing $\varphi > 1$ with $\sigma_y < \hat{\sigma}_V$, requires reducing, V, the number of fiber elements in the model, in order to maintain the same total material volume. This reduction in V is associated with the previously mentioned, increase in δ_c, which results in a decrease in σ_{δ_c} as well as a decrease in the critical cluster size $\hat{k}$ from the value $\hat{k} = 10$ in

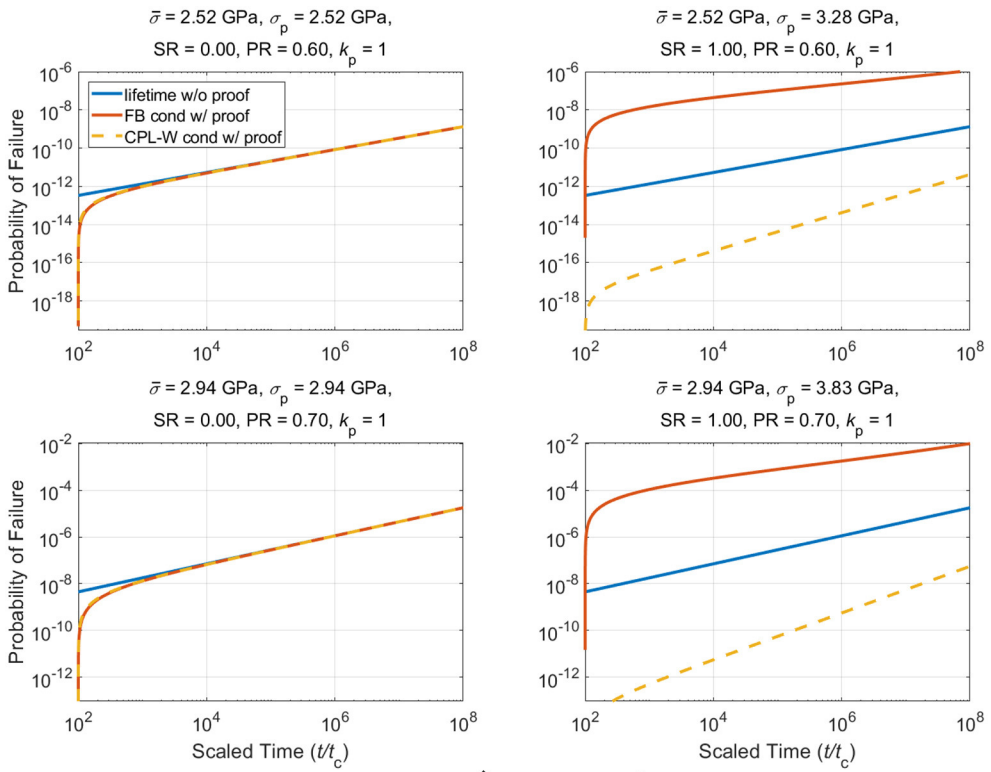

FIGURE 7 | COPV lifetime distribution where tows are modeled as being arranged in a planar array, and with matrix parameter $\varphi = 10$ and $\sigma_y = 0.25$ GPa.

Figure 1, to $\hat{k} = 7$ in **Figure 2** and to $\hat{k} = 6$ in **Figure 3**. This reduction in $\hat{k}$ causes a proportional lowering of the Weibull shape parameter for strength, $\hat{\alpha} = \hat{k}\zeta$ in (19) from $\hat{\alpha} = 50$ in **Figure 1** down to $\hat{\alpha} = 30$ in **Figure 3**, which happens to be a more realistic value for tows compared to those obtained experimentally, but still somewhat larger. This decrease in $\hat{\alpha}$ reflects an increase in the variability in tow strength.

A significant decrease also occurs in the Weibull scale parameter for tow strength, $\hat{\sigma}_V$, from $\hat{\sigma}_V = 7.80$ GPa in **Figure 1** to $\hat{\sigma}_V = 5.22$ GPain **Figure 2** and then to $\hat{\sigma}_V = 3.97$ GPa in **Figure 3** (Effects on $\hat{\sigma}_{V,\varphi}$ will be discussed later in connection with lifetime behavior). This amounts to decreases of as much as 50% in strength. Once again, the Weibull shape and scale parameter values for tow strength associated with **Figure 1** are overly optimistic compared to the more realistic values in **Figures 2**, **3**. Clearly non-linear matrix creep and yielding can result in large effect in terms of lowering the composite strength and increasing its variability compared to the case of $\varphi = 1$.

Figure 4 through **Figure 6** provide results similar to those in **Figure 1** through **Figure 3**, but for the case of hexagonal fiber packing and associated load-sharing. **Figures 4**, **5** involve using the parameter values $\phi = 2.5$ and $\gamma = 0.27$ in (55), which determines the number of fibers around a cluster susceptible to failure in growing a cluster. **Figure 6** is similar to **Figure 5**, except that now $\phi = \sqrt{4\pi}$ and $\gamma = 0.5$, as was used in (56), for determining the number of susceptible neighbors. Otherwise we maintain $\varphi = 10$ and $\sigma_y = 0.5$ GPa. Reductions are again needed in the number of fiber elements, V, with increasing δ_c, to maintain the same overall material volume, and the result is a large decrease in the critical cluster size $\hat{k}$ from $\hat{k} = 19$ in **Figure 4** to $\hat{k} = 12$ in **Figure 5** and to $\hat{k} = 10$ in **Figure 6**. Likewise a proportional lowering of the Weibull strength shape parameter, $\hat{\alpha} = \hat{k}\zeta$, occurs from $\hat{\alpha} = 95$ in **Figure 4** down to $\hat{\alpha} = 50$ in **Figure 6** as well as a large drop in the Weibull strength scale parameter from $\hat{\sigma}_V = 11.18$ GPain **Figure 4** to $\hat{\sigma}_V = 5.47$ GPa in **Figure 6**, which is a reduction by one-half.

Once again, the values seen in **Figure 4** for $\varphi = 1$ are overly optimistic compared to the more realistic values in **Figures 5**, **6**, as found in experiments, though still larger. Once again non-linear matrix creep and yielding can result in a large decrease in the strength of the composite and an increase in its variability.

Additional Features of Effects of φ and σ_y on the Lifetime Distribution of Tows

Figure 1 through **Figure 6** demonstrate the effects on the composite tow lifetime distribution not only from changes in φ and σ_y, but also from changes in the load-sharing arrangement of the fibers in the tow (planar vs. hexagonal in two versions).

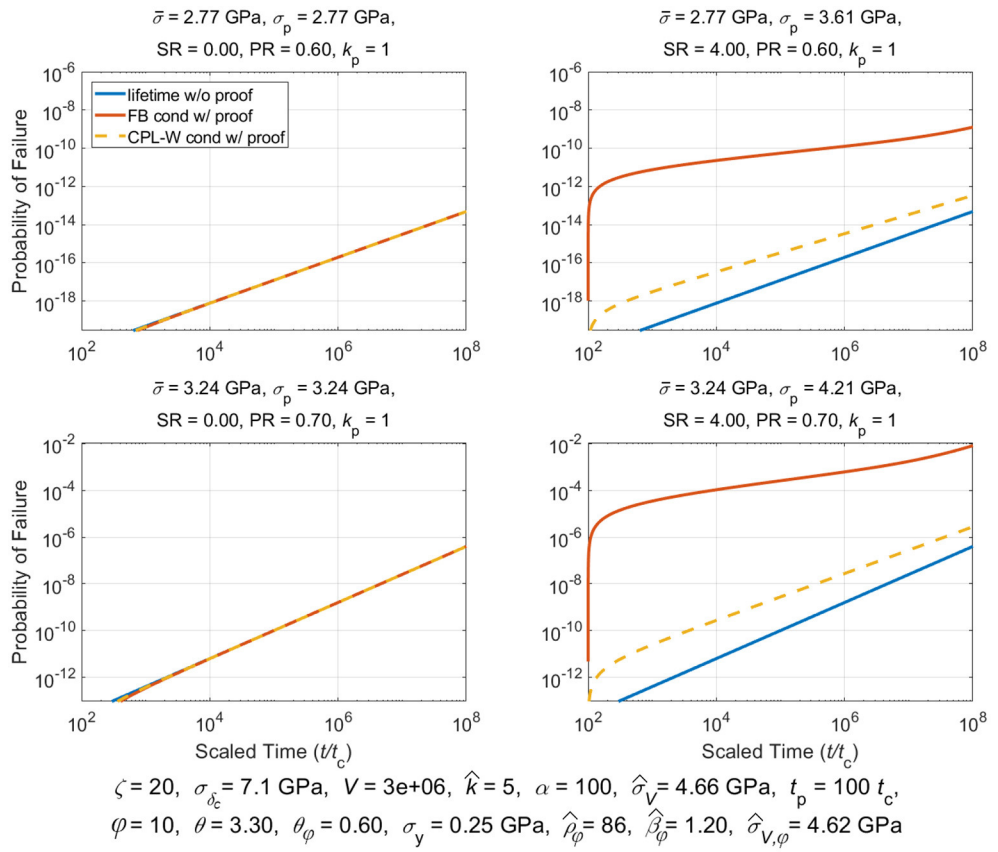

FIGURE 8 | COPV where tows are modeled as being arranged in a hexagonal array under (56) for the number of overloaded tows around a cluster, and where $\varphi = 10$ and $\sigma_y = 0.25$ GPa.

The latter changes are seen in comparing the two groups of figures, namely **Figure 1** through **Figure 3** with **Figure 4** through **Figure 6**.

In **Figure 1** through **Figure 3**, a major effect of the decrease seen in $\hat{k}$ from $\hat{k} = 10$ in **Figure 1** down to $\hat{k} = 6$ in **Figure 3**, is to decrease the Weibull lifetime shape parameter, from $\hat{\beta}_\varphi = 0.54$ to $\hat{\beta}_\varphi = 0.30$. Likewise the lifetime stress scale, $\hat{\sigma}_{V,\varphi}$, decreases from $\hat{\sigma}_{V,\varphi} = \hat{\sigma}_V = 7.80$ GPa down to $\hat{\sigma}_{V,\varphi} = 3.70$ GPa, a reduction by more than a factor of two. On the other hand the effect on $\hat{\rho}_\varphi$ is modest and its value increases from $\hat{\rho}_\varphi = 93$ in **Figure 1** to $\hat{\rho}_\varphi = 114$ in **Figure 3**. This is caused largely by the dependence of $\hat{\rho}_\varphi$ on $\hat{k}$ in (43). Otherwise, the plots in **Figure 1** through **Figure 3** show very similar behavior, with much of the difference in plotted probability values caused by the decrease in $\hat{\beta}_\varphi$ (and resulting increase in variability) thus increasing the failure probabilities since the effect of $\hat{\sigma}_{V,\varphi}$ is scaled out, and the change in $\hat{\rho}_\varphi$ is comparatively smaller.

Similarly in **Figure 4** through **Figure 6**, a major effect of the decrease in $\hat{k}$ from $\hat{k} = 19$ in **Figure 4** down to $\hat{k} = 10$ in **Figure 6**, is to decrease the Weibull shape parameter for lifetime from $\hat{\beta}_\varphi = 1.08$ in **Figure 4** to $\hat{\beta}_\varphi = 0.54$ in **Figure 6**. Note that since $\hat{\beta}_\varphi = 1.08 > 1$, which means $\tilde{\beta} = 1.08 > 1$ in the CPL-W model, a proof test in that model results in a slight increase in the probability of failure over time compared to having no proof test. Likewise the decrease in $\hat{k}$ also results in a large decrease in the Weibull lifetime stress scale, $\hat{\sigma}_{V,\varphi}$, decreases from $\hat{\sigma}_{V,\varphi} = \hat{\sigma}_V = 11.18$ GPa down to the more realistic value, $\hat{\sigma}_{V,\varphi} = 5.28$ GPa, again by almost a factor of two. Both parameters exhibit reductions by a factor of two. On the other hand, the effect on $\hat{\rho}_\varphi$ is a more modest increase from $\hat{\rho}_\varphi = 88$ in **Figure 4** to $\hat{\rho}_\varphi = 106$ in **Figure 6**, as a result of the dependence of $\hat{\rho}_\varphi$ on $\hat{k}$ in (43).

Otherwise, the plots in **Figure 1** through **Figure 6** show very similar behavior where much of the difference in plotted probability values is caused by the decrease in $\hat{\beta}_\varphi$ since the large effect of $\hat{\sigma}_{V,\varphi}$ is scaled out, and the change in $\hat{\rho}_\varphi$ is modest by comparison. Generally, the effects seen in **Figure 1** through **Figure 6** follow patterns previously discussed in [78].

Effects of φ and σ_y on COPV Strength Based on Tow Elements Having Weibull Strength

Figures 7, **8** show results for COPV strength and lifetime assuming tow elements have Weibull strength with shape parameter $\zeta = 20$ (a more conservative value than the theoretical values in **Figures 3**, **6**) and scale parameter that in both cases turns out to be $\sigma_{\delta_c} = 7.1$ GPa. Both figures assume $\varphi = 10$ and $\sigma_y = 0.25$ GPa for the interface between tows, and thus, the value of σ_{δ_c} is lower than $\sigma_{\hat{\delta}_c} = 8.0$ GPa for the case $\varphi = 1$ as a result of a factor of about 10 increase in tow element length δ_c as compared to $\hat{\delta}_c$. This element length change also results in a factor

of 10 reduction in V. Note that the results in **Figure 7** assume planar load-sharing among tows, whereas **Figure 8** assumes tows arranged and sharing load in a hexagonal configuration with (56) governing the number of overloaded tow elements surrounding a cluster of tow breaks.

The change in tow load-sharing mechanism leads to an increase in the critical cluster size, $\hat{k}$, from $\hat{k} = 3$ in **Figure 7**, to $\hat{k} = 5$ in **Figure 8**. This in turn causes a proportional increase in the Weibull shape parameter for strength, $\hat{\alpha} = \hat{k}\zeta$ in (19) from $\hat{\alpha} = 60$ in **Figure 7** to $\hat{\alpha} = 100$ in **Figure 8**, thus reflecting a substantial decrease in the variability in COPV strength. There is also a significant increase in the Weibull strength scale parameter, $\hat{\sigma}_V$, from $\hat{\sigma}_V = 4.25\,\text{GPa}$ in **Figure 7** to $\hat{\sigma}_V = 4.66\,\text{GPa}$ in **Figure 8**. This increase in $\hat{\sigma}_V$ of about 10% for a COPV is much less than in the case of tows, largely because the starting value of ζ is a larger value, 20, rather than 5, and the effect on the value of $\hat{k}$ is also much smaller. Nevertheless, changing the value of φ from $\varphi = 1$ to $\varphi = 10$ together with the choice of $\sigma_\gamma = 0.10\,\text{GPa} \ll \hat{\sigma}_V$ does have the effect of decreasing the COPV strength and increasing its variability (results for $\varphi = 1$ not shown).

Effects of φ and σ_γ on the Lifetime Distribution of COPVs in Stress-Rupture

Figures 7, **8** also demonstrate the effects on the composite lifetime distribution of changes in the tow load-sharing arrangement from a planar array to a hexagonal array. A major effect is again to increase $\hat{k}$ from $\hat{k} = 3$ in **Figure 7** to $\hat{k} = 5$ in **Figure 8**, which leads to an increase the Weibull shape parameter for lifetime, from $\hat{\beta}_\varphi = 0.60$ to $\hat{\beta}_\varphi = 1.20$. Likewise the Weibull lifetime stress scale, $\hat{\sigma}_{V,\varphi}$, increases from $\hat{\sigma}_{V,\varphi} = 4.20\,\text{GPa}$ to $\hat{\sigma}_{V,\varphi} = 4.62\,\text{GPa}$. On the other hand there is a decrease in $\hat{\rho}_\varphi$, from $\hat{\rho}_\varphi = 103$ to $\hat{\rho}_\varphi = 86$, which in part also contributed to the large increase in $\hat{\beta}_\varphi$. Otherwise, the plots show very similar behavior, with much of the difference in plotted probability values caused by the increase in $\hat{\beta}_\varphi$ since the effect of $\hat{\sigma}_{V,\varphi}$ is scaled out, and there a relatively smaller change in $\hat{\rho}_\varphi$. Again since $\hat{\beta}_\varphi = 1.20 > 1$, and thus $\tilde{\beta} = 1.20 > 1$ in the CPLW model, a proof test in that model results in a substantial increase in the probability of failure over time compared to having no proof test. Once again, however, the increase is modest compared to the large increase seen in the SFB model of the current work.

CONCLUSIONS

In this work we have generalized the SFB model derived in [78], by extending the linearly viscoelastic matrix creep behavior into the non-linear range. The linear viscoelastic version can be obtained from the current model by setting $\varphi = 1$. Since the general form of the SFB model does not change by adding non-linear viscoelasticity, the conclusions regarding the detrimental effects of proof testing still hold as were demonstrated in **Figure 1** through **Figure 8**.

A key advantage of the current non-linear creep model over the linear viscoelastic model with instantaneous shear modulus, G_e, is that all the above factors can be accounted for directly in the model when calculating the distribution for lifetime. This eliminates the need, in the linear model, to artificially account for fiber-matrix debonding or matrix shear failure and its effect on increasing the value δ_c when trying to make strength predictions using (17) or lifetime predictions using (41) together with (48) through (51). This is the critically important aspect of the new work.

Finally, the development of a stress-rupture model is certainly an important aspect of the overall technological challenge of designing and manufacturing highly reliable and human-safe composite structures, such as COPVS. However, such efforts still rely on the generation of experimental data, as well as drawing on databases of previous experimental work and the modeling approaches used to design the experiments and interpret the data. A comparison of various models that have been used (which are largely phenomenological such as the CPL-W model), is given in [1]. General and parametric features of experimental data for unidirectional composites that consist of a wide variety of fibers in a polymer matrix, as well as commonly used statistical methods (such as maximum likelihood) are discussed in [2]. Also, in [2] uncertainty distributions on model parameters are obtained using Monte Carlo simulation. In [3] a unified maximum-likelihood method is developed for the CPL-W model with the goal of reducing uncertainty in parameter and reliability estimation. Finally, in [4] further maximum likelihood analysis is devoted to removing bias and characterizing uncertainty in both model parameters and reliability estimates. Monte Carlo simulation is used to study uncertainty in the parameter and reliability estimates and to assess bias. In both [3] and [4] the method is demonstrated using strength and lifetime data generated on small carbon/epoxy COPVs tested at the NASA White Sands Test Facility over a two and a half year period.

DATA AVAILABILITY STATEMENT

The original contributions presented in the study are included in the article/**Supplementary Material**, further inquiries can be directed to the corresponding author/s.

AUTHOR CONTRIBUTIONS

All authors listed have made a substantial, direct and intellectual contribution to the work, and approved it for publication.

FUNDING

Funding for this work was provided under National Institute of Standards and Technology (NIST) agreement ID 70NANB14H323 for Stuart Leigh Phoenix and National Institute of Standards and Technology (NIST) agreement ID 70NANB18H222 for AE-W.

SUPPLEMENTARY MATERIAL

The Supplementary Material for this article can be found online at: https://www.frontiersin.org/articles/10.3389/fphy.2021.644815/full#supplementary-material

REFERENCES

1. Engelbrecht-Wiggans AE, Phoenix SL. Comparison of probabilistic models for stress rupture failure in continuous unidirectional fiber composite structures. *J Mater Sci.* (2018) 53:7431–52. doi: 10.1007/s10853-018-2101-2
2. Engelbrecht-Wiggans AE, Phoenix SL. Comparison of maximum likelihood approaches for analysis of composite stress rupture data. *J Mater Sci.* (2016) 51:6639–61. doi: 10.1007/s10853-016-9950-3
3. Engelbrecht-Wiggans AE, Phoenix SL. Analysis of stress rupture data on fiber composites: Part 1- A unified maximum likelihood method. *J Sp Saf Eng.* (2017) 4:9–14. doi: 10.1016/j.jsse.2017.03.002
4. Engelbrecht-Wiggans AE, Phoenix SL. Analysis of stress rupture data on fiber composites. Part 2. Determining uncertainty and removing bias in estimates. *J Sp Saf Eng.* (2017) 4:83–94. doi: 10.1016/j.jsse.2017.06.003
5. Pradhan S, Hansen A, Chakrabarti BK. Failure processes in elastic fiber bundles. *Rev Mod Phys.* (2010) 82:499–555. doi: 10.1103/RevModPhys.82.499
6. Alava MJ, Nukala PKVV, Zapperi S. Statistical models of fracture. *Adv Phys.* (2006) 55:349–476. doi: 10.1080/00018730300741518
7. Kun F, Zapperi S, Herrmann HJ. Damage in fiber bundle models. *Eur Phys J B.* (2000) 17:269–79. doi: 10.1007/PL00011084
8. Roy S, Biswas S, Ray P. Modes of failure in disordered solids. *Phys Rev E.* (2017) 96:063003. doi: 10.1103/PhysRevE.96.063003
9. Phoenix SL, Beyerlein IJ. Statistical strength theory for fibrous composite materials. *Compreh Comp Mater.* (2000) 1:559–639. doi: 10.1016/B0-08-042993-9/00056-5
10. Mahesh S, Phoenix SL, Beyerelin IJ. Strength distributions and size effects for 2D and 3D composites with Weibull fibers in an elastic matrix. *Int J Fract.* (2002) 115:41–85. doi: 10.1023/A:1015729607223
11. Alava MJ, Nukala PKVV, Zapperi S. Size effects in statistical fracture. *J Phys D Appl Phys.* (2009) 42:214012. doi: 10.1088/0022-3727/42/21/214012
12. Bazant ZP, Le J-L, Bazant M. Scaling of strength and lifetime probability distributions of quasibrittle structures based on atomistic fracture mechanics. *PNAS.* (2009) 106:11484–9. doi: 10.1073/pnas.0904797106
13. Phoenix SL, Ibnabdeljalil M, Hui C-Y. Size effects in the distribution for strength of brittle matrix fibrous composites. *Int J Solids Struct.* (1997) 34:545–68. doi: 10.1016/S0020-7683(96)00034-0
14. Roux S. Thermally activated breakdown in the fiber-bundle model. *Phys Rev E.* (2000) 62:6164–9. doi: 10.1103/PhysRevE.62.6164
15. Yewande OE, Moreno Y, Kun F, Hidalgo RC, Herrmann HJ. Time evolution of damage under variable ranges of load transfer. *Phys Rev E.* (2003) 68:026116. doi: 10.1103/PhysRevE.68.026116
16. Roy S, Biswas S, Ray P. Failure time in heterogeneous systems. *Phys Rev Res.* (2019) 1:033047. doi: 10.1103/PhysRevResearch.1.033047
17. Clemente MA, Gómez JB, Pacheco AF. Time to failure of dynamic local load-sharing fiber bundle models in 1 to 3 dimensions. *Physica D.* (2019) 390:1–8. doi: 10.1016/j.physd.2018.10.003
18. Coleman BD. Time dependence of mechanical breakdown phenomena. *J Appl Phys.* (1956) 27:862–66. doi: 10.1063/1.1722504
19. Coleman BD. A stochastic process model for mechanical breakdown. *Trans Soc Rheol.* (1957) 1:153–68. doi: 10.1122/1.548812
20. Coleman BD. Time dependence of mechanical breakdown in bundles of fibers. I. Constant total load. *J Appl Phys.* (1957) 28:1058–64. doi: 10.1063/1.1722907
21. Coleman BD. Time dependence of mechanical breakdown in bundles of fibers. III. The power- law breakdown rule. *Trans Soc Rheol.* (1958) 2:195–218. doi: 10.1122/1.548830
22. Tobolsky A, Eyring H. Mechanical properties of polymeric materials. *J Chem Phys.* (1943) 11:125–34. doi: 10.1063/1.1723812
23. Phoenix SL. The asymptotic distribution for the time to failure of a fibre bundle. *Adv Appl Probab.* (1979) 11:153–87. doi: 10.1017/S0001867800031748
24. Newman WI, Phoenix SL. Time-dependent fiber bundles with local load sharing. *Phys Rev E.* (2001) 63:021507. doi: 10.1103/PhysRevE.63.021507
25. Phoenix SL, Newman WI. Time-dependent fiber bundles with local load sharing. II. General Weibull fibers. *Phys Rev E.* (2009) 80:066115. doi: 10.1103/PhysRevE.80.066115
26. Mattsson A, Uesaka T. Time-dependent statistical failure of fiber networks. *Phys Rev E.* (2015) 92:042158. doi: 10.1103/PhysRevE.92.042158
27. Mattsson A, Uesaka T. Time-dependent breakdown of fiber networks: uncertainty of lifetime. *Phys Rev E.* (2017) 95:053005. doi: 10.1103/PhysRevE.95.053005
28. Halasz Z, Danku Z, Kun F. Competition of strength and stress disorder in creep rupture. *Phys Rev E.* (2012) 85:016116. doi: 10.1103/PhysRevE.85.016116
29. Ibnabdeljalil M, Phoenix SL. Creep rupture of brittle matrix composites reinforced with time dependent fibers: Scalings and Monte Carlo simulations. *J Mech Phys Solids.* (1995) 43:897–931. doi: 10.1016/0022-5096(95)00008-7
30. Kelly A, McCartney LN. Failure by stress corrosion of bundles of fibres. *Proc R Soc London A Math Phys Sci.* (1981) 374:475–89. doi: 10.1098/rspa.1981.0032
31. Iyengar N, Curtin WA. Time dependent failure in fiber-reinforced composites by fiber degradation. *Acta Mater.* (1997) 45:1489–502. doi: 10.1016/S1359-6454(96)00260-1
32. Goda K. Creep-rupture lifetime simulation of unidirectional metal matrix composites with andwithout time-dependent fiber breakage. *Int J Plasticity.* (2002) 18:1729–48. doi: 10.1016/S0749-6419(01)00038-9
33. Yoshioka N, Kun F, Ito N. Kinetic Monte Carlo algorithm for thermally induced breakdown of fiber bundles. *Phys Rev E.* (2015) 91:033305. doi: 10.1103/PhysRevE.91.033305
34. Linga, G, Ballone P, Hansen A. Creep rupture of fiber bundles: A molecular dynamics investigation. *Phys Rev E.* (2015) 92:022405. doi: 10.1103/PhysRevE.92.022405
35. Kun F, Hidalgo RC, Herrmann HJ, Pal KF. Scaling laws of creep rupture of fiber bundles. *Phys Rev E.* (2003) 67:061802. doi: 10.1103/PhysRevE.67.061802
36. Kovacs K, Nagy S, Hidalgo RC, Kun F, Herrmann HJ, Pagonabarraga I. Critcal rupture in a bundle of slowly relaxing fibers. *Phys Rev E.* (2008) 77:036102 doi: 10.1103/PhysRevE.77.036102
37. Hidalgo RC, Kun F, Herrmann HJ. Slow relaxation of fiber composites, variable range of interaction approach. *Physica A.* (2005) 347:402–410. doi: 10.1016/j.physa.2004.08.039
38. Lifshitz JM, Rotem A. Time-dependent longitudinal strength of unidirectional fiber composites. *Fibre Sci Technol.* (1970) 3:1–19. doi: 10.1016/0015-0568(70)90023-0
39. Iyengar N, Curtin WA. Time dependent failure in fiber-reinforced composites by matrix and interface shear creep. *Acta Mater.* (1997) 45:3419–29. doi: 10.1016/S1359-6454(96)00412-0
40. Ohno N, Miyake T. Stress relaxation in broken fibers in unidirectional composites: modeling and application to creep rupture analysis. *Int J Plasticity.* (1999) 15:167–89. doi: 10.1016/S0749-6419(98)00063-1
41. Koyanagi J, Hatta H, Ogawa F, Kawada H. Time-dependent reduction of tensile strength caused by interfacial degradation under constant strain duration in UD-CFRP. *J Compos Mater.* (2007) 41:3007–26. doi: 10.1177/0021998307082175
42. Phoenix SL, Schwartz P, Robinson HH. Statistics for the strength and lifetime in creep-rupture of model carbon/epoxy composites. *Compos Sci Technol.* (1988) 32:81–120. doi: 10.1016/0266-3538(88)90001-2
43. Otani H, Phoenix SL, Petrina P. Matrix effects on lifetime statistics for carbon fiber-epoxy microcomposites in creep-rupture. *J Mater Sci.* (1988) 26:1955–1970. doi: 10.1007/BF00543630
44. Mahesh S, Phoenix SL. Lifetime distributions for unidirectional fibrous composites under creep-rupture loading. *Int J Fract.* (2004) 127:303–60. doi: 10.1023/B:FRAC.0000037675.72446.7c
45. Nakada M, Miyano Y, Morisawa Y, Nishida H, Hayashi Y, Uzawa, et al. Prediction of statistical life time for unidirectional CFRTP under creep loading. *J Reinforced Plastics and Composites.* (2019) 38:938–46. doi: 10.1177/0731684419854213
46. Miyano Y, Nakada M. Accelerated testing methodology for durability of CFRP. *Composites Part B.* (2020) 191:107977 doi: 10.1016/j.compositesb.2020.107977
47. Blassiau S, Thionnet A, Bunsell AR. Micromechanisms of load transfer in a unidirectional carbon fibre–reinforced epoxy composite due to fibre failures. *Part.* 1: Micromechanisms and 3D analysis of load transfer: The elastic case. Compos Struct. (2006) 74:303–18. doi: 10.1016/j.compstruct.2005.04.013
48. Blassiau S, Thionnet A, Bunsell AR. Micromechanisms of load transfer in a unidirectional carbon fibre–reinforced epoxy composite due to fibre failures. Part. 2: Influence of viscoelastic and plastic matrices on the mechanisms of load transfer. *Compos Struct.* (2006) 74:319–31. doi: 10.1016/j.compstruct.2005.04.029

49. Blassiau S, Thionnet A, Bunsell AR. Micromechanisms of load transfer in a unidirectional carbon fibre-reinforced epoxy composite due to fibre failures: Part 3. Multiscale reconstruction of composite behaviour. *Compos Struct.* (2008) 82:312–23 doi: 10.1016/j.compstruct.2007.05.004
50. Bunsell AR, Thionnet A. Life prediction for carbon fibre filament wound composite structures. *Philosophical Magazine.* (2010) 90:4129–46. doi: 10.1080/14786430903575140
51. Thionnet A, Chou H-Y, Bunsell A. Fibre break failure processes in unidirectional composites. *Part.* 1: Failure and critical damage state induced by increasing tensile loading. *Appl Compos Mater.* (2015). 22:119–40. doi: 10.1007/s10443-014-9397-0
52. Thionnet A, Chou H-Y, Bunsell A. Fibre break failure processes in unidirectional composites. Part. 2: Failure and critical damage state induced by sustained tensile loading. *Appl Compos Mater.* (2015). 22:141–55. doi: 10.1007/s10443-014-9398-z
53. Thionnet A, Chou H-Y, Bunsell A. Fibre break failure processes in unidirectional composites. Part. 3: Unidirectional plies included in laminates. *Appl Compos Mater.* (2015). 22:157–69. doi: 10.1007/s10443-014-9399-y
54. Thionnet A, Bunsell AR. Fibre break failure processes in unidirectional composites: evaluation of critical damage states. *Phil Trans R Soc A.* (2015) 374:20150270. doi: 10.1098/rsta.2015.0270
55. Thionnet A, Bunsell A, Chou H-Y. Intrinsic mechanisms limiting the use of carbon fiber composite pressure vessels. *ASME J Press Vessel Technol.* (2016) 138:060910. doi: 10.1115/1.4032914
56. Farquhar DS, Mutrelle FM, Phoenix SL, Smith RL. Lifetime statistics for single graphite fibers in creep rupture. *J Mater Sci.* (1989) 24:2131–64. doi: 10.1007/BF02385436
57. Miyake T, Yamakawa N, Ohno N. Measurement of stress relaxation in broken fibers embedded in epoxy using Raman spectroscopy. *J Mater Sci.* (1998) 33:5177–83. doi: 10.1023/A:1004427819540
58. Holmes GA, Peterson RC, Hunston DL, McDonough WG, Schutte CL. The effect of non-linear viscoelasticity on interfacial shear strength measurements. In: Schapery RA, Sun CT, editors. *Time Dependent and Non-linear Effects in Polymers and Composites, ASTM STP1357.* West Conshohocken, PA: American Society for Testing and Materials. p. 98–117. doi: 10.1520/STP15831S
59. Beyerlein IJ, Zhou CH, Schadler LS. A time dependent micro-mechanical fiber composite model for inelastic zone growth in viscoelastic matrices. *Int J Sol Struct.* (2000) 40:2171–94. doi: 10.1016/S0020-7683(03)00021-0
60. Zhou CH, Schadler LS, Beyerlein IJ. Time-dependent micromechanical behavior in graphite/epoxy composites under constant load: a combined experimental and theoretical study. *Acta Mater.* (2002) 50:365–77. doi: 10.1016/S1359-6454(01)00353-6
61. Zhou CH, Beyerlein IJ, Schadler LS. Time-dependent micromechanical behavior in graphite/epoxy composites under constant load at elevated temperatures. *J Mater Sci.* (2003) 38:877–84. doi: 10.1023/A:1022348419344
62. Zhou CH, Schadler LS, Beyerlein IJ. Stress concentrations in graphite/epoxy model composites during creep at room temperature and elevated temperatures. *J Compos Mater.* (2004) 38:417–33. doi: 10.1177/0021998304040551
63. Lagoudas DC, Hui C-Y, Phoenix SL. Time evolution of overstress profiles near broken fibers in a composite with a viscoelastic matrix. *Int J Solids Struct.* (1989) 25:45–66. doi: 10.1016/0020-7683(89)90103-0
64. Beyerlein IJ, Phoenix SL, Raj R. Time evolution of stress redistribution around multiple fiber breaks in a composite with viscous and viscoelastic matrices. *Int J Solids Struct.* (1998) 35:3177–211. doi: 10.1016/S0020-7683(98)00010-9
65. Beyerlein IJ. Stress fields around cracks with a viscous matrix and discontinuous fiber bridging, *Compos Sci. Technol.* (2000) 60:2309–26. doi: 10.1016/S0266-3538(00)00027-0
66. Mason DD, Hui C-Y, Phoenix SL. Stress profiles around a fiber break in a composite with a non-linear, power law creeping matrix. *Int J Solids Struct.* (1992) 29:2829–54. doi: 10.1016/0020-7683(92)90143-H
67. Ohno N, Ando T, Miyake T, Biwa S. A variational method for unidirectional fiber-reinforced composites with matrix creep. *Int J Solids Struct.* (2002) 39:150–74. doi: 10.1016/S0020-7683(01)00147-0
68. Hedgepeth JM. Stress concentrations in filamentary structures. Washington, DC: NASA. (1961).
69. Hedgepeth JM, Van Dyke P, Dyke P Van. Local stress concentrations in imperfect filamentary composite materials. *J Compos Mater.* (1967) 1:294–309. doi: 10.1177/002199836700100305
70. Fichter WB. *Stress Concentration Around Broken Filaments in a Filament-Stiffened Sheet.* Washington, DC: NASA TN D-5453. (1969).
71. McCarthy ED, Kim JH, Heckert NA, Leigh SD, Gilman JW, Holmes GA. The fiber break evolution process in a 2-D epoxy/glass multi-fiber array. *Compos Sci Technol.* (2015) 121:73–81. doi: 10.1016/j.compscitech.2014.10.013
72. Smith RL, Phoenix SL, Greenfield MR, Henstenburg RB, Pitt RE. Lower-tail approximations for the probability of failure of 3-D fibrous composites with hexagonal geometry. *P Roy Soc Lond A.* (1983) 388:353–91. doi: 10.1098/rspa.1983.0087
73. Curtin WA. Size scaling of strength in heterogeneous materials *Phys Rev Lett.* (1998) 80:1445–8. doi: 10.1103/PhysRevLett.80.1445
74. Gupta A, Mahesh S, Keralavarma SM. Strength distribution of large unidirectional composite patches with realistic load sharing. *Phys Rev E.* (2017) 96:043002. doi: 10.1103/PhysRevE.96.043002
75. Habeeb CNI, Mahesh S. Strength distribution of planar local load-sharing bundles. *Phys Rev E.* (2015) 92:022125. doi: 10.1103/PhysRevE.92.022125
76. Mahesh S, Gupta A, Kachhwah US, Sheikh N. A fast algorithm to simulate the failure of a periodic elastic fibre composite. *Int J Fract.* (2019) 217:127–35. doi: 10.1007/s10704-019-00374-w
77. Yentl Swolfs S, Ignaas Verpoest I, Larissa Gorbatikh L. Issues in strength models for unidirectional fibre-reinforced composites related to Weibull distributions, fibre packings and boundary effects. *Compos Sci Technol.* (2015) 114:4249. doi: 10.1016/j.compscitech.2015.04.002
78. Engelbrecht-Wiggans AE, Phoenix SL. A stochastic model based on fiber breakage and matrix creep for the stress-rupture failure of unidirectional continuous fiber composites. *Int J Fract.* (2019) 217:1–34. doi: 10.1007/s10704-019-00359-9
79. Christensen RM. Interactive mechanical and chemical degradation in organic materials. *Int J Solids Struct.* (1984) 20:791–804. doi: 10.1016/0020-7683(84)90066-0

Conflict of Interest: The authors declare that the research was conducted in the absence of any commercial or financial relationships that could be construed as a potential conflict of interest.

frontiers in Physics

ORIGINAL RESEARCH
published: 13 April 2021
doi: 10.3389/fphy.2021.643602

Size Distribution of Emitted Energies in Local Load Sharing Fiber Bundles

Subhadeep Roy[1]* *and Soumyajyoti Biswas*[2]

[1] PoreLab, Department of Physics, Norwegian University of Science and Technology, Trondheim, Norway, [2] Department of Physics, SRM University - AP, Andhra Pradesh, India

We study the local load sharing fiber bundle model and its energy burst statistics. While it is known that the avalanche size distribution of the model is exponential, we numerically show here that the avalanche size (s) and the corresponding average energy burst ($\langle E \rangle$) in this version of the model have a non-linear relation ($\langle E \rangle \sim s^{\gamma}$). Numerical results indicate that $\gamma \approx 2.5$ universally for different failure threshold distributions. With this numerical observation, it is then possible to show that the energy burst distribution is a power law, with a universal exponent value of $-(\gamma + 1)$.

Keywords: fiber bundle model, local load sharing, energy emission, threshold activated dynamics, avalanches

1. INTRODUCTION

It is well-known experimentally that quasistatically stressed disordered solids produce intermittent response statistics [1], particularly in terms of acoustic emissions, that show scale-free size distributions. These intriguing dynamics is seen universally across scales from microscopic laboratory samples to the geological scale of earthquakes [2–6]. Empirically, the scale-free size distribution of breaking progression is known in different communities for decades. For example, in geoscience, this is known as the Gutenberg-Richter law, in magnetic domain walls as crackling noise, and so on.

The interests of statistical physicists in this context stems from the universal nature of the dynamics across length and energy scales. The scale-free variations of acoustic emissions, waiting time statistics, etc., are independent of the microscopic details of the underlying systems, which are very different from each other. Such behavior indicates critical dynamics, particularly self-organized critical dynamics for the system, where the universality hypothesis is still applicable, without having to fine-tune a driving parameter [7]. Such a phenomenon is therefore open for analysis with the tools of critical phase transitions, universality and therefore is an important step toward predictability of imminent failure [8–10].

As a consequence of the scale-free dynamics and potential applicability of the universality hypothesis, many generic models were proposed over the years that reproduce such a scale-free behavior. Such models include the fiber bundle model, random spring network, random fuse model, the Burridge-Knopoff model, and so on [5, 11–13]. The common underlying feature of these models is that they are threshold activated, driven, dynamical models. Particularly, for an external driving parameter crossing a pre-assigned threshold value for a single unit of these models, that unit is activated and influences the units in its "neighborhood," which may in-turn get activated and thereby initiating an "avalanche." As can be guessed, this type of dynamics is often related to sandpile models of self-organized criticality [14] and indeed such associations extensively explored in the past [15].

The two major parameters that influence the nature of the response in such models are the range of interaction [16] and the strength of the disorder [17, 18]. It was explored, particularly in the fiber

OPEN ACCESS

Edited by:
Ferenc Kun,
University of Debrecen, Hungary

Reviewed by:
Mikko Alava,
Aalto University, Finland
Sumanta Kundu,
Osaka University, Japan

***Correspondence:**
Subhadeep Roy
subhadeeproy03@gmail.com

Specialty section:
This article was submitted to Interdisciplinary Physics, a section of the journal Frontiers in Physics

Received: *18 December 2020*
Accepted: *08 March 2021*
Published: *13 April 2021*

Citation:
Roy S and Biswas S (2021) Size Distribution of Emitted Energies in Local Load Sharing Fiber Bundles. Front. Phys. 9:643602. doi: 10.3389/fphy.2021.643602

bundle model that for a moderate disorder, a scale-free avalanche statistics is only recovered for a "sufficiently" long-range of interaction [16, 19, 20]. In the random fuse model, where the interaction range is not parameters to be tuned, it was shown that the avalanche statistics is not a power-law in the large system size limit [21, 22]. This is in apparent contradiction with the fact that in reality, the interaction range in disordered elastic samples is not infinite i.e., not a mean-field-like interaction. However, experiments routinely reveal scale-free statistics.

One important distinction between the analytical and numerical results of avalanche dynamics and that of the experiments is that in the former it is the number of elements failing in an avalanche that is the measurable quantity, while in the latter it is the energy released in the avalanche. Now, in the mean-field limit of the fiber bundle model, it is straightforward to show that the avalanche size and the energy avalanche size are proportional, hence the two distributions are identical in shape. But this relation is no longer valid for local load sharing variants. In those cases, therefore, it is crucial to explore the size distributions of the energy emissions and compare that with experiments. In this work, we consider the simplest possible variant of the local load sharing fiber bundle model and analyze the energy avalanche statistics of that model. We then compare the results with experiments and also present a plausible argument for its form.

2. DESCRIPTION OF FIBER BUNDLE MODEL

After being introduced by Pierce [23], the fiber bundle model has been proven to be important yet arguably the simplest model to study failure processes in disordered solids. A conventional fiber bundle model consists of a set of linear elastic fibers or Hookean springs, attached between two parallel plates. The plates are pulled apart by a force F, creating a stress $\sigma = F/L$ on L fibers. Once the stress crosses the breaking threshold of a particular fiber, chosen from a random distribution, that fiber breaks irreversibly. The stress of broken fibers is then redistributed either globally among all surviving fibers (global load sharing or GLS scheme) or among the surviving nearest neighbors only (local load sharing or LLS scheme). For the GLS scheme [23, 24] no stress concentration occurs anywhere around the failed fibers as the stress of the failed fibers is shared among all surviving fibers. On the other hand, in LLS scheme [25–30], stress concentration is observed near a broken patch (set of neighboring broken fibers) and increases with the size of such patches. After such redistribution, the load per fiber increases initiating failure of more fibers starting an avalanche. At the end of an avalanche, either all fibers are broken (suggesting global failure) or the bundle comes to a stable state with few broken fibers where an increment of external stress is required to make the model evolve further. The last applied stress just before global failure is considered to be the nominal stress or strength σ_c of the bundle. The fraction of fibers that survive at σ_c just before global failure is defined as the critical unbroken fraction of fibers (U_c).

3. NUMERICAL RESULTS

We have studied the fiber bundle model numerically in both mean-field limit and with local load sharing scheme in one dimension, though the major part of the paper will deal with the latter only. Numerical simulations are carried out for system sizes ranging in between 10^3 and 10^7 and are averaged over 10^2–10^4 configurations. Our motive is to understand the dynamics of avalanches and corresponding energy bursts emitted during these avalanches as the model evolves with increasing externally applied stress. Unless otherwise stated, we will use a uniform distribution ranging from 0 to 1 in order to assign threshold values to individual fibers beyond which it breaks.

3.1. Relation Between *s* and *E*

Figure 1 shows a comparison between different avalanches and energy emitted during different avalanches for a bundle of size 10^5. The results are produced for a single configuration. As usual, an avalanche is defined as the number of fibers broken in-between two consecutive stress increments; k is the number of such stress increments in this case. While presenting the energy spectrum and the avalanches we have excluded the final avalanche leading to global failure.

The left panel of **Figure 1** shows the results for the GLS fiber bundle model while on the right panel, we have shown the results with the local load sharing (LLS) scheme. Note that the range of k for the LLS model is much less than the range of k with the GLS scheme. This is understandable since with the LLS scheme, the model is more unstable due to stress concentration and a large number of fibers are broken during the final avalanche. The model evolves with a lesser number of stress increments in this case prior to a global failure where the average size of the avalanches are smaller compared to that in the GLS scheme. Now, for an avalanche of size s, if n fibers with threshold values τ_1, τ_2, τ_3, $\cdots$, τ_n break, then the amount of energy emitted during this avalanche will be:

$$E(s) = \frac{1}{2}\sum_{i=1}^{n} \tau_i^2. \tag{1}$$

This follows from the assumption of linear elastic (stress $\propto$ strain) behavior of individual fibers up until their individual (brittle) failure points. With above formalism, for each stress increment k, we will obtain an avalanche $s(k)$ and a corresponding energy burst of magnitude $E[s(k)]$.

The energy spectrum follows a particular trend in the case of the GLS scheme. Since with the GLS scheme the fibers break in the increasing order of their threshold values, the energy emitted at $k+1$-th load increment will be higher than the energy emitted at k-th increment, even if the avalanche sizes happen to be the same at k and $k+1$. Due to this, the variations of s and E with increasing k looks exactly the same, only the values are scaled by a constant when we transfer from s to E. Such correlation between s and E is not present in the case of the LLS fiber bundle model. In the case of the LLS scheme, the fibers break due to the interplay between the local stress profile and the threshold values of the fibers themselves. Due to such dynamics, the fibers do not

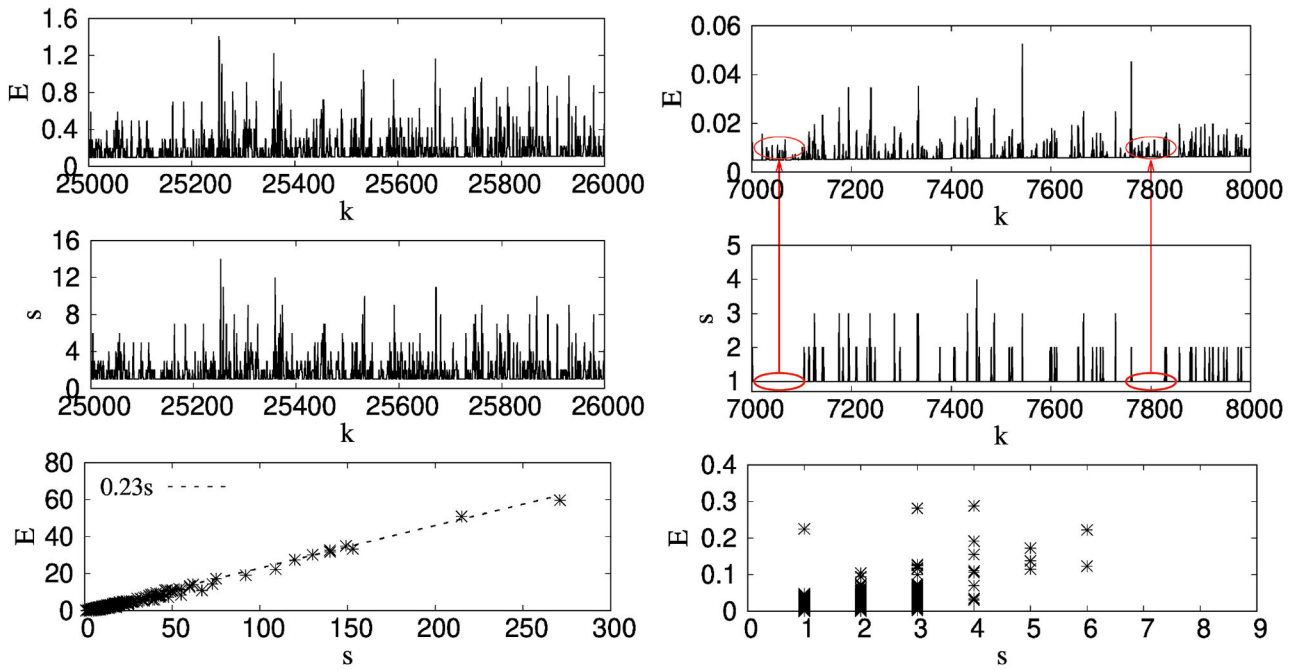

FIGURE 1 | The left panel, from top to bottom, shows the spectrum of energy values (E) with increasing number of avalanches k, avalanche sizes (s) with k and E vs. s for a certain avalanche for a GLS FBM. The right panel does the same but for a LLS FBM. We can see that, in case of a GLS FBM, there is a direct correspondence between the s and E values for a certain k. This means, higher s gives higher E. Since in case of GLS FBM, the fibers break in an increasing order of threshold values, we get, $E(k+1) > E(k)$ even if $s(k+1) = s(k)$. We do not see this direct correspondence between the s and E values with local load sharing scheme. For example, the red eclipses show the parts where only 1 fiber breaks at each k value but the corresponding E values show many different values without any particular order as the fibers themselves do not follow any order while breaking. This uncorrelated behavior between s and E.

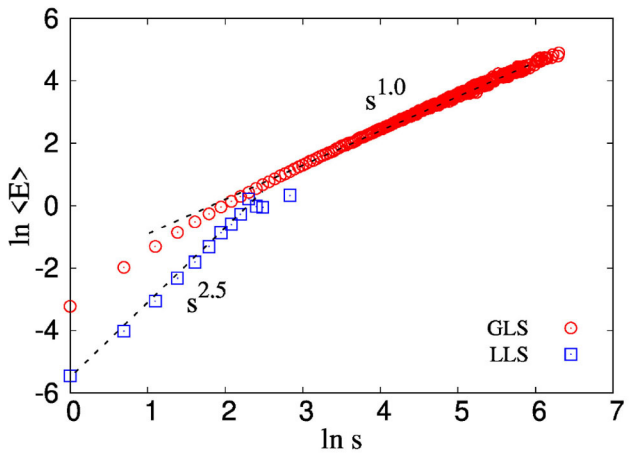

FIGURE 2 | The figure shows the variation of average energy $\langle E\rangle$ with avalanche size s for both GLS and LLS fiber bundle model. We observe $\langle E\rangle \sim s$, for GLS FBM. On the other hand, for LLS scheme, $\langle E\rangle \sim s^{\gamma}$, with $\gamma \approx 2.5$.

break in increasing order of their thresholds. Then, there might be scenarios where $E(k+1) < E(k)$ when $s(k+1) = s(k)$ or even $s(k+1) > s(k)$. The red ellipses in the right panel of **Figure 1** shows this absence of correlation between $s(k)$ and $E[s(k)]$. For both ellipses, $s = 1$ for that period. In spite of that, we see a fluctuation in energy values without a particular trend. This can be clearly understood from the lower row of **Figure 1** where E is expressed as a function s. Clearly, in case of GLS FBM, E increases in a linear manner with s while for LLS, the values of E and s are completely uncorrelated. In the following, we will discuss this relation between s and E in detail.

Figure 2 highlights how average of emitted energy $\langle E\rangle$ behaves as a function of avalanche size s for a bundle of size 10^5 and configuration 10^4. Results for both GLS and LLS schemes are shown in the figure. We observe the following behavior:

$$\langle E\rangle \sim \begin{cases} s & \text{, for GLS,} \\ s^{\gamma} & \text{, with } \gamma = 2.5 \text{ for LLS.} \end{cases} \tag{2}$$

This behavior can be used to understand the relation between distributions $P(s)$ of avalanche size s and $Q(\langle E\rangle)$ of average emitted energies $\langle E\rangle$. For this we simply need to implement a change in variable[1] scheme as follows:

$$Q(\langle E\rangle) \sim P[s(\langle E\rangle)].|s'(\langle E\rangle)| = P[s(\langle E\rangle)].|\frac{ds(\langle E\rangle)}{d\langle E\rangle}| \tag{3}$$

[1]Let's assume x and y are a continuous functions with p.d.f $f(x)$ and $g(y)$. Also, $y = u(x)$ is a function with inverse, which means it is possible to find $x = v(y)$. In this circumstances, $g(y)$ and $f(x)$ can be expressed as: $g(y) = f[v(y)].|v'(y)|$, where $|v'(y)| = |dv(y)/dy|$.

Change in variable: GLS scheme

In case of GLS scheme, we observe

$$\begin{aligned} \langle E\rangle(s) &\sim s \\ s(\langle E\rangle) &\sim \langle E\rangle \end{aligned} \tag{4}$$

This makes

$$s'(\langle E\rangle) = \frac{ds(\langle E\rangle)}{d\langle E\rangle} \sim 1 \tag{5}$$

We also know that the avalanche size distribution in case of GLS scheme is a scale free distribution with an exponent 2.5 [31].

$$P(s) \sim s^{-\beta}, \quad \text{with } \beta = 2.5 \tag{6}$$

Then, combining Equations (3), (4), (5), and (6), we get,

$$Q(\langle E\rangle) \sim P(\langle E\rangle).1 \sim \langle E\rangle^{-\beta}, \quad \text{with } \beta = 2.5 \tag{7}$$

Change in variable: LLS scheme

In case of LLS scheme, we observe

$$\begin{aligned} \langle E\rangle(s) &\sim s^{\gamma} \\ s(\langle E\rangle) &\sim \langle E\rangle^{-\gamma} \end{aligned} \tag{8}$$

This makes

$$s'(\langle E\rangle) = \frac{ds(\langle E\rangle)}{d\langle E\rangle} \sim (-\gamma)\langle E\rangle^{-(\gamma+1)} \tag{9}$$

where $\gamma = 2.5$. We also know that the avalanche size distribution in case of LLS scheme is an exponential distribution [32].

$$P(s) \sim e^{-s/s_0} \tag{10}$$

Then, combining Equations (3), (8), (9), and (10), we get,

$$Q(\langle E\rangle) \sim P(\langle E\rangle).\gamma\langle E\rangle^{-(\gamma+1)} \sim \gamma e^{-\frac{\langle E\rangle^{-\gamma}}{s_0}} E^{-(\gamma+1)} \tag{11}$$

In the limit of high E value, Equation (11) can be simplified as follows

$$Q(\langle E\rangle) \sim \langle E\rangle^{-\alpha} \quad \text{where } \alpha = \gamma + 1 = 3.5 \tag{12}$$

Above treatment shows that, in case of LLS scheme, in spite of an exponential distribution for avalanche sizes, the distribution of average emitted energy is still observed to be scale-free. Numerically we have found that this scale free behavior holds good for instantaneous values of E as well.

3.2. Distribution of s and E: Uniform Distribution

Figure 3a shows the avalanche size distribution $P(s)$ for a GLS fiber bundle model with system size ranging from 10^3 to 10^5. This scale-free decrease of $P(s)$ with s is already known in the literature. We also observe the same universal exponent 2.5 [31]. **Figure 3b** shows the corresponding distribution for the energy emitted. We observe the same scale-free distribution for the energy as well, with the same exponent 2.5. This behavior is consistent with Equations (6) and (7), respectively.

Figure 4a, on the other hand, shows the avalanche size distribution with the LLS scheme. The distribution is exponential as derived analytically by Kloster et al. [32]. The inset of the same results in log scale in order to compare them with the previous claim by Zhang and Ding [33], that $P(s)$ shows a scale-free behavior with a very high exponent closer to -4.8. This claim of scale-free nature is not substantiated and the exponential form for $P(s)$ is accepted in the literature.

The distribution of energy in **Figure 4b** shows a scale-free distribution, in spite of the fact that the avalanche size distribution is an exponential distribution. The exponent of the scale-free distribution is observed to an increasing function of the size of the bundle

$$Q(E) \sim E^{-\alpha(L)} \tag{13}$$

The above behavior is similar to Equation (12), but with a L dependent exponent instead of a constant value. To compare this L dependent exponent with the value in Equation (12), we have to study the variation of α in Equation (13) in details as the size of the bundle is increased. We have discussed this next.

Figure 5 shows the system size scaling of the behavior in Equation (13) as the size of the bundle is increased from 10^3 to 10^7. The behavior of $Q(E)$ in **Figure 4b** tells us that the slope of the distribution increases and $Q(E)$ itself decreases as we increase the size of the system. We assume this decrease in $Q(E)$ with L to be scale-free in nature and observed a nice collapse for all system sizes. The scaling we adopted is as follows:

$$Q(E) = L^{-\xi} E^{-\alpha(L)} \tag{14}$$

where $\alpha(L)$ scales to its value in the thermodynamic limit is a scale free behavior: $\alpha(L) = \alpha(\infty) - L^{-\eta}$. We will show this scaling explicitly later in this article. Taking logarithmic on both sides of Equation (14) we get,

$$\ln Q(E) = -\xi \ln L - [\alpha(\infty) - L^{-\eta}] \ln E \tag{15}$$

Figure 5a shows a good collapse with the results of **Figure 4b** using the following values of the fitting parameters: $\alpha(\infty) = 3.47$, $\eta = 0.14$, and $\xi = 0.55$. In addition, **Figure 5b** also shows the scaling of the exponent α explicitly as the model starts approaching the thermodynamic limit. We observe the following scaling,

$$\alpha(\infty) - \alpha(L) \sim L^{-\eta} \tag{16}$$

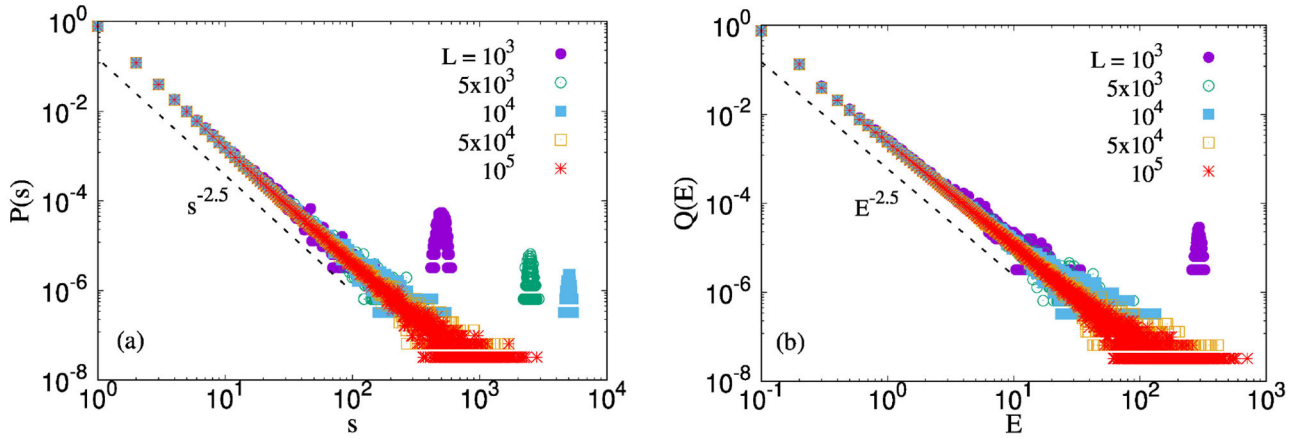

FIGURE 3 | Distribution of energies for an uniform distribution (0,1) and system sizes ranging in between 10^3 and 10^5. The results are shown for GLS FBM. **(a)** We already know that in the mean-field limit $P(s) \sim s^{-\beta}$, with $\beta \approx 2.5$. **(b)** We observe $Q(E) \sim E^{-\alpha}$ where $\alpha \approx 2.5$ as well independent of the system size.

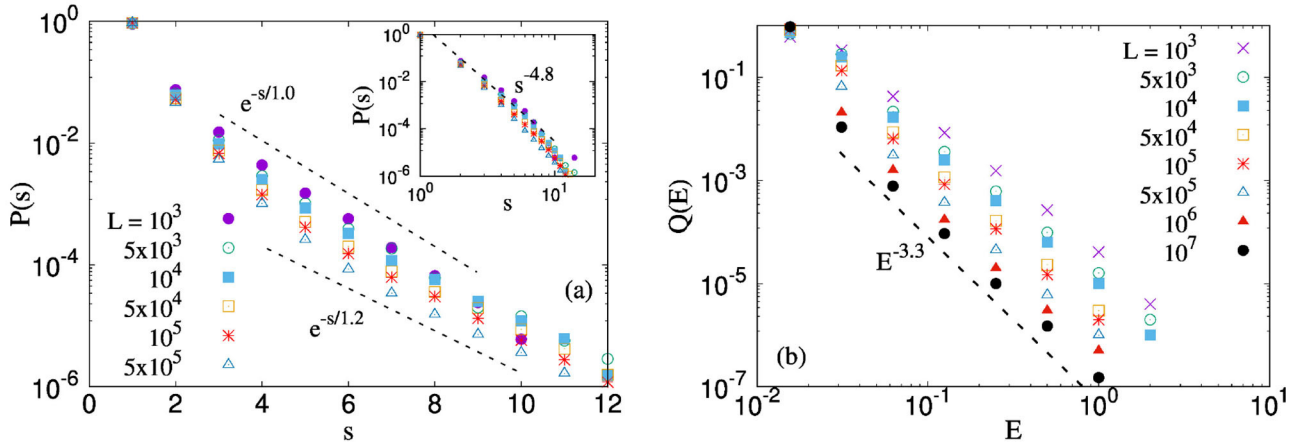

FIGURE 4 | Distribution of energies for an uniform distribution [0:1] and system sizes ranging in between 10^3 and 10^7. The results are shown for LLS FBM. **(a)** Avalanche size distribution for LLS FBM is an exponential function: $P(s) \sim e^{-s/s_0}$, where s_0 depends weakly on the system size. **(b)** Scale free distribution for energy emitted: $Q(E) \sim E^{-\alpha}$, where α is observed to increase slightly with system size.

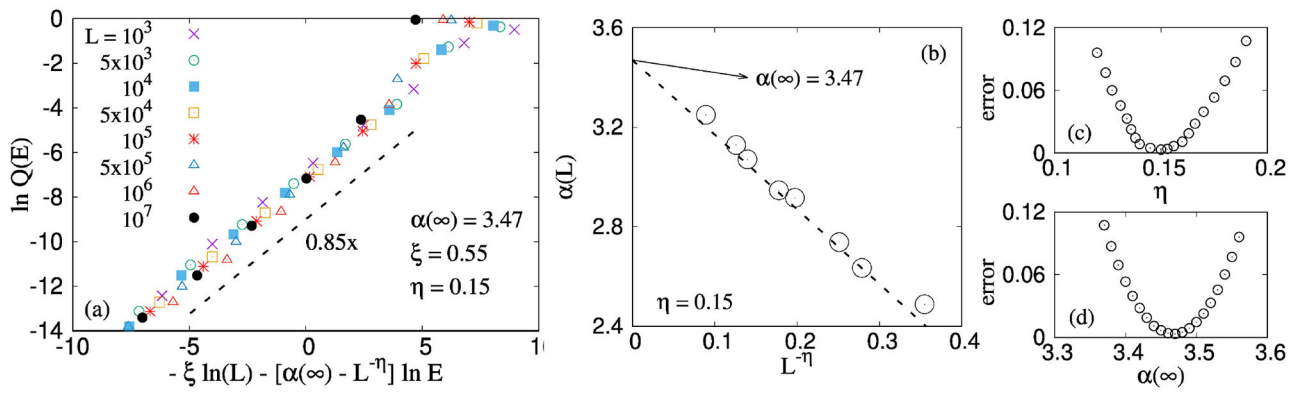

FIGURE 5 | (a) The finite size effect of $Q(E)$ is shown for uniform threshold distribution, which follows a scaling: $\ln Q(E) = -\xi \ln L - [\alpha(\infty) - L^{-\eta}] \ln E$ with $\eta = 0.15$, $\xi = 0.55$, and $\alpha(\infty) = 3.47$. **(b)** System size scaling of the exponent α as we approach the thermodynamic limit: $\alpha(\infty) - \alpha(L) \sim L^{-\eta}$, with $\eta = 0.15$ and $\alpha(\infty) = 3.47$. **(c,d)** The least square fit error as a function of exponent η and $\alpha(\infty)$, both with a minimum at a certain value. We consider the value of $\alpha(\infty)$ and η which produces the minimum error. This same procedure has been followed next while exploring the same thing for different threshold distributions.

where $\eta = -0.15$ and $\alpha(\infty)$ (= 3.47) has a value close to $\gamma + 1$ (see Equation 12). The fitting and the exponent η is calculated from the minimization of least square fit error. This is shown in **Figures 5c,d**. We choose a certain value of η and fit our numerical results. This in turn will produce a value of $\alpha(\infty)$ and corresponding least square fit error. The opposite can also be done where we can fix a certain $\alpha(\infty)$ value and the least square fit gives us the value of η and error associated with it. If we repeat this for a number of $\alpha(\infty)$ or η values, then we can express the error as a function of either of this parameters η (see **Figure 5c**) or $\alpha(\infty)$ (see **Figure 5d**). The dotted line in **Figure 5a** corresponds to the value of $\alpha(\infty)$ (= 3.47) and η (= 0.15) for which the least square fit error is minimum independent of whether the error is calculated with a constant $\alpha(\infty)$ or η.

3.3. Universality

So far, we have generated the numerical results where a uniform distribution from 0 to 1 is used to assign random thresholds to individual fibers. In this section, we will verify the universality of our results. For this purpose, we will mainly explore 4 other distributions: (i) linearly increasing from 0 to 1, (ii) linearly decreasing from 0 to 1, (ii) a Weibull

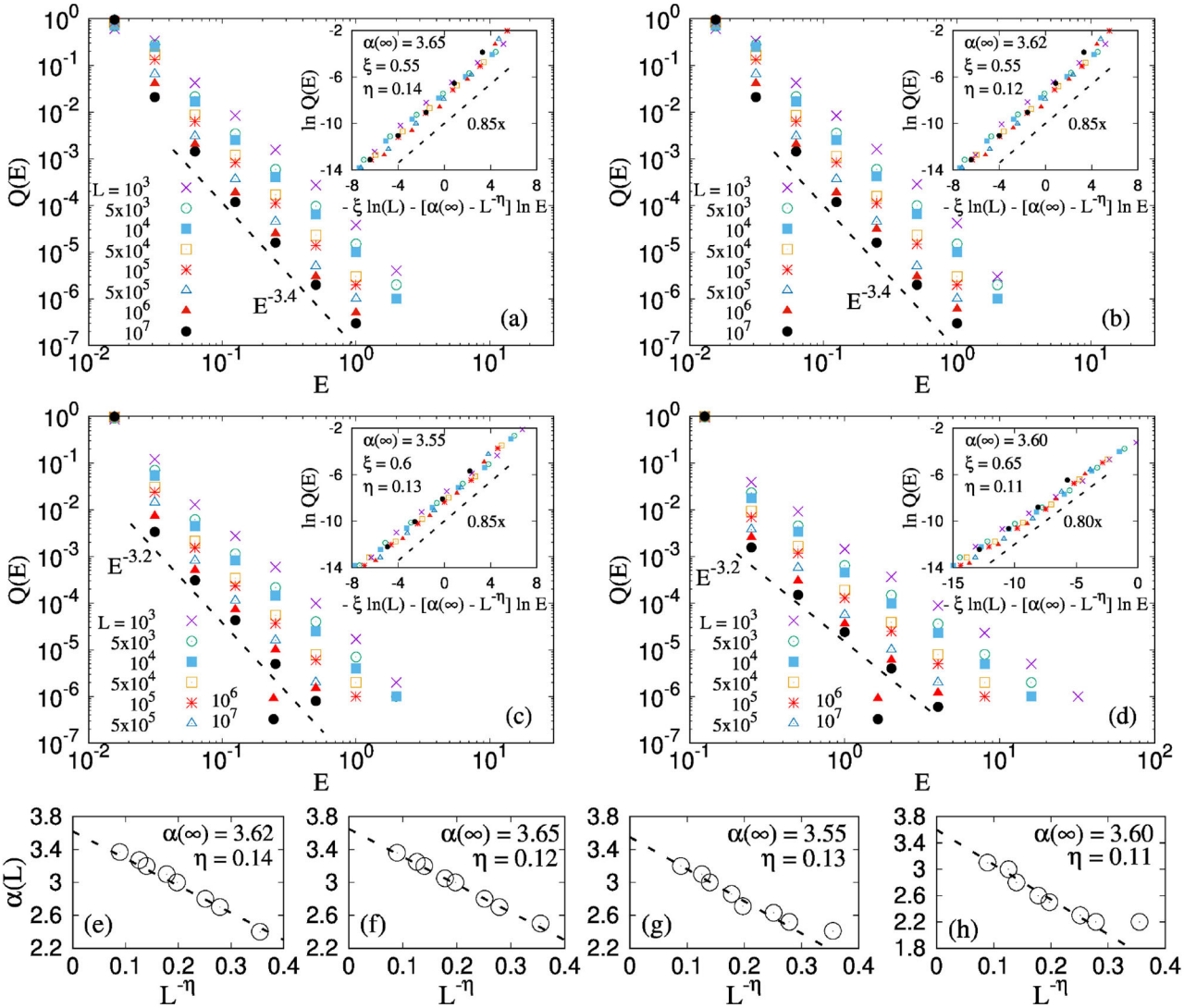

FIGURE 6 | (a) Distribution of energies for four different threshold distributions: **(a)** Linearly increasing [0:1], **(b)** Linearly decreasing [0:1], **(c)** Scale free distribution of exponent 2 between 0 and 1, **(d)** Weibull distribution with scale factor 1.0 and Weibull modulus 1.0. The system sizes varies in between 10^3 and 10^7. The results are shown for LLS FBM. We observe a scale free distribution for E: $Q(E) \sim E^{-\alpha}$ for all thresholds. The insets of figures **(a–d)** shows the system size collapse given by Equation (15). **(e–h)** Shows the exponent $\alpha(L)$ to obey the scaling showed in Equation 16. The value of η for above mentioned distributions are 0.14, 0.12, 0.13, and 0.11 respectively, similar to what is observed in the system size collapse.

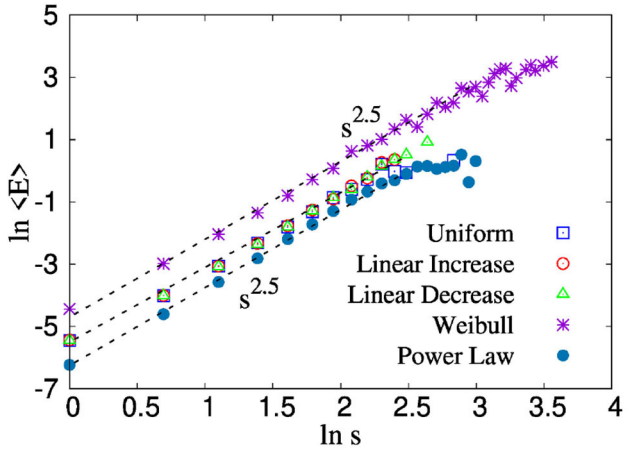

FIGURE 7 | The figure shows the variation of average energy $\langle E \rangle$ with avalanche size s for LLS fiber bundle model. We have produced the study for five different threshold distributions. We observe for all distributions, $\langle E \rangle \sim s^{\gamma}$, where γ has a value 2.5 independent of the nature of the distribution.

distribution with scale parameter 1 and Weibull modulus 1, and (iii) A power law distribution from 0 to 1 with exponent 2.0.

In all these cases, the energy burst size distributions were found to be scale-free with an exponent value close to -3.5 (see **Figures 6a–d**), as is predicted from Equation (12). The variation with system size also universal across these different threshold distributions. The insets of **Figures 6a–d** shows the same scaling given by Equation (15) and observed in **Figure 5a**. These results suggest that the scale-free nature of the energy burst size distribution in the local load sharing fiber bundle model is a universal feature.

Moreover, **Figures 6e–h** shows the system size scaling of the exponent $\alpha(L)$ (see Equation 16) for all four threshold distributions: linearly increasing, linearly decreasing, power law and Weibull, respectively.

We have further checked that the relation between an avalanche size and average energy burst size i.e., $\langle E \rangle \sim s^{2.5}$ is valid for all these threshold distributions, as can be seen from **Figure 7**. This holds good with the scale-free nature of energy burst distribution that we observed in Equations 6(a)–(d) for all four threshold distributions.

Finally, we have discussed in **Table 1**, all exponents that we observed in relation to burst size distribution for all five threshold distributions.

TABLE 1 | The table shows the exponents $\alpha(\infty)$ (Equation 16), η (Equation 15), and ξ (Equations 14, 15) related to the system size scaling of the energy size distribution.

Distributions	$\alpha(\infty)$	ξ	η
Uniform	3.47	0.55	0.15
Linearly increasing	3.65	0.55	0.14
Linearly decreasing	3.62	0.55	0.12
Power law	3.55	0.60	0.13
Weibull	3.60	0.65	0.11

4. DISCUSSIONS AND CONCLUSIONS

The local load sharing fiber bundle model is known to be lacking in reproducing the scale-free avalanche statistics often seen in the experimental setup of fracturing brittle solids. In all the interpolation schemes between global (equal) and local load sharing versions of fiber bundles, the avalanche size distribution $P(s)$ only show a cross-over between the mean-field ($P(s) \sim s^{-\beta}$) and local load sharing ($P(s) \sim e^{-s/s_0}$) limits. The mean-field limit, however, is a rather idealized condition for modeling real samples.

However, one important distinction between avalanche sizes (s) of the fiber bundle model and what is usually measured in the experiments is that in the latter case it is the energy burst (E) emitted in an avalanche that is measured. However, that distinction is not at all significant in the mean-field i.e., the global load-sharing limit of the model, because in that limit $\langle E \rangle \sim s$. However, in the local load sharing version, we numerically find $\langle E \rangle \sim s^{\gamma}$. Given an exponential nature for the avalanche size distribution in the local load sharing limit and this numerical observation, it is possible to show that the size distribution of the energy bursts is scale-free $[Q(\langle E \rangle) \sim \langle E \rangle^{-\alpha}]$ with $\alpha = \gamma + 1$ (see Equation 12). Moreover, we have numerically established that this same scale free distribution exists for instantaneous values of the energy emitted and not only for the average emitted energy. We have then numerically checked that $\gamma \approx 2.5$ for various different threshold distributions (see **Figure 6**) and independently checked that the size distribution exponent for the energy bursts are close to -3.5 (see **Figures 4**, **7**). Indeed, there are indications in experiments with sandstones that the avalanche amplitude distribution was exponential while the energy burst distribution was found to be a power law (see e.g., [34, 35]). Our results reproduce the same for the local load sharing fiber bundle model.

In conclusion, the local load sharing fiber bundle model is shown to have a non-trivial relation between the avalanche size (number of fibers broken) and the energy burst size (elastic energy released from the broken fibers). Consequently, the energy burst size distribution is shown to have scale-free nature, with an exponent value independent of the threshold distributions of the fibers. Given that experimentally one measures the energy released, these results indicate that local load sharing fiber bundles can have a significant role in modeling fracture of brittle solids without having to resort to the equal load sharing mean-field limit.

DATA AVAILABILITY STATEMENT

The raw data supporting the conclusions of this article will be made available by the authors, without undue reservation.

AUTHOR CONTRIBUTIONS

SR did the numerical simulations. SB has written the first draft of the paper. All authors have edited the manuscript afterwards up to the final version.

FUNDING

This work was partly supported by the Research Council of Norway through its Centres of Excellence funding scheme, project number 262644.

ACKNOWLEDGMENTS

The authors thank Prof. Bikas K Chakrabarti and Prof. Purusattam Ray for his valuable comments.

REFERENCES

1. Bonamy D, Bouchaud E. Failure of heterogeneous materials: a dynamic phase transition? *Phys Rep*. (2011) 498:1. doi: 10.1016/j.physrep.2010.07.006
2. Herrmann H, Roux S, (editors). *Statistical Models for the Fracture of Disordered Media*. Amsterdam: Elsevier (1990).
3. Chakrabarti BK, Benguigui L. *Statistical Physics of Fracture and Breakdown in Disordered Systems*. Oxford: Oxford University Press (1997).
4. Kawamura H, Hatano T, Kato N, Biswas S, Chakrabarti BK. Statistical physics of fracture, friction, and earthquakes. *Rev Mod Phys.* (2012) 84:839. doi: 10.1103/RevModPhys.84.839
5. Biswas S, Ray P, Chakrabarti BK. *Statistical Physics of Fracture, Breakdown, and Earthqauke: Effect of Disorder and Heterogeneity*. Singapore: Wiley-VCH (2015).
6. de Arcangelis L, Godano C, Grasso JR, Lippiello E. Statistical physics approach to earthquake occurrence and forecasting. *Phys Rep.* (2016) 628:1. doi: 10.1016/j.physrep.2016.03.002
7. Bonamy D, Santucci S, Ponson L. Crackling dynamics in material failure as the signature of a self-organized dynamic phase transition. *Phys Rev Lett.* (2008) 101:045501. doi: 10.1103/PhysRevLett.101.045501
8. Koivisto J, Ovaska M, Miksic A, Laurson L, Alava MJ. Predicting sample lifetimes in creep fracture of heterogeneous materials. *Phys Rev E.* (2016) 94:023002. doi: 10.1103/PhysRevE.94.023002
9. Kádár V, Pál G, Kun F. Record statistics of bursts signals the onset of acceleration towards failure. *Sci Rep.* (2020) 10:2508. doi: 10.1038/s41598-020-59333-4
10. Biswas S, Castellanos DF, Zaiser M. Prediction of creep failure time using machine learning. *Sci Rep.* (2020) 10:16910. doi: 10.1038/s41598-020-72969-6
11. Pradhan S, Hansen A, Chakrabarti BK. Failure processes in elastic fiber bundles. *Rev Mod Phys.* (2010) 82:499. doi: 10.1103/RevModPhys.82.499
12. Hansen A, Hemmer PC, Pradhan S. *The Fiber Bundle Model: Modeling Failure in Materials*. Singapore: Wiley-VCH (2015).
13. Ray P, Date G. Spatial scaling in fracture propagation in dilute systems. *Physica A*. (1996) 229:26. doi: 10.1016/0378-4371(95)00431-9
14. Bak P, Tang C, Wiesenfeld K. Self-organized criticality: an explanation of $1/f$ noise. *Phys Rev Lett.* (1987) 59:381. doi: 10.1103/PhysRevLett.59.381
15. Pradhan S, Chakrabarti BK. Precursors of catastrophe in the Bak-Tang-Wiesenfeld, Manna, and random-fiber-bundle models of failure. *Phys Rev E.* (2001) 65:016113. doi: 10.1103/PhysRevE.65.016113
16. Biswas S, Roy S, Ray P. Nucleation versus percolation: Scaling criterion for failure in disordered solids. *Phys Rev E.* (2015) 91:050105. doi: 10.1103/PhysRevE.91.050105
17. Roy S, Ray P. Critical behavior in fiber bundle model: A study on brittle to quasi-brittle transition. *Europhys. Lett*. (2015) 112:26004. doi: 10.1209/0295-5075/112/26004
18. Sinha S, Roy S, Hansen A. Phase transitions and correlations in fracture process where disorder and stress compete. *Phys. Rev. Research*, (2020) 2:043108. doi: 10.1103/PhysRevResearch.2.043108
19. Roy S, Biswas S, Ray P. Modes of failure in disordered solids. *Phys Rev E.* (2017) 96:063003. doi: 10.1103/PhysRevE.96.063003
20. Kun F, Pál G, Varga I, Main IG. Effect of disorder on the spatial structure of damage in slowly compressed porous rocks. *Philos Trans R Soc A.* (2019) 377:20170393. doi: 10.1098/rsta.2017.0393
21. Shekhawat A, Zapperi S, Sethna JP. From damage percolation to crack nucleation through finite size criticality. *Phys Rev Lett.* (2013) 110:185505. doi: 10.1103/PhysRevLett.110.185505
22. Moreira AA, Oliveira CLN, Araujo NAM, Herrmann HJ, Andrade JS. Fracturing highly disordered Materials. *Phys. Rev. Lett*, (2012) 109:255701. doi: 10.1103/PhysResLett.109.255701
23. Pierce FT. Tensile tests for cotton yarns, "The weakest link" theorems on the strength of long and composite specimens. *J Text Inst.* (1926) 17:355. doi: 10.1080/19447027.1926.10599953
24. Daniels HE. The statistical theory of strength of bundles of threads. *Proc R Soc Lond Ser A.* (1945) 183:405. doi: 10.1098/rspa.1945.0011
25. Phoenix SL. The asymptotic distribution for the time to failure of a fiber bundle. *Adv Appl Probab.* (1979) 11:153. doi: 10.1017/S0001867800031748
26. Smith RL, Phoenix SL. Asymptotic distributions for the failure of fibrous materials under series-parallel structure and equal load-sharing. *J Appl Mech.* (1981) 48:75. doi: 10.1115/1.3157595
27. Newman WI, Phoenix SL. Time-dependent fiber bundles with local load sharing. *Phys Rev E.* (2001) 63:021507. doi: 10.1103/PhysRevE.63.021507
28. Harlow DG, Phoenix SL. The chain-of-bundles probability model for the strength of fibrous materials I: analysis and conjectures. *J Compos Mater.* (1978) 12:314. doi: 10.1177/002199837801200308
29. Harlow DG, Phoenix SL. Probability distributions for the strength of fibrous materials under local load sharing I: two-level failure and edge effects. *Adv Appl Probab.* (1982) 14:68. doi: 10.1017/S0001867800036715
30. Smith RL. *Proc R Soc Lond Ser A.* (1982) 382:179. doi: 10.1098/rspa.1982.0095
31. Kloster M, Hansen A, Hemmer PC. Burst avalanches in solvable models of fibrous materials. *Phys Rev E.* (1997) 56:2615. doi: 10.1103/PhysRevE.56.2615
32. Hammer PC, Hansen A. The distribution of simultaneous fiber failures in fiber bundles. *ASME J Appl Mech*. (1992) 59:909. doi: 10.1115/1.2894060
33. Zhang SD, Ding EJ. Burst-size distribution in fiber-bundles with local load-sharing. *Phys Lett A*. (1994) 193:425. doi: 10.1016/0375-9601(94)90534-7
34. Pradhan S, Stroisz AM, Fjær E, Lund HK, Sønstebø EF, Roy S. Fracturing tests on reservoir rocks: analysis of AE events and radial strain evolution. *48th US Rock Mechanics/Geomechanics Symposium Proceedings*, American Rock Mechanics Association (ARMA). (2014) 14:7442.
35. Pradhan S, Stroisz AM, Fjær E, Stenebråten JF, Lund HK, Sønstebø EV. *Stress-induced fracturing of reservoir rocks: Acoustic monitoring and μCT image analysis*. *Rock Mech Rock Eng.* (2015) 48:2529. doi: 10.1007/s00603-015-0853-4

Conflict of Interest: The authors declare that the research was conducted in the absence of any commercial or financial relationships that could be construed as a potential conflict of interest.

frontiers in Physics

ORIGINAL RESEARCH
published: 28 April 2021
doi: 10.3389/fphy.2021.642754

A Thermodynamic Framework for Stretching Processes in Fiber Materials

A. Arango-Restrepo[1,2], *J. M. Rubi*[1,2,3] *and Srutarshi Pradhan*[3]*

[1]*Departament de Fisica de La Matèria Condensada, Universitat de Barcelona, Barcelona, Spain,* [2]*Institut De Nanociencia I Nanotecnologia, Universitat De Barcelona, Barcelona, Spain,* [3]*PoreLab, Department of Physics, Norwegian University of Science and Technology, Trondheim, Norway*

Fiber breakage process involves heat exchange with the medium and energy dissipation in the form of heat, sound, and light, among others. A purely mechanical treatment is therefore in general not enough to provide a complete description of the process. We have proposed a thermodynamic framework which allows us to identify new alarming signals before the breaking of the whole set of fibers. The occurrence of a maximum of the reversible heat, a minimum of the derivative of the dissipated energy, or a minimum in the stretching velocity as a function of the stretch can prevent us from an imminent breakage of the fibers which depends on the nature of the fiber material and on the load applied. The proposed conceptual framework can be used to analyze how dissipation and thermal fluctuations affect the stretching process of fibers in systems as diverse as single-molecules, textile and muscular fibers, and composite materials.

Keywords: fiber bundle model, alarming signal, mesoscopic nonequilibrium thermodynamics, Fokker–Planck equation, dissipation, entropy production

OPEN ACCESS

Edited by:
Antonio F. Miguel,
University of Evora, Portugal

Reviewed by:
Antonio Heitor Reis,
University of Evora, Portugal
Zhi Zeng,
Hefei Institutes of Physical Science (CAS), China

***Correspondence:**
Srutarshi Pradhan
srutarshi.pradhan@ntnu.no

Specialty section:
This article was submitted to Interdisciplinary Physics, a section of the journal Frontiers in Physics

Received: *16 December 2020*
Accepted: *08 February 2021*
Published: *28 April 2021*

Citation:
Arango-Restrepo A, Rubi J M and Pradhan S (2021) A Thermodynamic Framework for Stretching Processes in Fiber Materials. Front. Phys. 9:642754. doi: 10.3389/fphy.2021.642754

1 INTRODUCTION

When external load/stretch is applied on fiber materials composed of elements with different strength thresholds, weaker elements fail first. As the surviving elements have to support the load, stress (load per element) increases and that can trigger more element failure. With continuous loading/stretching, at some point the system collapses completely, that is, the external load/stretch is above the strength of the whole system at that point. Such a system collapse is known as "catastrophic failure" for that system.

There are several physics-based approaches [1–3] that can model such a scenario. Fiber bundle model (FBM) is one of those models, and FBM has become a useful tool for studying fracture and failure [4–6] of composite materials under different loading conditions. The simplicity of the model allows achieving analytic solutions [5, 7] to an extent that is not possible in any of the fracture models studied so far. For these reasons, FBM is widely used as a model of breakdown that extends beyond disordered solids. In fact, fiber bundle model was first introduced by a textile engineer [4]. Later, physicists took interest in it, mainly to explore the failure dynamics and avalanche phenomena in this model [8–10]. Furthermore, it has been used as a model for other geophysical phenomena, such as snow avalanche [11], landslides [12, 13], biological materials [14], or even earthquakes [15].

Although stretching processes in FBM have been analyzed extensively [1–6], mainly by the physics community, a concrete thermodynamic description for the stretching process is still lacking in this field. In the efforts to unveil the stretching failure phenomena, thermodynamics

seems to be an important tool because it allows incorporating variables such as temperature, entropy, reversible heat, entropy production rate, and energy dissipation to thus unify stretching failure dynamics and energy analysis, especially where surface effects, heat release, and sound emission, due to energy dissipation, are present when dealing with the stretching failure of fibrous materials.

In this article, we intend to develop a thermodynamic framework to analyze not only the energetics of the stretching failure phenomena but also the dynamics by means of nonequilibrium thermodynamic formalism at all scales, from a single molecule to a macrostructure. We believe that our thermodynamic framework could carry over to other problem areas, eventually also outside the physical sciences such as molecular biology and nanotechnology.

We arrange the article as follows: After the Introduction (**section 1**), we give a short background of studies on stretching of FBM in **section 2**. In several subsections of **section 2**, we discuss strength and stability in FBM, energy variations during stretching, and warning signs of catastrophic failure. In **section 3**, we introduce a proper thermodynamic framework of the stretching process and analyze the mesoscopic regime and small-fluctuation regime. All the simulation results are presented in **section 4**, including dynamics and energetics, the Fokker–Plank approach, and the role of fluctuations on the stretching process. We make some conclusions at the end (**section 5**).

2 BACKGROUND: STRETCHING OF A FIBER BUNDLE

In 1926, F. T. Peirce introduced the fiber bundle model [4] to study the strength of cotton yarns in connection with textile engineering. Some static behavior of such a bundle (with equal load sharing by all the surviving fibers, following a failure) was discussed by Daniels in 1945 [16], and the model was brought to the attention of physicists in 1989 by Sornette [17].

In this model, a large number of parallel Hookean springs or fibers are clamped between two horizontal platforms; the upper one (rigid) helps hanging the bundle, while the load hangs from the lower one. The springs or fibers are assumed to have different breaking strengths. Once the load per fiber exceeds a fiber's own threshold, it fails and cannot carry the load any more. The load/stress it carried is now transferred to the surviving fibers. If the lower platform deforms under loading, fibers closer to the just-failed fiber will absorb more of the load than those further away, and this is called the local load sharing (LLS) scheme [18]. On the other hand, if the lower platform is rigid, the load is equally distributed to all the surviving fibers. This is called the equal load sharing (ELS) scheme. Intermediate range load redistribution is also studied (see [19]).

2.1 Strength and Stability in a Fiber Bundle Model

Let us consider a fiber bundle model having N parallel fibers placed between two stiff bars (**Figure 1**). Under an external force,

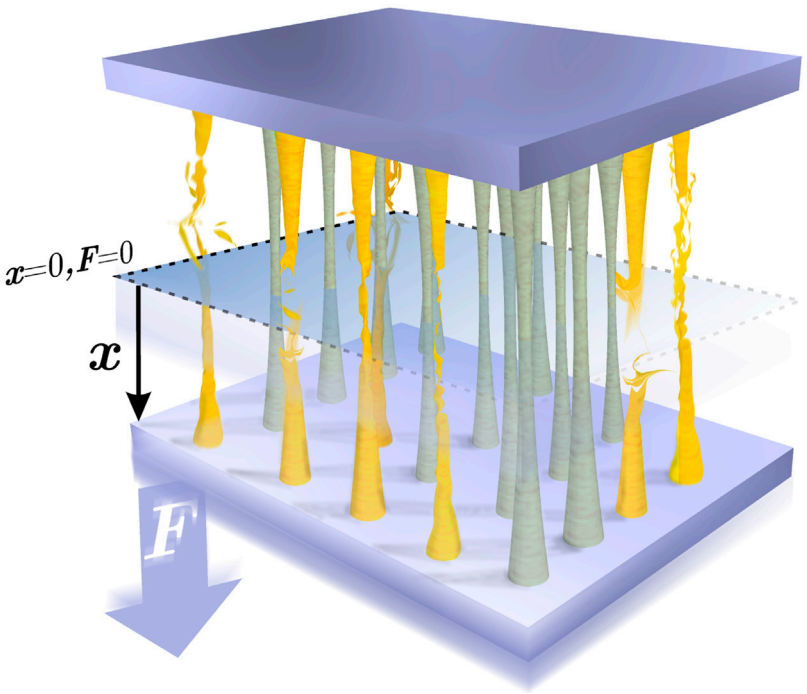

FIGURE 1 | Illustration of the system. Under the application of a constant external force F, the set of fibres are stretched by a length x. As the fibers have different strength thresholds, some of them break (yellow fibres) resulting in the increment of load for the non-broken fibres (grey fibres).

the system responds linearly with an elastic force. The dimensionless elastic force F_e for a given dimensionless stretch value x (ranging from 0 to 1) is $F_e = \kappa x$, where κ is the dimensionless spring constant $\kappa = k_e L_m/F$ with k_e as the elastic constant of the material, L_m as the maximum stretching length, and F as the external force (applied load). If the stretch x exceeds this threshold, the fiber fails irreversibly. In the equal load sharing (ELS) model, the bars are stiff and the applied load F is shared equally by the intact fibers.

2.1.1 Fiber Strength Distribution

The strength thresholds of the fibers are drawn from a probability density $p(x)$. The corresponding cumulative probability is given by

$$P(x) = \int_0^x p(y)dy \tag{1}$$

from which we can obtain the number of non-broken fibers as a function of the average deformation of the set of fibers x:

$$n(x) = N[1 - P(x)]. \tag{2}$$

The fraction of broken fibers, or damage, is then given by $m(x) = 1 - n(x)/N$. For a uniform distribution, one has $p(x) = 1$, $P(x) = x$, and $n(x) = N(1 - x)$.

2.1.2 The Critical/Failure Strength

The bundle exhibits an elastic force

$$F_e(x) = N[1 - P(x)]\kappa x. \tag{3}$$

The normalized elastic force (F_e/N) vs. the average stretch x is represented in **Figure 2** for a uniform probability distribution.

The elastic force maximum is the strength of the bundle and the corresponding stretch value (x_c) is the critical stretch beyond which the bundle collapses. Two distinct regimes of the system can be recognized: one stable, for $0 < x \leq x_c$, and another unstable, for $x > x_c$.

The critical stretch value follows from the condition $dF_e/dx = 0$. In the case of a uniform threshold distribution, using the corresponding values of $p(x_c)$ and $P(x_c)$, we obtain $x_c = 1/2$.

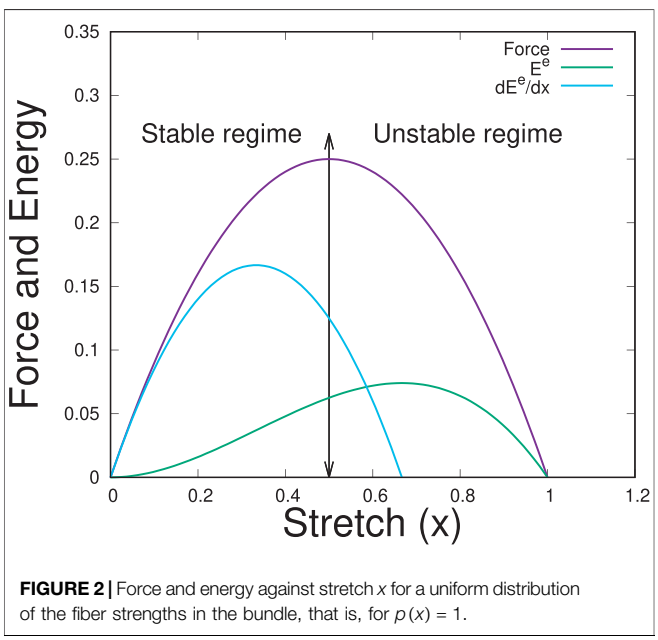

FIGURE 2 | Force and energy against stretch x for a uniform distribution of the fiber strengths in the bundle, that is, for $p(x) = 1$.

2.2 Energies in Fiber Bundle Model During Stretching

When N is large, one can express the elastic E_e and the breaking E_b energies in terms of the stretch x as

$$E_e(x) = \frac{N\kappa}{2} x^2[1 - P(x)] \tag{4}$$

and

$$E_b(x) = \frac{N\kappa}{2} \int_0^x dy[p(y)y^2]. \tag{5}$$

For a uniform distribution within the range $(0, 1)$, setting $p(x) = 1$ and $P(x) = x$ in **Eqs. 4**, **5**, we get $E_e(x) = \frac{N\kappa}{2} x^2(1 - x)$ and $E_b(x) = \frac{N\kappa}{6} x^3$. Clearly, breaking energy increases steadily with the stretch, but elastic energy reaches a maximum (see **Figure 2**).

2.3 The Warning Signal of a Catastrophic Failure

The elastic energy reaches a maximum value which falls in the unstable region of **Figure 2**, after the critical value of the extension. Its knowledge is thus not useful to predict the catastrophic failure point of the system. However, the maximum value x_{max} of dE_e/dx appears before x_c (see **Figure 2**). To obtain the relation between x_{max} and x_c, we take the derivative of dE_e/dx, with respect to x, in which for a uniform distribution, the solution of $d^2E_e(x)/dx^2 = 0$ gives

$$x_{max} = \frac{2}{3} x_c. \tag{6}$$

The rate of change of the elastic energy thus shows a peak before the failure comes [20].

3 THERMODYNAMICS OF STRETCHING PROCESSES

The stretching failure of fibers/materials is seen at a small scale, for example, during stretching of molecules in biological objects [21]. Similar stretching failure phenomena are also observed on a much bigger scale, like in the case of bridges made of long cables [22]. The observation in Ref. [20] that elastic energy variation could be a useful indicator of upcoming stretching-induced failure motivates us to construct a proper thermodynamic framework for such stretching failure phenomenon. For this purpose, we are going to introduce some new concepts like thermal bath, irreversible energy dissipation, and entropy production, and we believe that such a framework will help explore some new features of stretching failure behavior in

general. In this section, we will compute the energy dissipated and the heat released in the stretching process and show that dissipation provides a warning signal of the failure.

3.1 Energetics

Due to the load F, the system experiences an external work W which affects the elastic and breaking energies and the entropy S as well. Energy conservation can thus be formulated as

$$W = \Delta E_e + \Delta E_b + T\Delta S, \tag{7}$$

where $T\Delta S$ is the heat released Q_r in the process and ΔE_d the energy dissipated, with T the temperature. All the terms in this equations are measured in units of FL_mN. The elastic energy of the fibers as a function of the elongation results from the elastic energy per fiber times the number of unbroken fibers (**Eq. 2**):

$$\Delta E_e(x) = \frac{n(x)}{N}\varphi(x), \tag{8}$$

where $\varphi(x) = \frac{\kappa}{2}x^2$. The breaking energy results from the elastic energy which transforms into kinetic and surface energy. An infinitesimal change of this energy is related to the infinitesimal change of the damage through $dE_b(x) = \varphi(x)dm(x)$. Therefore, its total change is

$$\Delta E_b(x) = \int_0^x \varphi(z)\left[\frac{\partial m(z)}{\partial z}\right]dz. \tag{9}$$

The work done by the external force is the sum of the work done on each fiber:

$$W(x) = \frac{1}{FN}\sum_{i=1}^{n(x)} w_i(x) \approx \frac{1}{FN}\int_0^n w(x)dn', \tag{10}$$

where the work per fiber w is

$$w_i(x) = -\int_0^x \frac{F}{n(y)}dy. \tag{11}$$

Changes in the entropy in the stretching process are expressed as

$$\Delta S = \Delta_r S + \Delta_i S, \tag{12}$$

where $\Delta_r S$ is the entropy supplied to the system by its surroundings and $\Delta_i S$ is the entropy produced in the process. The second law of thermodynamics states that $\Delta_i S \geq 0$, where the zero value holds for reversible stretching (at quasi-equilibrium). The entropy supplied can be positive or negative; the sign depends on the interaction of the system with its surroundings [23]. For a closed system that may exchange heat with the surroundings, it is given by the Carnot–Clausius expression

$$\Delta_r S = \frac{Q_r}{T}, \tag{13}$$

where Q_r is the reversible or compensated heat, supplied for the surroundings, and T is the temperature of the environment. The irreversible change of the entropy, or the total entropy produced, at average elongation x is given by

$$\Delta_i S = \int_0^t \frac{n(x)}{N}\sigma dt', \tag{14}$$

where σ is the entropy production rate. The Goudy–Stodola theorem relates the total energy dissipated ΔE_d to the entropy produced $\Delta_i S$ [24]:

$$\Delta E_d = T\Delta_i S. \tag{15}$$

At this point, it is important to distinguish between reversible heat Q_r and dissipated energy E_d. The former is the energy in the form of heat supplied from or toward the surroundings in order to keep the temperature of the system constant. This quantity can be measured, for instance, by using a calorimeter. The latter is the free energy lost that can be transferred as heat, sound, or light, to mention just few forms of energy. The energy dissipated is thus not necessarily related to a measurable heat flux or to a measurable temperature change in the neighborhood of the system. This is the reason why reversible heat is frequently referred on the literature as measurable heat [23].

3.2 Mesoscopic Nonequilibrium Thermodynamics

When the fibers are immersed in a heat bath, their length can fluctuate. The effect of these fluctuations is negligible when the energy of the fibers is much greater than the thermal energy k_BT, which is the limit of validity of a purely mechanical treatment. For smaller system energies, the fluctuations become increasingly important. This is the case, for example, in the stretching of DNA [25]. Here, we analyze the dynamics of the elongation fluctuations and compute the entropy production rate and the energy dissipated in the process.

The probability density $\rho(x,t)$ to find a fiber with length x at dimensionless time t fulfills the continuity equation

$$\frac{\partial \rho(x,\,t)}{\partial t} = -\frac{\partial J(x,\,t)}{\partial x} \tag{16}$$

ensuing from probability conservation. In this equation, J is the probability current which vanishes at the boundaries ($x = 0$ and $x = 1$). The entropy production rate σ of the stretching process follows from mesoscopic nonequilibrium thermodynamics [26]:

$$\sigma(t) = -\frac{1}{T}\int_0^1 J(x,t)\frac{\partial \mu(x,t)}{\partial x}dx. \tag{17}$$

By coupling linearly, the flux J and its conjugated thermodynamic force (chemical potential gradient $\partial\mu/\partial x$), we obtain the dimensionless current

$$J(x,t) = -\rho(x,t)\frac{\partial \mu(x,t)}{\partial x} \tag{18}$$

which corresponds to Fick's diffusion law written in a dimensionless form where $t = t'D/L_m^2$ is the dimensionless time and D is the diffusivity [26]. The chemical potential is related to the free energy of the system through $\mu(x,t) = \left(\frac{\partial G}{\partial n}\right)_{T,P}$, which in turn is given by

$$\begin{aligned}\Delta G &= \Delta H - T\Delta_r S \\ &= \int_0^n \int_0^x \frac{1}{n(y)}dydn - n(x)\frac{\varphi(x)}{N} + \frac{k_BT}{FL_m}n(x)\ln\rho(x)\end{aligned} \tag{19}$$

with H being the enthalpy to which the elongation work and the elastic (potential) energy contribute. From now on, we will use the dimensionless force per fiber $f = FL_m/k_BT$. Taking the derivative of the Gibbs free energy with respect to the number of non-broken fibers n and considering **Eq. 2**, we obtain the chemical potential

$$\mu(x,t) = \int_0^x \frac{1}{n(y)}dy - \varphi(x) + \frac{1}{f}\ln\rho. \tag{20}$$

For large values of f, the entropic contribution is very small. Notice that the signs of the enthalpic terms have been changed because the external work is done in the direction of the movement, while the elastic force has the opposite direction.

Substituting **Eq. 20** in **Eq. 18** and the resulting flux in **Eq. 16**, we obtain the Fokker–Planck equation describing the evolution of the probability distribution

$$\frac{\partial\rho(x,t)}{\partial t} = \frac{\partial}{\partial x}\left[N\frac{\rho(x,t)}{n(x)} - \rho(x,t)\frac{\partial\varphi(x)}{\partial x} + \frac{1}{f}\frac{\partial\rho(x,t)}{\partial x}\right]. \tag{21}$$

The average elongation of the fibers corresponds to the first moment of the probability density ρ, and the solution of this equation is

$$\overline{x}(t) = \int_0^1 x\rho(x,t)dx. \tag{22}$$

Taking the time derivative of **Eq. 22** and using the conservation law (**Eq. 16**), we obtain

$$\dot{\overline{x}}(t) = \int_0^1 J(x,t)dx \tag{23}$$

from which we can interpret J as the local stretching velocity.

3.3 Small Fluctuation Regime

When fluctuations are very small, the variance of the probability distribution takes very small values, and therefore, we could approximate $\rho(x,t)$ by a delta function centered on $\overline{x}$: $\delta[x-\overline{x}(t)]$. By combining **Eqs. 18**, **20** and substituting $\rho(x,t)$ by the delta function, we obtain

$$J(x,t) = \delta[x-\overline{x}(t)]\left(\frac{1}{f} + \frac{N}{n(x)} - \kappa x\right), \tag{24}$$

where we have used the definition of φ. Integrating now **Eq. 24** in x, we obtain the stretching velocity

$$\dot{\overline{x}}(t) = \frac{1}{f} + \frac{N}{n(\overline{x})} - \kappa\overline{x}, \tag{25}$$

where the first term on the right side is the entropic contribution, the second results from the presence of the load, and the third is due to the elastic force which opposes to the elongation of the fibers. For very small fluctuations, the entropy production rate **Eq. 17** is $\sigma(t) = \dot{\overline{x}}^2$. Using this result into **Eq. 14**, and the equality $\dot{\overline{x}} = d\overline{x}/dt$, we obtain the irreversible entropy change

$$\Delta_i S(\overline{x}) = \int_0^{\overline{x}} \frac{n(\overline{x})}{N}\dot{\overline{x}}d\overline{x}. \tag{26}$$

4 RESULTS AND DISCUSSION

In this section, we obtain analytic expressions and numerical results for the dynamics and energetics of the stretching process assuming a uniform distribution of the strength thresholds of the fibers, $P(x) = x$. In order to simplify the notation, from now on, x will stand for the average value $\overline{x}$.

4.1 Dynamics and Energetics for Small Fluctuations

4.1.1 Dynamics

The average stretching velocity for a uniform distribution is obtained from **Eq. 25**, which is now written as

$$\dot{x}(t) = \frac{1}{f} + \frac{1}{1-x} - \kappa x. \tag{27}$$

Its derivative with respect to the elongation given by

$$\frac{d\dot{x}(t)}{dx} = \frac{1}{(1-x)^2} - \kappa \tag{28}$$

has a minimum around $x = 1 - \sqrt{1/\kappa}$, for $\kappa \geq 1$, indicating that for large enough values of κ, the stretching velocity exhibits a non-monotonic behavior. By integrating **Eq. 27**, we obtain the expression relating t and x:

$$t = -\frac{1}{2\kappa}\ln[1-\kappa x(1-x)] - \frac{1}{\sqrt{(4-\kappa)\kappa}}\left\{\tan^{-1}\left[\frac{\sqrt{\kappa}(1-2x)}{\sqrt{4-\kappa}}\right] - \tan^{-1}\left(\frac{\sqrt{\kappa}}{\sqrt{4-\kappa}}\right)\right\}. \tag{29}$$

For $\kappa \geq 4$, this equation diverges or is imaginary, which indicates that the process is not possible. From this relation, we can anticipate the asymptotic form of x through the behavior of the inverse tangent.

4.1.2 Energetics

From the dynamic of the process, we can compute the work, the energies, and the heat involved. The work follows from **Eqs. 10**, **11**:

$$W = -x(\ln x - 1). \tag{30}$$

The breaking energy, computed from **Eq. 9**, is

$$\Delta E_b = \frac{\kappa}{6}x^3. \tag{31}$$

As expected, the breaking energy increases as the elongation increases. From **Eq. 8**, the elastic energy change is

$$\Delta E_e = \frac{\kappa}{2}(1-x)x^2, \tag{32}$$

and its derivative

$$\frac{d\Delta E_e}{dx} = \frac{\kappa}{2}x(2-3x) \tag{33}$$

From these expressions, we observe that the maximum of ΔE_e is located at $x = 2/3$, whereas the maximum of $\frac{d\Delta E_e}{dx}$ is found at

$x = 1/3$. Through these values, we can analyze the different stages of the process. At $x = 1/3$, the system loses its capacity to store energy and the process enters a metastable regime. At $x = x_c$, the capacity to respond effectively to the action of the external load decreases and the process enters an unstable state. Finally, at $x = 2/3$, the system cannot store more energy in the form of elastic energy and falls into an imminent failure regime.

On the other hand, the energy dissipated (**Eq. 15**) is

$$\Delta E_d \approx \frac{x}{f}\left(1 - \frac{x}{2}\right) + x - \frac{\kappa}{12}(4 - 3x)x^3, \tag{34}$$

which decreases when κ increases because at a large elastic constant, more elastic energy can be stored to be subsequently transformed into kinetic energy after the breaking of the fibers. The first derivative of the energy dissipated, given by

$$\frac{d\Delta E_d}{dx} \approx \frac{1}{f}(1 - x) + 1 - \kappa(1 - x)x^2, \tag{35}$$

must be positive, according to the second law which imposes that $0 \le \kappa \le 13/2$, for $f \gg 1$. Combining this restriction with that inherent to **Eq. 29**, we conclude that the stretching process is feasible for $0 \le \kappa \le 4$. Analyzing the derivative of the dissipated energy, we find that it has a minimum at $x \approx 2/3$, located close to the maximum of the elastic energy. The dissipated energy may thus give us information about the transition to the imminent failure regime.

Finally, the reversible heat Q_r is obtained by using **Eq. 7**:

$$Q_r = W - \Delta E_d - \Delta E_e - \Delta E_b \tag{36}$$

Its derivative with respect to the elongation

$$\frac{dQ_r}{dx} = -\ln x - \frac{1}{f}(1 - x) - 1 - \kappa x(1 - x)^2 \tag{37}$$

shows that the maximum of Q_r depends on κ and is given by

$$x^* \approx \left(368 - 54\kappa + 4\kappa^2\right)/1000. \tag{38}$$

From this expression, one can see that for $\kappa \ge 3/4$, the maximum of Q_r lies before the maximum of the derivative of the elastic energy. This result indicates that by measuring the maximum of the reversible heat (the point at which the process becomes exothermic $dQ_r/dx < 0$), we can know beforehand what is the state at which the system reaches the metastable regime. For $0 \le \kappa \le 3/4$, the maximum lies in between $x = 1/3$ and $x = 0.368$, that is, in the metastable region.

Another way to find alarming signals is to calculate the intersection point of the curves $d\Delta E_e/dx$ and dQ_r/dx, x^*, which can be obtained from **Eqs. 33**, **37**, for $f \gg 1$:

$$x^* \approx \left(368 - 118\kappa + 24\kappa^2 - 2\kappa^3\right)/1000. \tag{39}$$

For $1/3 \le \kappa \le 4$, this point is located at the metastable regime. Thus, by measuring the heat released and computing the elastic energy, we can estimate the value of elongation just before the system enters the metastable region. Finally, from **Eq. 28**, we see that for $1 \le \kappa \le 9/4$, the minimum of the stretching velocity is located before the maximum of the change of the elastic energy ($x = 1/3$), whereas for $9/4 \le x \le 4$ it is situated in the metastable regime, before the process reaches the unstable stage.

4.2 Fokker–Planck Approach

To analyze the dynamic and the energetics of the process in the case in which fluctuations are not necessarily small, we will use the Fokker–Planck equation (**Eq. 21**) from which we can obtain the average elongation of the fibers and the energy dissipated. We have solved this equation by implementing the finite difference method in the software MATLAB 2017b. The results for ρ, represented in **Figure 3**, show a Gaussian-like behavior. We can observe that as the process progresses, the solution displaces to the right. In the inset, we represent the variance for $f \gg 1$, which increases linearly with the elongation of the fibers. The small value of the variance indicates that the assumption of small fluctuations is justified in this case.

By using **Eqs. 2**, **22**, we compute the average elongation and the number of non-broken fibers which are represented in **Figure 4**. Both quantities exhibit a quasi-linear behavior and an asymptotic behavior close to the breaking point. This comes from the fact that by decreasing the number of non-broken fibers, the force

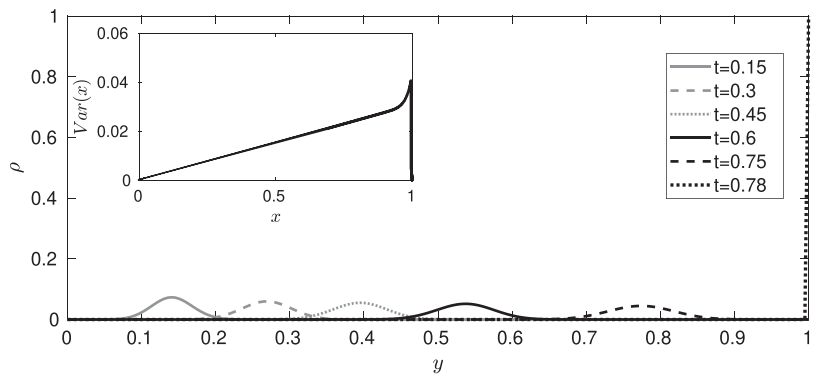

FIGURE 3 | Probability density as a function of the elongation y at different times, for $\kappa = 2$. Gaussian-like solutions displace to the right because of the action of the external force. The inset shows the variance of the probability distribution as a function of the average elongation of the set of fibers x. The variance increases linearly, then nonlinearly, and finally it decays to zero.

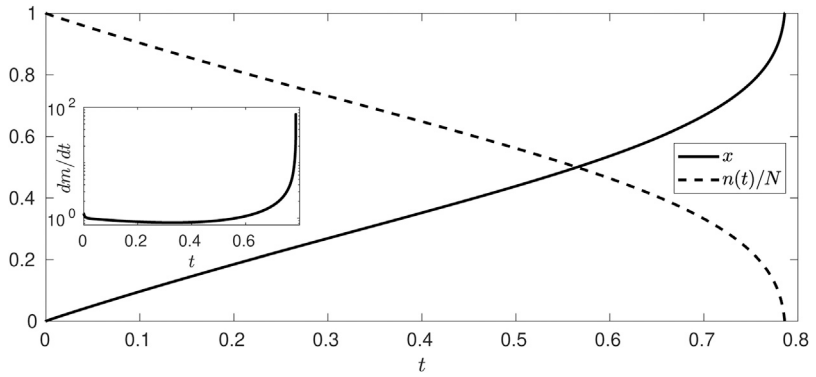

FIGURE 4 | Average elongation of the set of fibers x (continuous line) and fraction of non-broken fibers n/N (dashed line) as a function of time t, for $\kappa = 2$. The inset represents the rate of damage to the fiber bundle, which exhibits a non-monotonic behavior, thus evidencing the competition between elastic and external forces in the stretching process.

exerted per fiber increases, thus triggering an accumulative effect, typical of catastrophic events. The inset of the figure shows a non-monotonic behavior of the damage rate, evidencing the competition between the elastic and external forces in the stretching process in which finally the load force per fiber becomes much higher and the rate increases exponentially.

The stretching velocity $\dot{x}$ follows from the dynamics of x. By taking the derivative of $\dot{x}$ with respect to x, we obtain the change of the stretching velocity as a function of the average elongation. In **Figure 5**, we show the behavior of both quantities for $\kappa = 2$. We observe the existence of a minimum of the stretching velocity around $x = 0.29$ which appears before the system reaches the maximum change of the elastic energy (the transition toward the metastable regime).

From the dynamics of the process, we can calculate the energy dissipated by using **Eqs. 14**, **15**, **17**. **Figure 6** shows the energetics of the process. As predicted from the analytical results, we observe a maximum of the elastic energy and of the reversible heat. Furthermore, the maximum of Q_r is located around $x = 0.366$, independently of the values of κ. Additionally, the net reversible heat at the end of the process ($Q_r(x = 1)$) is zero, which shows that the stretching process is endothermic at small deformations and exothermic at larger deformations. The irreversible heat released results in measurable changes in the temperature of the environment.

The derivatives of the different energies with respect to x are represented in **Figure 7**. Before the imminent failure regime, the behavior of the temporal derivatives coincides with that of the spatial derivatives due to the fact that in this regime, x is linear in time, as follows from **Eq. 29**. The results obtained confirm that the derivative of the elastic energy has a maximum at $x = 1/3$ and its primitive a maximum at $x = 2/3$, while the derivative of the breaking energy always grows. They also confirm that both derivatives take the same value at $x = 1/2$. The derivative of the reversible heat always decreases, which indicates that the net flux of reversible heat is much higher at the beginning of the process. The curve of this derivative intersects that of the derivative of the elastic energy around $x = 1/5$, for $\kappa = 2$, while for lower values of κ, the intersection point moves to the right, being $\kappa = 1/2$ the highest value of κ at which the crossing takes place before the process reaches the metastable regime.

From **Figure 7**, we also confirm the fact that the derivative of the dissipated energy is always positive, in accordance with the second law of thermodynamics. Interestingly, the minimum of this derivative is found around $x = 1/2$ (independently of the

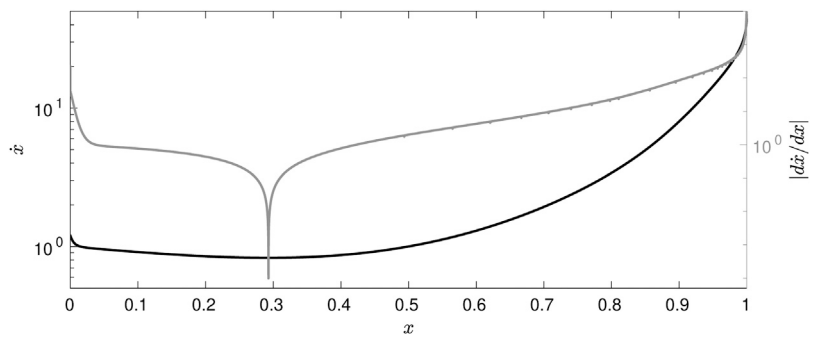

FIGURE 5 | Stretching velocity $\dot{x}$ (left grid, black continuous line) and absolute value of $d\dot{x}/dx$ (right grid, gray continuous line) as a function of the average elongation x, for $\kappa = 2$ represented in the logarithmic scale.

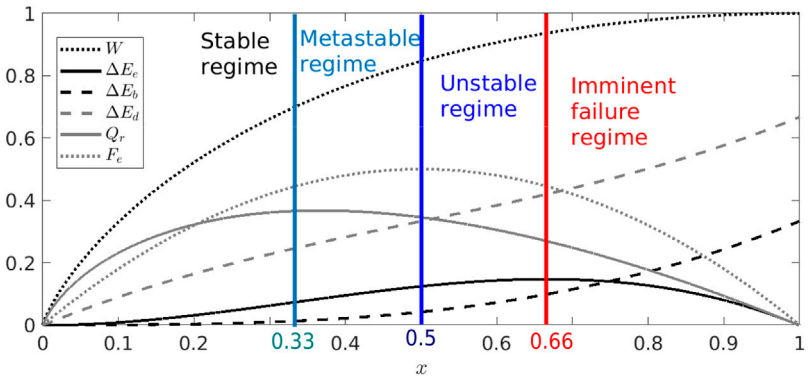

FIGURE 6 | Energetics as the stretching progress, for $\kappa = 2$. The work done W (dotted black line) is computed from **Eq.10**, the elastic energy ΔE_e (continuous black line) is computed from **Eq. 8**, the breaking energy ΔE_b (dashed black line) is computed from **Eq. 9**, the dissipated energy ΔE_d (dashed gray line) is computed from **Eqs. 14**, **17**, and the reversible heat Q_r (continuous gray line) is computed from **Eqs. 7**, **12**. The metastable regime threshold (light blue line) is located at $x = 1/3$, the unstable regime threshold (blue line) is located at $x = 1/2$, while the imminent failure threshold (red line) is located at $x = 2/3$.

value of κ), which is the same value at which the derivatives of the elastic and breaking energy coincide.

4.3 Role of the Fluctuations in the Stretching Process

The role that fluctuations play in the process can be estimated by comparing the value of the relevant quantities when we use the small fluctuation approach or when we adopt a Fokker–Planck description for the same value of κ. **Figure 8** shows the change of the stretching velocity with position. In particular, for $\kappa = 2$, the location of the minimum of this quantity computed from both approaches is the same, meaning that close to the minimum the system is practically insensitive to the presence of fluctuations. However, for small elongations, the velocities are slightly different, while at the imminent failure regime, they differ considerably due to the presence of fluctuations.

As shown in **Figure 9**, energy dissipation and reversible heat are affected by fluctuations at all stages of the process. The dissipated energy is overestimated in the approach of small fluctuations, whereas the reversible net heat $(Q_r(x = 1))$ is very sensitive to fluctuations, as concluded from the fact that this quantity is different in both approaches.

Figures 8, **9** show that the small fluctuation approach adequately describes the dynamics but not the energetics. The high accuracy in the dynamics is due to the almost Gaussian nature of the probability with a sufficiently small variance which is represented in **Figure 3**. The observed disparity in the reversible heat and energy dissipated lies in the approximation used. Additionally, the small deviation of the stretching velocity is accumulated, thus affecting the energy dissipated in the case of small fluctuation. Differences between both approaches become even more patent at smaller values of κ and f when the effect of the fluctuations is less important.

5 CONCLUSION

We have proposed a thermodynamic framework that analyses the role played by dissipation in a fiber stretching process, describes

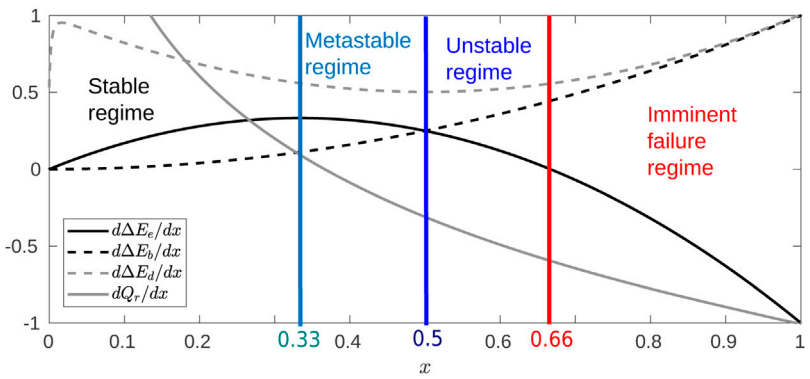

FIGURE 7 | Derivatives for the energies of the stretching process as a function of the average elongation x, for $\kappa = 2$. $d\Delta E_e/dx$: continuous black line; $d\Delta E_b/dx$: dashed black lines; $d\Delta E_d/dx$: dashed gray line; and dQ_r/dx: continuous gray line. Metastable regime transition: light blue line at $x = 1/3$; unstable regime transition: blue line at $x = 1/2$; and imminent failure regime transition: red line at $x = 2/3$.

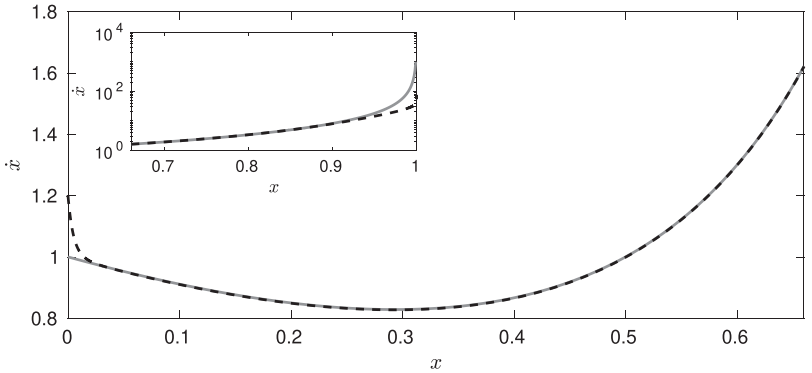

FIGURE 8 | Results for the stretching velocity $\dot{x}$ as a function of the average elongation x before the imminent failure regime, for $\kappa = 2$. The inset shows $\dot{x}$ in the imminent failure regime. The continuous gray line is obtained by assuming small fluctuations, while the dashed black line shows the behavior of that quantity for larger fluctuations obtained from the numerical solution of the Fokker–Planck equation.

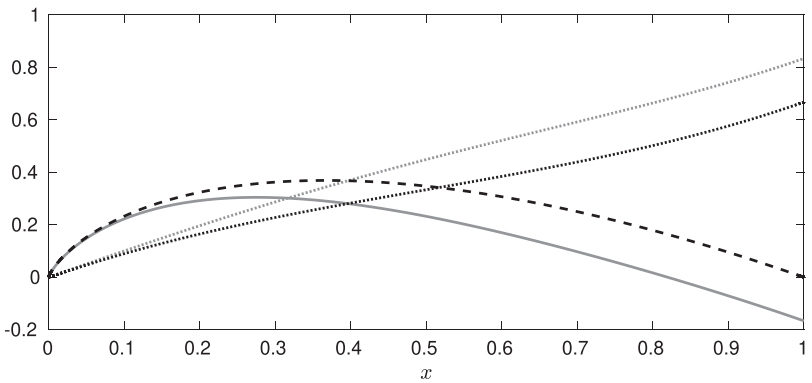

FIGURE 9 | Dissipated energy and reversible heat as a function of the average elongation x, for $\kappa = 2$. Results for ΔE_d and Q_r obtained when fluctuations are small are represented, respectively, by dotted and continuous gray lines. The same quantities for larger fluctuations, computed from the Fokker–Planck equation, correspond to the dotted and dashed black lines, respectively.

its different stages, and obtains new alarming signals before the whole set of fibers break. Our thermodynamic framework has identified relevant regimes (metastable, unstable, and imminent failure) as well as provided new transition indicators in terms of stretching velocity variation and entropy production rate, which is an important quantity to measure the energy efficiency of processes [27]. Specifically, we have shown that the maximum of the reversible heat may emerge before the process enters into the unstable regime. For some values of κ and small fluctuations, this maximum is located in the stable regime. In the same line, we found that the minimum of the entropy production rate is located around the transition to the unstable regime, and that for small fluctuations, this minimum defines the starting of the imminent failure regime for all values of κ. We have also proved that when the heat release flux is equal to the entropy production rate, in this intersection, the system is close to the transition toward the metastable regime. Similarly, we found that the minimum of the stretching velocity is always located in the stable zone, but the exact location strongly depends on the value of κ.

Under this approach, a more general analysis of the stretching process as a function of $\kappa = k_e L_m/F$ could be performed to investigate the effect of the relation between force and elastic constant on the dynamics. Additionally, for a small system with a low number of fibers, the approach can be applied to investigate biological stretching failure processes such as fiber muscle elongations and biochemical stretching as in DNA chains. Finally, as the stretching process releases heat and dissipates energy, we can have considerable temperature changes which can influence the individual failure of elements [28–30]. Further work is therefore needed on this issue.

DATA AVAILABILITY STATEMENT

The raw data supporting the conclusions of this article will be made available by the authors, without undue reservation.

AUTHOR CONTRIBUTIONS

AAR and JMR developed the idea, proposed the thermodynamic formalism used, and wrote the first version of

the article. SP suggested the problem and supervised the results obtained. All authors contributed equally to the discussion of the manuscript.

ACKNOWLEDGMENTS

The authors are grateful to the Research Council of Norway for its Center of Excellence Funding Scheme, project no. 262644, and to PoreLab which partially funded the stay of JMR in Tronndheim. AAR and JMR acknowledge financial support of MICIU (Spanish government) under Grant No. PGC2018–098373-B-I00 and of the Catalan government under Grant 2017-SGR-884. AAR is grateful for the financial support through an APIF 2017–2018 scholarship from the University of Barcelona. We would like to thank Signe Kjelstrup, Dick Bedeaux, Alex Hansen, and in general the members of PoreLab for interesting discussions during the visit of two of us (JMR and AAR) to PoreLab.

REFERENCES

1. Chakrabarti BK, and Benguigui LG. *Statistical Physics of Fracture and Breakdown in Disordered Systems*. 55 Oxford and New York, NY: Oxford University Press (1997). 176 p.
2. Herrmann HJ, and Roux S. *Statistical Models for the Fracture of Disordered Media*. North Holland: Elsevier (1990). 353 p.
3. Biswas S, Ray P, and Chakrabarti BK. *Statistical Physics of Fracture, Breakdown, and Earthquake: Effects of Disorder and Heterogeneity*. Weinheim, Germany: John Wiley & Sons (2015). 344 p.
4. Peirce FT. Tensile Tests for Cotton Yarns: "The Weakest Link" Theorems on the Strength of Long and of Composite Specimens. *J Textile Inst* (1926) 17: T355–368. doi:10.1080/19447027.1926.10599953
5. Pradhan S, Hansen A, and Chakrabarti BK. Failure Processes in Elastic Fiber Bundles. *Rev Mod Phys* (2010) 82:499–555. doi:10.1103/RevModPhys.82.499
6. Hansen A, Hemmer PC, and Pradhan S. *The Fiber Bundle Model: Modeling Failure in Materials*. Weinheim, Germany: John Wiley & Sons (2015). 256 p.
7. Pradhan S, and Chakrabarti BK. Precursors of Catastrophe in the Bak-Tang-Wiesenfeld, Manna, and Random-Fiber-Bundle Models of Failure. *Phys Rev E* (2001) 65:016113. doi:10.1103/PhysRevE.65.016113
8. Hemmer PC, and Hansen A. The Distribution of Simultaneous Fiber Failures in Fiber Bundles. *J Appl Mech* (1992) 59:909–14. doi:10.1115/1.2894060
9. Pradhan S, Hansen A, and Hemmer PC. Crossover Behavior in Burst Avalanches: Signature of Imminent Failure. *Phys Rev Lett* (2005) 95: 125501. doi:10.1103/PhysRevLett.95.125501
10. Pradhan S, and Hemmer PC. Relaxation Dynamics in Strained Fiber Bundles. *Phys Rev E* (2007) 75:056112. doi:10.1103/PhysRevE.75.056112
11. Reiweger I, Schweizer J, Dual J, and Herrmann HJ. Modelling Snow Failure With a Fibre Bundle Model. *J Glaciol* (2009) 55:997–1002. doi:10.3189/002214309790794869
12. Cohen D, Lehmann P, and Or D. Fiber Bundle Model for Multiscale Modeling of Hydromechanical Triggering of Shallow Landslides. *Water Resour Res* (2009) 45:W10436. doi:10.1029/2009WR007889
13. Pollen N, and Simon A. Estimating the Mechanical Effects of Riparian Vegetation on Stream Bank Stability Using a Fiber Bundle Model. *Water Resour Res* (2005) 41:W07025. doi:10.1029/2004WR003801
14. Pugno NM, Bosia F, and Abdalrahman T. Hierarchical Fiber Bundle Model to Investigate the Complex Architectures of Biological Materials. *Phys Rev E* (2012) 85:011903. doi:10.1103/PhysRevE.85.011903
15. Sornette D. Mean-Field Solution of a Block-Spring Model of Earthquakes. *J Phys France* (1992) 2:2089–96. doi:10.1051/jp1:1992269
16. Daniels HE, and Jeffreys H. The Statistical Theory of the Strength of Bundles of Threads. I. *Proc R Soc Lond Ser A. Math Phys Sci* (1945) 183:405–35. doi:10.1098/rspa.1945.0011
17. Sornette D. Elasticity and Failure of a Set of Elements Loaded in Parallel. *J Phys A: Math Gen* (1989) 22:L243–50. doi:10.1088/0305-4470/22/6/010
18. Harlow DG, and Phoenix SL. Approximations for the Strength Distribution and Size Effect in an Idealized Lattice Model of Material Breakdown. *J Mech Phys Sol* (1991) 39:173–200. doi:10.1016/0022-5096(91)90002-6
19. Hidalgo RC, Moreno Y, Kun F, and Herrmann HJ. Fracture Model With Variable Range of Interaction. *Phys Rev E* (2002) 65:046148. doi:10.1103/PhysRevE.65.046148
20. Pradhan S, Kjellstadli JT, and Hansen A. Variation of Elastic Energy Shows Reliable Signal of Upcoming Catastrophic Failure. *Front Phys* (2019) 7:106. doi:10.3389/fphy.2019.00106
21. Bering E, Kjelstrup S, Bedeaux D, Rubi JM, and de Wijn AS. Entropy Production Beyond the Thermodynamic Limit From Single-Molecule Stretching Simulations. *J Phys Chem B* (2020) 124:8909–17. doi:10.1021/acs.jpcb.0c05963
22. Li D, Ou J, Lan C, and Li H. Monitoring and Failure Analysis of Corroded Bridge Cables Under Fatigue Loading Using Acoustic Emission Sensors. *Sensors* (2012) 12:3901–15. doi:10.3390/s120403901
23. De Groot SR, and Mazur P. *Non-Equilibrium Thermodynamics*. New York, NY: Courier Corporation (2013). 510 p.
24. Bejan A, Tsatsaronis G, and Moran M. *Thermal Design and Optimization*. New York, NY: John Wiley & Sons (1996). 560 p.
25. Rubi JM, Bedeaux D, and Kjelstrup S. Thermodynamics for Single-Molecule Stretching Experiments. *J Phys Chem B* (2006) 110:12733–7. doi:10.1021/jp061840o
26. Reguera D, Rubí JM, and Vilar JMG. The Mesoscopic Dynamics of Thermodynamic Systems. *J Phys Chem B* (2005) 109:21502–15. doi:10.1021/jp052904i
27. Kjelstrup S, Bedeaux D, Johannessen E, and Gross J. *Non-Equilibrium Thermodynamics for Engineers*. 2nd ed. World Scientific (2017). 510 p.
28. Roux S. Thermally Activated Breakdown in the Fiber-Bundle Model. *Phys Rev E* (2000) 62:6164–9. doi:10.1103/PhysRevE.62.6164
29. Pradhan S, and Chakrabarti BK. Failure Due to Fatigue in Fiber Bundles and Solids. *Phys Rev E* (2003) 67:046124. doi:10.1103/PhysRevE.67.046124
30. Pradhan S, Chandra AK, and Chakrabarti BK. Noise-Induced Rupture Process: Phase Boundary and Scaling of Waiting Time Distribution. *Phys Rev E* (2013) 88:012123. doi:10.1103/PhysRevE.88.012123

Conflict of Interest: The authors declare that the research was conducted in the absence of any commercial or financial relationships that could be construed as a potential conflict of interest.

frontiers in Physics

ORIGINAL RESEARCH
published: 17 May 2021
doi: 10.3389/fphy.2021.675309

Criterion for Imminent Failure During Loading—Discrete Element Method Analysis

Wojciech Dębski[1]*, *Srutarshi Pradhan*[2] and *Alex Hansen*[2]

[1] Department of Theoretical Geophysics, Institute of Geophysics Polish Academy of Sciences (PAS), Warsaw, Poland,
[2] PoreLab, Department of Physics, Norwegian University of Science and Technology (NTNU), Trondheim, Norway

It has recently been reported that the equal load sharing fiber bundle model predicts the rate of change of the elastic energy stored in the bundle reaches its maximum before catastrophic failure occurs, making it a possible predictor for imminent collapse. The equal load sharing fiber bundle model does not contain central mechanisms that often play an important role in failure processes, such as localization. Thus, there is an obvious question whether a similar phenomenon is observed in more realistic systems. We address this question using the discrete element method to simulate breaking of a thin tissue subjected to a stretching load. Our simulations confirm that for a class of virtual materials which respond to stretching with a well-pronounced peak in force, its derivative and elastic energy we always observe an existence of the maximum of the elastic energy change rate prior to maximum loading force. Moreover, we find that the amount of energy released at failure is related to the maximum of the elastic energy absorption rate.

Keywords: Fiber Bundle Model, Discrete Element Method, Bayesian error estimation, tensional fracturing, energy variation, collapse point

OPEN ACCESS

Edited by:
Matjaž Perc,
University of Maribor, Slovenia

Reviewed by:
Takahiro Hatano,
Osaka University, Japan
Daniel Bonamy,
Commissariat à l'Energie Atomique et aux Energies Alternatives (CEA), France

***Correspondence:**
Wojciech Dębski
debski@igf.edu.pl

Specialty section:
This article was submitted to Interdisciplinary Physics, a section of the journal Frontiers in Physics

Received: *02 March 2021*
Accepted: *12 April 2021*
Published: *17 May 2021*

Citation:
Dębski W, Pradhan S and Hansen A (2021) Criterion for Imminent Failure During Loading—Discrete Element Method Analysis. Front. Phys. 9:675309. doi: 10.3389/fphy.2021.675309

1. INTRODUCTION

Fracturing, breaking, or more generally fragmentation of solid materials is a common physical processes that we meet in our daily lives. At the same time, it is one of the most complex processes covering a huge range of length and energy scales from atomic scale (breaking of chemical bonds) up to earthquakes (kilometer scale). This, together with a huge diversity of materials composition and variety of loading conditions leads to the aforementioned complexity. On the other hand, the fracture processes are extremely important for both industry and society. There is thus no surprise that a huge effort has been made to understand the fracture process in order to use it efficiently in controlled conditions (industry) and to prevent catastrophic failures (engineering, earthquakes). Furthermore, breaking/fracture dynamics plays central role in geophysical phenomena, such as snow avalanches [1], landslides [2, 3] as well as in stretching in biological materials [4]. The study of the breaking process has recently led to a discovery of a robust phenomenon which occurs before catastrophic failure (collapse) of composite materials under stress [5]. It has been found that the simple Fiber Bundle Model (FBM), a representative of fibrous materials, predicts existence of a maximum of the elastic energy absorption rate prior to a catastrophic failure point, namely the strain value at which the fiber bundle sustains the largest loading (stretching) force. Although the FBM has been proved to be a very powerful theoretical tool [6] it is based on some simplifications with respect to realistic processes. The obvious question thus arises if similar phenomena can also be predicted by other methods capable of grasping more realistic breaking scenarios. To answer this question, we have turned our attention toward numerical simulations of the breaking process

by means of the Discrete Element Method (DEM) [7]. The two methods, FBM and DEM, we are dealing with in this paper, represent two complementary approaches to the study of fracture or breaking processes.

The Fiber Bundle Model [8] represents an approach which, through appropriate generalizations and simplifications, attempts to grasp the most important elements of fracturing process in composite materials. On the other hand, the numerical Discrete Element Method [7, 9] has the capability of describing more realistic failure processes using the principles of a classical dynamics. Both methods exhibit some similarities which make their conjecture an interesting and efficient way of transferring theoretical concepts to realistic physical scenarios. Let us briefly discuss this point. The basic feature of both methods is a discrete representation of the medium under investigation. The FBM represents it as a finite number of fibers joining two clamps stretching the medium [6]. In the DEM approach the medium is represented by an assemble of interacting and bonded particles subjected to an external loading. Upon this loading, the fibers in FBM and inter-particles bonds in DEM, bearing part of an external load, break according to assumed rules if the stretching force exceeds some threshold values. The threshold probability distribution of fibers strength and the model of inter-particle interactions fully and uniquely determine the dynamics of the system. In the current application we have further enhanced this similarity by choosing in DEM simulations a classical, elastic-brittle interaction model. It assumes that bonds joining near-neighborhood particles are represented by perfectly elastic "springs" which break if extended over some critical value, just like the fibers in the FBM model. The fibers and inter-particle bonds braking possibilities make both methods highly non-linear and capable of addressing problems with non-trivially evolving boundary conditions, like, for example, creating a free surface by fracturing.

The most obvious difference between the two methods is that fibers in FBM are clamped between two rigid bars, which is not the case in the DEM approach. The inter-particle bonds in DEM can be viewed as a "micro-fibers" joining only neighborhood particles. However, it is worth to mention that during a loading evolution a coherent behavior of these micro-fibers can lead to the creation of macroscopic "super-fibers" joining loading clamps, like fibers in the FBM. Moreover, if particles are randomly packed, the inter-particle bonds are randomly orientated in space, in contradiction to the FBM fibers which are always parallel to the external load. Comparing both approaches we would finally point out that DEM inherently includes geometry of the analyzed body, while FBM does not. At first sight, this seems to be in a favor of DEM but it also leads to some serious shortages of the method. The inclusion of geometrical aspects into fracture simulations mixes kinematic (e.g., acoustic wave propagation effects) and dynamical effects due to bond-breaking. It makes the inference about breaking process much more complex. On the other hand, this feature of DEM as well as the aforementioned similarities open up a possibility of transmitting concepts from the FBM abstraction level to the "real world."

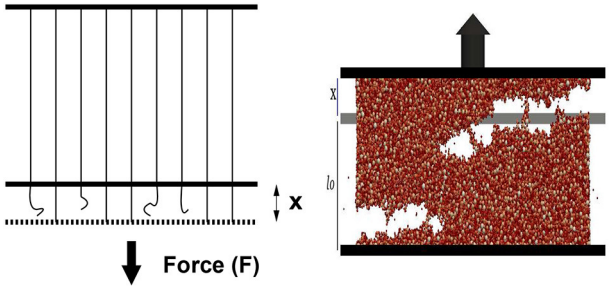

FIGURE 1 | (Left) the fiber bundle model—parallel fibers are placed between two rigid bars and are stretched by an amount x by applying a force F at the lower bar. (Right) The discrete element model—a thin tissue built of interconnected spherical particles vertically stretched using a constant velocity. The initial length of the fibers (left) and the initial height of the tissue are also shown.

In this work we explore the possibility of verifying the appearance of the maximum of an elastic energy absorption rate prior to the catastrophic failure predicted by the FBM [5] is also visible in DEM simulations. To answer this question, we have designed a series of numerical simulations of stretching a thin tissue. The limitation to such a quasi-two-dimensional case (often referred to as a 2.5D problem) is fully intentional. On one hand, we want to avoid possible complications introduced by a fully 3D approach, but on the other hand we wish to allow for a full development of local inter-particle interactions, which requires a full 3D neighborhood of each particle. The underlying concept of the theoretical analysis and numerical simulations is sketched in **Figure 1**, where the cartoon of stretched bundle of fibers and the stretched thin tissue built of spherical particles are shown. In the case of the FBM, stretched fibers break sequentially from the weakest to the strongest. In case of the DEM simulations, dragging up the upper horizontal edge of the tissue causes the breaking of inter-particle bonds and finally leads to its failure. For the sake of clarity, the most important parameters are graphically illustrated in **Figure 2** using an example of DEM simulated loading curves, describing the evolution of dragging force, elastic energy and its derivative with extension of the sample.

Answering the posed question goes through the following steps: After the Introduction (section 1) we give a short background of the studies on breaking of FBM in section 2. In several subsections of section 2 we discuss strength and stability in FBM, energy variations during breaking process and the prediction concerning the existence of a "precursor" of the collapse point. In the next section (section 3) the DEM method is shortly presented, followed by a detailed description of performed numerical simulations in section 4. The simulation results are discussed in section 5, and we give some final remarks and conclusions in section 6.

2. FIBER BUNDLE MODEL

When we stretch a system, composed of elements with different strength thresholds, weaker elements fail first. As the

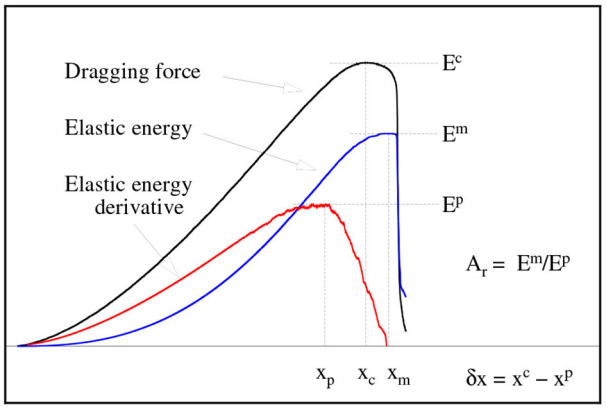

FIGURE 2 | Illustration of parameters used in the analysis. In the case of the DEM analysis, the vertical deformation (strain) parameters, x, x_c, and x_p, are scaled by the initial height l_0 of the tissue.

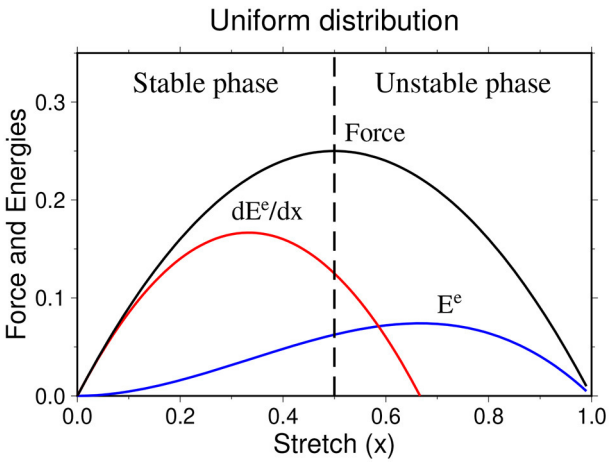

FIGURE 3 | Force (black curve), elastic energy (blue curve), and elastic energy change rate (red curve) against the stretch x for uniform distribution of the fiber strengths in the bundle.

surviving elements have to support the force, stress (force per element) increases and that can trigger more element-failure. With continuous stretching, at some point the system collapses completely.

There are several physics-based models [10–12] that can describe such a scenario. The FBM is one of those models being a useful tool for studying fracture and failure [6, 13, 14] of composite materials under different stretching conditions. In 1926, Peirce introduced the Fiber Bundle Model [8] to study the strength of cotton yarns in connection with textile engineering. Some static behavior of such a bundle was discussed by Daniels in 1945 [13] and the model was brought to the attention of physicists in 1989 by Sornette [15], who then proceeded mainly to explore the failure dynamics and avalanche phenomena in this model [16–18].

The simplicity of the model allows one to achieve analytic solutions [14, 19] to an extent that is not possible in any of the other fracture model. For these reasons, FBM is widely used as a model of fracture-failure that extends beyond disordered solids.

In the FBM (**Figure 1**), a large number of parallel Hookean springs or fibers are clamped between two horizontal clamps; the upper one (fixed) helps hanging the bundle while the load hangs from the lower one. The springs or fibers are assumed to have different breaking strengths. Once the load per fiber exceeds a fiber's threshold, it fails and can not carry load any more. The load/stress it carried is now transferred to the surviving fibers. If the lower platform deforms under loading, fibers closer to the just-failed fiber will absorb more of the load compared to those further away. Examples of such models are the Soft Clamp FBM [20] or the one proposed by Hidalgo et al. [21]. The extreme version of such models is the Local Load Sharing FBM [22] where the forces carried by the failed fiber is absrobed by its sucrviving neighbors. If the lower clamp is rigid, the load is equally distributed to all the surviving fibers. This is the Equal Load Sharing (ELS) FBM.

We will in the following only discuss the ELS FBM, which we refer to as the FBM in the following.

2.1. Strength and Stability of the Fiber Bundle Model

Let us consider a fiber bundle model having N parallel fibers. Each fiber responds linearly with a force f to the stretch value x as $f = \kappa x$, where κ is the spring constant. If the stretch x exceeds the strength threshold, the fiber fails irreversibly.

The strength thresholds of the fibers are drawn from a probability density $p(x)$ described by the corresponding cumulative probability $P(x)$. For example, for the uniform distribution on the unit interval we have

$$p(x) = 1; \qquad P(x) = x. \tag{1}$$

If N_f fibers have failed at a stretch x, then the bundle carries a force

$$F = (N - N_f)\kappa x = N(1 - P(x))\kappa x \tag{2}$$

which for the uniform distribution is a parabola as shown in **Figure 3**.

The force-maximum is the strength of the bundle and the corresponding stretch value x_c is the critical stretch beyond which the bundle collapses. Therefore, there are two distinct phases of the system: stable phase for $0 < x \leq x_c$ and unstable phase for $x > x_c$. The critical stretch value is found by setting $dF(x)/dx = 0$:

$$1 - x_c p(x_c) - P(x_c) = 0. \tag{3}$$

and the solution for the uniform threshold distribution reads

$$x_c = \frac{1}{2}. \tag{4}$$

In a similar way, one may calculate the critical strength of the bundle by putting x_c value in the force expression (Equation 2).

$$\frac{F_c}{N} = \frac{1}{4}. \tag{5}$$

2.2. Energy Variation and Warning Sign of Collapse

Work of an external load stretching the bundle converts into elastic energy of the fibers E^e and is partially released as damage energy E^d of broken fibers. When N is large, one can express E^e and E^d in terms of the stretch x as [5]

$$\mathrm{E}^e(x) = \frac{N\kappa}{2}\, x^2 \left(1 - P(x)\right) \,, \tag{6}$$

and

$$\mathrm{E}^d(x) = \frac{N\kappa}{2} \int_0^x dy \left[p(y) y^2\right] \,. \tag{7}$$

For the uniform distribution within the range $(0, 1)$, the Equations (6, 7) reads

$$\mathrm{E}^e(x) = \frac{N\kappa}{2}\, x^2(1 - x), \tag{8}$$

and

$$\mathrm{E}^d(x) = \frac{N\kappa}{6} x^3. \tag{9}$$

Clearly, the damage energy increases steadily with the stretch, but elastic energy has a maximum. Setting $d\mathrm{E}^e(x)/dx = 0$, one gets the condition for the position of the elastic energy maximum

$$2(1 - P(x_m)) - x_m p(x_m) \;=\; 0, \tag{10}$$

whose solution for the uniform distribution reads [5].

$$x_m = 2/3 = 4/3\, x_c. \tag{11}$$

Although the elastic energy has a maximum, it appears after the critical extension value, i.e., in the unstable phase of the system. Therefore, it can not help us to predict the catastrophic failure point of the system.

The situation is different if we consider the rate of elastic energy change $\mathcal{E}(x) = d\mathrm{E}^e(x)/dx$ which reads [5]

$$\mathcal{E}(x) = \frac{N\kappa}{2} \left[2x \left(1 - P(x)\right) - x^2 p(x)\right]. \tag{12}$$

Now, one can demonstrate that $\mathcal{E}(x)$ has a maximum and, this maximum appears before the critical extension value x_c (**Figure 3**). Indeed, one can calculate the value of stretch $x = x_p$ at which $\mathcal{E}$ has a maximum.

Taking derivative of $d\mathcal{E}/dx$,

$$\frac{d\mathcal{E}(x)}{dx} = \frac{N\kappa}{2} \left[2 \left(1 - P(x)\right) - 4xp(x) - x^2 p'(x)\right]; \tag{13}$$

where $p'(x)$ stands for derivative of $p(x)$. Setting $d\mathcal{E}(x)/dx = 0$ at $x = x_p$ we get the following solution for the uniform distribution

$$x_p = \frac{2}{3}\, x_c. \tag{14}$$

Thus, the rate of change of elastic energy shows a maximum before the actual failure appears. This result has been proven under weak conditions and demonstrated also for other probability distributions [5]. The obvious question at this moment is what information about upcoming failure this "precursor" provide us with. To answer this question, let us reformulate the problem at hand in the following way.

Let us assume that we know that maximum of the elastic energy absorption rate occurs at given x_p and let us assume that its value at x_p is $\mathcal{E}_{max}$. Knowing these two values can we predict quantitatively a failure time (measured in units of x) and can we predict its size in term of the released elastic energy? The answer can be obtained from equations describing the dependences of E^e and $\mathcal{E}$ on x as well as conditions for their maxima. The relations between x_c, x_m and x_p for a general power law distribution

$$\begin{aligned} p(x) &= (1 + \alpha) x^\alpha \,, \\ P(x) &= x^{1+\alpha} \,, \end{aligned} \tag{15}$$

where $\alpha > 0$ and $0 \le x \le 1$ reads

$$\begin{aligned} x_c &= \left(\tfrac{3+\alpha}{2}\right)^{\frac{1}{1+\alpha}} x_p \\ x_m &= (2 + \alpha)^{\frac{1}{1+\alpha}}\, x_p \end{aligned} \tag{16}$$

For the purpose of later comparison with DEM simulations, we introduce another parameter, δ_x, describing the delay of the critical value with respect to x_p: $\delta_x = x_c - x_p$, and the coefficient Γ quantifying a retardation of the point when elastic energy reaches maximum x_m with respect to x_c:

$$x_m = x_c + \Gamma\, \delta_x, \tag{17}$$

in terms of the δ_x scale.

For the power law distribution, the explicit form for δ_x anf Γ reads

$$\delta_x = \left[\left(\frac{3 + \alpha}{2}\right)^{\frac{1}{1+\alpha}} - 1\right] x_p, \tag{18}$$

and

$$\Gamma = \frac{(2 + \alpha)^{\frac{1}{1+\alpha}} - \left(\frac{3+\alpha}{2}\right)^{\frac{1}{1+\alpha}}}{\left(\frac{3+\alpha}{2}\right)^{\frac{1}{1+\alpha}} - 1}. \tag{19}$$

Both δ_x and Γ are monotonically decreasing functions of α and reach their maxima for the uniform distribution: $\delta_x(\alpha = 0) = 1/6$ and $\Gamma(\alpha = 0) = 1$, which means that in this case x_p and x_m are symmetrically located with respect to x_c.

Next, let us define yet another quantity A^r which relates the maximum of elastic energy $\mathrm{E}^e(x)$ to the maximum of the energy absorption rate $\mathcal{E}(x)$.

$$A^r \;=\; \frac{\mathrm{E}^e_{max}}{x_p\, \mathcal{E}_{max}} = \frac{\mathrm{E}^e(x_m)}{x_p \mathcal{E}(x_p)}, \tag{20}$$

so

$$\mathrm{E}^e_{max} = A^r x_p\, \mathcal{E}_{max} \tag{21}$$

The x_p factor assures not only the dimensionality of A^r but also leads to A^r independent of x_p for power law distribution, as shown below. For a given probability distribution A^r reads

$$A^r = \frac{1}{2}\,\frac{x_m^3\,p(x_m)}{3x_p^3\,p(x_p) + x_p^4\,p'(x_p)}. \tag{22}$$

For the power law distribution (Equation 15) the explicit form of A^r can be easily found

$$A^r = \frac{1}{2}\,\frac{(2+\alpha)^{\frac{3+\alpha}{1+\alpha}}}{3+\alpha}. \tag{23}$$

Let us note, that in this case A^r is constant, independent of x_p, and reaches its maximum value for uniform distribution $A^r(\alpha = 0) = 4/3$.

Interpretation of Equations (16), (21), and (22) is quite simple. For the considered power law distribution, the pair of parameters $(x_p, \mathcal{E}_{max})$ fully determines the upcoming failure, both a moment of its occurrence (x_c) as well as the amount of elastic energy (E^e_{max}) which is released during the catastrophic failure.

3. DISCRETE ELEMENT METHOD

The Discrete Element Method (DEM) [7] is the numerical method originally developed for simulating the behavior of granular media. It represents a medium under consideration as an ensemble of geometrical, perfectly elastic objects (originally circles in 2D) that interact with each other by repulsive forces due to surface contacts. The original Cundal idea has been extended by incorporating more complex particle interaction schemes and, particularly, by introducing bonds between particles—internal forces [23, 24] joining particles in a single piece. This has changed the DEM method to the modern simulation technique situated between the molecular dynamics from one side and the fluid (continuum) mechanics from other side [9, 25, 26].

The most important feature of the DEM method is a mathematical representation of the medium by a set of interacting finite size particles whose dynamics directly follows from the Newton equations of motion. Such a direct approach has an obvious advantage. It does not use any continuity, conservation, or other assumptions typical for continuum mechanics. One of the most important consequences is that DEM is particularly suitable for solving problems with complex, non-trivially evolving boundary conditions. This is just the case of a fracturing process.

Finally, let us note that DEM is a particular numerical technique of solving general multi-body static or dynamic tasks. Thus, in the application discussed here it allows to simulate temporal evolution of objects prior to fracture nucleation similar to continuum mechanics, through a period of development of a micro-fracture system and dynamical breaking like fracture mechanics, and, finally, can also include post-failure dynamics. This last issue is very interesting because laboratory data cannot provide reliable information about just-after-failure situation, which, on the other hand, seems to be crucial for large scale (seismology) analysis and is also interesting from a theoretical point of view [24, 27].

There exists a number of implementations of the DEM method as ready-to-use software. Our choice for the analysis presented here is the Esys-Particle software developed at the University of Queensland, Australia [28, 29]. We have chosen this particular software for many reasons as discussed in Debski and Klejment [30]. A detailed description of the software can be found in Abe et al. [28].

The Esys-Particle software provides a number of inter-particle interaction models and methods of simulating external loads. In our analysis we have used the standard elastic-brittle interaction model [9, 24]. The most essential element of this model are elastic bonds joining pairs of neighborhood particles and representing Hookean attracting or repulsing central force if bonded particles change their relative distance:

$$\vec{F} = -k_n \delta r \frac{\vec{r}}{|\vec{r}|}, \tag{24}$$

where $\vec{r}$ is a vector of relative position of particles, δr denotes a change of particle distance and k_n is a strength of inter-particle interaction ("spring constant"). However, if a distance between the particles increases by more then a critical distance b_d, the bond breaks and disappears. If all bonds attached to a given particle break it becomes the "unbonded particle." Summarizing, the used inter-particle interaction model is fully defined by a pair of parameters $(k_n,\ b_d)$.

DEM simulates temporal evolution of a given system by an explicit time integration of equations of motion for all particles including external and inter-particle forces. At each time step positions and velocities of the particles and the acting forces are calculated and used to move the particles from the current to new positions. Then the time is increased by a predefined time step and procedure is repeated until a stopping criterion is met. Within the Esys-Particle software the Verlet integration schemata is used what assure conservation of system energy [28].

4. NUMERICAL EXPERIMENT—SETUP AND DATA PROCESSING

Our DEM simulations deal with the simplest fracture dynamics task, namely the fracturing of materials under tensional load (mode 1 in the standard fracture mechanics classification). Taking into account the goal of the analysis, all performed simulations were conducted using the setup shown in **Figure 1** with the following details.

Firstly, to avoid possible complications due to the full 3D analysis and speed up (lengthy) calculations we have considered only a 2.5D case—a thin tissue. Its size was assumed to be: depth D = 5 mm, height L = 25 mm, and width W = 80 mm. This numerical sample was built of spherical particles with radii in the range 0.2–0.6 mm distributed according to the log-normal distribution truncated to this range. Particles were randomly distributed in space, which we have achieved by means of the GenGeo algorithm [28]—a part of the Esys-Particle software. The sample consists altogether of almost 25,000 particles bonded

by almost 125 thousand bonds. The same numerical sample was used in all simulations.

Secondly, the time step of the evolution was chosen to assure stability of computations and read $dt = 10^{-7}$ s. However, in many cases we have to go down to $dt = 10^{-8}$ s, especially for cases with very small k_n and b_d to get numerically stable solutions. This was possible because of the reduced dimensionality (2.5D) of the sample. Typically, to get the sample break into two disconnect parts we need to perform around 10^6–10^7 time steps. Only in few cases we need to wait until over 10^8 time steps are completed. The small time steps have the advantage of providing us with a very dense sampling of the evolution process.

In all simulations, the sample was numerically "glued" to the bottom and the upper plates by assuming that the particles of the uppermost and the lower-most layers of the samples interacted with the appropriate plates much stronger than with each others. In all simulations, the lower plate was fixed and the upper one was moving up with a maximum velocity of 50 mm/s. This dragging velocity has been selected as a tread-off between a computational efficiency and an attempt of reaching a quasi-static loading. It has been reached by gradual change of loading velocity from zero to the prescribed value during an initial period which varied depending on the (k_n,b_d) parameters used. In the case of microscopic parameters for which breaking occurred at large strains (larger than about 20%), this initial period was relatively short and took 10,000 time steps. However, for cases when samples break at much smaller strains, such a beginning of loading was too abrupt and has often lead to numerical problems. For such cases, we changed the loading velocity, much slower extending the initial period up to 10^6 time steps, at the price of slowing down computation by over two orders of magnitude.

Finally, we have performed a quite exhaustive scan over a space of microscopic parameters (k_n, b_d). In each simulation, all particle bonds have shared the same k_n and b_d parameters. The scanned values of microscopic interaction parameters were following. The threshold distance b_d ranged between 10^{-3} mm up to 5 mm. The scanned values of the strength of bonds k_n varied from 10 N/mm up to 10^7 N/mm. The scan of the (k_n, b_d) space was not uniform mainly for technical reasons. The region of large k_n and simulatneously small b_d was beyond our current computational capacities since large k_n requires (numerical stability) very small dt and small b_d would need a very gentle loading. Estimated computational time for such a setup was tens of weeks. Instead, we have put more attention to a region of small $k_n$and a transition from small to large b_d.

Yet another parameter of particles, namely their density was kept constant in all simulations as a parameter less important for the breaking dynamics. Its value was a priori set to $\rho = 2.5 \cdot 10^{-4}\mathrm{g/mm}^3$.

The goal of our DEM simulations was to create "realistic data" which could support or falsify predictions of the fiber bundle model. The richness of internal structure of the used DEM sample, a large range of explored interaction parameters, and the natural difference between the two methods discussed above have opened a question how this comparison should be done. Should we use all simulation results, or should we restrict ourselves to a specific subset only. Our experience [30] has shown that among simulated by DEM breaking mechanisms we can find both brittle-like processes which can be adequately described by the FBM method but also complex cases for which the FBM method probably fails. Taking this into account we have finally decided to accept for analysis only those simulation results for which well-pronounced peaks in the loading force and elastic energy derivative were visible. We have imposed no restrictions on the variation of elastic energy. The reason for this selection criterion was that only in such cases we could estimate the δ_x parameter with acceptable accuracy and thus avoid serious problems with an analysis of reliability of the obtained "numbers." Nevertheless, in some cases even this weak criterion has failed and some simulations have to be rejected from analysis "by hand." This happened whenever the complexity of breaking process has lead either to masking the critical value x_c (very large estimation errors), or made its identification doubtful when many local maxima of the force were observed. Using a specific selection criterion, no matter how weak it is, it always rises a question if the obtained results are not biased by such selection. We will come back to this point in the conclusion section. To summarize this part, almost 200 DEM simulations were finally analyzed.

A comparison of DEM simulations with the FBM predictions requires reading out of simulation data the position of maxima (x_c, x_m, and x_p) and corresponding values of F_c, E^e_{max}, and $\mathcal{E}_{max}$. It was usually quite easy in the case of E^e_{max} but often problematic for $\mathcal{E}_{max}$, and F_c. This issue has raised the problem of a proper treatment of appearing uncertainties. For this reason and to make the analysis as precise as possible we used a composite data pre-processing schemata assuring the maximum required accuracy. Considering x_c, x_p, and the corresponding F_c, $\mathcal{E}_{max}$values we have used the following approach.

First, the curves $F(x)$, $\mathrm{E}^e(x)$ were filtered (low pass). The used filters (convolutional or non-convolutional type) and their parameters were selected interactively. The goal of this filtering was to remove the high frequency oscillations (see discussion of noise origins below) from the data. The same filter was used for both $F(x)$ and $\mathrm{E}^e(x)$ to avoid relative phase shifts. Next, the derivative $\mathcal{E}(x)$ of elastic energy was calculated. This has been done using the pseudo-spectral approach (high-order finite different method) as follows: For each x we have locally fitted a 3rd order polynomial to $\mathrm{E}^e(x)$ using near-neighborhood x points.

In the next step, the maximum of $\mathcal{E}(x)$ curve was estimated using a local 3rd order polynomial fit around its noisy maximum as shown in **Figure 4**. The x_p and $\mathcal{E}_{max}$values were approximated by a position and a value of the obtained fit. The same fitting procedure was used for estimating the position of maximum of $F(x)$.

We have preferred this more complex procedure of estimating the location of the maxima instead of an additional low pass filtering of $\mathcal{E}(x)$ and direct search for it because this way we have avoided an additional phase shift (introduced always by a filtering procedure).

The obtained values of maxima location can, in principle, be used to calculate the δ_x parameter. However, such a direct approach unavoidably leads to loss of estimation precision. Since this parameter is the most important for our analysis, we have

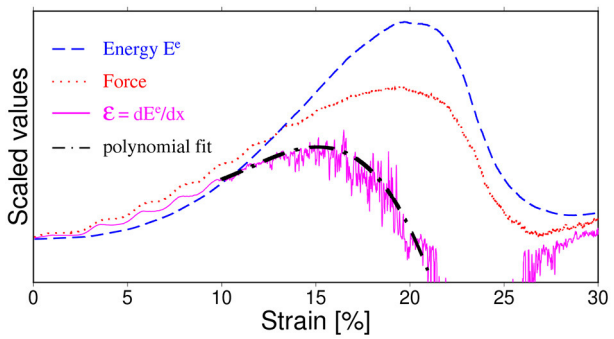

FIGURE 4 | An example of simulated loading curves and the illustration of the procedure of estimation of maxima of $F(x)$ and $\mathcal{E}(x)$ curves by means of a polynomial approximation. The maximum of $\mathcal{E}(x)$ is found by fitting a 3rd order polynomial to an appropriate curve around its noisy maximum. The same procedure was used for getting x_c from $F(x)$.

thus used yet another, more advanced Bayesian approach [31] capable to explore information about δ_x provided by a given dataset in the optimum way. The details of the method can be found in, for example, Tarantola [31] and Debski [32] and here let us recall only the most important points of the method.

A task of estimating the unknown parameters (here δ_x) from a given data set can be cast into a task of joining of the whole available information about the thought parameters. This information comes from observation (data) theory (relation between thought and measured quantities) and *a priori* existing estimations. The important fact is that all information contributing to the final estimation is essentially imprecise. Thus, first of all any data are subjected to uncertainties due to the limited accuracy of any measurement/simulation. Theoretical uncertainties arise from possibly approximate relations between thought parameters and those which have been measured or simulated. Finally, the existing (if at all) *a priori* information is often quite vague.

From the mathematical point of view, the idea of joining information is formulated using the Bayesian interpretation of probability [33]. It takes the form of constructing the so-called *a posteriori* probability distribution, which in the most often met situations reads [31, 32]

$$\sigma(m) = f(m)\exp\left(-||dat^{obs} - dat(m)||\right), \tag{25}$$

where m stands for the thought parameters, dat^{obs} and $dat(m)$ are observational data and theoretical prediction for a given m, and $||\cdot||$ stands for a norm measuring a "distance" between observations and predictions. Finally, the $f(m)$ is a probability distribution describing our *a priori* knowledge. It can be proved [31] that $\sigma(m)$ provides the quantitative description of all available information about m.

An application of this approach for estimation of the δ_x parameters takes a few steps. First, we identify m with δ_x: $m = \delta_x$. Next, as "observational" data we chose the function $F(x)$. Finally, we have assumed that around their maxima the $F(x)$ and $\mathcal{E}(x)$ curves are similar enough so locally one can write

$$F(x) \approx const.\mathcal{E}(x + \delta_x). \tag{26}$$

This last assumptions simply tells that the peak of $\mathcal{E}(x)$, when scaled and shifted by δ_x, should coincide with the peak of $F(x)$. One can try to provide deeper arguments for such assumption, based, for example, on the FBM prediction (see **Figure 3**), but in our case it basically follows from the observation of an occurrence of such coincidences (see, e.g., the upper left panel in **Figure 5**).

The choice of the norm $||\cdot||$ in Equation (25) should reflect the expected observational and theoretical uncertainties [32]. In cases of tasks with "data" represented by continuous functions, the cross-correlation of dat^{obs} and $dat(m)$ is most often used. However, we have preferred another choice, namely

$$||dat^{obs} - dat(m)|| = \sum_i |F(x_i) - \mathcal{E}(x_i + \delta_x)|, \tag{27}$$

where $|\cdot|$ stands for the absolute value and the sum is over all strain values in predefined range. This l_1-based norm is more robust than the classical cross-correlation norm (essentially equivalent to least-squares norm) and easily accommodates even large differences for a finite number of x_i arguments [32]. However, if one or both curves have large gradients within the summation range using such norm can lead to seriously biased *a posteriori* probability distribution [31]. In consequence, estimated solutions can also be subjected to uncontrolled systematic errors.

While plotting the output results we used the convention according to which a vertical elongation of the sample (strain) was expressed by percentage of an initial sample height, i.e.,

$$x = \frac{l - l_0}{l_0} \times 100\% \tag{28}$$

To enable the visualizations all plotted quantities, like elastic energy E^e, its derivative ($\mathcal{E}$), and stretching force F, etc., were separately normalized.

5. RESULTS

The performed simulations have provided numerical evidence that can be used to support or falsify the FBM prediction, thus being a proxy of experimental measurements. Adopting this point of view and by analogy to real experiments, the important question arises about uncertainties inherent to the simulation results. The simulations provide us with macroscopic quantities, like total elastic energy absorbed by the sample and stored in inter-particle bonds, deformation of the sample, number of broken bonds, and total force acting on the upper, moving up plate. They also provide data allowing to construct snapshots of microscopic state of the sample at any time during the simulation. Each of these quantities is subjected to uncertainties coming from different sources. We have identified three of them, namely numerical errors, statistical fluctuations and effects of additional physical processes. Since the last issue is strictly connected with observed breaking mechanisms, we describe uncertainty and breaking mechanism analysis together.

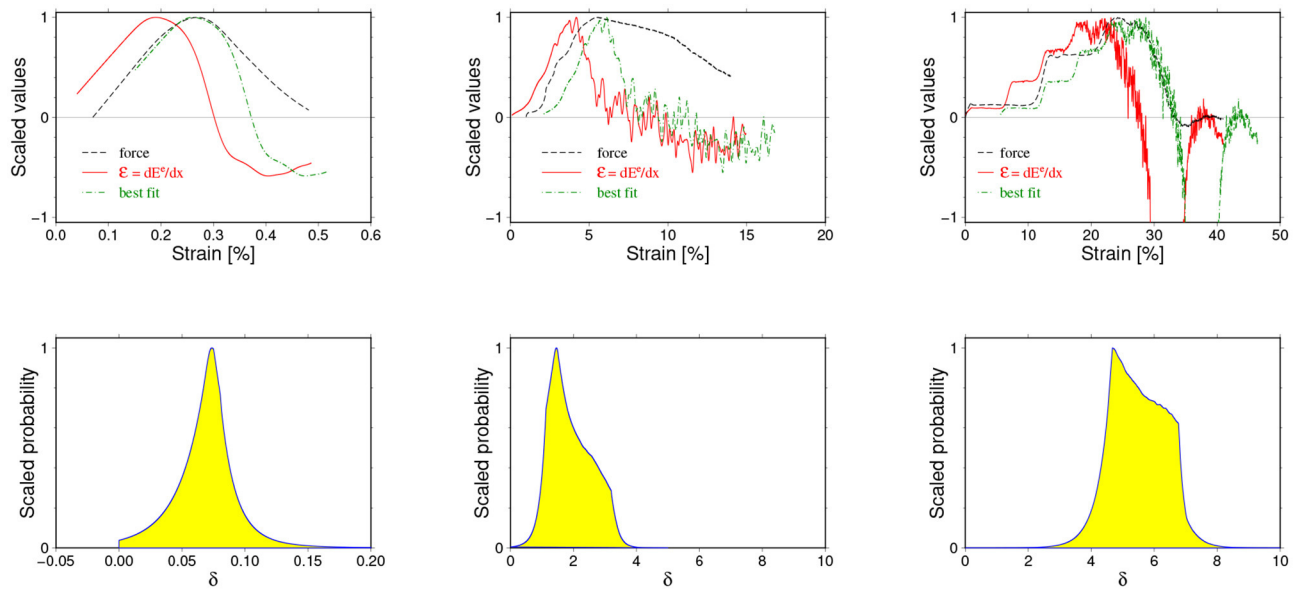

FIGURE 5 | Three examples of an estimation of the delay parameter δ_x using the Bayesian (probabilistic) approach. The curves $F(x)$, $\mathcal{E}(x)$, and $\mathcal{E}(x+\delta_x)$ for the optimal δ_x value are shown in the upper row. The lower row shows corresponding *a posteriori* probability distributions. The shown cases correspond to one of the best (almost noise-free) simulation results (left column) with well matching F and $\mathcal{E}$ curves, a typical situation (middle column) and a "difficult" case when acoustic waves strongly disturbed the breaking process.

5.1. Uncertainty Analysis

Numerical simulations, depending on the assumed aims, can be viewed either as an extension of theoretical analysis toward situations that cannot be treated analytically due to the complexity of the problem or as an extension of experimental data. This double point of view causes some controversy with respect to how numerical errors should be treated. The first (modeling) approach concentrates only on achieving the highest possible theoretical accuracy as numerical simulations are treated as a direct extension of the underlying theory. The error analysis is in this case straightforward and concentrates on such issues as the accuracy of the approximations to the underlying equations and the stability of the numerical scheme that, by the way, can be quite complex from a technical point of view. On the other hand, if the simulation is to provide observational data, we need a much broader approach to the uncertainty analysis. We have to include not only the issue of numerical uncertainties, but also characteristics of the simulated processes. This essentially complicates matters.

The DEM method, like any other numerical implementations of analytical models, has limitations and introduces unavoidably some approximations resulting in numerical uncertainties. The two most important factors are at present an accuracy of approximations of derivatives in original continuous physical equations and the stability of the time integration [34]. The last issue has generated much attention and has lead to the formulation of various so-called stability conditions (see, for example [9] for an analysis). Their basic meaning is to assure that none of the particles constituting the sample move too far from their current positions in a single time step. If such motion should happen, the interactions with neighborhood particles will lead to extremely large, non-physical forces acting between neighboring particles and as a consequence generate spurious high-frequency oscillations or even blowing up the whole sample. This instability is in fact the main source of numerical noise in DEM simulations and can be controlled (diminished) by choosing appropriately small time steps. However, it is very difficult to completely get rid of this type of noise, especially if the simulations contain large numbers of particles. In such systems, there is always a finite chance that at a given evolution stage, internal forces will exceed the stability limit due to fluctuations and the particles (especially the smallest ones) will locally start high frequency oscillations. However, in many cases such artificial oscillations are quite efficiently dumped by the interactions with surrounding particles during the next couple of time steps. If there remains as stationary noise, the simulation can often be accepted and noise can be removed by standard low pass data filtering. We refer to this particular feature of DEM as *soft stability*.

The significant feature of the performed simulations is their multi-body character. We model the behavior of a system of a large number of interacting objects. We would then expect the occurrance of statistical fluctuations in the macroscopic variables, such as drag force, elastic energy, etc. From our point of view, such fluctuations can be treated as a noise disturbing the simulation results.

The last identified source of final uncertainties was the fact that the DEM simulations inherently include the geometry of the sample and (implicitly) the finite speed of stress and strain development inside it. In consequence, we have always simulated not only a "pure" breaking process but

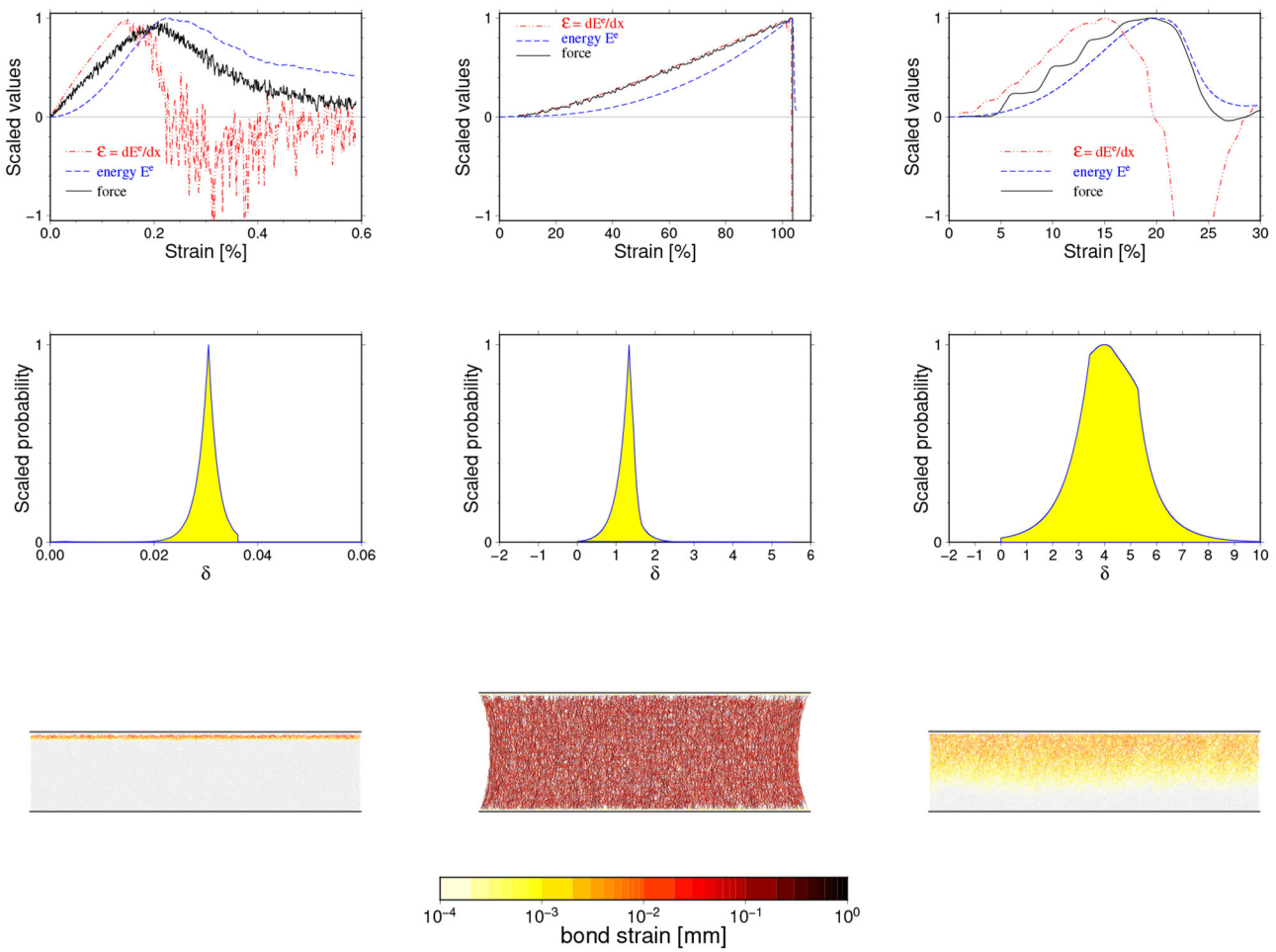

FIGURE 6 | Three types of noise encountered in performed simulations: numerical noise (left column), statistical fluctuations (middle column), and disturbances due to additional physical processes (right column). The $F(x)$, $\mathcal{E}(x)$, and $E^e(x)$ curves are shown in the uppermost row, the corresponding *a posteriori* probability distributions for δ_x parameter in the middle one, and selected snapshots of samples micro-structures in the lower-most row. The snapshots show the inter-particle bonds strains and use the same color scale. See text for detailed explanations.

also additional physical processes, among which generating of acoustic waves and stress diffusions were the most important. Under some favorable conditions, these additional physical processes seriously influenced our simulations and have not allowed to identify the critical value at all. In most cases, however, they only significantly contributed to the final, *a posteriori* uncertainties.

The described types of simulation uncertainties are presented in **Figure 6**, where examples of numerical noise, statistical fluctuations and creation of acoustic waves and their influence on observed parameters are shown. In addition, we include in this figure (middle row) the *a posteriori* distributions for the δ_x parameter estimated for the presented cases and examples of snapshots of the internal state of the samples illustrating mechanisms of generation of a given type of noise. For the purpose of this illustration, we adopted special measures. First of all, we have slightly increased the numerical noise (left column in **Figure 6** by enlarging the time step in this case. Moreover, we have started this simulation with abrupt loading which has led to some minor instabilities already at the beginning of simulation. These continued as stationary high frequency noise. On the other hand, to illustrate statistical fluctuation type noise (middle column) we have decreased the evolution time step to diminish the numerical noise and also have gently started loading. In the last cases (right column), no special measures have been applied.

A few conclusions can be drawn from **Figure 6**. First of all, we observe that the numerical noise and statistical fluctuations lead to quite similar effects: a high frequency, low amplitude oscillation visible in the $F(x)$ and $\mathcal{E}(x)$ curves. In practice, these two types of noise are indistinguishable. On the other hand, the existence of acoustic waves leads to a characteristic undulation of the $F(x)$ curve and, in the presented case, has significantly masked the critical value and decreased the accuracy of the estimation of x_c. The conclusion is that a low-pas filtering of the data can efficiently remove numerical and fluctuation noise, but not errors introduced by additional physical processes.

Secondly, the numerical noise can appear at any stage of evolution and can hardly be visible as a disturbance of the microscopic state (provided we are within a soft stability limit). On the other hand, the statistical fluctuations appear only if the sample has accommodated enough elastic energy uniformly distributed over the whole sample making the system reach a quasi-equilibrium state. The existence of acoustic waves is clearly visible in the snapshots as a time propagating disturbance.

The most interesting is, however, a comparison of the *a posteriori* distribution for δ_x parameters estimated by the Bayesian inversion method (middle row in **Figure 6**) which brings us information on how to identify how a given type of noise influences the δ_x estimation. In all cases we have observed a unimodal distribution whose shape essentially follows the l_1 norm-based likelihood function we have used. The "width" of this distribution is a measure of the accuracy of δ_x estimation. The smallest uncertainties are (or can be) due to the numerical noise. The statistical fluctuations lead to larger, though still moderate uncertainties. Finally, the largest errors are potentially introduced by the acoustic waves. Although the presented cases are for illustration only and hence arbitrary chosen, they suggest that the most important source of the final uncertainties are acoustic waves, or more generally, additional physical processes accompanying the breaking process in the DEM simulation [30]. In the next section, we discuss, among other issues, the contribution of the different observed breaking mechanisms to the types of noise.

Finally, let us note that the contribution of the numerical noise is not only small if the simulation is properly run, but in principle it can be highly suppressed by reducing the time step used. In practice, the reducing of time steps leads to much longer, often unacceptable computations, so that some level of numerical noise has to be accepted. Although it can easily be removed by low pass filtering, it marks its existence in *a posteriori* errors. It is not clear how the influence of statistical fluctuations on the final uncertainties can be diminished. A more advanced analysis, taking into account the possibility of resizing the sample, is apparently needed in this case. Finally, the uncertainties due to additional physical processes seems to be irreducible and the only way of avoiding them is a proper selection of the simulation setup.

5.2. Breaking Mechanisms

Within the set of performed simulations we have observed a variety of different breaking mechanisms. Some of them were qualitatively quite similar to the FBM predictions illustrated in **Figure 3**, and some were apparently quite different. The observed difference in simulated breaking processes were obviously due to different values of the $(k_n,\ b_d)$ parameters because all others conditions (micro-structure of the sample and loading conditions) were kept the same. It is thus obvious that the richness of breaking modes arises directly from a non-linearity of the breaking of particle-particle bonds controlled by $(k_n,\ b_d)$. However, we have to point out an important role of microscopic structure of the sample in a fragmentation process. Actually, for a given virtual material defined by $(k_n,\ b_d)$ an actually breaking process is determined by a micro-structure of the sample—a particle distribution in the sample. It determines which bonds break first, in which direction a fracture tip progress, etc. In our case the particles are distributed randomly and the sample is heterogeneous at the particles level. It introduces some randomness to our simulations. In principle, it is the same for all performed simulations because we have always used the same sample. However, in reality it is not exactly a case because the micro-structure of the sample is continuously changing from the time the first particle-particle bond breaks. The complex, non-linear feedback between a pair of $(k_n,\ b_d)$ parameters and the internal micro-structure during the breaking process causes that at the breaking stage we are efficiently dealing with slightly different samples for different $(k_n,\ b_d)$ parameters.

For the purpose of our analysis we divide the observed breaking mechanisms qualitatively in the following into four categories, shortly describing their main features.

The first class of observed breaking mechanisms, referred to as ductile-like, is characterized by a very wide maximum of elastic energy around the failure point x_c. An example of variation of the force, elastic energy and its derivative with the sample deformation is shown in **Figure 7**. This figure also provides a histogram illustrating the change of the rate of bond breaking during the simulation. Three snapshots of the sample's internal state illustrating this breaking mechanism ares shown in **Figure 8**.

For this type of simulated breaking process, we observe a fast initial absorption of external work and nucleation of fracturing followed by a very slow destruction of the sample. During this continuous damage stage, the force needed for keeping the constant stretching speed exhibit significant fluctuations with many local maxima. The breaking process was apparently much more complex than predicted by FBM (**Figure 3**). For this type of breaking mechanisms, it was impossible to identify the critical strain x_c at which samples reached the unstable phase. For this reason we have not considered such cases in analysis that follows. It is interesting, however, that even in this case the energy absorption rate curve demonstrated a well-defined maximum, which appeared prior to any loading force maximum as visible in **Figure 7**—following in a sense the FBM predictions.

The second class of observed fracture process consists of brittle-like processes during which collapse of the sample occurred very quickly after the beginning of loading without a visible "necking" of the sample. They always have a form of tearing out a few uppermost (or lower-most) layers from the remaining body of the sample in a cleavage-like process. **Figure 9** shows a post-failure state of the sample broken this way and **Figure 9** the corresponding loading curves and broken bonds. Apparently, such a breaking scenario is most similar to the one modeled by the FBM (**Figure 3**). An additional advantage of this breaking mechanism is that a relatively high accuracy of the δ_x estimation may be achieved due to neither statistical fluctuations nor acoustic waves have adequate room for development. However, such cases require a very gentle beginning of loading to avoid numerical instabilities.

The collapse of the sample occurred at very small strains and happened very quickly as a result of the bonds were breaking only in a narrow strain range around a well-pronounced critical

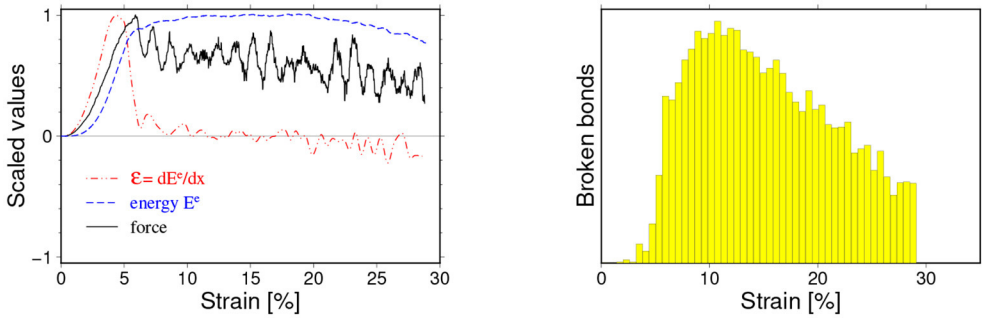

FIGURE 7 | An example of the ductile-like breaking mechanism. (Left) Force (F)—thick black curve, Elastic energy (E^e)—thin blue solid curve and the energy absorption rate ($\mathcal{E}$)—dashed red curve as functions of strain x. (Right) number of broken bonds in a fixed strain interval against x. A relatively fast increase of elastic energy at an initial phase is followed by a long-lasting stage of slowly changing elastic energy (left). At this stage, a slow destruction of the sample is observed (right) and the loading force needed to keep stretching speed constant exhibits significant fluctuations. The particle-particle interaction parameters for this case read: $k_n = 10^7$ N/mm, $b_d = 0.01$ mm.

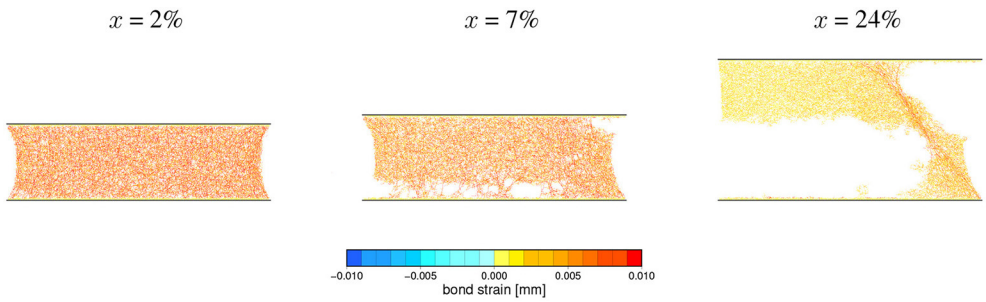

FIGURE 8 | Snapshots of the microscopic state of a sample undergoing a ductile-like breaking process at strains (x = 2, 7, 24%) indicated above the panels. Short colored segments represent inter-particle bonds existing at a given loading stage and their extension with respect to initial values are mapped by colors. The corresponding loading curves are shown in **Figure 7**.

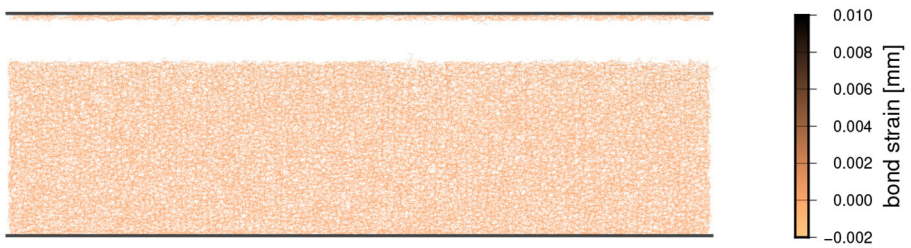

FIGURE 9 | Snapshots of a microscopic state of a sample undergoing a pure brittle cleavage-like breaking process. Short colored segments represent the inter-particle bonds existing at a given loading stage and their extension with respect to the initial values are mapped by colors. The corresponding loading curves are shown in **Figure 10**.

value x_c. The energy absorption rate curve $\mathcal{E}(x)$ has its maximum ahead of the critical strain x_c. We have observed mechanisms of this type only for the smallest values of critical bonds strains $b_d < 0.1\ mm$ regardless of the considered values of k_n.

In many simulations we have observed a breaking mechanism referred to as hyper-elastic. In a way similar to the brittle cases, the damaged energy is released in a small well-localized region around x_c. What distinguishes this scenario from the brittle scenario is a long initial stage of building-up the internal elastic energy of the sample and as a consequence a significant necking of the sample prior to breaking, typical for real ductile materials. **Figure 11** shows loading curves for such cases, and a sequence of snapshots characteristic for this type of breaking process is shown in **Figure 12**.

Apparently as **Figure 12** demonstrates, in such cases we are encountering a more complex breaking process than what is

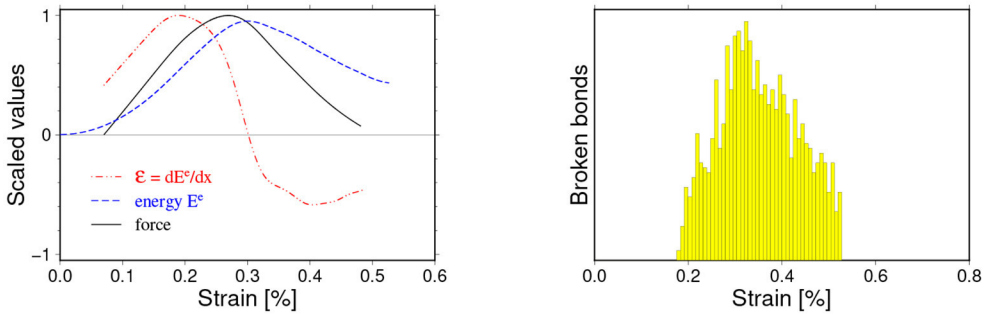

FIGURE 10 | An example of loading curves for the pure brittle cleavage-like breaking mechanisms (see **Figure 7** for the description). In this case, the fracture occurs at very small deformations and is very well-localized around the critical strain x_c. The particle-particle interaction parameters for this case read: $k_n = 10$ N/mm, $b_d = 0.1$ mm.

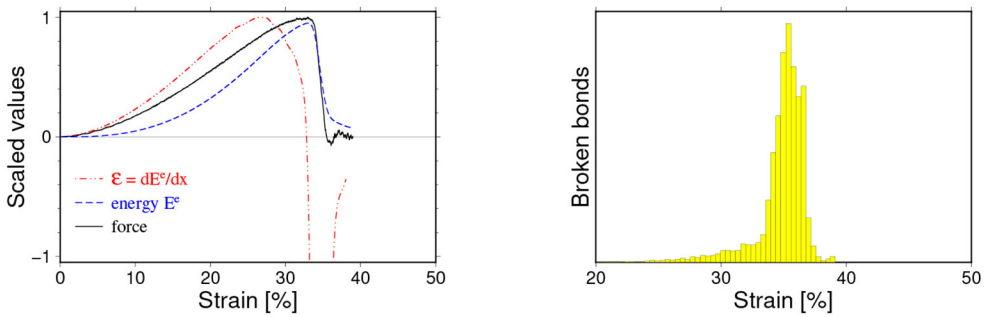

FIGURE 11 | Loading curves for the hyper-elastic breaking mechanisms (see **Figure 7** for the description). In this case the fracture has occurred at relatively large deformations but, like in the brittle cases, has been very well-localized around the critical strain x_c, and the accumulated elastic energy is almost entirely and quickly released. The particle-particle interaction parameters for this case read: $k_n = 10^5$ N/mm, $b_d = 0.4$ mm.

described in the FBM. However, in spite of this, the basic features of the failure process seen in the FBM are still preserved. For this type of fracturing we observe a well-pronounced peaks of $F(x)$, $\mathcal{E}(x)$, and usually a delayed but also well visible wider peak of $\mathrm{E}^e(x)$. Only in such cases a favorable conditions for developing statistical fluctuations occurred, because the sample (depending on values of microscopic parameters k_n, b_d) could absorb and store a large amount of internal energy. Simulations leading to this type of breaking process were quite susceptible to generating numerical noise which usually appeared around the critical value because at this stage the internal forces approaches their maximum values and numerical instabilities could easily develop. If such a noise was stationary or was diminishing, the simulation was accepted. Otherwise, the simulation was repeated with a smaller time step. In some cases, especially for cases with shorter initial stable phase we observed the development of acoustic waves propagating through the sample. However, the energy they were carrying was much smaller than the accumulated elastic energy, so their existence practically lead to some increase of final uncertainty only.

The final class of the observed mechanisms can be referred to as semi-ductile. One of the distinct features of events of this class is the presence of clearly visible acoustic waves in the stable loading phase. In some cases they lead to a small undulation of $F(x)$, $\mathrm{E}^e(x)$ or its derivative. However, in some cases they can completely dominate the loading phase of the evolution. In such extreme cases they can even prohibit a precise identification of the critical stretch. The loading curves for such an extreme case when strong acoustic waves have been generated from the beginning of the process is shown in **Figure 13**.

For events of this class we still can identify the critical value, and the maximum of the energy absorption rate but often with much lower accuracy. The $\mathrm{E}^e(x)$ curves are quite wide and their maxima are often noticeably shifted toward larger x with respect to x_c similar to ductile cases. However, unlike the ductile cases, $F(x)$ is relatively smoothly decaying with increasing x. The slowly decreasing of the elastic energy after reaching the critical value indicates a complex breaking mechanism. Indeed, we observe for such cases, the failure goes through the development of a multi-crack-systems. The micro-crack interact with each other and coalesce, which finally leads to a failure of the sample. This breaking mechanism is much slower than the fracturing process typical for hyper-elastic cases (fast horizontal fracture) or brittle one (cleavage process). The series of snapshots shown in **Figure 14** illustrates both above mentioned features.

All analyzed DEM simulations are finally shown on the scatter plot in **Figure 15**. The four categories of breaking mechanisms are represented at this figure by different colors. In spite of

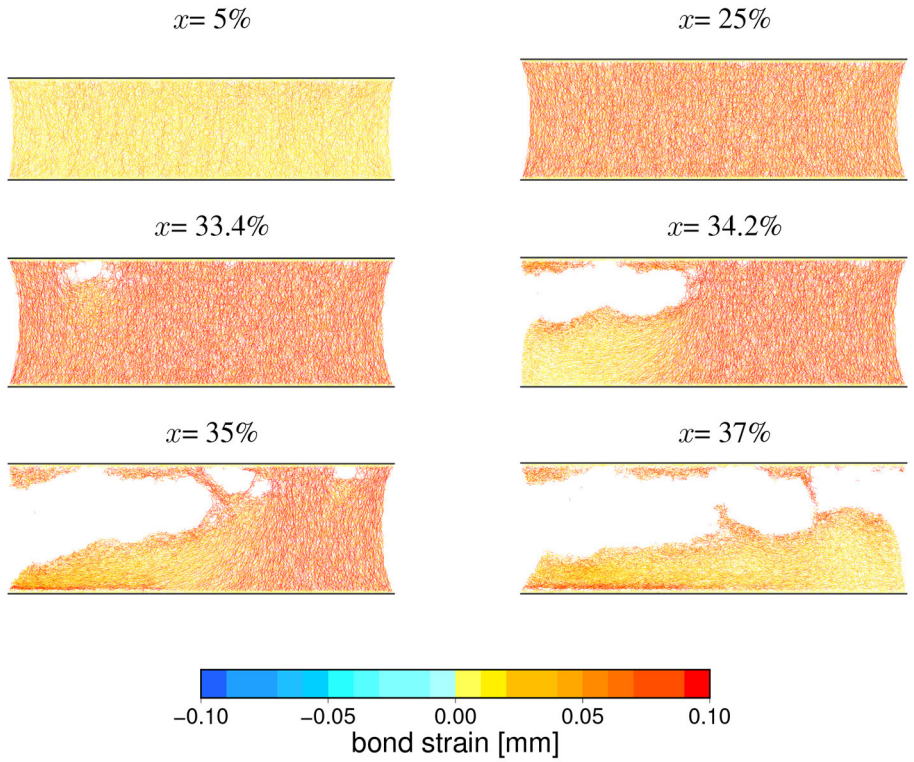

FIGURE 12 | Snapshots of the microscopic state of a sample undergoing a hyper-elastic breaking process at selected (indicated above panels) strains. Short colored segments represent inter-particles bonds existing at given loading stage and their extension with respect to initial values are mapped by colors. The corresponding loading curves are shown in **Figure 9**. A release of an internal elastic stress by developing fracture system is clearly visible. The particle-particle interaction parameters for this case read: $k_n = 10^5$ N/mm, $b_d = 0.4$ mm.

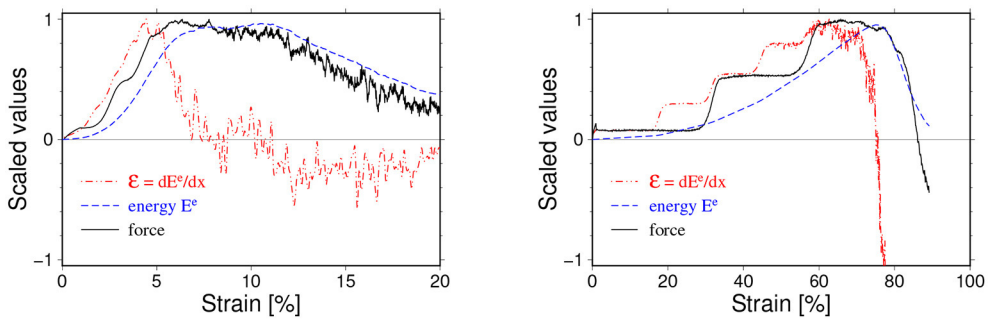

FIGURE 13 | Two examples of loading curves for semi-ductile breaking mechanisms with moderate (left) and strong amplitude acoustic waves generated and developing from the beginning of loading (see **Figure 7** for the description). The wavelength of the acoustic waves for the case shown in the left panel is about 1/3 of critical strain and their presence manifest themselves in irregular increase of the loading force in the initial loading stage strain. In the case shown in the right panel neither the critical stress x_c nor the maximum of energy absorption rate can be found with acceptable accuracy due to the strong acoustic waves. The particle-particle interaction parameters for the case shawn on left read: $k_n = 10^5$ N/mm, $b_d = 0.05$ mm and for the case shown on right $k_n = 10^2$ N/mm, $b_d = 0.6$ mm.

the fact that the proposed categorization is merely qualitative conclusions are quite obvious. The brittle-like processes are observed only for weak (small k_n) and rigid (small b_d) virtual materials. On the other hand the hyper-elastic cases were observed for stronger (large k_n) but flexible (large b_d) materials. The semi-ductile cases were observed for intermediate values of the (k_n, b_d) parameters with a probably (insufficient space sampling) smooth transition toward the ductile type in a region of small b_d and large $k_n$parameters. Star symbols are used to distinguished at **Figure 15** cases for which the maximum of elastic energy is a significantly delayed ($\Gamma > 5$) with respect to the critical strain. Surprisingly, within the given set of simulated cases such events are mostly located along the brittle—semi-ductile boundary. This issue will be analyzed elsewhere.

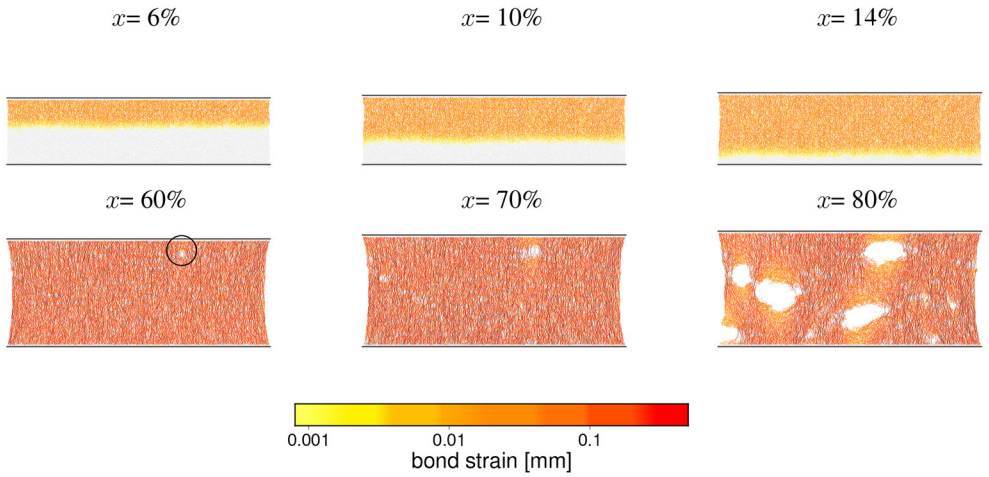

FIGURE 14 | Snapshots (at indicated deformations x) of the microscopic state of a sample undergoing a semi-ductile breaking process. The corresponding loading curves are shown in right panel in **Figure 13**. The most essential features for this class of processes are: (a) the development and propagation of acoustic waves (upper row) and (b) multi-crack fracturing pattern (lower row). The first visible signature of development of the fracture system, appearing at about 60% strain is marked by a circle in the lower left panel and at 80% strain the sample is still far away from breaking apart. Such a slow failure process is typical for this class of processes and differentiates it from hyper-elastic ones (see **Figure 12**). The particle-particle interaction parameters for this case read: $k_n = 10^2$ N/mm, $b_d = 0.6$ mm.

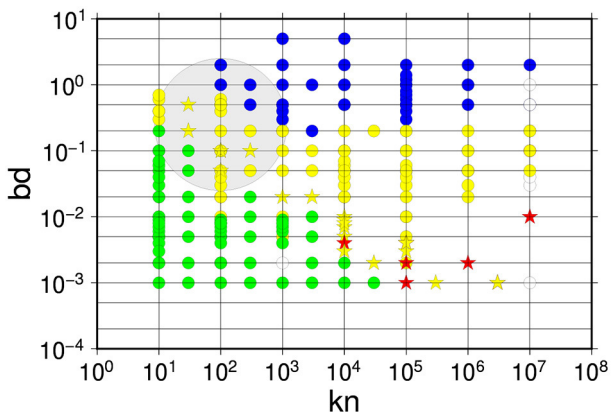

FIGURE 15 | The scatter plot of all analyzed events on the k_n-b_d plane. Different colors represent different categories of observed breaking mechanism: green—brittle, blue—hyper-elastic, yellow—semi-ductile, red—ductile, respectively. The star symbols depict cases for which the maximum of elastic energy is significantly delayed ($\Gamma > 5$) with respect to the critical strain. For few cases we could not determine (for technical reasons) the delay parameter Γ and such cases are left as open (white) circles. The region of (k_n, b_d) parameters for which strong acoustic waves were observed is shaded in gray.

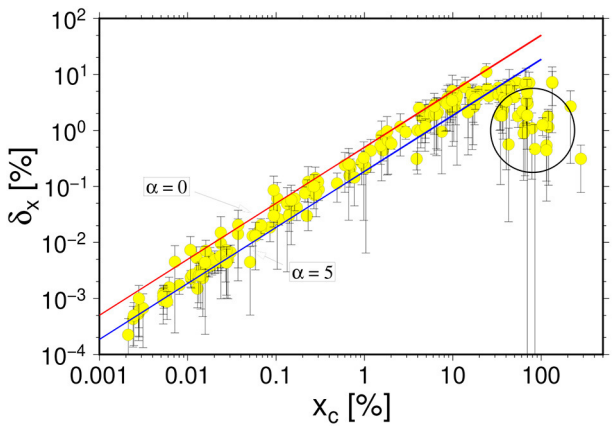

FIGURE 16 | The delay $\delta_x = x_c - x_p$ between the critical stress x_c and the strain at which the elastic energy absorption rate reaches maximum for all but ductile-like simulation results. The dashed curves show the FBM predictions for power law distributions with $\alpha = 0$ and 5. The circled events show systematically underestimated δ_x values due to used procedure of δ_x calculation (see text for details).

5.3. Signature of Imminent Failure

Answering the main question posed at the beginning of this paper, let us begin the discussion of results by gathering the information on the δ_x parameter from all analyzed numerical simulations. The result is shown in **Figure 16**.

The most obvious conclusion from this figure is that within the class of analyzed events we have always observed a positive value of δ_x. Estimated uncertainties indicate the significance of this result. It holds for all observed critical strains x_c. We observe the monotonic, almost linear increase of δ_x with x_c over the range $0.01 < x_c < 10$. Distortions observed at the smallest x_c are most probably due to the resolution limit imposed by a necessity of using a low pass filter to remove noise. Much more interesting is a saturation of $\delta_x(x_c)$ at large x_c. Actually, two effects are visible for the largest x_c values. The first one is the existence of a group of events for which δ_x values are significantly smaller than the remaining ones. This group is circled in **Figure 16**. A closer inspection of breaking mechanisms

for this group of events reveales that all have the same breaking pattern shown at the uppermost, middle panel in **Figure 6**. For such curves with large gradients the used method of constructing the likelihood function often fails [31] and leads to serious under-, or overestimation of the parameters. This is exactly the case for this group of events.

It could have been corrected, however we have not done it since it would go beyond the main goal of the paper and was of relatively low importance for the group of events we analyzed. Besides this technical issue, we observe an apparent saturation of the $\delta_x(x_c)$ curve. This effect may have different origins. One of them can be a finite size of the used sample. We are also recall a limitation of the DEM method in connection with a proper description of materials with large Poisson ratios [35]. However, it can also be a signature of approaching the limits of applicability of the FBM model. This issue requires further investigations.

The visible deviations at extremely small and large x_c do not, however, change the main conclusions, that for over three orders of magnitude of x_c the numerical DEM results are in a very good agreement with the FBM predictions concerning the positivity of δ_x and its dependence on x_c. The obtained results fits perfectly with the FBM predictions for power law fiber strength distributions with exponents in the range $0 < \alpha < 5$.

We provide complementary information and independent support for the FBM predictions in the plot of the A^r coefficient against x_c, as shown in **Figure 17**. We have here plotted it dividing all events into three categories with respect to the Γ parameter. Let us recall here that according to Equation (17) this dimensionless parameter measures the retardation of the point when internal elastic energy reaches a maximum value with respect to the critical value x_c. The larger the parameter Γ, the latter the elastic energy maximum, and the wider a peak of the elastic energy. Two curves corresponding to the FBM predictions for the power law distributions with exponents $\alpha = 0,$ and 5 are also shown.

For the majority of events characterized by the critical strain x_c lower than about 10% we have obtained an almost constant value of A^r in full compliance with the FBM predictions (see Equation 23). The agreement for the power law distribution with exponents in the range $0 < \alpha < 5$ is remarkably good, and the range of α for which it holds agrees with the analysis for δ_x. In the case of A^r we also observe a systematic deviations from the FBM model for the largest x_c. The reasons for this deviation are most probably the same as in the case of δ_x parameters and will be discussed elsewhere.

The most intriguing result shown in **Figure 17** is, however, the existence of a group of events for which values of A^r are much larger than 4/3, i.e., the value predicted by FBM as the superior limit. For these few exceptional events we have observed $A^r \sim 3$ and Γ over 5, (the FBM prediction is $\Gamma < 1$), thus much beyond the FBM limits. It has to be noticed that these exceptional events appear at critical strains for which other, compliant with FBM solutions exist and they are not influenced by the data processing methods, which was the case for the δ_x parameter for the largest x_c. Detailed examination of the loading curves and the snapshots of the breaking process have

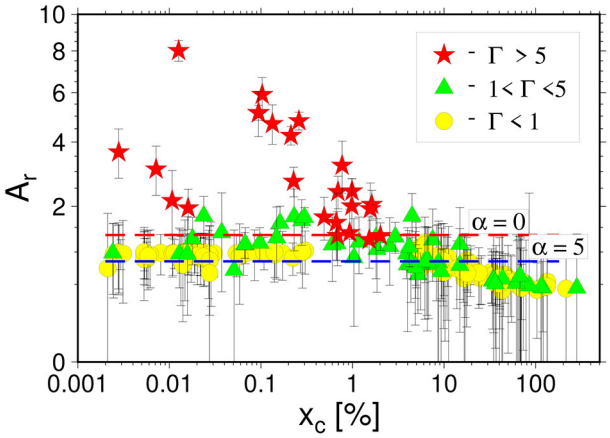

FIGURE 17 | The ratio A^r of the maximum of elastic energy released during the final failure to the product of maximum of elastic energy increase rate and x_p against x. Horizontal lines shows the prediction of the FBM model for power distribution with $\alpha = 0$—red line and $\alpha = 5$—blue line. Errors are mainly due to imprecise estimation of x_p and $\mathcal{E}_{max}$. The plotted values have been divided into three groups depending on the value of Γ expressing the retardation of the energy maximum x_m with respect to x_c (see Equation 17): the maximum of energy just follows the x_c point ($\Gamma < 1$), intermediate case ($1 < \Gamma < 5$) and the case when the energy maximum occurs far away from x_c.

indicated that all these events exhibit semi-ductile, complex breaking mechanism, and that is why their common feature are large values of Γ. It is thus not astonishing that they do not fit the FBM predictions for which the breaking mechanism is a simple "one-step" process. When the critical value is reached the loading process switches from the stable to the unstable phase leading to an immediate breaking of the sample and hence release of the whole reservoir of energy. It is astonishing that for this group of events, the deviation from the FBM prediction for A^r we observe simultaneously no departures from the FBM results concerning the positivity of x_c. Actually, observation of the existence of such events is one of the two most important results of our analysis.

6. DISCUSSION AND CONCLUSIONS

Considering the posed question whether the signature of imminent failure predicted by the FBM method is also visible in the DEM simulations, we can positively answer *yes*. In all analyzed simulations we observe the existence of a precursory maximum of an elastic energy absorption rate prior to the critical strain at which the loading force reaches the maximum. We have also observed a very good agreement of the DEM simulation results with the FBM predictions for the variation of the δ_x–a difference between the critical strain and the strain at which precursor maximum occurs, and the A^r–the scaled ratio of total absorbed energy and maximum of the absorption rate parameters. The advanced error analysis allows us to recognize and qualitatively take into account the sources of major errors providing solid evidence for the above conclusions. All these arguments provide a strong support

for the Fiber Bundle Model. However, a few observed facts forces us to pose some important physical questions and prevent us from drawing too optimistic but possibly too naive conclusions.

The first issue is a possible bias/limitation introduced by the selection procedure we have applied to the DEM simulations. We have considered only cases with a well-pronounced peak in the force and the energy absorption rate curves. The motivation of such selection is purely technical—we wished to assure a satisfactory accuracy of identifying of the critical value and the point at which the energy absorption rate reaches maximum. Among almost 200 performed simulations, only eight have been rejected due to failing this condition, which suggests it to be quite reasonable. However, consequences of such a procedure, even if it looks reasonable, go much beyond the technical issue itself. Actually, the applied criterion resulted in restriction of our analysis to processes in which force, energy absorption rate, and also elastic energy (although it was not required) were single-modal. By this we understand that the corresponding loading curves were quite compactly localized around the critical strain and do not exhibit a presence of significant secondary local maxima. What is the physical meaning of this fact?

The well-pronounced single, peaks in force, elastic energy, and energy absorption rate function mean that the breaking is essentially a "one-step" process. When initiate at the critical strain it unavoidably leads to a breaking of an object apart and release of the whole absorbed and stored internal energy. For such cases, the DEM simulations indeed confirm the existence of a precursory phenomena preceding the imminent failure, as predicted by FBM [5]. The DEM simulations have shown that this phenomenon also holds if more complex, but still essentially "one-step" processes are considered. The situation changes essentially if more complex breaking processes are considered. The existence of such processes has recently been reported [30] and in a restricted form of semi-ductile cases also appeared in our simulations. For such processes we found a "soft" breaking the FBM predictions: the A^r, and Γ parameters significantly differs from the FBM predictions but the δ_x parameter follows closely the FBM solution. An open question thus arises if the existence of the precursor phenomenon predicted by FBM can still be observed in case of more complex processes or not. For example, one can imagine the breaking process consisting of a series of smaller sub-failures. Will the system inform us about an approaching final failure in such a case? The answer is open.

Another, more elementary issue is related to how the external work done by the loading forces is absorbed and stored in the sample. In the fiber bundle model, the whole work is absorbed as elastic energy of the stretched fibers. Upon breaking a fiber, the elastic energy it has stored is released as the damage energy [5] and, what is important, it decouples from the model. By this we mean that the released energy does not influence the state of remaining fibers. In the DEM method, the situation is more complex. The energy released by a bond breaking is, in the first step, converted directly to the kinetic energy of particles originally joined by the bond. In the next steps, this "damage" energy either transforms (most of it) into elastic energy of remaining bonds attached to particles or remains to be a kinetic energy of vibrating particles. The first situation occurs if particles can hardly move or if they can carry a minimum kinetic energy due to their small masses. If this situation occurs, DEM directly mimics the FBM approach. However, DEM can also simulate an opposite situation, when the released energy can (to some extent) remain as kinetic energy of the originally bonded particles [30] and so does not decouple from the system. The obvious questions to be answered in the future are how such elastic-kinetic energy conversion mechanism modifies the FBM predictions, is this process responsible for the complexity of ductile-like breaking process, and so forth.

In the light of the above comments, the results of our analysis can be summarized in a general way as follows: When the external force is stretching a body, part of its work (all in an ideal case) converts into the internal energy of the body. If this energy transfer is dominated by building up an elastic energy and the final breaking of the body is a single-step process, then we observe a robust signal-precursor of the upcoming failure. The reaching of the maximum by the elastic energy absorption rate is just a signature that a catastrophic failure is approaching. The obtained results immediately poses further important questions. The first, and the most important one is, what are the limits of applicability of the FBM method when applied to description of breaking solid materials. Another one is whether the inclusion of mechanisms of conversion of the external work into kinetic energy (heat) of particles/fibers change the conclusion about relation between the maximum energy absorption rate and the critical value or not.

DATA AVAILABILITY STATEMENT

The raw data supporting the conclusions of this article will be made available by the authors, without undue reservation.

AUTHOR CONTRIBUTIONS

WD performed the DEM simulattions. SP and AH performed the FBM analysis. All authors equally contributed to data analysis and interpretations as well as preparing the manuscript.

FUNDING

This work was partially supported by the Research Council of Norway through its Centers of Excellence funding scheme, project number 262644. This research was supported in part by a subsidy from the Polish Ministry of Education and Science for the Institute of Geophysics, Polish Academy of Sciences.

REFERENCES

1. Reiweger I, Dual JSJ, Herrmann HJ. Modelling snow failure with a fibre bundle model. *J Glaciol*. (2009) 55:997. doi: 10.3189/002214309790794869
2. Cohen D, Lehmann P, Or D. Numerical modelling of riverbed grain size stratigraphic evolution. *Water Resour Res*. (2009) 45:W10436. doi: 10.1029/2009WR007889
3. Pollen N, Simon A. Estimating the mechanical effects of riparian vegetation on stream bank stability using a fiber bundle model. *Water Resour Res*. (2005) 41:W07025. doi: 10.1029/2004WR003801
4. Pugno NM, Bosia F, Abdalrahman T. Hierarchical fiber bundle model to investigate the complex architectures of biological materials. *Phys Rev E*. (2012) 85:011903. doi: 10.1103/PhysRevE.85.011903
5. Pradhan S, Kjellstadli JT, Hansen A. Variation of elastic energy shows reliable signal of upcoming catastrophic failure. *Front Phys*. (2019) 7:106. doi: 10.3389/fphy.2019.00106
6. Hansen A, Hemmer PC, Pradhan S. *The Fiber Bundle Model*. Veinheim: Wiley-VCH (2015). doi: 10.1002/9783527671960
7. Cundall PA. A computer model for simulating progressive, large-scale movement in blocky rock systems. *Proc Symp Int Soc Rock Mech*. (1971) 2:2–8.
8. Peirce FT. Tensile tests for cottom yarns. "The weakest link" theorems on the strength of long and composite specimens. *J Text Ind*. (1926) 17:355. doi: 10.1080/19447027.1926.10599953
9. O'Sullivan C. *Particulate Discrete Element Modelling, a Geomechanics Perspective*. New York, NY: Routledge; Taylor and Francis Group (2011).
10. Chakrabarti BK, Benguigui LG. *Statistical Physics of Fracture and Breakdown in Disordered Systems*. Oxford: Oxford University Press (1997).
11. Herrmann HJ, Roux S. *Statistical Models for the Fracture of Disordered Media*. Amsterdam: Elsevier (1990).
12. Biswas S, Ray P, Chakrabarti BK. *Statistical Physics of Fracture, Breakdown, and Earthquake*. Berlin: Wiley-VCH (2015). doi: 10.1002/9783527672646
13. Daniels HA. The statistical theory of the strength of bundles of threads. *Proc Roy Soc A*. (1945) 183:243. doi: 10.1098/rspa.1945.0011
14. Pradhan S, Hansen A, Chakrabarti BK. Failure processes in elastic fiber bundles. *Rev Mod Phys*. (2010) 82:499. doi: 10.1103/RevModPhys.82.499
15. Sornette D. Elasticity and failure of a set of elements loaded in parallel. *J Phys A*. (1989) 22:L243. doi: 10.1088/0305-4470/22/6/010
16. Hemmer PC, Hansen A. The distribution of simultaneous fiber failures in fiber bundles. *ASME J Appl Mech*. (1992) 59:909. doi: 10.1115/1.2894060
17. Pradhan S, Hansen A, Hemmer PC. Crossover behavior in burst avalanches: signature of imminent failure. *Phys Rev Lett*. (2005) 95:125501. doi: 10.1103/PhysRevLett.95.125501
18. Pradhan S, Hemmer PC. Relaxation dynamics in strained fiber bundlesi. *Phys Rev E*. (2007) 75:056112. doi: 10.1103/PhysRevE.75.056112
19. Pradhan S, Chakrabarti BK. Precursors of catastrophe in the Bak-Tang-Wiesenfeld, Manna, and random-fiber-bundle models of failure. *Phys Rev E*. (2002) 65:016113. doi: 10.1103/PhysRevE.65.016113
20. Batrouni GG, Hansen A, Schmittbuhl J. Heterogeneous interfacial failure between two elastic blocks. *Phys Rev E*. (2002) 65:036126. doi: 10.1103/PhysRevE.65.036126
21. Hidalgo RC, Kun F, Herrmann HJ. Fracture model with variable range of interaction. *Phys Rev E*. (2002) 65:046148. doi: 10.1103/PhysRevE.65.046148
22. Harlow DG, Phoenix SL. Approximations for the strength distribution and size effect in an idealized lattice model of material breakdown. *J Mech Phys Solids*. (1991) 39:173. doi: 10.1016/0022-5096(91)90002-6
23. Potyondy D, Cundall P. A bonded-particle model for rock. *Int J Rock Mech and Min Sci*. (2004) 41:1329–64. doi: 10.1016/j.ijrmms.2004.09.011
24. Zhao Z. Application of discrete element approach in fractured rock masses. In: Shojaei A, Shao J, editors. *Porous Rock Fracture Mechanics*. Woodhead Publishing (2017). p. 145–76. doi: 10.1016/B978-0-08-100781-5.00007-5
25. Egholm DL. A new strategy for discrete element numerical models: 1. Theory. *J Geophys Res*. (2007) B5:B05203. doi: 10.1029/2006JB004557
26. Ergenzinger C, Seifried R, Eberhard P. A discrete element model to describe failure of strong rock in uniaxial compression. *Granular Matter*. (2011) 13:341–64. doi: 10.1007/s10035-010-0230-7
27. Kun F, Varga I, Lennartz-Sassinek S, Main IG. Approach to failure in porous granular materials under compression. *Phys Rev E*. (2013) 88:062207. doi: 10.1103/PhysRevE.88.062207
28. Abe S, Boros V, Hancock W, Weatherley D. *ESyS-Particle Tutorial and User's Guide. Version 2.3.1*. (2014). Available online at: https://launchpadnet/esys-particle
29. Weatherley D, Boros V, Hancock WR, Abe S. Scaling benchmark of EsyS-Particle for elastic wave propagation simulations. In: *2010 IEEE Sixth International Conference on e-Science*, Brisbane (2010). p. 277–83. doi: 10.1109/eScience.2010.40
30. Debski W, Klejment P. Earthquake physics beyond the linear fracture mechanics: a discrete approach. *Phil Trans R Soc A*. (2021) 379:20200132. doi: 10.1098/rsta.2020.0132
31. Tarantola A. *Inverse Problem Theory and Methods for Model Parameter Estimation*. Philadelphia, PA: SIAM (2005). doi: 10.1137/1.9780898717921
32. Debski W. Probabilistic inverse theory. *Adv Geophys*. (2010) 52:1–102. doi: 10.1016/S0065-2687(10)52001-6
33. Jeffreys H. *Theory of Probability*. Oxford: Clarendon Press (1983).
34. Gottlieb D, Lustman L, Tadmor E. Stability analysis of spectral methods for hyperbolic initial-boundary value problems. *J Numer Anal*. (1987) 24:241–58. doi: 10.1137/0724020
35. Rojek J, Zubelewicz A, Madan N, Nosewicz S. The discrete element method with deformable particles. *Int J Numer Methods Eng*. (2018) 114:828–60. doi: 10.1002/nme.5767

Conflict of Interest: The authors declare that the research was conducted in the absence of any commercial or financial relationships that could be construed as a potential conflict of interest.

frontiers in Physics

ORIGINAL RESEARCH
published: 03 November 2021
doi: 10.3389/fphy.2021.752086

From Nucleation to Percolation: The Effect of System Size when Disorder and Stress Localization Compete

*Subhadeep Roy**

PoreLab, Department of Physics, Norwegian University of Science and Technology, Trondheim, Norway

A phase diagram for a one-dimensional fiber bundle model is constructed with a continuous variation in two parameters guiding the dynamics of the model: strength of disorder and range of stress relaxation. When the range of stress relaxation is very low, the stress concentration plays a prominent role and the failure process is nucleating where a single crack propagates from a particular nucleus with a very high spatial correlation unless the disorder strength is high. On the other hand, a high range of stress relaxation represents the mean-field limit of the model where the failure events are random in space. At an intermediate disorder strength and stress release range, when these two parameters compete, the failure process shows avalanches and precursor activities. As the size of the bundle is increased, it favors a nucleating failure. In the thermodynamic limit, we only observe a nucleating failure unless either the disorder strength is extremely high or the stress release range is high enough so that the model is in the mean-field limit. A complex phase diagram on the plane of disorder strength, stress release range, and system size is presented showing different failure modes - 1) nucleation 2) avalanche, and 3) percolation, depending on the spatial correlation observed during the failure process.

Keywords: disordered systems, fiber bundle model, stress release range, nucleation and growth, percolation, spatial correlation

OPEN ACCESS

Edited by:
Ferenc Kun,
University of Debrecen, Hungary

Reviewed by:
Bikas K. Chakrabarti,
Saha Institute of Nuclear Physics (SINP), India
Purusattam Ray,
Institute of Mathematical Sciences, Chennai, India

***Correspondence:**
Subhadeep Roy
subhadeeproy03@gmail.com

Specialty section:
This article was submitted to Interdisciplinary Physics, a section of the journal Frontiers in Physics

Received: *02 August 2021*
Accepted: *07 October 2021*
Published: *03 November 2021*

Citation:
Roy S (2021) From Nucleation to Percolation: The Effect of System Size when Disorder and Stress Localization Compete. Front. Phys. 9:752086. doi: 10.3389/fphy.2021.752086

1 INTRODUCTION

It is nearly a century since Alan Arnold Griffith developed his energy criterion for the fracture propagation of cracks in near-continuous solids [1, 2]. His celebrated work has revolutionized the world of materials science. Griffith considered a single sharp crack in an otherwise homogeneous elastic medium. In Griffith's theory, the crack propagation is considered as an equilibrium problem where the balance between two energies: reduction of strain energy, and increment in surface energy is measured during the crack propagation. He found that the critical stress σ_c to cause a crack of length l, to extend is $\sigma_c = (2Yg/\pi l)^{1/2}$ [3], where Y is Young's modulus and g is the surface energy per unit area. However, this is an idealized case that requires a pre-existing crack or notch in a homogeneous medium to concentrate the applied stress. In general, the initiation of a fracture in a solid is a much more complex process. Most engineering materials are far from homogeneous, there will always be a distribution of dislocations, flaws, and other heterogeneities present. The nucleation and propagation of a crack in heterogeneous systems are not understood because of the complexities of the stress singularities at the crack tip [4]. As the applied stress is increased, micro-cracks are likely to occur randomly on the heterogeneity and are uncorrelated. As the density of micro-cracks increases, the stress fields of the micro-cracks interact and the micro-cracks become correlated. The micro-cracks eventually may coalesce to form a through-going fracture. This irreversible process is a

part of damage mechanics and is an integral part of the nucleation and propagation of fracture in heterogeneous environments.

During the failure process of a disordered system, a complex interplay is observed between quenched heterogeneities and local stress concentration. The former one leads to non-localized damage mechanics while the latter favors the formation of localized cracks. As a consequence of this interplay, we observe system size dependence of nominal stress distribution [5–7], scale-free avalanche size statistics [8–11], self-affine crack morphology [12], etc. In the limit of infinitesimal disorder strength, the crack grows within a disordered system in a nucleating manner [13–16]. On the other hand, when disorder strength is infinitely high, the effect of local stress concentration becomes irrelevant and the failure process is random in space [17, 18] like percolation. The reason behind the damage mechanics at high disorder is the heterogeneities in a material that create energy barriers which act as a resistance on the way of crack propagation and ultimately arrest the crack motion: a phenomenon known as lattice trapping or intrinsic crack resistance [19–24]. At intermediate disorder, the situation is more interesting, where the failure process takes place through a number of avalanches showing scale-free distributions of energies emitted during the avalanches [9] and mean-field exponents [25–28].

Tuning the strength of disorder is not achievable easily in experiments. Though through heat treatment one can tune the length scale of disorder in phase-separated glasses [29]. Earlier experiments also studied the role of a varying disorder strength during pattern formation in random spring network [30–32], the study of roughness of a fracture surface [33], the transition from nucleation to damage mechanics in random fuse network [34, 35], etc. Linear elastic fracture mechanics, on the other hand, predicts the load distribution around an Inglis crack [36, 37] to be $1/r^2$-type where r is the distance from the crack tip. However, this form for relaxation of local stress can be affected by many parameters like correlation among defects [38] and effect of the limited size of the sample [39]. This in turn can change the dynamics of crack propagation. We will explore here the effect all three important parameters: disorder strength, stress release range and sample size in detail.

In this article, we study the spatial correlation during failure process of a fiber bundle model (FBM) [40, 41]. Fiber bundle model is very effective yet arguably the most simplest model to understand failure process of heterogeneous materials. The effect of a variable stress release range has already been observed in the context of this model [42, 43]. With a very low stress release range, the failure process is observed to be nucleating and at the same time, the failure abruptness is affected by the size of the bundle [42, 44]. The spatial correlation, in this limit, decreases as the disorder strength is increased [45]. On the other hand, at a very high stress release range (the mean-field limit), the failure abruptness is not a function of system size and only controlled by the strength of disorder [46]. A high thermal fluctuation as well leads to a failure process, random in space, with the same universality class of a site percolation [47]. When we combine both the effects of stress release range and disorder strength, the model produces rich relaxation dynamics with different modes of failure – abrupt, non abrupt, nucleating, and random in space [48]. The avalanche statistics as well as the effect of system sizes has also been discussed recently in the context of fiber bundle model [49, 50]. Moreover, the record statistics in the avalanche statistics and study of elastic energy has been observed to be a vital key to predicting an upcoming failure [51]. The occurrence of different regimes with increasing disorder strength is also observed in spin systems as well. Recent work in the random field Ising model shows many small avalanches at high disorder and depinning behavior when disorder strength is very weak. At an intermediate critical value of disorder strength, avalanches of all possible sizes are observed [52, 53]. A study similar to the present one is explored in the context of random fuse network [34, 35]. In the former study, the avalanche size distribution as well as the system size scaling of average avalanche size and average crack size. In the latter study, the authors have studied the masses of the largest cluster, the mass of the backbone (the number of burnt bonds forming the chain that effectively disconnects the bottom from the top of the system), and how those masses scale with the system size in order to compare them with percolation. Here we carry out a study, similar to what was observed in the resistor network for a variable stress release range and construct a phase diagram on the plane of disorder, stress release range and system size. We have mainly studied the behavior of crack density to observe the spatial correlation. The crack density is explored earlier by the same author [42, 48] but a systematic study with system size, especially a systematic study of maximum crack density with the size of the bundle was missing there. Such a study is carried out in the present article and can offer a nice insight into the fracture pattern.

2 DESCRIPTION OF FIBER BUNDLE MODEL

After its introduction by Pierce in 1926 [54], the fiber bundle model [40] has been proven to be very effective in understanding the failure event of a disordered system. Due to this, fiber bundle model is growing popularity among engineering, material science as well as academics. This model is very effective yet arguably the most simple model guided by threshold activated dynamics.

A conventional fiber bundle model consists of L parallel Hookean fibers in between two plates which are pulled apart creating a stress σ on each fiber. The fluctuation among the strength values of individual fibers is the measure of disorder within the model. In the present work, we chose such strength values (h) from a power law distribution with a slope −1 and span from $10^{-\beta}$ to 10^{β}.

$$p(h) \sim \begin{cases} h^{-1}, & \left(10^{-\beta} \le h \le 10^{\beta}\right) \\ 0. & (\text{otherwise}) \end{cases} \tag{1}$$

Here β is related to the span of the distribution and a measure of disorder strength. We have chosen such a distribution as such long-tailed power-law distribution [55] has already been observed for the distribution of material strength. A certain fiber breaks irreversibly when the stress applied on it exceeds its strength. The stress of that fiber is then redistributed among rest of the model.

Here, we have adopted a generalized rule for stress redistribution. If σ_i is the stress on the broken fiber i, then the stress redistribution on fiber j at a distance r_{ij} from fiber i will be as follows

$$\sigma_j \rightarrow \sigma_j + \frac{r_{ij}^{-\gamma}}{Z}\sigma_i \tag{2}$$

Where σ_j is the stress on fiber j and Z is the normalization factor given by

$$Z = \sum_{i,k} r_{ik}^{-\gamma} \tag{3}$$

Where k runs overall intact fibers. Two extreme limits of this redistribution rule are global load sharing (GLS) [54] and local load sharing (LLS) [4, 56] limit. γ has a very low value for the former case and stress of the broken fiber here is redistributed among all surviving fibers in almost same amount. This is also the mean-field limit of the model. In the other extreme limit, γ has a very high value and a large amount of the redistributed stress is carried by the neighboring fibers of the broken one only. The effect of stress concentration is most prominent here. Earlier studies show a critical value γ_c of the stress release range, for both 1d [42] and 2d [43], around which the model transit from the mean-field limit to the local load sharing limit. After such redistribution, due to the elevated local stress profile, further fibers may also break starting an avalanche. With such a process, the bundle may break through a single avalanche or comes to a steady state with some fibers broken and some intact. In the latter situation, the external stress is increased to break the next weakest fiber starting a new avalanche. Such process goes on until all fibers are broken.

3 NUMERICAL RESULTS

A one dimensional fiber bundle model is studied numerically with varying disorder strength (β), stress release range (γ), and system sizes (L). In *Local Load Sharing Fiber Bundle Model: Variation in* β, we explore the local load sharing limit of the model which can be achieved by setting a very high γ. On the other hand, *Generalized Model: Variation in Both* β *and* γ, deals with a generalized version of the model where the stress of a broken fiber is redistributed depending on the exponent γ keeping β constant. β is varied between 0.4 and 2.0 while γ varies from 0 to 3. The size of the bundle varies from 10^3 to 10^5.10^4 realizations (bundle replications) are considered for our numerical simulation. *Universality* shows numerical results for uniform and Weibull threshold distribution, discussing the universal behavior of our result. Finally, in *Discussions* we have provided the concluding remarks on the present article.

3.1 Local Load Sharing Fiber Bundle Model: Variation in β

In this section, we have studied the fiber bundle model in the local load sharing limit. In this limit, the stress of a broken fiber is redistributed among the nearest neighbors only. This scenario can be achieved by setting a very high value of γ.

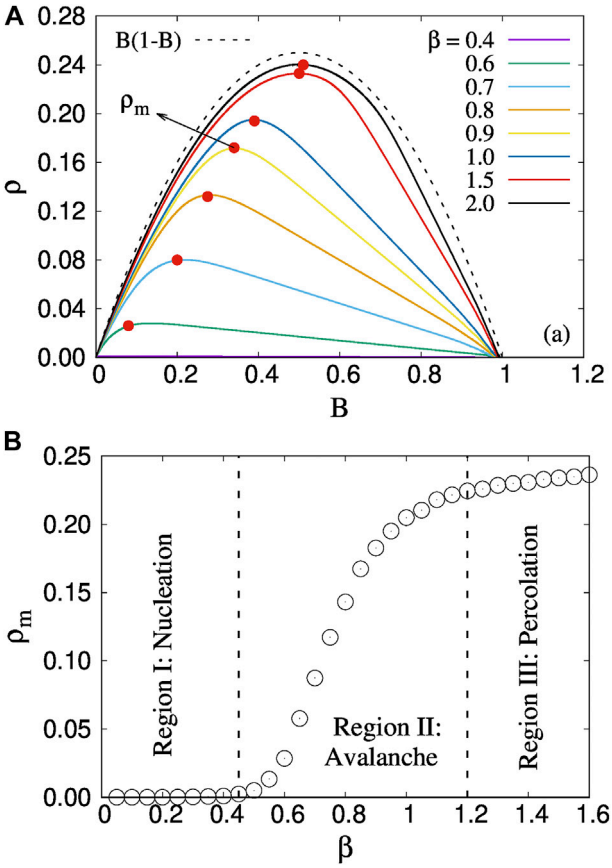

FIGURE 1 | (A) Variation of patch density ρ with fraction broken B for β values ranging from 0.4 to 2.0. The red dots denotes ρ_m, the maximum possible patch density. The dotted line is the locus of $B(1-B)$ and represents random failure events for a 1d bundle. **(B)** Variation of ρ_m as the disorder strength β is varied continuously. We see three different regions (1) ρ_m is 1/L here suggesting a single crack propagates through the bundle in a nucleating manner (2) Here number of cracks originates and the number increases with β (3) The failure process here random in space. ρ_m has a value close to 0.25 here. The system size is kept constant at 10^5.

We start our numerical simulation by observing the characteristics of the patches (or cracks) that are generated within the bundle during the evolution of the model. A certain patch is defined by the combination of an intact fiber and a broken fiber in its neighborhood. If we denote the intact fiber by 1 and broken fiber by 0, then any (1,0) or (0,1) combination on the one-dimensional chain of fibers will be characterized as a patch or crack. The patch density ρ at time t is defined by the number of patches at that time, normalized by the size L of the system. We also note the fraction B of broken fibers at time t. B is defined as the number of broken fibers divided by size L of the system. *Time*, in this case, is represented as the sum of stress increment and redistribution steps (see Ref. 1 for details). **Figure 1** shows the

[1]At a certain point during the evolution of the model, if it goes through m stress increment with $n_1, n_2, \ldots, n_m$ redistribution steps for $1st, 2nd, \ldots, mth$ stress increment, then the time corresponding to this scenario will be:$m + \sum_m n_m$.

variation of ρ with B for different disorder strength values ranging in between 0.4 and 2.0 for a bundle of size $L = 10^5$.

Figure 1A shows a non-monotonic behavior of ρ when B increases from 0 to 1. Earlier papers [42, 48] have already discussed that such crack density shows a non-monotonic behavior as the model evolves. $B = 0$ stands for the initial configuration where all fibers are intact while we obtain $B = 1$ when all fibers are broken. The patch density ρ is zero for $B = 0$ as no cracks are there in the bundle. On the other hand, when the model is close to the failure point, there will be a single patch, making $\rho = 1/L$ when B approaches 1. At an intermediate B, ρ reaches a maximum value ρ_m. Before this maxima, ρ is an increasing function of B as new patches are generated within the bundle. After the maxima, the patches start to coalesce with each other and we observe a lesser and lesser number of cracks with increasing time (hence increasing B). **Figure 1A** shows as disorder strength is increased, ρ_m shifts to a higher value. We will discuss the variation of ρ_m with disorder next. The dotted line in the same figure is the locus of $\rho = B(1 - B)$. This dotted line represents failure events random in space for a 1d FBM. This can be understood as follows. If B is the fraction of fibers broken, then the probability of having a broken and an intact fiber will be B and $(1 - B)$ respectively. A patch then will be created by placing an intact fiber beside a broken one, the probability of which will be $B(1 - B)$ on a 1d lattice. By equating $d\rho/dB$ for this locus to zero we get the maximum $\rho_m = 0.25$ and the B value to be 0.5 at this maxima. The failure pattern becomes more and more random when β, the disorder strength, is high enough. On the other hand, when the disorder strength is very low ($\beta = 0.4$), we see $\rho = 1/L$ independent of the value of B. This suggests a pure nucleating failure starting from the very beginning until the global failure.

Figure 1B shows the variation of ρ_m explicitly when β is continuously varied. We observe three different regions.

1) Nucleation ($\beta \leq 0.4$) – Here ρ_m has a value close to $1/L$. This suggests that only a single crack is generated within the bundle in this limit and this crack nucleates to create global failure. Due to the low strength of the disorder, the failure process here is guided by the local stress concentration at the crack tips.
2) Percolation ($\beta \geq 1.2$) – In this limit the behavior of B vs ρ matches closely with $\rho = B(1 - B)$. ρ_m has a value close to 0.25. The failure events are random in space here making it reminiscent of percolation in 1d lattice. The failure process is completely guided by the disorder strength and the local stress concentration is almost non-existing.
3) Avalanche ($0.4 < \beta < 1.2$) – in the intermediate disorder strength, there is an interplay between the disorder strength and the local stress concentration. The failure process here starts in a percolating manner but later the local stress concentration takes over making the rest of the failure events nucleating. We will be discussing this spatial correlation in more detail later in this paper.

Figure 2A shows how the maximum patch density ρ_m responds to the size of the bundle. The results are repeated for three different β values 0.3, 0.7, and 1.2, in order to cover all three regions – nucleation, avalanche, and percolation,

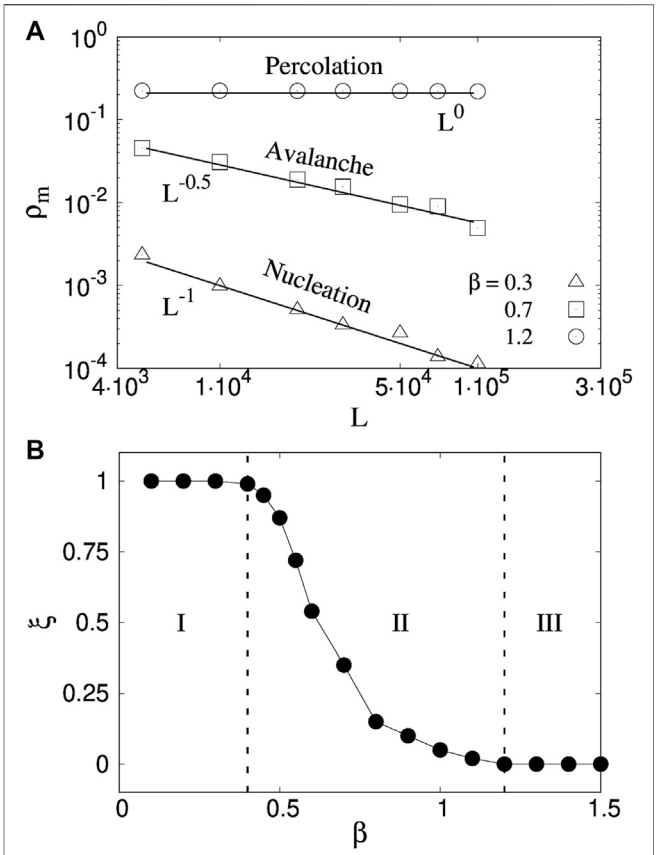

FIGURE 2 | (A) Effect of system size L on ρ_m for $\beta = 0.3$, 0.7 and 1.2. L is varied in between 5×10^3 and 10^5. Three regions are observed here (1) Nucleation: $\rho_m \sim L^{-1}$ (2) Avalanche: $\rho_m \sim L^{-\xi(\beta)}$ (3) Percolation: $\rho_m \sim L^0$. **(B)** Variation of ξ with β. $\xi = 1$ and 0 in the region 1 and 3 respectively. In the intermediate region II, ξ decreases continuously with β.

mentioned above. When disorder strength β is low (0.3), ρ_m decreases with L in a scale-free manner with exponent −1. This suggests that the maximum number of cracks observed in the bundle decreases with increasing size and the model goes towards nucleation more and more as the model approaches the thermodynamic limit. On the other hand, for $\beta = 1.2$, ρ_m is independent of L and saturates at a value close to 0.25. As mentioned above, the failure process is percolating here and remains the same irrespective of the size of the bundle. In the intermediate disorder, where the disorder strength and local stress concentration compete with each other, we observe

$$\rho_m \sim L^{-\xi(\beta)} \tag{4}$$

Where the exponent ξ is a function of β.

Figure 2B shows the variation of exponent ξ with the strength of disorder β. ξ remains at 1 for low β where the failure is nucleating, gradually decreases in region avalanche, and becomes constant at 0 in the limit of percolation. The nature of patch density remains the same in the percolation region ($\xi = 0$) only. In both avalanche and nucleation, fewer patches grow as the size of

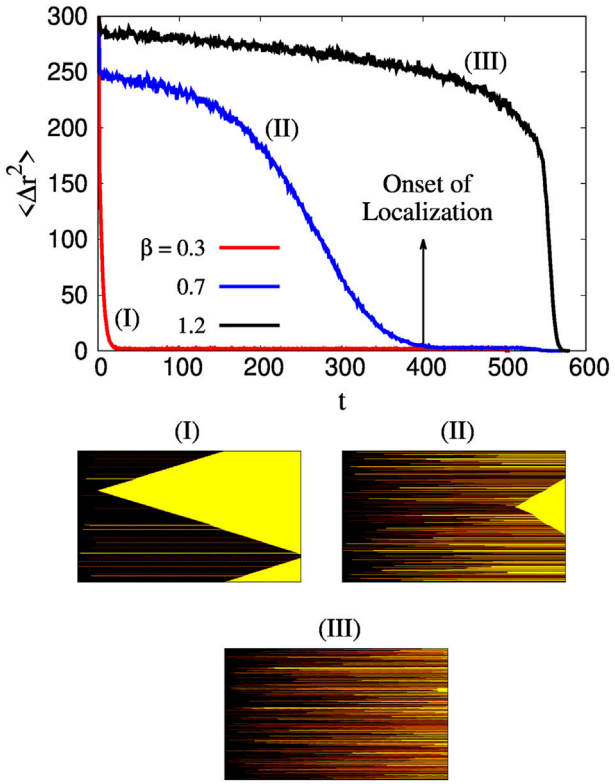

FIGURE 3 | Variation of $\langle \Delta r^2 \rangle$ with time t for three different disorder strengths β = 0.3, 0.7 and 1.2. $\langle \Delta r^2 \rangle$ is average square distance between consecutive rupture events. $\langle \Delta r^2 \rangle$ starts from a high value and decreases to 1 with time suggesting pure nucleation beyond this point. The spatial correlation is shown explicitly for three different cases (1) nucleation (2) avalanche and (3) percolation.

the bundle is increased, suggesting that the effect of the local stress concentration becomes more prominent here as the model goes towards the thermodynamic limit.

Here, we will discuss a dynamic parameter that helps us to understand the onset of the nucleation process with time more clearly. As explained earlier, time t here is analogous to the total number of redistribution plus stress increment steps prior to the global failure. We start by breaking the weakest fiber, say i, at time $t = 0$ by the first stress increment. Let us assume further n_1 fibers break at the next time step ($t = 1$) upon redistributing the stress carried by the weakest fiber. We consider the distance Δr between these two consecutive events to be the minimum of distances between fiber i and other n_1 fibers that break after redistribution. Here, Δr is not the exact lattice distance as only intact fibers are considered while calculating it. The distance across a broken patch is considered to be one independent of the size of the patch. This is due to the LLS scheme that we have adopted. Whenever a fiber at a notch breaks and the redistributed stress breaks the fiber at the other notch, the failure is still nucleating, no matter how large this patch is. Next, we square this distance and average it over 10^4 realizations to get $\langle \Delta r^2 \rangle$ at time $t = 0$. Next, we move our reference frame to the fiber among those n_1 fibers that had the minimum distance from fiber i. Let's denote this new fiber as j. If further n_2 fibers break in the next redistribution, $\langle \Delta r^2 \rangle$ at $t = 1$ will be calculated by the same procedure: find Δr from the minimum of distances between fiber j and those n_2 fibers, square it and average over 10^4 realizations. Such a parameter was explored earlier by Stormo et. al [57] in the context of the soft clamp model to point out the onset of localization. **Figure 3** shows this variation of $\langle \Delta r^2 \rangle$ with time t for β = 0.3, 0.7 and 1.2. For all three disorder strength values, $\langle \Delta r^2 \rangle$ starts from a high value at low t and then decreases towards 1 when t is high. A high value of $\langle \Delta r^2 \rangle$ suggests the fibers that break consecutively are far from each other. This is a spatially uncorrelated failure. On the other hand, when $\langle \Delta r^2 \rangle = 1$, the consecutive failures take place from the neighboring fibers only. This behavior stands for pure nucleation. For β = 0.3, $\langle \Delta r^2 \rangle$ becomes 1 very fast and stays there independent of t until the bundle reaches global failure. For β = 1.2, we observe the opposite behavior where $\langle \Delta r^2 \rangle$ stays at a high value for a long time and falls to 1 just before global failure. The former behavior is nucleating (1) while the latter one is percolating (3). The visualization of the failure process for both (1) and (3) is shown below **Figure 3**. The x-axis of each plot is time and the y-axis is fiber index. The color gradient is over the local stress profile. The yellow color stands for the failed fibers. For (1), we see a single crack growing in a nucleating manner from the very beginning. For (3), on the other hand, there are no nucleating yellow-colored fibers and the rupture events are spatially uncorrelated. For the avalanche (2) behavior, there is a spatially uncorrelated failure in the beginning as well as nucleation close to global failure. **Figure 3** shows the point for β = 0.7 where $\langle \Delta r^2 \rangle$ becomes 1 indicating onset of localized (nucleating) failure events.

Finally, we have constructed the phase diagram of disorder strength β and system size L to show all three failure processes. In **Figure 4**, $1/\beta$ is plotted against $1/L$. This is done in this way so that the origin (0,0) of this plot corresponds to $L \to \infty$ and $\beta \to \infty$, an infinite disorder in the thermodynamic limit. As discussed earlier, if the disorder strength is increased, we start with nucleation, go through an avalanche, and finally reach

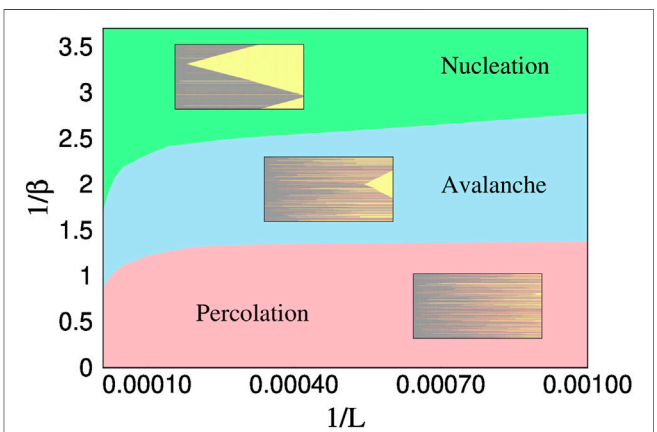

FIGURE 4 | Phase diagram of disorder strength β and system size L. $1/\beta$ is plotted against $1/L$ to make the coordinate (0,0) represent infinite disorder at thermodynamic limit. Three regions – nucleation, avalanche and percolation are observed. The spatial correlation during fiber rupture is shown with yellow being the broken patch.

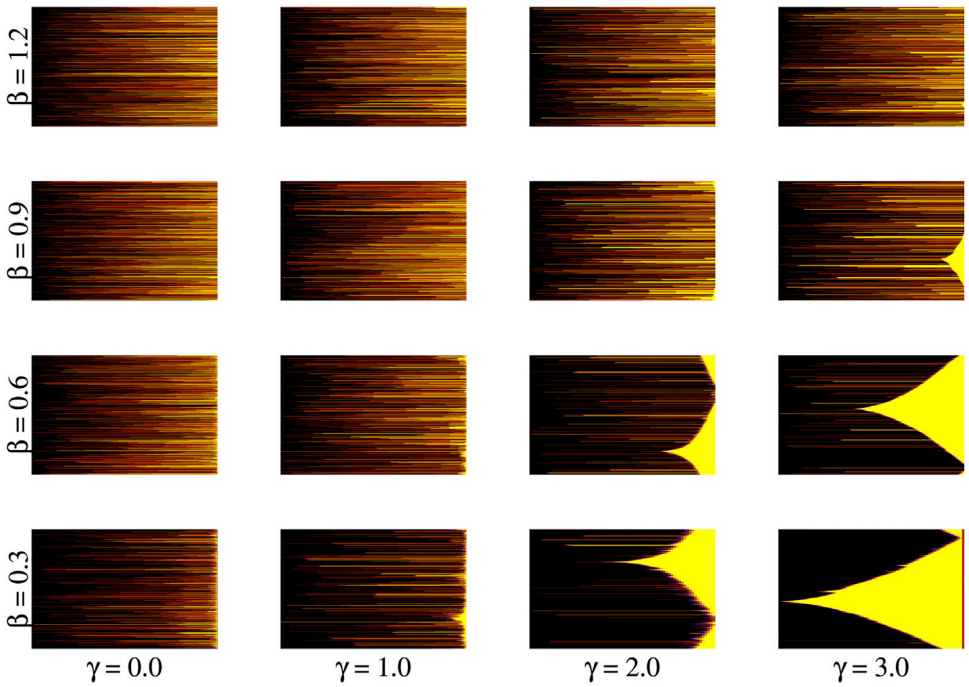

FIGURE 5 | The figure shows spatial correlation during a failure process when β varies between 0.3 and 1.2 and γ varies between 0 and 3. Nucleating failure is observed for high γ and low β. The spatial correlation reduces as γ is decreases (pushes the model towards MF limit) or β is increased.

percolation behavior. The spatial correlation in rupturing events are shown in the corresponding phases. Now, if the disorder strength is kept constant and the size of the bundle is increased, a percolating behavior moves towards avalanche and an avalanche behavior moves towards nucleation. Due to weak dependence of parameters like ρ_m on L (see **Figure 2**), it will not be possible to see (as the system size has to be very high) this change from percolation to avalanche if we are well inside the percolation region. To see this change at relatively lower system sizes, it is required to keep the disorder strength at a value so that the model is closer to the percolation-avalanche interface. The opposite happens if the system size is decreased instead of increasing. This suggests we observe only nucleating failure in the thermodynamic limit unless the disorder is infinitely high. This effect of disorder was explored earlier in the context of random fuse network by Shekhawat et al. [34] and Moreira et al. [35]. We observe that the fiber bundle model in one dimension follows the same trend.

3.2 Generalized Model: Variation in Both β and γ

In this section, the model is studied with a continuous variation in both γ when β. We start our numerical simulation by observing the spatial correlation through the rupture events with increasing time as the bundle fails.

Figure 5 shows such correlation for β values ranging in between 0.3 and 1.2 and γ values within 0 and 3. For each small figure, the x-axis shows the time t and the y-axis shows the fiber index. From left to right, the figures are plotted for increasing values of γ keeping the disorder strength β constant. On the other hand, from bottom to the top, the figures are plotted with increasing β and keeping γ constant. We observe the following behavior:

For *low* β and *high* γ, the fibers break in a nucleating manner. Due to the low stress release range, the stress concentration plays a crucial role and dominates the failure process. Moreover, due to the low value of disorder strength, the probability that the fibers break with redistribution (without any increment in external stress) from the neighborhood is high. On the other hand, for *high* β and *low* γ, the fluctuation between threshold strength as well as the stress release range is high. As a result, we observe rupture events random in space and through increment in external stress.

Now, keeping the β fixed at a low value, as we decrease γ, the model slowly goes towards the mean-field limit. In this limit, the stress of the broken fibers are redistributed among all surviving fibers. This increases the chance that whenever one fiber breaks, the next rupture event may take place from somewhere which is not the neighborhood of the broken fiber. The failure process, in this case gradually deviates from the nucleating behavior as γ decreases.

Instead, if we keep γ fixed at a high value and increase β, the fluctuation among fiber strengths increases. Here, the stress of the broken fiber is redistributed in the neighborhood (as γ is high) but due to this increase in fluctuation we will find more strong fibers in this neighborhood that will finally arrest the growth of a crack - a phenomena known as lattice trapping or intrinsic crack resistance [19–24]. This forces the growth of a different crack from a different place.

As discussed in **Figure 5**, a single crack or a number of cracks are observed in the bundle depending on what the values of

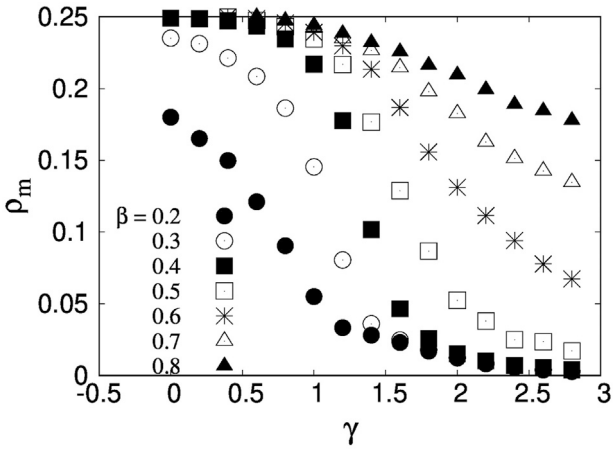

FIGURE 6 | Variation of maximum number of cracks (ρ_m) with γ for β values ranging in between 0.2 and 0.8. ρ_m has a high value for low γ and gradually decreases with γ and tends to saturate towards a low value. For low β, ρ_m decreases close to $1/L$ for high γ, suggesting propagation of a single crack. On the other hand, for low γ and high β, $\rho_m \approx 0.25$, suggesting a failure process which is random in space.

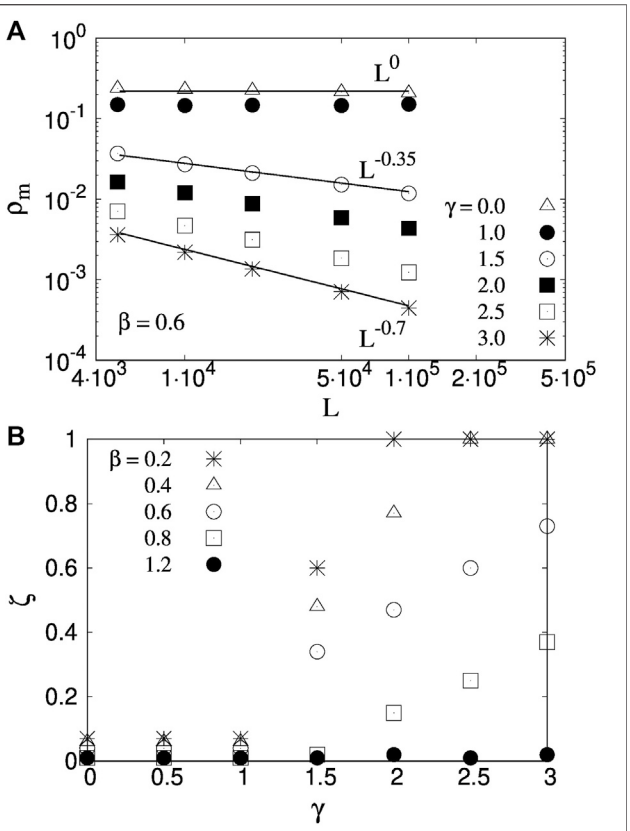

FIGURE 7 | (A) System size effect of ρ_m for $\beta = 0.6$ and γ between 0 and 3. We observe $\rho_m \sim L^{-\zeta}$, where ζ is an increasing function of γ. **(B)** Variation of ζ with γ for $0.2 \leq \beta \leq 1.2$. For low γ, $\zeta \approx 0$ independent of β. For high γ, on the other hand, $\zeta = 1$ depending on whether β is low enough or not.

disorder strength β and the stress release range γ are. In **Figure 6**, we have studied how the maximum number of cracks (ρ_m) varies as we vary both β and γ. At first, we observe the variation of ρ_m with γ for a constant value of β. The study is then repeated for β values ranging in between 0.2 and 0.8.

For low γ, ρ_m has a higher value and decreases as γ increases and crosses the critical value γ_c [42]. The results can be discussed in three parts. At an intermediate disorder ($0.3 \leq \beta \leq 0.5$), ρ_m saturates close to 0.25 for low γ and decreases to $1/L$ when γ is high. A ρ_m value close to $1/L$ suggests there is only one crack that propagates throughout the system. On the other hand, as already discussed in the manuscript, ρ_m close to 0.25 suggests a failure process random in space. In this limit, all three regions are accessible with a variation in γ.

At low β (<0.3), we observe that ρ_m goes to $1/L$ for high γ but does not approach 0.25 even if γ is very low. In this limit, we do not see a percolation like a random failure. This is due to very low disorder strength, where the bundle breaks very abruptly before it can reach the real maximum value of ρ_m (≈0.25) at low γ. On the other hand, for high β (>0.5), ρ_m reaches 0.25 easily at low γ but do not reach $1/L$ for high γ. In this case, ρ_m does not reach $1/L$ even at high γ due to the intrinsic crack resistance caused by the high fluctuation in threshold strength, which arrests an propagating crack in the process. As a result, a nucleating failure is not observed here.

Figure 7A shows the system size effect of ρ_m for $\beta = 0.6$ and for wide range of stress relaxation γ ($0 \leq \gamma \leq 3$). We observe ρ_m to decrease in a scale-free manner with system size L,

$$\rho_m \sim L^{-\zeta} \tag{5}$$

Where ζ is an increasing function of γ. At low γ, ρ_m is almost independent of L and saturates around 0.25. When γ is high, ρ_m responds to the change in L very sharply and decreases as L increases.

The variation of the exponent ζ is shown in **Figure 7B** ζ has a value close to 0 independent of disorder strength β when γ low. At such a low value of γ, the model is in the mean field limit and changing the system size does not change the dynamics of the model. As γ increases, the model slowly deviates from the mean-field limit and the effect of local stress concentration becomes more and more prominent. In this limit, ζ starts to increase slowly. When γ crosses a certain value that depends on β, ζ finally reaches 1. A Higher value of β will require a higher γ value in order to obtain $\zeta = 1$. Finally, when β is very high, ζ remains close to 0 independent of the stress release range γ. Here, the failure process is random in space, independent of both β and γ.

Figure 8 shows above mentioned three regions from the study of the maximum number of cracks (ρ_m) when both disorder strength β and the stress release range γ are varied simultaneously. The color gradient in **Figure 8** is on ρ_m, with a maximum value of 0.25 (lightest color) and minimum value of $1/L$ (darkest color) which is 10^{-5} as the size of our bundle is 10^5. We observe ρ_m to have the lowest value for lowest possible β and highest possible γ.

This is due to the fact that fluctuation among local strength values are minimum here and at the same time stress release range is also minimum making the local stress concentration most prominent. At

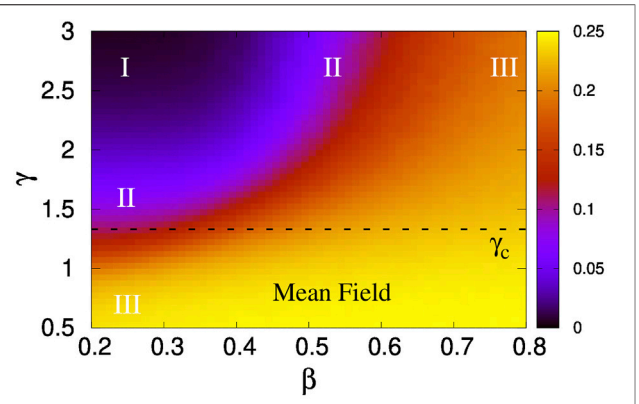

FIGURE 8 | Histogram of ρ_m on the plane of γ vs β. The brightest color corresponds to $\rho_m \approx 0.25$ while the darkest color stands for $\rho_m \approx 1/L$. At low β, as γ increases, we go from region 3 (percolation) to 2 (avalanche) to 1 (nucleation). Same transition is observed when β decreases at high γ.

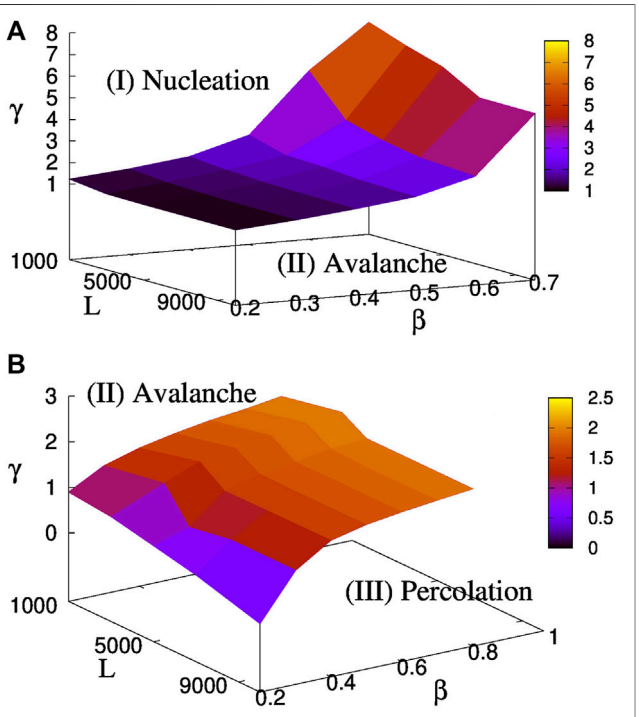

FIGURE 9 | (A) and **(B)** respectively shows the plane of transition from avalanche to nucleation and percolation to avalanche respectively. The three parameters constructing the plane are: disorder strength (β), stress release range (γ) and system size (L).

this situation, as we decrease γ, we go towards percolation (light color) through avalanche region. The same behavior is observed ($1 \rightarrow 2 \rightarrow 3$) if we increase β keeping γ fix. The figure also shows the existence of γ_c [42, 43], the value of γ below which the model enters the mean-field limit. For $\gamma < \gamma_c$, we have almost an uniform gradient of light color suggesting ρ_m is close to 0.25 here independent of β. We observe a very small change in the color gradient if we increase γ at a high β.

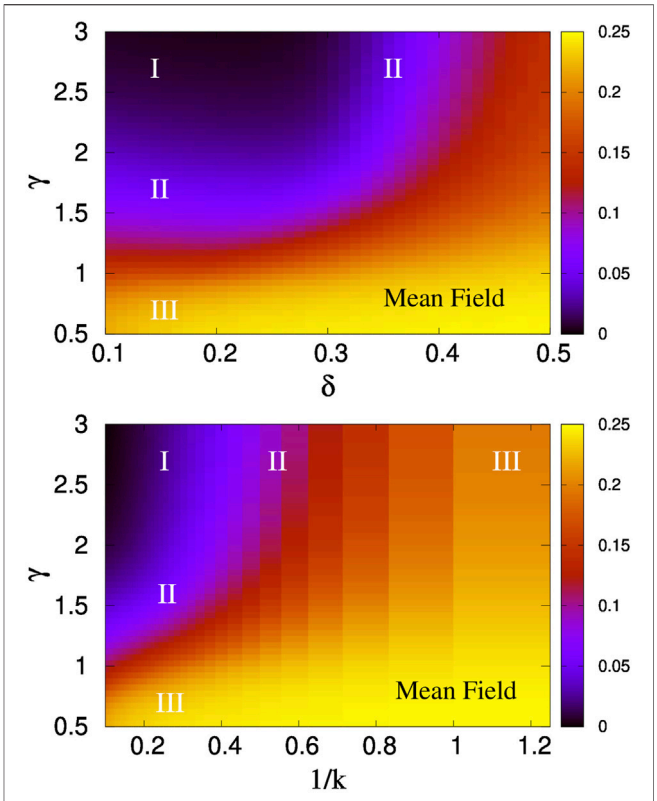

FIGURE 10 | Variation of ρ_m for uniform (upper) and Weibull (lower) distribution when both the disorder strength (δ or k) and stress release range (γ) is varied continuously. Three distinct regions (1) nucleation (2) avalanche and (3) percolation, is observed independent of the choice of threshold distribution.

Figure 9 shows different regions – nucleation, avalanche and percolation, with their unique nature of crack propagation during the failure process when the disorder strength (β), stress release range (γ), and system size (L) are continuously varied. **Figure 9A** shows the plane separating the region nucleation from avalanche. The plane seems to diverge for high β. This is due to the fact that, at high beta the fluctuation among fiber strength values will be high and the γ value will also have to be very high to make the local stress concentration prominent enough to create nucleation. At the same time, since an increasing L has already been seen to favor nucleating failure, we achieve such nucleation at relatively lower γ value at higher L when β is kept fixed. **Figure 9B**, on the other hand, shows the plane between avalanche and percolation. We observe the same effect of L here – as L increases, the transition from percolation to avalanche takes place at a lower value of γ. At the same time, as β increases, we have to go to a higher γ value to enter the avalanche region from percolation. The sudden upward curvature of *nucleation – avalanche* plane at high β suggests that if the disorder strength is extremely high, we might not get a nucleation region. Similarly, the sudden downward curvature of *avalanche – percolation* plane at low β suggests that if the disorder strength is extremely low, we might not get a percolation region.

4 UNIVERSALITY

In this section we will discuss the universality of our study by using two different distributions other than the power law. For this purpose, we have adopted an uniform and a Weibull distribution as described below:

$$p(h) \sim \begin{cases} \frac{1}{2\delta}, & (0.5-\delta \le h \le 0.5+\delta) \\ 0. & (\text{otherwise}) \end{cases} \tag{6}$$

Where δ is the half-width of the distribution as well as the measure of the disorder strength.

$$p(h) \sim \left(\frac{k}{\lambda}\right)\left(\frac{h}{\lambda}\right)^{k-1} e^{-\left(\frac{h}{\lambda}\right)^k} \tag{7}$$

Where k and λ are the Weibull modulus and scale parameter respectively. k controls the disorder strength in this case. We vary δ from 0 to 0.5 while k is varied between 1 and 10. The scale parameter λ is kept constant at 1. Similar to the power law distribution, the uniform distribution is also a bounded distribution while the Weibull distribution is open.

Figure 10 shows the variation of ρ_m when both disorder strength and stress release range is tuned continuously. The results for uniform distribution are shown in the left figure. The right figure shows the same for the Weibull distribution. Similar to **Figure 8**, the color gradient represents the variation in ρ_m that spans from $1/L$ to 0.25. The results suggest that all three regions (1) nucleation (2) avalanche, and (3) percolation, are observed independent of the choice of the threshold distribution. As γ increases, the model goes from the nucleating failure to a failure process random in space. On the other hand, a spatially correlated failure process is not observed by increasing δ up to 0.5 (the distribution spans from 0 to 1) as the disorder strength is not large enough. Though for Weibull distribution, both nucleating and random failure is observed at high and low k respectively.

5 DISCUSSIONS

As we have already discussed, two major factors governing the mode of failure in disordered solids are the strength of heterogeneities and the effective range over which the stress field is modified following a local rupture event. On the other hand, studies in random resistor network model [34, 35] claims the failure mode, in the large system size limit, to be always nucleation-driven unless the strength of disorder is extremely high. Qualitatively this is the main finding of the present paper as well as what was observed in the random fuse network model earlier [34, 35]. The simplicity of the fiber bundle model allows us to include extra parameters like stress release range compared to the random fuse network model and study its effect as well on the spatial correlation as the model evolves. The precursor events (such as scale-free size distribution of rupture events prior to global failure and scale free distribution of emitted energies during such avalanches), previously seen in the statistical models [7, 58], would imply that a nucleation-like failure would not be achievable even in the large system size limit. Such precursor events are observed experimentally [59] as well for which the extreme disorder is not necessarily the physical condition. The stress release range (analogous to fracture process zone in real experiments) comes into play here that might cause a different mode of failure, other than nucleation, even when the system size is high.

In conclusion, we present a detailed study in fiber bundle model by varying main three parameters, strength of disorder, range of stress relaxation and system size, that determines the dynamics of the model as it is acted by an external stress. An increasing disorder strength (increasing β) or stress release range (decreasing γ) favors a failure that is random in space. On the other hand, an increasing system size makes the failure more and more nucleating. The avalanche behavior is observed for all β or γ. If β is very high then it is difficult to achieve the nucleating behavior unless the value of γ is very high. On the other hand, when β is low, achieving nucleating failure is easy but it is difficult to observe pure random failure by decreasing γ. Finally, for the intermediate β value, we achieve both nucleation and percolation like failure by increasing and decreasing γ respectively.

DATA AVAILABILITY STATEMENT

The raw data supporting the conclusions of this article will be made available by the authors, without undue reservation.

AUTHOR CONTRIBUTIONS

The author confirms being the sole contributor of this work and has approved it for publication.

FUNDING

The work was supported by the Research Council of Norway through its Centres of Excellence funding scheme, project number 262644.

REFERENCES

1. Dieter GE. *Mechanical Metallurgy*. McGraw Hill Education (1989).
2. Lawn B. *Fracture of Brittle Solids*. Cambridge: Cambridge Solid State Science Series (1993).
3. Knott JF. *Fundamentals of Fracture Mechanics*. New York: Butterworths (1973).
4. Phoenix SL. The Asymptotic Distribution for the Time to Failure of a Fiber Bundle. *Adv Appl Probab* (1979) 11:153–87. doi:10.1017/s0001867800031748
5. Harlow DG, and Phoenix SL. The Chain-Of-Bundles Probability Model for the Strength of Fibrous Materials I: Analysis and Conjectures. *J Compos Mater* (1978) 12:195–214. doi:10.1177/002199837801200207
6. Bazant ZP. Scaling Theory for Quasibrittle Structural Failure. *Proc Natl Acad Sci* (2004) 101:13400–7. doi:10.1073/pnas.0404096101
7. Alava MJ, Nukala PKVV, and Zapperi S. Statistical Models of Fracture. *Adv Phys* (2006) 55:349–476. doi:10.1080/00018730300741518
8. Hemmer PC, and Hansen A. The Distribution of Simultaneous Fiber Failures in Fiber Bundles. *J Appl Mech* (1992) 59:909–14. doi:10.1115/1.2894060

9. Petri A, Paparo G, Vespignani A, Alippi A, and Costantini M. Experimental Evidence for Critical Dynamics in Microfracturing Processes. *Phys Rev Lett* (1994) 73:3423–6. doi:10.1103/physrevlett.73.3423
10. Garcimartín A, Guarino A, Bellon L, and Ciliberto S. Statistical Properties of Fracture Precursors. *Phys Rev Lett* (1997) 79:3202–5. doi:10.1103/physrevlett.79.3202
11. Salminen LI, Tolvanen AI, and Alava MJ. Acoustic Emission from Paper Fracture. *Phys Rev Lett* (2002) 89:185503. doi:10.1103/physrevlett.89.185503
12. Bonamy D, and Bouchaud E. Failure of Heterogeneous Materials: A Dynamic Phase Transition? *Phys Rep* (2011) 498:1–44. doi:10.1016/j.physrep.2010.07.006
13. Duxbury PM, Beale PD, and Leath PL. Size Effects of Electrical Breakdown in Quenched Random Media. *Phys Rev Lett* (1986) 57:1052–5. doi:10.1103/physrevlett.57.1052
14. Duxbury PM, Leath PL, and Beale PD. Breakdown Properties of Quenched Random Systems: The Random-Fuse Network. *Phys Rev B* (1987) 36:367–80. doi:10.1103/physrevb.36.367
15. Chakrabarti BK, and Benguigui LG. *Statistical Physics of Fracture and Breakdown in Disordered Systems*. Oxford: Oxford Science Publications (1997).
16. Manzato C, Shekhawat A, Nukala PKVV, J. Alava M, Sethna JP, and Zapperi S. Fracture Strength of Disordered Media: Universality, Interactions, and Tail Asymptotics. *Phys Rev Lett* (2012) 108:065504. doi:10.1103/physrevlett.108.065504
17. Roux Sp., Hansen A, Herrmann H, and Guyon E. Rupture of Heterogeneous media in the Limit of Infinite Disorder. *J Stat Phys* (1988) 52:237–44. doi:10.1007/bf01016411
18. Hansen A, and Schmittbuhl J. Origin of the Universal Roughness Exponent of Brittle Fracture. Surfaces: Stress-Weighted Percolation in the Damage Zone.. *Phys Rev Lett* (2003) 90:045504. doi:10.1103/physrevlett.90.045504
19. Thomson R, Hsieh C, and Rana V. Lattice Trapping of Fracture Cracks. *J Appl Phys* (1971) 42:3154–60. doi:10.1063/1.1660699
20. Curtin WA, and Mater J. On Lattice Trapping of Cracks. *J Mater Res* (1990) 5:1549–60. doi:10.1557/jmr.1990.1549
21. Rice JR. Dislocation Nucleation from a Crack Tip: An Analysis Based on the Peierls Concept. *J Mech Phys Sol* (1992) 40:239–71. doi:10.1016/s0022-5096(05)80012-2
22. Pérez R, and Gumbsch P. Directional Anisotropy in the Cleavage Fracture of Silicon. *Phys Rev Lett* (2000) 84:5347–50. doi:10.1103/physrevlett.84.5347
23. Bernstein N, and Hess DW. Lattice Trapping Barriers to Brittle Fracture. *Phys Rev Lett* (2003) 91:025501. doi:10.1103/physrevlett.91.025501
24. Mattoni A, Colombo L, and Cleri F. Atomic Scale Origin of Crack Resistance in Brittle Fracture. *Phys Rev Lett* (2005) 95:115501. doi:10.1103/physrevlett.95.115501
25. Hansen A, and Hemmer PC. Burst Avalanches in Bundles of Fibers: Local versus Global Load-Sharing. *Phys Lett A* (1994) 184:394–6. doi:10.1016/0375-9601(94)90511-8
26. Zapperi S, Ray P, Stanley HE, and Vespignani A. First-Order Transition in the Breakdown of Disordered Media. *Phys Rev Lett* (1997) 78:1408–11. doi:10.1103/physrevlett.78.1408
27. Zapperi S, Nukala PKVV, and Simunovic S. Crack Roughness and Avalanche Precursors in the Random Fuse Model. *Phys Rev E* (2005) 71:026106. doi:10.1103/physreve.71.026106
28. Zapperi S, Nukala PKVV, and Šimunović S. Crack Avalanches in the Three-Dimensional Random Fuse Model. *Physica A: Stat Mech its Appl* (2005) 357:129–33. doi:10.1016/j.physa.2005.05.071
29. Dalmas D, Lelarge A, and Vandembroucq D. Crack Propagation through Phase-Separated Glasses: Effect of the Characteristic Size of Disorder. *Phys Rev Lett* (2008) 101:255501. doi:10.1103/physrevlett.101.255501
30. Malakhovsky I, and Michels MAJ. Effect of Disorder Strength on the Fracture Pattern in Heterogeneous Networks. *Phys Rev B* (2007) 76:144201. doi:10.1103/physrevb.76.144201
31. Ray P, and Date G. Spatial Scaling in Fracture Propagation in Dilute Systems. *Physica A: Stat Mech its Appl* (1996) 229:26–35. doi:10.1016/0378-4371(95)00431-9
32. Parihar RPS, Mani DV, Banerjee A, and Rajesh R. Role of Spatial Patterns in Fracture of Disordered Multiphase Materials. *Phys Rev E* (2020) 102:053002. doi:10.1103/physreve.102.053002
33. Silberschmidt VV. Effect of Material's Randomness on Scaling of Crack Propagation in Ceramics. *Int J Fract* (2006) 140:73–85. doi:10.1007/s10704-005-3994-8
34. Shekhawat A, Zapperi S, and Sethna JP. From Damage Percolation to Crack Nucleation through Finite Size Criticality. *Phys Rev Lett* (2013) 110:185505. doi:10.1103/physrevlett.110.185505
35. Moreira AA, Oliveira CLN, Hansen A, Araújo NAM, Herrmann HJ, and Andrade JS, Jr. Fracturing Highly Disordered Materials. *Phys Rev Lett* (2012) 109:255701. doi:10.1103/physrevlett.109.255701
36. Schmittbuhl J, Roux S, Vilotte J-P, and Jorgen Måløy K. Interfacial Crack Pinning: Effect of Nonlocal Interactions. *Phys Rev Lett* (1995) 74:1787–90. doi:10.1103/physrevlett.74.1787
37. Ramanathan S, Ertaş D, and Fisher DS. Quasistatic Crack Propagation in Heterogeneous Media. *Phys Rev Lett* (1997) 79:873–6. doi:10.1103/physrevlett.79.873
38. Peng C-K, Havlin S, Schwartz M, and Stanley HE. Directed-polymer and Ballistic-Deposition Growth with Correlated Noise. *Phys Rev A* (1991) 44:R2239–R2242. doi:10.1103/physreva.44.r2239
39. Xia ZC, and Hutchinson JW. Crack Patterns in Thin Films. *J Mech Phys Sol* (2000) 48:1107–31. doi:10.1016/s0022-5096(99)00081-2
40. Hansen A, Hemmer PC, and Pradhan S. *The Fibre Bundle Model*. Germany: Wiley VCH (2015).
41. Chakrabarti BK, Biswas S, and Pradhan S. Cooperative Dynamics in the Fiber Bundle Model. *Front Phys* (2021) 8:613392. doi:10.3389/fphy.2020.613392
42. Biswas S, Roy S, and Ray P. Nucleation Versus Percolation: Scaling Criterion for Failure in Disordered Solids. *Phys Rev E* (2015) 91:050105(R). doi:10.1103/physreve.91.050105
43. Hidalgo RC, Moreno Y, Kun F, and Herrmann HJ. Fracture Model with Variable Range of Interaction. *Phys Rev E* (2002) 65:046148. doi:10.1103/physreve.65.046148
44. Roy S. Predictability and Strength of a Heterogeneous System: The Role of System Size and Disorder. *Phys Rev E* (2017) 96:042142. doi:10.1103/PhysRevE.96.042142
45. Sinha S, Roy S, and Hansen A. Phase Transitions and Correlations in Fracture Processes Where Disorder and Stress Compete. *Phys Rev Res* (2020) 2:043108. doi:10.1103/physrevresearch.2.043108
46. Roy S, and Ray P. Critical Behavior in Fiber Bundle Model: A Study on Brittle to Quasi-Brittle Transition. *Epl* (2015) 112:26004. doi:10.1209/0295-5075/112/26004
47. Sinha S, Roy S, and Hansen A. Crack Localization and the Interplay between Stress Enhancement and thermal Noise. *Physica A: Stat Mech its Appl* (2021) 569:125782. doi:10.1016/j.physa.2021.125782
48. Roy S, Biswas S, and Ray P. Modes of Failure in Disordered Solids. *Phys Rev E* (2017) 96:063003. doi:10.1103/physreve.96.063003
49. Kadar V, Danku Z, and Kun F. Size Scaling of Failure Strength with Fat-Tailed Disorder in a Fiber Bundle Model. *Phys Rev E* (2017) 96:033001. doi:10.1103/PhysRevE.96.033001
50. Kadar V, and Kun F. System-size-dependent avalanche statistics in the limit of high disorder. *Phys Rev E* (2019) 100:053001. doi:10.1103/PhysRevE.100.053001
51. Kadar V, Pal G, and Kun F. Record Statistics of Bursts Signals the Onset of Acceleration Towards Failure. *Sci Rep* (2020) 10:2508. doi:10.1038/s41598-020-59333-4
52. Tadic B, Mijatovic S, Janicevic S, Spasojevic D, and Rodgers GJ. The Critical Barkhausen Avalanches in Thin Random-Field Ferromagnets with an Open Boundary. *Scientific Rep* (2019) 9:6340. doi:10.1038/s41598-019-42802-w
53. Spasojevic D, Mijatovi S, Navas-Portella V, and Vives E. Crossover from Three-Dimensional to Two-Dimensional Systems in the Nonequilibrium Zero-Temperature Random-Field Ising Model. *Phys Rev E* (2018) 97:012109. doi:10.1103/PhysRevE.97.012109
54. Pierce FT. 32—X.—Tensile Tests for Cotton Yarns v.—"The Weakest Link" Theorems on the Strength of Long and of Composite Specimens. *J Text Inst* (1926) 17:355. doi:10.1080/19447027.1926.10599953
55. Fisher RA, and Tippett LHC. Limiting Forms of the Frequency Distribution of the Largest or Smallest Member of a Sample. *Math Proc Camb Phil Soc* (1928) 24:180–90. doi:10.1017/s0305004100015681
56. Smith RL, and Phoenix SL. Asymptotic Distributions for the Failure of Fibrous Materials under Series-Parallel Structure and Equal Load-Sharing. *J Appl Mech* (1981) 48:75–82. doi:10.1115/1.3157595

57. Stormo A, Gjerden KS, and Hansen A. Onset of Localization in Heterogeneous Interfacial Failure. *Phys Rev E* (2012) 86:025101(R). doi:10.1103/physreve.86.025101
58. Roy S, and Biswas S. Size Distribution of Emitted Energies in Local Load Sharing Fiber Bundles. *Front Phys* (2021) 9:643602. doi:10.3389/fphy.2021.643602
59. Baro J, Corral A, Illa X, Planes A, Salje EKH, Schranz W, et al. Statistical Similarity between the Compression of a Porous Material and Earthquakes. *Phys Rev Lett* (2013) 110:088702. doi:10.1103/physrevlett.110.088702

Conflict of Interest: The author declares that the research was conducted in the absence of any commercial or financial relationships that could be construed as a potential conflict of interest.

Publisher's Note: All claims expressed in this article are solely those of the authors and do not necessarily represent those of their affiliated organizations, or those of the publisher, the editors and the reviewers. Any product that may be evaluated in this article, or claim that may be made by its manufacturer, is not guaranteed or endorsed by the publisher.

Advantages of publishing in Frontiers

OPEN ACCESS
Articles are free to read for greatest visibility and readership

FAST PUBLICATION
Around 90 days from submission to decision

HIGH QUALITY PEER-REVIEW
Rigorous, collaborative, and constructive peer-review

TRANSPARENT PEER-REVIEW
Editors and reviewers acknowledged by name on published articles

Frontiers
Avenue du Tribunal-Fédéral 34
1005 Lausanne | Switzerland

Visit us: www.frontiersin.org
Contact us: frontiersin.org/about/contact

REPRODUCIBILITY OF RESEARCH
Support open data and methods to enhance research reproducibility

DIGITAL PUBLISHING
Articles designed for optimal readership across devices

FOLLOW US
@frontiersin

IMPACT METRICS
Advanced article metrics track visibility across digital media

EXTENSIVE PROMOTION
Marketing and promotion of impactful research

LOOP RESEARCH NETWORK
Our network increases your article's readership